Improving Environmental Aspects of Perovskite Solar Cells by Lead Alternatives

Zur Erlangung des akademischen Grades einer
DOKTORIN der INGENIEURWISSENSCHAFTEN (Dr.-Ing.)

von der KIT-Fakultät für
Elektrotechnik und Informationstechnik
des Karlsruher Instituts für Technologie (KIT)

angenommene
DISSERTATION

von

Julia Rebecca Zillner (M.Sc.)
geb. in Augsburg

Tag der mündlichen Prüfung: 28.01.2022

Hauptreferent: Prof. Dr. Michael Powalla
Korreferent: Prof. Dr. Karl Leo

Abstract

The development of new renewable and regenerative technologies is in high demand in order to reduce greenhouse emissions, thus minimizing the negative effects of climate change. Perovskite solar cells are, for this purpose, a very promising newcomer in solar cell technology with enormous efficiency improvements in the last few decades. However, these highly efficient solar cells are lead-containing compounds which can have critical implications for commercialization and general acceptance.

Hence, for a reduced impact on human health and an improved environmental sustainability, this work investigates two chemical elements in lead-alternative perovskite compounds and their potential in stable and efficient perovskite solar cells.
Tin instead of lead is a clear candidate to meet these criteria, having already demonstrated decent solar cell performance compared to other lead-alternatives. In 1:1 tin-lead mixed perovskite solar cells, a strategy to replace the unfavorable hole transport layer (HTL) polyethylene dioxythiophene polystyrene sulfonate (PEDOT:PSS) and to implement a methylammonium (MA^+)-free perovskite absorber was pursued to lay the foundations for a more stable solar cell architecture. Furthermore, new unique findings were demonstrated for the commonly used tin(II)fluoride (SnF_2) additive in tin perovskite absorbers. A SnF_2 accumulation at the PEDOT:PSS interface was discovered. The accumulated SnF_2 reacts with the PEDOT:PSS forming a tin(II)sulfide (SnS) interlayer, which, as SnS a p-type semiconductor, should beneficially impact the solar cell performance. By thoroughly optimizing the perovskite interfaces and perovskite crystalline morphology to minimize recombination losses, the solar cell efficiency could be increased up to 6.6 % with a high open-circuit voltage (V_{OC}) of up to 670 mV for formamidinium tin iodide ($FASnI_3$)-based perovskite solar cells. A high reactivity of these absorbers in the ambient atmosphere was verified by tin oxidation, highlighting the necessity of solar cell preparation and encapsulation in an inert atmosphere. Stability analysis of these tin-containing perovskite solar cells in ambient atmosphere and under thermal stress revealed that the solar cell deterioration seems to be dominated by the degradation of the solar cell stack rather than solely the perovskite itself.
As tin perovskite absorbers' human health and environmental impact are controversially discussed, a second substitute element, bismuth, is explored. It can be integrated into highly sustainable perovskite-like crystalline compounds. A strategy to deposit and modify homogeneously and dense cesium bismuth iodide ($Cs_3Bi_2I_9$) perovskite films with different band-gap energies was implemented. Furthermore, first solar cell devices were demonstrated.

This work highlights the trade-off between high solar cell performance, and environmental and human health aspects. Tin-containing perovskite absorbers achieve high solar cell efficiencies with low human health and environmental impact, whereas bismuth-based perovskite solar cells accomplish poor solar cell performance but are considered to have no impact on human health

and the environment.
The work contributes to the general knowledge of lead-free perovskites with new insights into strategies for PEDOT:PSS- and MA^+-free devices, the working principle of SnF_2, and approaches to reduce recombination losses by interfacial and morphology engineering.

Kurzfassung

Die Reduktion von Treibhausgasen ist essentiell um die negativen Auswirkungen des Klimawandels zu limitieren. Um dies zu erzielen, bedarf es der Entwicklung neuer, regenerativer Technologien zur Energiewandlung. Perowskitsolarzellen sind hierfür eine vielversprechende Photovoltaiktechnologie, welche in den letzten Jahren enorme Effizienzsteigerungen erreichen konnten. Die Kommerzialisierung und gesellschaftliche Akzeptanz dieser Technologie wird jedoch durch das dabei eingesetzte Blei erschwert.

Um Auswirkungen auf die menschliche Gesundheit zu reduzieren und die Umweltverträglichkeit zu verbessern, werden in dieser Arbeit zwei chemische Elemente als Alternativen zu Blei in Perowskitverbindungen und deren Potential in stabilen, effizienten Perowskitsolarzellen erforscht.
Zinn ist dabei ein besonders vielversprechender Bleiersatz. Dies begründet sich vor allem in seiner Verträglichkeit für Mensch und Umwelt sowie den hohen Solarzellwirkungsgraden. In dieser Arbeit wurde eine Strategie für 1:1 Zinn-Blei gemischte Perowskitsolarzellen entwickelt, die ungünstige Löchertransportschicht PEDOT:PSS (Polyethylendioxythiophen- Polystyrolsulfonat) und den Methylammonium (MA^+)-haltigen Perowskitabsorber zu ersetzen. Dies legt die Grundlage für eine stabilere Solarzellarchitektur. Des Weiteren, wurden neue Erkenntnisse zum Mechanismus des häufig eingesetzten Zinnfluoride (SnF_2) Additives in Zinn-Perowskitsolarzellen erlangt. Es wurde eine bevorzugte Akkumulation des SnF_2 an der PEDOT:PSS Grenzfläche nachgewiesen. Darüber hinaus reagiert das akkumulierte SnF_2 mit dem PEDOT:PSS unter Bildung einer Zinnsulfid (SnS) Zwischenschicht, wodurch ein positiver Einfluss auf die Solarzellleistung erwartet wird, da SnS ein p-Halbleiter ist. Durch umfangreiche Optimierung der Grenzschichten und des Perowskitabsorbers zur Reduktion von Rekombinationsverlusten, konnten Solarzelleffizienzen von bis zu 6,6 % für Zinn-Perowskitsolarzellen mit hohen Leerlaufspannungen von bis zu 670 mV erzielt werden. Stabilitätsanalysen von Zinnhaltigen Perowskitsolarzellen unter atmosphärischen Umgebungsbedingungen haben deren hohen Oxidationsempfindlichkeit verifiziert, wodurch deren Herstellung und Operation unter inerten Bedingung notwendig ist. Des Weiteren, scheint die Solarzelldegradation in atmosphärischer Umgebung und bei Hitze durch die Verschlechterung der Solarzellschichten dominiert zu werden und nicht durch die Degradation des Perowskitabsorbers selbst.
Da der Einfluss von Zinn-Perowskiten auf Mensch und Umwelt kontrovers diskutiert wird, wurde ein weiteres Substitutionselement, Bismut, untersucht. Die Verwendung dieses in Perowskitartigen Verbindungen zeichnet sich durch deren hohen Verträglichkeit für Mensch und Umwelt aus. In dieser Arbeit wurde eine Strategie verfolgt, um homogene, kompakte $Cs_3Bi_2I_9$-basierte Filme mit variablen Bandlücken abzuscheiden. Mittels der hergestellten Solarzellen konnten Solarzelleigenschaften dieses Materials nachgewiesen werden.

Diese Arbeit betrachtet das Spannungsfeld zwischen der Verträglichkeit der verwendeten Perowskitabsorber für Mensch und Umwelt und der Leistung von Solarzellen. Zinn-haltige Perowskitabsorber erzielen hohe Wirkungsgrade, erhöhen jedoch lediglich die Verträglichkeit für Mensch und Umwelt. Wohingegen, Bismut basierte Absorber verträglich für Mensch und Umwelt sind, aber herausfordernd geringe Solarzellleistungen aufweisen.
Diese Arbeit reiht sich in das allgemeine Verständnis bleifreier Perowskitabsorber ein. Neue Erkenntnisse wurden hinsichtlich einer Strategie für PEDOT:PSS- und MA^+-freier Bauelemente, dem Verständnis des SnF_2-Mechanismus und neuer Ansätze zur Reduktion von Rekombinationsverlusten mittels Grenzflächen- und Morphologieoptimierungen gewonnen.

Preface

An dieser Stelle möchte mich bei allen bedanken, die mich auf dem Weg meiner wissenschaftlichen Arbeit unterstützt und begleitet haben.

Mein besonderer Dank gilt zunächst meinem Doktorvater Prof. Dr. Michael Powalla, der mir die Möglichkeit gegeben hat am ZSW meine Doktorarbeit anfertigen zu dürfen. Die zahlreichen wissenschaftlichen Diskussionen haben den Weg zu dieser Arbeit geebnet.

Zudem möchte ich Prof. Dr. Karl Leo für das Übernehmen des Korreferats danken.

Ferner Dank ich Dr. Erik Ahlswede für seine intensive, wissenschaftliche Betreuung, die Einführung in die Thematik und die Zeit für die zahlreichen Gespräche.

Ich danke auch den Kollegen der NeMa-Gruppe für die freundliche und hilfsbereite Arbeitsatmosphäre. Insbesondere möchte ich mich für die Vielzahl an wissenschaftlichen Auseinandersetzungen, Versuchsplanungen, Analytikmessungen sowie Unterstützung im Labor danken. Auch über diese Gruppe hinaus hat mich das ZSW herzlich aufgenommen und mich tatkräftig bei der Umsetzung meiner Arbeit unterstützt.

Des Weiteren möchte ich den externen Projektpartnern Hans-Gerd Boyen und Philip Schulz für deren Einsatz in weiteren Analytikmethoden sowie wissenschaftlichen Erörterungen danken.

Besonders für die zahlreichen Aufmunterungen möchte ich auch meinen Bürokollegen, Tim und Mario, danken.

Mein besonderer Dank gilt natürlich zuletzt Florian und meiner Familie, welche mich auf dem Weg zu meiner Dissertation unermüdlich, liebevoll unterstützt und ermutigt haben.

List of content

Abbreviations and symbols

ABI	$A_3Bi_2I_9$
ACN	acetonitrile (CH_3-CN)
BA^+	butylammonium ($(CH_3-CH_2-CH_2-CH_2-NH_3)^+$)
BiI_3	bismuth iodide (bismuth(III) iodide)
bis-PCBM	bis-$PC_{60}BM$ (bis-(1-[3-(methoxycarbonyl)-propyl]-1-phenyl)-[6.6]C_{62})
Bi_2S_3	bismuthsulfide (bismuth(III) sulfide)
$Bi(xt)_3$	bismuth xanthate (bismuth(III) O-3,3-dimethylbutan-2-yl dithiocarbonate)
BCP	bathocuproine (2,9-dimethyl-4,7-diphenyl-1,10-phenanthroline)
Br^-	bromide
CB	chlorobenzene
$Cs_3Bi_2I_9$	cesium bismuth iodide
Cl^-	chloride
Cs^+	Cesium
CsI	cesium iodide
DCB	dichlorobenzene (1,2-dichlorbenzene)
DMF	dimethylformamide
DMSO	dimethylsulfoxide
EDX	energy-dispersive X-ray spectroscopy
E_g	band-gap energy
EtOH	ethanol
ETL	electron transport layer
ETM	electron transport material
EQE	external quantum efficiency
FA^+	formamidinium ($(NH_2-CH=NH_2)^+$)
FAI	formamidiniumiodide
$FASnI_3$	formamidinium tin iodide
FA_2SnI_6	di-formamidinium tin hexa-iodide
$FAPbI_3$	formamidinium lead iodide
FF	fill factor
FTO	fluorine-doped tin oxide
FWHM	full width at half maximum
GIXRD	grazing incidence X-ray diffraction
H_2O	water
HAXPES	hard x-ray photoelectron spectroscopy

HCl	hydrochloric acid
HI	hydrogen iodide
HTL	hole transport layer
HTM	hole transport material
I^-	iodide
I_2	diiod
ICBA	indene-C_{60} bisadduct
IPA	isopropanol
ITO	indium tin oxide ($In_{0.74}Sn_{0.08}O_{0.18}$)
IQE	internal quantum efficiency
$J(V)$-curves	current-density–voltage dependency curves
J_{SC}	short-circuit current density
J_{mpp}	current density at the maximum power point
LUMO	lowest unoccuppied molecular orbital
MA^+	methylammonium ($(CH_3-NH_3)^+$)
MAI	methylammonium iodide
$MAPbI_3$	methylammonium lead iodide
$MA_3Bi_2I_9$	methylammonium bismuth iodide
MPP	maximum power point
NP	nanoparticle
NMP	N-Methyl-2-pyrrolidone
Pb^{2+}	lead
PbSCN	leadthiocyanate
PbI_2	lead iodide
PEA^+	phenethylammonium ($(C_6H_5-CH_2-CH_2-NH_3)^+$)
PEAI	phenethylammoniumiodide
PEA_2SnI_4	phenethylammonium tin iodide
PEDOT:PSS	polyethylene dioxythiophene polystyrene sulfonate (poly(3,4-ethylene dioxythiophene) polystyrene sulfonate)
PCBM	$PC_{60}BM$ ([6,6]-phenyl-C_{61}-butyric acid methyl ester)
PCE	power conversion efficiencyat standard test conditions
PMMA	poly(methyl methacrylate) (Poly(methyl 2-methylpropenoate))
PL	photoluminesce
PTAA	poly(triaryl amine) (Poly[bis(4-phenyl)(2,4,6-trimethylphenyl)amine])
RT	room temperature
SEM	scanning electron microscopy
SiO_2-NP	silicon oxide nanoparticle
Spiro-OMeTAD	conductive fluorene (2,2',7,7'-Tetrakis[N,N-di(4-methoxyphenyl)amino]-9,9'-spirobifluorene))
TCO	transparent conductive oxide
TRPL	transient resolved photoluminescence

Sn^{2+}	tin(II)
Sn^{4+}	tin(IV)
SnI_2	tin(II)iodide
SnI_4	tin(IV)iodide
SnF_2	tin(II)fluoride
SnO_2	tin(IV)oxide
SnS	tin(II)sulfide
SnS_2	tin(IV)sulfide
TiO_2	titanium oxide
tBP	4-tert butyl pyridine
TEOS	tetraelthylorthosilicate
ToF-SIMS	Time of Flight - Secondary Ion Mass Spectronomy
V_{OC}	open-circuit voltage
V_{mpp}	voltage at the maximum power point
XRD	X-ray diffraction
XRF	X-ray fluorescence
XPS	X-ray photoelectron spectroscopy
ZSW	Zentrum für Sonnenenergie- und Wasserstoff-Forschung Baden-Württemberg

1 Introduction and objectives

In 2015 190 countries agreed to reduce global warming by 1.5°C compared to the pre-industrial time, in the so-called "Paris Agreement" [1]. To achieve this goal, the European Union (EU) agreed to reduce greenhouse gas emissions by 55 % by 2030 compared to the year 1990 [1]. Photovoltaic is a key technology to accomplish this goal [2]. It is a renewable, non-fossil energy power technology with multiple versatile applications.

The development of new photovoltaic technologies could support this goal by improving solar cell performance and enabling new application areas. Perovskite solar cells as an upcoming new photovoltaic technology are very promising for these purposes. Perovskite solar cells have achieved high efficiencies of up to 25.5 % [3]. Furthermore, their fabrication is cost-efficient and their energy payback time is favorable [4]. This is achieved by non-vacuum, low-temperature preparation processes, and only low material consumption as absorber layers of less than 1 µm thickness are sufficient for effective light absorption [4]. Moreover, flexible and light-weight modules can be produced to allow completely new application areas in building-integrated photovoltaics (BIPV), vehicle-integrated photovoltaics (VIPV) and wearable devices [4].

Besides these outstanding advantages, some challenges still have to be faced for commercializing of this technology. These include concerns about the human health and environmental impact, its stability, and process scalability.
Human health and environmental concerns are caused by the lead-containing perovskite absorber used in the highly efficient solar cells. Already a small lead concentration of 1 ppm in the human blood is considered to have long-term consequences on human health [5]. Furthermore, the EU restricts the amount of lead in new electric and electronic devices to 0.1 wt.% [6]. This is only 1 % of the lead expected in lead-based perovskite solar cells [7]. Consequently, the EU can hinder the commercialization of lead-based perovskite solar cells in the European market. Thus, lead alternatives in perovskite absorbers should be explored in advance.

Ideal lead-alternative perovskite solar cells should fulfill the following requirements for these absorbers:

- no risk for human health and the environment from the perovskite absorber, its precursor compounds, and possible degradation products
- beneficial physical and chemical properties for solar cell applications, allowing high solar cell conversion efficiencies
- sufficient stability in ambient atmosphere
- economically reasonable material and production costs

Since fulfilling all of the above requirements is challenging up to now, compromises have to be made. Often there is a trade off between human health and environmental impact, and solar cell performance.
Tin is so far the most promising lead-alternative as these perovskite absorbers achieve the highest

solar cell performance [8, 9]. These are advantageous considering human health and environmental aspects. However, their impact is still controversially reported [10, 11], and their stability is highly challenging as tin easily oxidizes, deteriorating the perovskite bulk phase [12, 13].
Bismuth-like-perovskite absorbers are non-toxic, environmentally friendly [14], and have sufficient ambient stability [15]. But, these absorbers suffer from unsatisfactory solar cell performance so far [16].

This work considers the hurdles of commercializing perovskite technology: substituting lead with another element to reduce its impact on human health and the environment, and achieving insights into the perovskite absorber stability.
The overall aims of this work are the following:

- investigating lead substitution by tin
  - tin-lead mixed perovskite absorbers; examine a PEDOT:PSS-alternative-HTL in MA^+-free perovskite solar cells
  - tin perovskite absorbers; investigate the mechanism behind the commonly used SnF_2 additive, improve charge layer interfaces and perovskite morphology to boost the solar cell performance
  - stability analysis of these tin-containing perovskite absorbers
- studying lead substitution by bismuth in lead-free bismuth-based compounds; implement a perovskite deposition method, optimize perovskite morphology and investigate strategies to reduce the huge band-gap energy

This work is structured into six chapters.
Chapter 2 lays the fundamentals of perovskite solar cells, lead-alternative perovskite absorbers, and perovskite solar cells' stability. The preparation- and characterization methods used in this work are described in chapter 3. As a lead alternative in perovskite absorbers, tin is investigated in chapter 4, because of its advantages considering human health and environmental aspects. Further, environmentally friendly and non-toxic bismuth-like perovskite absorbers are explored in chapter 5. Lastly, a summary and perspective are given in chapter 6.

Since chapters 4 and 5 are the main parts of this work, a detailed description is outlined in the following.

In chapter 4, perovskite absorbers with lead being replaced by tin are explored to improve sustainability.
Therefore, tin-lead mixed perovskite absorbers with partially replaced lead by tin are investigated in the beginning (chapter 4.1). The focus is placed on solar cell stack modification by substituting the HTL PEDOT:PSS (subchapter 4.1.1) and investigating an MA^+-free perovskite composition (subchapter 4.1.2).
The amount of lead is further reduced by exploring pure tin perovskite absorbers in chapter 4.2. The impact of the commonly used additive SnF_2 on the perovskite bulk is analyzed in subchapter 4.2.1. Furthermore, charge layer interfaces are modified to improve the solar cell performance by optimized perovskite morphology, energy band alignment, and passivate perovskite defects (subchapter 4.2.2). The perovskite crystal phase is textured to improve crystal morphology, and its impact on solar cell performance is analyzed in subchapter 4.2.3.

As the stability of tin-containing perovskites is crucial for the overall solar cell performance, this aspect is investigated in chapter 4.3. The reactivity of the perovskite absorbers in the ambient atmosphere is analyzed in subchapter 4.3.1. Further, aging tests are performed by thermal stress (see subchapter 4.3.2).

In chapter 5, bismuth perovskite-like solar cells are optimized as a non-toxic and environmentally friendly perovskite absorber. A strategy for homogeneous and dense perovskite deposition is implemented in chapter 5.1. In addition, the impact of modified perovskite crystalline morphology on solar cell performance is analyzed. In chapter 5.2 methods to reduce the huge band-gap are examined.

2 Fundamentals of perovskite solar cells with improved sustainability

This chapter outlines the unique properties of perovskite absorbers. Perovskite are outstanding semiconductors for solar cell applications due to their high charge carrier mobilities [17, 18], low exciton binding energies [19], high absorption coefficients [20], long charge carrier diffusion length [17, 21], and adjustable band-gap energies [22–24]. Based on these characteristic properties, a solar cell efficiencies of up to 25.5 % were achieved in literature [3].

The physical fundamentals of perovskite solar cells, in general, will be described in chapter 2.1. Structural and electronic characteristics of perovskite solar cells resulting in a facile way of band-gap tune-ability are outlined in chapter 2.1.1. The working mechanism of perovskite absorbers in solar cells will be described in chapter 2.1.2. Besides the high power conversion efficiency, the perovskite technology also faces some challenges like toxicity, environmental and stability concerns. The toxic and environmental worry can be lowered by replacing the unfavorable lead with less harmful alternatives, discussed in chapter 2.2. The degradation process has to be understood to enhance the perovskite solar cell stability. Intrinsic perovskite phase instability, changes of perovskite absorbers by external stress conditions, and deterioration of interfaces are known to negatively influence the solar cell performance (outlined in chapter 2.3).

2.1 Hybrid perovskite solar cells

This chapter describes the basics of perovskite solar cells, focusing on the unique perovskite's crystallographic structure and band structure. Moreover, the application of perovskite absorbers in solar cells is outlined, and their working principles are introduced.

Perovskite originally solely describes a crystal structure, which Rose first established by discovering and characterizing the inorganic material $CaTiO_3$ in 1839 [25]. The first hybrid inorganic-organic perovskite MASnIBr (Methylammonium tin iodine bromide) was synthesized and analyzed many years later in 1978 by Weber [26]. In 2009 Kojima incorporated the hybrid inorganic-organic perovskite methylammonium lead iodide ($MAPbI_3$) in a solar cell the first time with 3.8 % efficiency [27]. Since then, the hybrid inorganic-organic perovskite compound gained increasing interest as an absorber material for solar cells. More than 23000 reports have been published until now since the first time the perovskite material has shown promising results as a solar cell material in 2005.[1]

[1] Number of publications found searching for *perovskite solar cells* in *web of science* in October 2021

2.1.1 Concept of perovskite absorbers

The following chapter outlines the crystallographic structure and band structure, as they will be relevant in the optimization strategy of the lead alternative perovskite absorbers in chapter 4. As opto-electronic and charge carrier properties are minor considered in this work, the reader is addressed for these purposes to the reviews of Frohna et al. [28], Jena et al. [29], or Kim et al. [30].

Crystallographic Structure

This paragraph gives an overview of the perovskite crystallographic structure in dependency on its composition and temperature.

Perovskite compounds typically have an ABX_3 chemical formula. The idealized perovskite crystallizes in a cubic phase with corner-sharing BX_6 octahedra sitting at each corner and an A cation in the middle of the cube (see figure 2.1). For hybrid organic-inorganic perovskites, the monovalent cation A is most likely methylammonium (MA^+), formamidinium (FA^+) or cesium (Cs^+); whereas B is a divalent metal cation typically either lead (Pb^{2+}) or tin(II) (Sn^{2+}) and X a monovalent halide anion, e.g. iodide (I^-), chloride (Cl^-) and/or bromide (Br^-) [28].

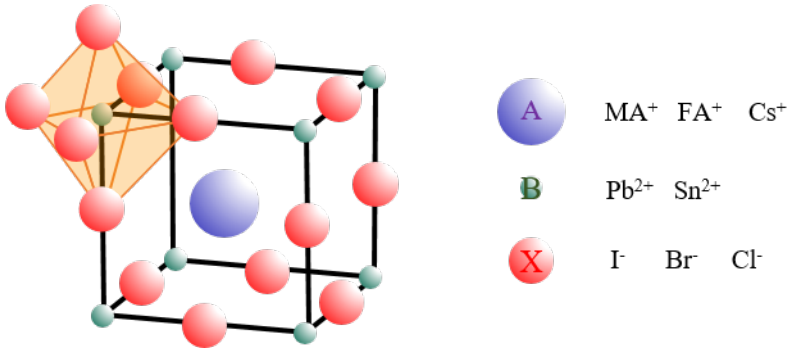

Figure 2.1: Schematic illustration of the cubic ABX_3 perovskite structure.

For predicting the likelihood of forming a stable cubic perovskite crystal, the Goldschmidts tolerance factor t and octahedral factor μ could be taken into consideration [31, 32]:

$$t = \frac{r_A + r_X}{\sqrt{2}(r_B + r_X)}, \qquad \mu = \frac{r_B}{r_X} \tag{2.1}$$

with r describing the radius of the ions A, B, and X, respectively. An ideal cubic perovskite structure is formed for t=1 [33]. The compound crystallizes in a perovskite phase for $0.81 < t < 1.11$ [33]. A symmetrically cubic phase is favored for t=0.9-1 [31, 32, 34]. A slightly distorted perovskite structure, like a tetragonal or orthorhombic one by BX_6 octahedra tilting, is preferred for t=0.8-0.9 [31,32,34]. If the A cation is too large (t>1), lower-dimensional perovskites will be formed [32, 33]. For too small cation A (t<0.71), non-perovskites will be likely formed [31, 32]. Further μ defines the form of the BX_6 octahedra. This considers if the cation B fits in the octahedra of X-anions. A symmetrically octahedra is formed for $0.4 < \mu < 0.9$ [32, 33].

Typically hybrid inorganic-organic perovskite surpasses multiple phase transitions in dependence on the temperature [28]. Some of these phases can even be photoinactive, thus unfavorable for solar cell devices applications [35]. Phase transition temperatures are dependent on the perovskite composition [28, 36–38]. $MAPbI_3$, for example, generally crystallizes in a tetragonal crystal structure at room temperature. The cubic phase is formed at temperatures above 330 K. When decreasing the temperature below 160 K, the orthorhombic phase is preferred [38–40]. Whereas for the $FASnI_3$ perovskite, the cubic phase is already formed below room temperature. The transition to the tetragonal phase is around 255 K and to the orthorhombic phase at 155 K [41, 42].

Band structure

The perovskite composition also affects the band structure. The band structure of perovskite absorbers are formed by hybridization of the X anion and B cation, thus are dependent on the corner-sharing BX_6 octahedra (see Fig. 2.2). Thereby the valence band (VB) is built by an antibonding hybrid of the X anion p-orbital (X_p) and B cation s-orbital (B_s). Whereas the conduction band (CB) is in principle influenced by the antibonding hybridization of the X anion p-orbital (X_p) and B cation p-orbital (B_p). However, it is dominated by the B_p orbital since the X_p orbital energy is very shallow compared to the B_p orbital [28, 43].

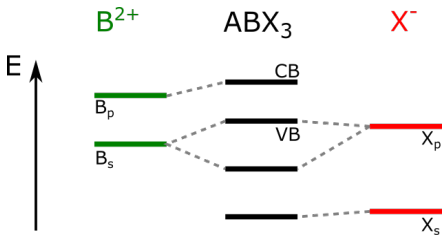

Figure 2.2: Simplified schematic illustration of the antibonding hybridization of the s and p atomic orbital of the cation B (B_s, B_p) with the p atomic orbital of the anion X (X_p) in perovskite absorbers forming the conduction (CB) and valence band (VB).

Based on the described hybridization theory, the band-gap tuning of the perovskite absorber is outlined in the next section. The impact of common X and B ions on the band structure is outlined.

For X anions, substituting the iodide with other halogen ions like bromide or chloride, the valence band is dominated by the halides increasing electronegativity of the halides, resulting in a downshift [43, 44]. Whereas the conduction band increases by a confinement effect due to smaller B-X distance [43]. Thus the band-gap energy is in general increased from iodide to bromide to chloride. For example, the band-gap of $MAPbI_xBr_{1-y}$ can be modified from 1.6 to 2.3 eV with enhancing bromide concentration [22, 23].

Moreover, altering the B cation can drastically tune the band-gap energy, e.g. replacing lead by tin. The valence and conduction band energy increases due to a higher atomic orbital energies of tin as it has a smaller electronegativity [43]. However, the valence band shift is more pronounced [43]. This results in a lowered band-gap energy of up to 1.2 eV for tin-lead mixed perovskite absorbers [24] and tin compounds in general [43].

Illustrated strategies only hold if changes in the crystal structure are negligible [43]. Structural changes are mainly due to non-fitting A cation in the perovskite cube, resulting in either BX_6 octahedra tilting or increased distance between these. Since the valence band is formed by

an antibonding hybridization of the metal and halide, decreasing the overlap between these by structural changes reduces the valence band energy [28,43,45]. The conduction band is expected to be less influenced by changes of the A cation [28, 43, 45]. Substituting FA^+ by Cesium (Cs^+) in $FASnI_3$ perovskite leads to a reduction of the unit cell, so increasing the B-X atomic overlap and thus destabilizing the valence band resulting in an energy increase. Moreover, the band-gap is reduced. While doing so in a formamidinium lead iodide ($FAPbI_3$) perovskite distorts the BX_6 octahedra, thus decreasing the B-X atomic overlap stabilizing the valence band by reducing its energy. Additionally, the band-gap is enhanced [45].

2.1.2 Perovskite absorbers in solar cells

After a brief introduction of the basic perovskite properties, the application of these absorbers in solar cells is outlined in this chapter.

Perovskite absorbers are in principle considered to be intrinsic semiconductors. Würfel supposed the following working mechanism for an intrinsic semiconductor in a solar cell, schematically illustrated in figure 2.3 [46].

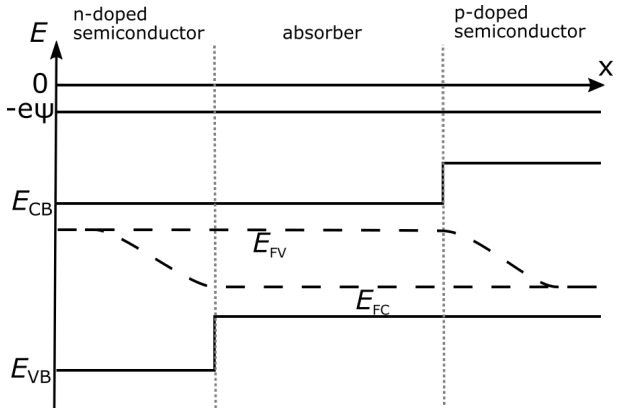

Figure 2.3: Adapted and modified schematic illustration of the solar cell working principle [46]. An intrinsic semiconductor with an electron (n-doped semiconductor) and hole membrane (p-doped semiconductor) are shown under illumination. E displays the energy of the conduction (E_{CB}) and valence (E_{VB}) band, their corresponding fermi levels (E_{FV}, E_{FC}) and the electrical potential $e\psi$.
Absorbing light in the intrinsic semiconductor leads to the quasi-fermi energy splitting of E_{FV} and E_{FC}. Electrons (holes) can flow to the left (right), whereas holes (electrons) are blocked at the n-type (p-type) semiconductor.

Excitons are generated by absorbing light in the perovskite, leading to the quasi-fermi level splitting in the intrinsic semiconductor.
Perovskites have a high absorption coefficient [20], thus enable absorber thicknesses of only some hundreds of nanometers. Further, the absorption can be easily modified by the band-gap energy. As a next step, the exciton has to be converted into free charges. For perovskite materials, the exciton binding energy, is in general, lower than the thermal activation energy [19]. Thus no external driving force is needed to create free charges. These free charges need then to be transported to the electrodes of the solar cell before they recombine. The recombination probability is lowered by a high charge carrier mobility [17, 18] and long charge carrier diffusion length [17, 21], which are both fulfilled sufficiently by perovskite absorbers.

“Membranes“ further favor the charge extraction by letting pass either electrons or holes. Those membranes are n- (or p-type) semiconductors with adjusted conduction (valence) band energy for efficient electrons (holes) transport with huge band-gap energies forming an energetic barrier for holes (electrons) at this interface. In principle, the energetic band structure can be adjusted by either tuning the perovskite absorber properties (band-gap tuning) or modifying the p- or n-type semiconductors using different materials.

The following possible planar solar cell architectures for perovskite solar cells based on the presented mechanism above are outlined. Accordingly, the solar cell stack consists of at least the perovskite absorber layer, the n- and p-type semiconductor layer, named electron transport layer, and hole transport layer. This stack is sandwiched between two electrode materials for charge extraction. At least one of them must be transparent, so that light can be transmitted and absorbed at the perovskite layer. These layers can be arranged in two main device architectures. When the incident light passes the hole transporting layer before the perovskite layer, the device is defined as a p-i-n or inverted stack (Figure 2.4 a). Depositing the layers in reverse order will lead to the n-i-p or standard stack (Figure 2.4 b) [28, 47].

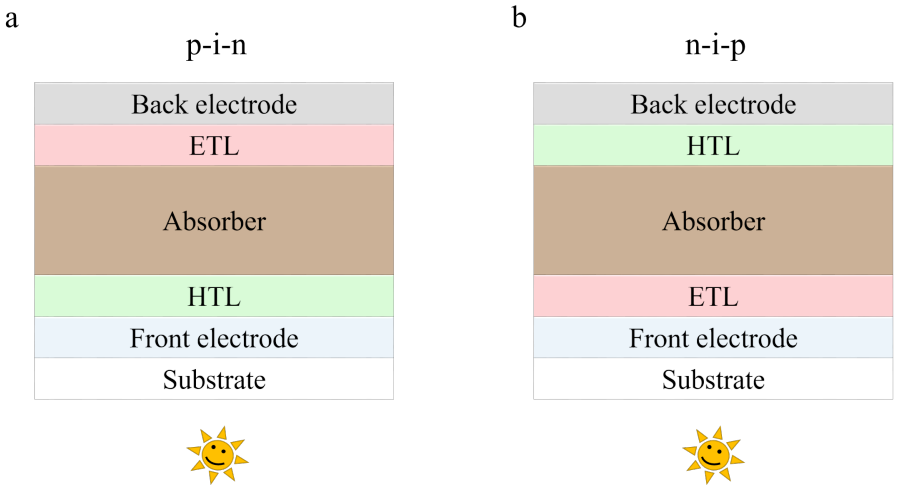

Figure 2.4: Illustration of possible planar perovskite solar cell architecture with illumination from the bottom glass side. a: p-i-n or inverted architecture; b: n-i-p or standard architecture.

Examples for ETL and HTL material are given based on the relevance for this work. Conventional electron transport layer (ETL) materials are the inorganic titanium oxide (TiO_2) and organic C_{60} derivatives. For fabricating a TiO_2 layer, sintering temperatures of 500°C are needed [48]. Since these high temperatures would damage the perovskite, this ETL material can only be used in n-i-p devices. Additionally, those layers have to be deposited on fluorine-doped tin oxide (FTO) as transparent conductive oxide (TCO) material since indium tin oxide (ITO) would degrade at those high temperatures, too. Organic C_{60} derivatives like $PC_{60}BM$ (PCBM), indene-C_{60} bisadduct (ICBA), bis-$PC_{60}BM$ (bis-PCBM) in combination with bathocuproine (BCP) are alternatives to high temperature processed ETL materials. Those have favorable band alignments [49, 50] and the ability to passivate perovskite defects at their surface and grain boundaries [51].

One of the most established HTL materials is the conductive fluorene (Spiro-OMeTAD) because of its high performance in solar cells and easy layer deposition [52]. For p-i-n devices, the HTL material poly(triaryl amine) (PTAA) or PEDOT:PSS are typically used. PEDOT:PSS is cost-effective, processable at low temperature, and facilely deposited by spin-coating [53]. PTAA is an alternative hole transport material (HTM) for PEDOT:PSS with a high solar cell performance [54] but complex processing due to its hydrophobic surface [55].

Relevant HTL, ETL, and perovskite materials in chapters 4 and 5 of this work are summarized in figure 2.5 with their band energies.

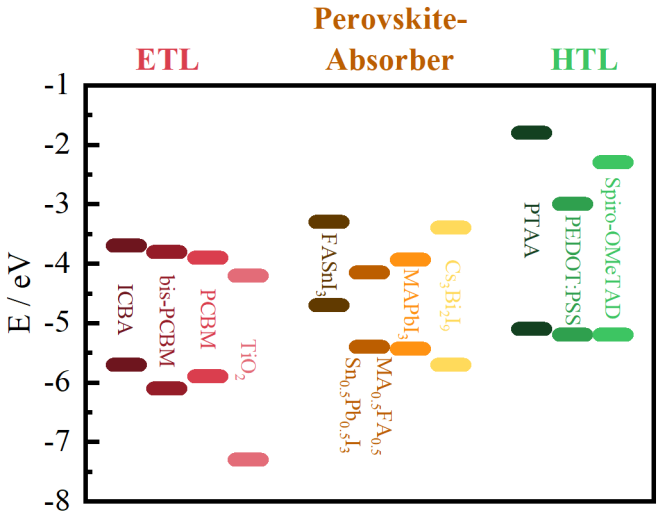

Figure 2.5: Adapted and modified schematic illustration of exemplary perovskite, HTL, and ETL energy levels [16, 47, 56–58].

2.2 Lead alternatives for improved sustainability

The toxicity and environmental harm of lead-containing highly efficient perovskite absorbers can be a hurdle to the perovskite solar cell commercialization. Thus substitution possibilities are highly discussed and researched in foresight. The European Union restricted the lead amount to 0.1 wt.% for electrical and electronic devices [6], which is only 1% of the expected lead in perovskite solar cells [7]. Already 10 ppm lead in the human blood can influence human health. Furthermore, environmental concerns should be kept in mind, too [5].

As already highlighted in chapter 2.1.2, the band structure of hybrid perovskite absorber can be assigned to the hybridization of the lead orbitals. Thus the electronic configuration of lead results in the outstanding properties of perovskite absorbers. Consequently, to achieve at least similar properties with lead-free devices, the lead-alternative should have a similar electronic configuration (filled 6s-orbital and almost empty 6p-orbital). Lead-alternatives fulfilling these criteria can be easily found close to the lead position in the periodic table, as seen in the cutout of the periodic table (figure 2.6).
Lead-free perovskite should have chemical and physical properties beneficial for solar cells application. These are high absorption coefficients in the solar spectrum, appropriate charge

transport properties (low effective masses, high charge mobilities), and suitable, direct band-gaps. Furthermore, compounds with high comparability for human health and the environment, and high ambient stability are favored. Moreover, the fabrication route of the perovskite absorber should be facile and cost-effective with moderately harmful and dangerous chemicals.

In the following, a general overview of lead-free compounds is given. These are compared according to their solar cell performance, toxicity, environmental impact, fabricating route, and stability. Lead alternative elements are divalent cations of group 14 (tin, germanium) or trivalent cations from group 15 (bismuth, antimony). Double perovskites combining monovalent cations of group 11 (copper, silver) and trivalent cations of group 15 are also possible lead-alternatives. These lead alternative elements are summarized in figure 2.6.

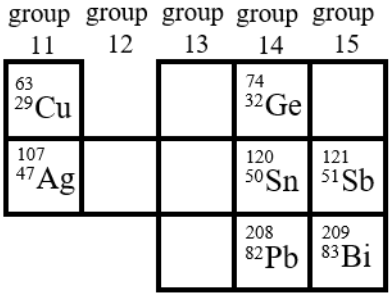

Figure 2.6: Relevant lead-alternative elements illustrated as a cut out of the periodic table.

The group 14 elements (tin, germanium) are the most promising lead alternatives as similar electronic configurations let expect comparable physical and chemical properties [59,60]. Moreover, they have the same oxidation state, thus can form the usual ABX_3 perovskite structure [61]. Furthermore, their precursor salts are less toxic than the lead analogs. Especially Ge salts seem to be environmentally friendly and less harmful for human health [15]. The biggest hurdle of these perovskite compounds is their stability since they easily oxidize to the corresponding B^{4+} ion. This is probably the reason for lower solar cell efficiencies compared to lead-based perovskite solar cells [60]. Ge-based perovskite absorbers generally have high band-gap energies due to a distorted crystal structure by the smaller ionic radius of Ge^+ [15, 61]. $CsGeI_3$ perovskite has the lowest band-gap energy of 1.6 eV. Nevertheless, for this composition, a solar cell efficiency higher than 1 % has not been achieved so far due to poor perovskite morphology and fast oxidation [59, 60]. Tin-based perovskite solar cells are far more promising with already achieved efficiencies of over 14 % [9] and are therefore described in more detail in chapter 2.2.1. Outstanding results were achieved by Chen et al., who combined Sn and Ge in the perovskite absorber. The stability is improved in this study by a "native-oxide surface passivization". The $CsSn_{0.5}Ge_{0.5}I_3$ composition revealed an appropriate band-gap energy of around 1.5 eV with a solar cell efficiency of 7% [62]. These hybrid systems can be promising alternatives if they are deposited by a low-cost method from a solution. So far, the described result was achieved by thermally evaporating the perovskite layer [62].

Improved environmental stability are reported for the trivalent cation compounds of antimony (Sb^{3+})- and bismuth (Bi^{3+}) [61]. Since these ions have a higher oxidation state, they cannot form the typically BX_6 octahedra network. Instead a perovskite-like $A_3B_2X_9$ structure is formed [63]. This generally leads to low structural dimensionality resulting in high exciton energies and unfavorable charge transport properties (low mobilities, high resistivities) due to

limited interaction between neighboring ions in the perovskite-like structure [61]. Furthermore, they often have indirect band-gaps [61]. With $MA_3Sb_2I_9$, a efficiency of 2.04% is reported [64]. However, for fabricating this compound, unfavorable hydrogen iodide (HI) seems to be necessary [64]. Moreover, antimony is expected to be toxic [65]. Consequently, antimony substitutions are not favored with respect to solar cell performance, fabrication methods, and toxicity. Bismuth compounds are the most promising candidates with respect to toxic and environmental concerns [66], and will be discussed in more detail in chapter 2.2.2.

Outstanding stability in ambient conditions [61], a moderate impact on human health [56, 63], and a 3D structural dimensionality [61] can be achieved by double perovskites [63]. Those merge properties of two elements. However, most combinations reveal compounds with indirect band-gaps larger than 2 eV, low electronic dimensionality, and unfavorable charge transport [61]. The $Cs_2AgBiBr_6$ compound is the most promising candidate of these double perovskite with an efficiency of around 2.5% [67, 68]. However, these perovskite layers have to be fabricated at high temperatures of up to 250°C leading to unfavorable preparation process [67, 68].

Further Bi-related alternatives are the $Ag_aBi_bI_x$ (with $x = a+3b$) compounds, named rudorffites-based perovskite [15]. Those have similar stability behavior as the discussed one before but have promising lower direct band-gap energies of around 1.7-1.9 eV [69]. With sulfur-doped Ag_3BiI_6 absorbers a high efficiency of up to 5.4% could be reached [70]. These precursor compounds are non-toxic, which would make those very promising alternatives for lead-free perovskite solar cells. However, fabricating routes of these perovskite layers again include HI [70], which is a very strong acid, so fabricating does not fulfill the conditions of facile synthesis.

Other lead-free perovskites can be made from copper (Cu) or titanium (Ti). For some titanium-based perovskites, promising electronic and optical properties were calculated [71]. Even for Cs_2TiBr_6, an efficiency of already 3% could be reached [72]. These Ti(IV) compounds seems to be promising regarding the low toxicity of the CsBr and $TiBr_4$ educts and stability. Unfortunately, these high solar cell performances have only been achieved so far by thermal evaporation.
Cu-based compounds are until now less explored and revealed efficiencies of less than 1% [63, 73]. These up to now low achieved efficiency can be related to a low absorption coefficient, high effective mass of holes, and low conductivity due to the 2D dimensionality [63]. Furthermore, these suffer from the reduction of Cu^{2+} ions to Cu^{+} [63].

During this consideration, tin and bismuth have shown to be promising lead-alternatives. Thus these perovskite alternatives are investigated in more detail in the following subchapters.

2.2.1 Tin as a lead alternative

Tin is the most promising lead alternative achieving high efficiencies of over 14% [9] for lead-free solar cells and up to 21.7 % [8] for lead-reduced ones. These materials have beneficial solar cell properties like direct band gaps [61], high charge carrier mobilities [63], and a 3D dimensional order [42]. Furthermore, these perovskite absorbers offer facile fabrication routes such as solution processing similarly to the lead-based ones.

Tin $ASnX_3$ perovskite

The following will address the stat-of-the-art of tin perovskite absorbers and their challenges.

First of all, Sn^{2+} easily oxidizes to Sn^{4+} forming Sn-vacancies defects acting as recombination sites in solar cell devices [12, 13]. Further, crystallization of the tin perovskite layer is in general faster than for their lead analogs. Thus forming compact, pinhole-free layers with few surface defects is challenging [13]. Lastly, tin perovskite solar cells suffer from high V_{OC} losses which is due to a high defect density [13, 74] and unfavorable band alignment with charge carrier interfaces [13]. Described effects often influence each other and can not be solved individually. Some known ways to overcome these challenges are considered in the following.

Oxidation of the tin perovskite absorber from Sn^{2+} to Sn^{4+} during solar cell fabrication can be reduced straightforwardly by carefully preparing the perovskite film in an inert atmosphere with less than 1 ppm oxygen and water and using chemicals with low oxygen and water residues. Moreover, reducing agents can be used to prevent and retard oxidation processes. A widespread reducing agent is SnF_2. It prevents the oxidation processes and decreases the overall Sn vacancy concentration [75]. Other reducing agents, often used in combination with SnF_2, are hydrazine, triethylphosphine, and hypophosphorous acid [76–79].

By chemical engineering, the nucleation and fast crystallization of tin perovskites can be controlled, improving the perovskite morphology. There are, in general, two possibilities known: either slowing down the drying process or using additives to influence nucleation and crystal growth. The drying process of the perovskite layer can be controlled by recrystallizing the perovskite [80] or by a dimethylsulfoxide (DMSO) vapor treatment during perovskite layer annealing [81]. Smoother pinhole-free perovskite layer could be achieved with both techniques. Besides this method, coordinating additives with SnX_2 [82–84] or the Sn-perovskite [85] influence the nucleation and crystal growth rate, improving perovskite morphology. Examples for these additives are the huge cation phenethylammonium iodide [86], ethylenediammonium diiodide [85], 5-ammoniumvaleric acid iodide [82, 87] and thiocyanate anions [83, 84] to name some.
Since inserting huge cations on side A is a widely used approach in tin perovskite solar cells, these are outlined in more detail in the following. Besides already named improved perovskite morphology, those huge cations also influence the perovskite layer's crystallographic morphology by forming quasi-2D interlayers in the 3D perovskite bulk, improving their perovskite film crystallinity and crystal orientation. Commonly used bulky cations are phenethylammonium (PEA^+) [83, 84, 86, 88–91], butylammonium (BA^+) [77, 91, 92] and 5-ammoniumvaleric acid (AVA^+) [82, 87]. The expected unique nucleation and crystallization processes of pure 2D, mixed 2D/3D, and pure 3D systems leads to their characteristic crystallographic properties [93]. In 3D systems nucleation and crystallization takes place at the solution/air surface and in the bulk, which leads to randomly oriented crystallites [93]. The usage of bulky cations suppresses the random bulk nucleation and crystallization present in 3D systems, in favor for a controlled nucleation and crystallization from the solution/air surface only, leading to highly oriented crystallites [93]. Thus an increased control of crystalline ordering in 2D/3D mixed perovskite is achieved [93]. Challenges for devices arise if the huge cation organic interlayers grow parallel to the substrate. This can limit the charge transport due to the insulating big cation spacer. However, improved device stability due to enhanced hydrophobicity at the surface can be achieved [90, 94]. The crystal facet orientation can be manipulated by adding formamidinium thiocyanate (FASCN) [84] or ammonium chloride (NH_4Cl) [33], which favors

perpendicular growth of the organic spacer by interacting with Sn^{2+}. These crystallographic improvements in general improve solar cell performance [83, 88] and stability [12] since defects are reduced by higher-ordered films decreasing dark recombination states and starting sites for degradation processes.

V_{OC} losses are suspected to result from high band offsets between the perovskite and charge layers. The band offsets can be adjusted by perovskite composition and/or charge transport layer modification. Different cations and anions can generally tune the perovskite's band energies (see chapter 2.1.1). Liu et al. added PTN-Br to the perovskite precursor solution to adjust the valence band [95]. Moreover, the addition of ethylenammonium alters the conduction and valence band of the perovskite [94]. Additionally, forming 2D interlayers influence the perovskite absorber band-structure [77, 90, 96, 97]. Charge layer interface alignment can be further done by either modifying the charge transport layers [98] or using other charge transport materials (ICBA) [99].

The impact of tin-based perovskite solar cells on human health and the environment remains debatable and uncertain [100]. Only a limited number of studies access this concerns of tin perovskites and its related compounds.
Two experimental studies report on contradictory impact, as a non-negligible toxicity of tin(II)iodide (SnI_2) were observed for zebrafishes [10], whereas tin perovskite plant absorption was reduced [11] compared to their lead analogs.
However, a wide research group often considers tin-based perovskite to be less harmful to the environment and human health [61, 101–103], as the degradation product of the perovskite and precursor material SnI_2 is the water-insoluble tin oxide (SnO_2) [104].
In this work tin perovskite will be regarded as lead-alternative with mitigated toxicity and environmental harm, following the majority opinion of researchers.

Tin-lead mixed $ASn_zPb_{1-z}X_3$ perovskites

Tin-lead mixed perovskite absorbers are a compromise of improved solar cell performance and stability to only mitigated human and environmental concerns of the lead, as they only reduce the lead content.
The solar cell efficiencies of those perovskite absorbers are far higher than those of pure tin perovskite ones. Xiao has shown a high efficiency of 21.7% for a $FA_{0.7}MA_{0.3}Sn_{0.5}Pb_{0.5}I_3$ composition [8]. In addition, they generally have higher stability than the pure tin perovskite absorbers [104, 105] (further illustrated in the chapter on the perovskite stability 2.3.2). Moreover, these tin-lead mixed perovskites have an anomalous band-gap behavior, making low band-gap energies of 1.2 eV possible [106, 107]. These low band-gap energies provide the possibility to use those tin-lead mixed perovskite solar cells as bottom cells in tandem devices [106, 107].

Besides outlining the advantages of tin-lead mixed perovskite absorbers, the following chapter will focus on their main challenges and strategies to solve these. The challenges are, in general, quite similar to the pure tin ones, so only a short overview is given. Extended reviews are given by Zhu et al. [107], Wang et al. [106], and Cao et al. [100].

Similar to pure tin-based perovskite solar cells, the fast reaction of SnI_2 makes it challenging to control the perovskite layer formation. So comparable strategies to pure tin perovskites are used to achieve increasing morphological control. Improved perovskite layer formation can be realized by adding DMSO into the precursor solution [108] or using thiocyanate additives [109, 110].

Even if the stability of tin-lead mixed perovskite absorbers is improved compared to that of pure tin ones, the oxidation of Sn_2^+ is still problematic. Reducing agents to retard or prevent oxidation are SnF_2 [111], ascorbic acid [112], and tin powder [113, 114]. Inserting huge cations like BA^+ to form a 2D/3D mixed perovskite film enhance the ambient stability as well [115].

MA^+-free perovskite compositions and PEDOT:PSS-alternative-HTL have been less explored in tin-lead mixed perovskite devices [116]. However, this is a general strategy in lead-based perovskite solar cells [28, 117]. Already first studies showed detrimental effects of PEDOT:PSS [118] and MA^+ [119] also in tin-lead mixed perovskite solar cells. The general motivation for replacing MA^+ in lead-based solar cells [120–126] will be outlined in detail in the stability review, chapter 2.3. Further, PEDOT:PSS is known for his hygroscopic and acidic nature [116, 127–129] (also outlined in more detail in the stability review, chapter 2.3) .

In summary, tin-containing perovskite solar cells still have not reached the lead-based ones regarding their solar cell performance and stability. The impact of tin perovskite on the environment and human health seems to be less harmful than the lead-based ones, but have to be explored in the future.

2.2.2 Bismuth as a lead alternative

As already highlighted, bismuth is a promising alternative to lead, due to its low environmental and human health impact [14]. The precursor materials for perovskite layer fabricating and the $A_3Bi_2I_9$ (ABI) perovskite are very stable [15].

Since bismuth is a trivalent cation, it can-not form the typical ABX_3 perovskite structure due to charge imbalance. Instead, a perovskite-like structure $A_3Bi_2I_9$ is formed, where the $Bi_2I_9^{3-}$ is an isolated framework without corner-sharing octahedra as in the typical perovskite structures [130]. In figure 2.7 the typical $A_3Bi_2I_9$ is displayed.

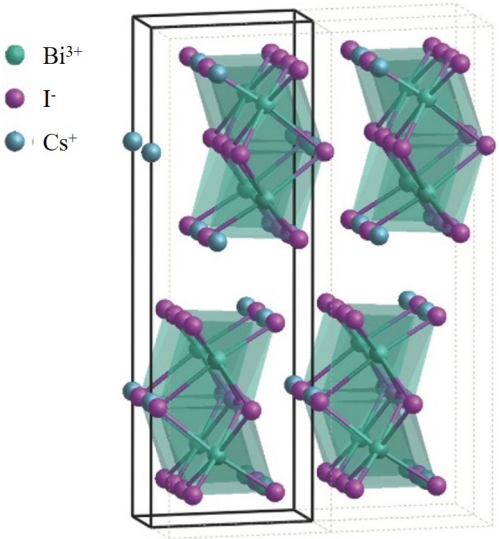

Figure 2.7: Schematic illustration of the $A_3Bi_2I_9$ crystal structure modified and adapted with permission from [131].

Most ABI perovskite solar cells suffer from low efficiency of around 1% due to low dimensionality [15] resulting in high exciton binding energies of around 100-300 meV [15], huge indirect band-gap energies (~1.8-2.9 eV [15]), worse perovskite morphology, and high background carrier density [69]. Strategies to face those challenges are considered in the following.

Forming a dense, homogeneous perovskite layer is essential for high-performing solar cells. The fast reaction of the precursor salt bismuth iodide (BiI_3) and methylammonium iodide (MAI) leads to a fast crystallization with undesired grain formation [29, 132]. Fabrication of appropriate ABI perovskite films is, therefore, challenging [29, 132]. Different solvent engineering techniques were performed to control the crystallization process. This can be done by using different solvents having higher boiling temperatures or forming complexes with precursor materials. By this, the supersaturation level is increased during nucleation and crystal growth, leading to compact perovskite layers. Solvents therefore are DMSO, 4-tert butyl pyridine (tBP) and N-Methyl-2-pyrrolidone (NMP) [132, 133]. Further methods are solvent annealing or re-crystallization of the film with the precursor solvent [16, 134].

Incorporating trivalent elements, like gallium and indium, to form a dual cation Cs_3BiXI_9 perovskite can lower the huge band-gap [135]. Additionally, theoretical calculation showed that integrating selenium and sulfur is expected to reduce the bandgap as well [136]. Vigneshwaran et al. reduced the band-gap energy from 2.04 eV to 1.45 eV for methylammonium bismuth iodide ($MA_3Bi_2I_9$) by inserting sulfur, but no application in solar cells is reported [137].

The outlined advantages and challenges of bismuth and tin-containing perovskite absorbers in the last chapter highlight the different strategies in the research field of lead substitution in perovskite absorbers. A compromise between either a low (at least at present) solar cell performance for bismuth-based perovskites or of an uncertain impact on the environment and human health (up to now) and instability issues for tin-based perovskite absorbers have to be made.

2.3 Stability of perovskite solar cells

Besides the toxicity concerns, the stability of perovskite solar cells is an additional challenge needed to be faced for commercializing this technology. The stability of perovskite solar cells includes several aspects, schematically depicted in figure 2.8.
Understanding overall perovskite solar cells' stability, insights into critical preparation conditions initiating the degradation process, and its stability in operation have to be gained. Therefore, a systematic investigation of aging conditions and sample designs is needed. The material stability of a perovskite film by intrinsic and extrinsic conditions is the first step (see figure 2.8a). Intrinsic stability testing is generally performed by aging the samples in a inert atmosphere, e.g., storing these in a nitrogen-filled glovebox (see figure 2.8a). Further, the degradation of perovskite absorbers under extrinsic conditions like light, temperature (85°C), atmosphere (oxygen, nitrogen, humidity) is commonly explored. These stress parameters can be combined and cycled in advanced tests [138]. These tests are extended by analyzing the extrinsic solar cells' stability. Exploring solar cells discloses additional material intermixing and interaction affecting the device stability(see figure 2.8b) [138]. Final aging tests in the laboratory would include the stress of encapsulated devices in long-term (see figure 2.8c). Up to now, there are no

standardized test protocols and long-term experience for perovskite solar cells [138]. However, a typical experiment for encapsulated devices is the *damp heat* at 85°C with 85 %rH for 1000 hours leaned to the standardized silicon solar cell testing [139]. As a last step the devices have to be tested in outdoor conditions (see figure 2.8d).

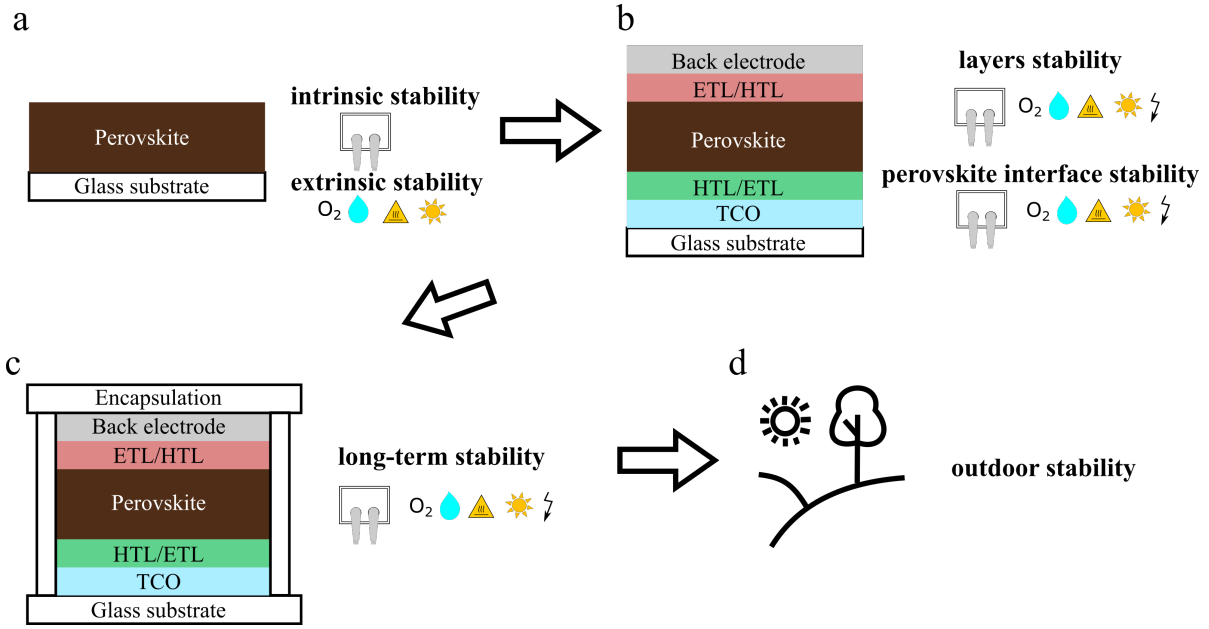

Figure 2.8: Simplified illustration of a systematic stability study of perovskite solar cells. It outlines the perovskite film (a), perovskite solar cell (b), encapsulated device investigation (c) and outdoor stability (d) under intrinsic (glovebox), oxygen, humid, heat, illuminated and electrical bias conditions.

As this work focuses on lead-alternatives and in detail on tin-containing perovskite solar cell optimization (see chapter 4), the literature screening on the stability of perovskite solar cells will focus on absorbers. As the stability of tin-containing perovskite solar cells is challenging due to the fast tin oxidation, only the first short-term aging tests (100 days) are generally reported [140]. So far, commonly, the intrinsic - or encapsulated stability testing is investigated. Furthermore, testing in an ambient atmosphere is presented [140]. The stability at elevated temperature, light, and electrical bias is not commonly explored. Thus, in the following, degradation processes are illustrated on tin-containing perovskite absorbers, as long as the literature provides information. Otherwise, examples of lead perovskite are outlined.
The intrinsic stability issues of perovskite absorbers will be discussed in chapter 2.3.1 and the extrinsic ones in chapter 2.3.2. Degradation mechanisms concerning the perovskite solar cell stack, like perovskite interfaces and other layers deterioration, will be presented in chapter 2.3.3.

2.3.1 Intrinsic stability of perovskite absorbers

This chapter outlines the material stability of perovskite absorbers excluding external stress factors from ambient atmosphere, light, and temperature, are excluded, here referred to 'intrinsic stability'. Two main aspects of the intrinsic stability of perovskite absorbers need to be considered: phase stability and ion migration.

Perovskite absorbers crystallize in different phase structures based on their composition and temperature (see chapter 2.1.1). The preferred crystal structure is predicted by the Goldschmidt factor, as already shown in equation 2.1. A perovskite phase is formed for t between 0.8 to 1. By composition engineering of mixing several anion and cations having varying sizes, the Goldschmidt factor can be optimized to the middle of this perovskite phase zone. Moreover, the cubic phase seems to be more stable than the distorted one [29]. A higher stability of the cubic multi-cation perovskite, optimized to the middle of the perovskite zone by altering the ions, was experimentally shown compared to the tetragonal $MAPbI_3$ perovskite [29]. However, secondary phases should be avoided especially in multi-cation perovskite systems [29].

Besides phase stability, ion migration is a common intrinsic challenge, too. The potential of ion migration is dependent on the defect density, interstitial spaces, size and charge of the ion, and the ion jumping rate. It is not clear if ion migration only occurs by an external electric field or not. Iodine is very prone to ion migration [141–143]. Ion migration is thought to be prevented by minimizing grain boundaries, which would cause high defect density that would acts as a channel for ion migration [29]. However, Wu et al. and Luo et al. showed that ion migration also occurs in single crystals with no grain boundaries [144, 145]. So the mechanism of ion migration has not been accurately specified up to now [29]. Another strategy to minimize ion migration can be realized by mixed perovskites. For example the ion migration barrier energy (estimated by DFT calculations) is enhanced by inserting the alkali metals Rb^+, K^+, Na^+, Li^+ as these inhabit at interstitial sites formation [29].

2.3.2 Perovskite absorbers under extrinsic conditions

The impact of extrinsic stress conditions like oxygen, moisture, light, and heat on the perovskite absorber material are described in the following. Especially, oxygen and moisture stability are relevant during solar cell preparation, as under operation the contact to these can be prevented by sample encapsulation.

The decomposition of tin perovskite absorbers in ambient atmosphere can be easily traced by the transition from a black-colored film to a transparent one. The deterioration of the perovskite absorber is influenced by oxygen and moisture. The process is described by the following reaction circle [146]:

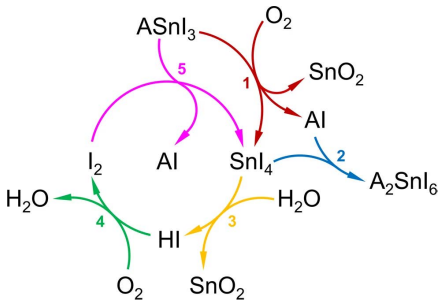

Figure 2.9: Decomposition scheme of tin perovskite absorber $ASnI_3$ in ambient atmosphere. Reaction 1: Oxidation of the $ASnI_3$ to tin(IV)oxide (SnO_2), AI and tin(IV)iodide (SnI_4). Side reaction 2: Reaction of AI and SnI_4 to form A_2SnI_6 perovskite. Reaction 3: Hydrolyses of the SnI_4 to HI with the by-product SnO_2. Reaction 4: Further oxidation of HI to form diiod (I_2) with water as a by-product. Reaction 5: Decomposition of the $ASnI_3$ in the presence of I_2 to SnI_4 with the by-product AI. Adapted from [146].

The decomposition of the $ASnI_3$ perovskite is initialized by an oxidization to SnI_4 with the by-products SnO_2 and AI (reaction 1). The formed SnI_4 can hereby either react with the AI to form a vacancy-ordered Sn(IV) double perovskite A_2SnI_6 (reaction 2) or hydrolyses in moisture atmosphere to HI and SnO_2 (reaction 3). The HI can further oxidizes to I_2 and water (H_2O) (reaction 4). The I_2 triggers the further decomposition of the $ASnI_3$ perovskite to AI and SnI_4 (reaction 5), restarting the decomposition cycle.
This reaction scheme highlights the impact of oxygen and moisture on the deterioration of tin perovskites. Pure moisture would not deteriorate the tin perovskite, as the illustrated decomposition is initialized by oxygen. Dry oxygen would lead to SnI_4, which further decomposes to A_2SnI_6, but no HI and I_2 would be formed. However, small amounts of oxygen in a slight moisture atmosphere would lead to a complete decomposition as the process is self-sustaining [146].

As the deterioration of tin perovskite in ambient atmosphere was outlined, the improved unique stability by adding lead into the perovskite to form tin-lead mixed perovskite is derived.
In general, two degradation mechanisms are possible for tin-containing perovskites in the first reaction-step. The tin and iodide in the perovskite compound can be (i) both or (ii) only the tin is oxidized. In reaction (i) the bonds of tin and iodide need to be broken as both elements are oxidized. Whereas, for process (ii) only the tin bonds are broken. Thus process (i) needs higher activation energy than (ii). In reaction (i), the compound decomposes to SnO_2 and I_2, whereas for (ii), these are SnI_4 and SnO_2. As the (ii) process is the less energetic one, this one is favored for tin perovskites. However, tin-lead perovskites decompose via the (i) process with higher activation energy. The (ii) process requires directly interacting Sn-I octahedra, which are limited in tin-lead mixed perovskite. Thus decomposition is forced to occur via the (i) reaction, actually being energetically less favorable. The tin-lead mixed perovskite thus requires higher activation energy than the pure tin ones leading to a higher stability of tin-lead mixed ones. Indeed, the activation energy for tin perovskite is 537 meV, whereas it is 731 meV for tin-lead mixed perovskites. The following chemical reaction summarizes the oxidation of tin-containing perovskites: [104]

$$2\,ASnI_3 + O_2 \longrightarrow 2\,AI + SnO_2 + SnI_4$$

$$2\,ASn_{0.5}Pb_{0.5}I_3 + O_2 \longrightarrow 2\,AI + PbI_2 + SnO_2 + I_2$$

Besides adding lead to the perovskite system, adding Cs^+ as an A-cation to the pure tin perovskite also improves the resistance to oxygen. This is considered to reduce the lattice and thus the Sn-I bonds (as long as phase stability is observed), strengthening these. [104]
However, there are even more strategies to prevent tin oxidation, shortly addressed in the following. Excess of Sn^{2+} by tin halides SnX_2 is a common method to suppress tin(IV) (Sn^{4+}) formation [12, 147–149]. Metal oxide barriers [62], functionalized organic molecules at the perovskite surface [96, 109] and large hydrophobic organic layers [83, 90, 150, 151] (also described as 2D perovskite layers) can enhance the resistance to oxygen [150]. Besides a hydrophobic coating, those large organic molecules lead to a more compact and higher crystalline perovskite film growth with reduced defects. Defects are preferable starting sides for oxygen and water infiltration [12].
The oxidation during the fabricating process can be prevented by using materials with high purity (Sn(II) halides, solvents) and processing in inert atmosphere conditions with low water and oxygen content [13]. Effective encapsulation would be a mechanical barrier to prolong the lifetime of perovskite solar cells.

While the impact of oxygen and moisture on tin containing perovskite is highly explored, the influence of light is rarely investigated [12, 114]. Thus, this is illustrated on lead perovskites in the following.

A combined impact of light and oxygen is reported for lead-based perovskite absorbers [152,153]. Absorbing light, superoxides are formed by transferring the electron from the excited perovskite to an oxygen molecule, as described in the following reaction scheme.

$$CH_3NH_3PbI_3 + O_2 \xrightarrow{\text{light}} CH_3NH_3PbI_3^{\bullet} + O_2^{-}$$

This superoxide reacts with the perovskite by deprotonating the MA^+ in $MAPbI_3$ and thus destroying the perovskite [152].

$$4\,CH_3NH_3PbI_3^{\bullet} + O_2^{-} \longrightarrow 2\,I_2 + 4\,CH_3NH_2 + 4\,PbI_2 + 2\,H_2O$$

Decomposition takes preferable place at defect sites, thus grain boundaries [12,154]. Theoretical calculation showed the crucial impact of iodine vacancies, which is further promoted by the fact that the most prominent defects at the surface are iodine vacancies [154]. Consequently, perovskite layer with large grains, lower defect densities and passivating iodine vacancies are expected to enhance stability [154]. Furthermore, preventing the formation of the superoxide species reducing the time scale of the excited perovskite by effectively extracting the electrons increases the stability [152,153]. By composition engineering of the perovskite to replace MA^+, enhances the stability as well [123,155,156]. Substituting the cation MA^+ with less acidic ones like FA^+ or Cs^+, which have a lower deprotonating capacity, will decrease the reaction probability with superoxides [12,157]. Moreover, bromide incorporating is thought to increase the stability since bromide decreased the protonation ability of MA^+ due to the higher electronegativity and thus stronger interaction with MA^+ [12,158].

Lastly, the temperature impact on perovskite stability needs to be considered since these undergo phase transitions in dependency on temperature [38, 157]. As tin perovskite solar cells are considered to have the cubic or pseudo-cubic phase at room temperature, no phase transition is expected for these compounds at elevated temperatures [42, 159, 160]. Since solar cells have to surpass a testing temperature of 85°C based on the proposed standard testing procedure for perovskite photovoltaic [138], the perovskite absorber should be stable at those temperature regimes. However, MAI irreversibly decomposes into NH_3 and CH_3I at these temperatures [120–124]. Higher temperature resistance was shown by Saliba et al. by composition engineering of the perovskite absorber [156].

2.3.3 Stability of perovskite solar cell devices

Having outlined the intrinsic and extrinsic stability of perovskite absorbers, interacting of charge transport layers and metals with the perovskite absorber in solar cell device are discussed in the following.

Effects of charge transport layers' stability are introduced. A failure of the device can be observed by a deterioration of charge transport properties, increased interface defects, and molecule penetration into and out of the perovskite structure. In general inorganic charge transport layers are considered to have higher ambient stability, while organic ones can be fabricated more easily at low temperatures, which is beneficial for the perovskite material stability [29].
In the following, the stability of relevant charge transport materials is presented. Fullerenes are

often used as ETM due to their passivation capacity of surface defects, thus improving perovskite solar cell performance [51, 157]. This further reduces the ion migration by passivated surface defects [161]. But these can suffer from morphological changes at elevated temperature forming clusters [162]. These morphological changes can already be observed by slightly increased temperature during light soaking [163]. Moreover, a very commonly used HTM is PEDOT:PSS due to its good conductivity, easy processing, and cost-effectiveness [157]. But PEDOT:PSS is acidic and hygroscopic. This can etch the indium tin oxide underneath, destroy the perovskite layer on top and insert water into the device [127–129]. Alternatively, PTAA can be used as a HTM having high solar cell performance [54] and improved stability [164].

Although the metal electrode is not in direct contact with the perovskite, its influence needs to be considered as well. Two main processes are reported, which reduce perovskite solar cell stability. One is the penetration of electrode atoms into the device, thus destroying the charge transport layer and perovskite by reacting with these. Domanski et al. reported Au penetration into the device, which could be prevented by inserting a Cr interlayer [165]. Further ion migrating from the perovskite can react and destroy the metal electrode. Guerrero and Kato revealed decomposition of the silver electrode by a reaction of silver and iodide. Both suggested that iodide is migrating from the perovskite layer through the charge transport layer [166, 167]. Guerrero introduced an alternately Cr_2O_3/Cr electrode combination to prevent the reaction of silver with iodide [166].

The conclusion and main findings from the literature screening are summarized in figure 2.10. This illustration highlights the trade-off between solar cell efficiency, perovskite stability, and the human health and environmental impact of lead and lead-alternative perovskite absorbers. The decision for investigating these lead-alternative perovskite absorbers (Bi, Sn, SnPb) in this work are based on making different compromises to the before named requirements.
Lead perovskite solar cells achieve a solar cell efficiency up to 25.5 % [3] and sufficient stability. However, due to the lead, their concerns on human health and the environment is relatively huge [5]. Using tin instead of lead is advantageous when considering human health and environmental aspects [61,101–103]. But up to now, limitations in the solar cell efficiencies have to be accepted (PCE=14 % [9]). Further, tin oxidation is challenging in terms of stability [146]. Tin-lead mixed perovskite absorbers lie between pure lead and pure tin ones in view of their human health and environmental aspects, solar cell performance and stability [8, 104]. Bismuth perovskite absorbers are outstanding due to their environmental friendliness and non-toxicity for humans [14], and high stability [15]. Nonetheless, poor solar cell efficiencies are so far reported (PCE=3 % [16]).

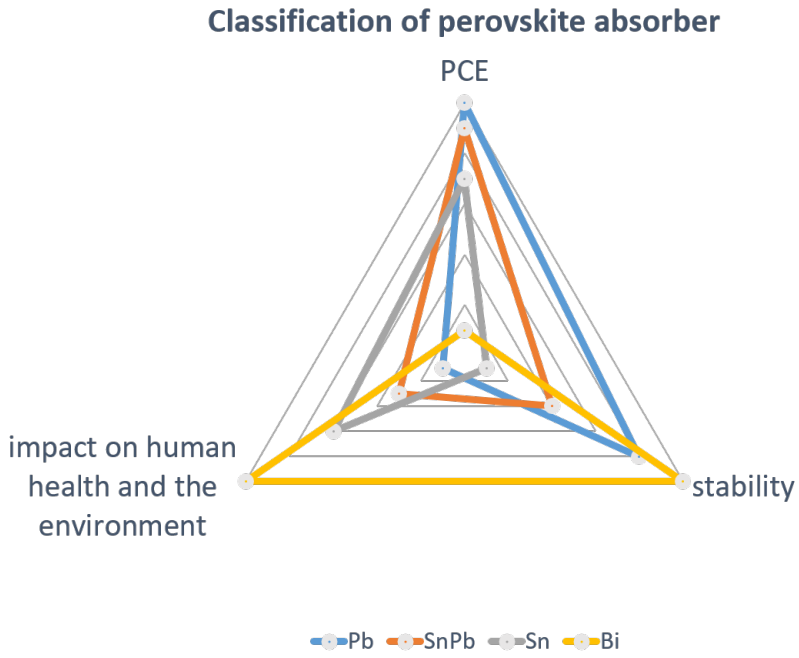

Figure 2.10: Schematic classification of Pb, SnPb, Sn, Bi perovskite absorber in regard to their power conversion efficiency, ambient stability, impact on the human health and environment.

3 Preparation and characterization methods

This chapter 3 outlines relevant methods for preparing (subchapter 3.1) and characterizing (subchapter 3.2) perovskite films and solar cells. The corresponding results will be discussed in chapter 4 and 5.

3.1 Preparation methods of perovskite solar cells

This chapter refers to the preparation methods of the perovskite films and solar cells prepared and characterized in this work. The subchapters are structured according to their preparation technique. Thus, subchapter 3.1.1 describes prepared layers from solution and suspension by spin coating, like perovskite and charge transport layers. Subchapter 3.1.2 illustrates the post-doping technique for perovskite layers by vapor deposition. The synthesis of bismuth xanthate ($Bi(xt)_3$) used as an additive in perovskite precursor solutions is described in the following subchapter 3.1.3. The last two subchapters describe electrodes' deposition by either physical vapor deposition (subchapter 3.1.4) or sputtering (subchapter 3.1.5). The used chemicals and materials are summarized in table A.1 in the appendix with their specific material properties.

The general used solar cell architectures in chapters 4 and 5 are illustrated in figure 3.1. These give an overview of the used solar cell stack in each chapter and the principle deposition technique.
For the p-i-n tin-containing perovskite solar cells PEDOT:PSS as HTL and a combination of PCBM with BCP as ETL are utilized as a reference solar cell architecture. ITO and silver are used as transparent front - and back contact. For tin-lead mixed perovskite solar cells an additional HTL option PTAA is used. For tin perovskite solar cells additional C_{60} derivatives replace the PCBM. Bismuth-based perovskite solar cells are prepared in an n-i-p architecture using commercially available FTO as TCO, TiO_2 as an ETL, Spiro-OMeTAD as HTL and gold as the back electrode.

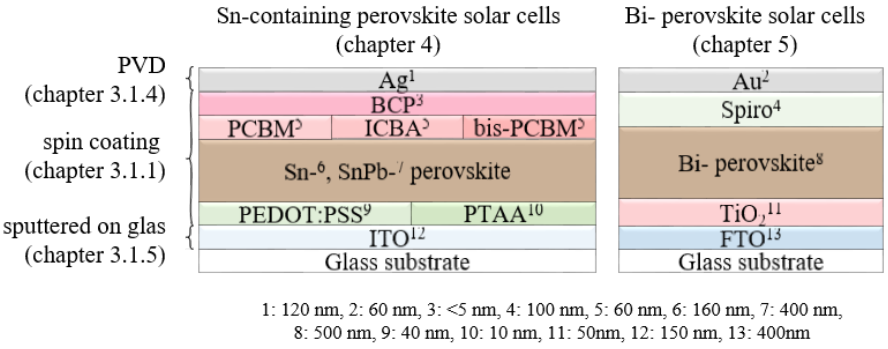

Figure 3.1: Schematic illustration of solar cell architectures used in this work with their layer thicknesses.

The solar cells in this work have an active area of 0.24 cm^2, which is defined by an overlap of the patterned transparent electrode and the back electrode, which is precisely deposited through a mask (see figure 3.2).

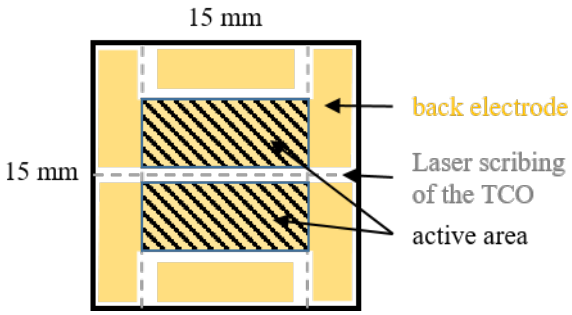

Figure 3.2: Illustration of the solar cell design on a 15 × 15 mm^2 glass sample yielding two solar cells with an active area of 0.24 cm^2 used in this thesis.

3.1.1 Layer deposition from solution via spin-coating

The following section will give an overview of layer deposition from solution or suspension by spin coating. A short description of the principle layer deposition procedure will be presented, further expanding with precise parameters summarized in tables. The first paragraph will describe the perovskite layer deposition. Further HTL and ETL preparation methods will be given. In the end, interlayers, which can-not be assigned to the other categories, will be outlined.

Perovskite layer deposition by spin-coating

All perovskite layers are prepared by a one-step method. Thus precursor solutions are generally prepared by dissolving all precursor salts in stoichiometric amounts. All parameters referred to the precursor solution preparation are described in table 3.1, like used precursor salts, additives, solvents, the concentration of precursor solution, solvation time, and temperature. Perovskite layers are prepared by spin-coating (parameters see table 3.2) the precursor solution on a sample with an already deposited charge transport layer. The perovskite crystallization is initiated by increasing the concentration over the supersaturation level by dripping with an antisolvent or fast drying with a nitrogen flow during the spin-coating process. Subsequently, the perovskite layer is annealed (time and temperature see table 3.2).
Since Sn^{2+} can easily oxidize, tin-containing perovskite solar cells need to be prepared in an inert atmosphere. Preparation of the perovskite precursor solution, perovskite layer deposition, and all layers deposited after the perovskite layer are thus executed in a nitrogen-filled glovebox with an oxygen content lower than 0.1 ppm and water lower than 1ppm.

Table 3.1: Parameters for the perovskite precursor solution preparation.

perovskite absorber	precursor salts	additives (c[a])	solvents[b]	c / M	temperature	time
Bi	BiI_3, CsI	no	DMF:DMSO 7:3 [c]	0.75	100°C [d], RT[e]	over night
Sn	SnI_2, FAI, PEAI	SnF_2 (0.15)	DMF:DMSO 4:1	0.6	RT	2 h
SnPb	SnI_2, PbI_2, FAI, MAI, CsI	SnF_2 (0.075), PbSCN (0.0175)	DMF:DMSO 4:1	1.2	RT	2 h

[a] c = M(additive)/M(perovskite)
[b] volume ratio
[c] BiI_3 predissolved in DMF and CsI predissolved in DMSO
[d] for the CsI presolution
[e] for the BiI_3 presolution

Table 3.2: Parameters for the perovskite layer deposition by spin-coating.

perovskite absorber	spin coating parameters	crystallization initiation	drying
Bi	10 s 1000 rpm, 20 s 6000 rpm	N_2 gas quenching after 15s	100-300°C for 20 min
Sn	10 s 1000 rpm, 20 s 6000 rpm, 1 s 4000 rpm, 1 s 2000 rpm	antisolvent quenching with anisol after 25 s	40°C 10min, 100°C 5 min
SnPb	10 s 1000 rpm, 20 s 6000 rpm, 1 s 4000 rpm, 1 s 2000 rpm	antisolvent quenching with anisol after 25-75 s	100°C 5 min

Hole transport layer deposition by spin-coating

All of the characterized devices in chapters 4 and 5 include HTL for efficient solar cell performance. The HTL used in solar cells in this work are PEDOT:PSS, PTAA, and Spiro-OMeTAD. HTL are deposited by spin coating from a solution or suspension and possible layer drying on a heat plate. Relevant deposition parameters are summarized in table 3.3.

Table 3.3: Parameters for hole transport layer deposition by spin-coating.

hole transport material	solvent	concentration	spin coating parameters	drying
Spiro-OMeTAD	CB	75 mg/mL	4000 rpm 35s	no
PEDOT:PSS	suspension in water	as received	3s 500 rpm, 55s 4000rpm, 1s 2000 rpm	120°C 10 min
PTAA	DCB	3 mg/mL	1000 rpm 35s	100°C 10 min

Electron transport layer deposition by spin-coating

For efficient electron extraction in the solar cell, ETL are used in the solar cell devices. As illustrated in figure 3.1, different C_{60}-derivates (PCBM, bis-PCBM, ICBA) combined with a BCP layer are used as ETL. Alternatively, TiO_2 was deposited as ETL in Bi-based perovskite solar cells. All these layers are prepared by spin-coating their solution. All relevant parameters concerning the solutions and deposition are given in table 3.4.

Table 3.4: Parameters for electron transport layer deposition by spin-coating.

electron transport material	solvent	concentration	spin coating parameters	drying	miscellaneous
TiO_2	IPA	0.25 M	45 s 2000 rpm, 3 s 100 rpm	10 min 150°C, 30 min 16.7 °C/min, 45 min 500°C	additive: 45 µL 1.5 M HCl in EtOH
C_{60}-derivates	DCB	40 and 50 mg/mL	30 s 1000 rpm, 5 s 4000 rpm	–	application at 60°C
BCP	EtOH	1 mg/mL	34 s 3000 rpm	–	–

Interlayer deposition by spin coating

In this last paragraph, interlayer depositions are summarized. The used interlayers in this thesis are silicon oxide nanoparticle (SiO_2-NP) and poly(methyl methacrylate) (PMMA). The SiO_2-NP are synthesized by the Stöber process [168,169]. For more details about the synthesis, the reader is referred to the appendix of this work. These two interlayers were deposited by spin coating according to the protocols summarized in table 3.5.

Table 3.5: Parameters for the interlayer deposition by spin coating.

interlayer	solvent	concentration	spin coating parameters	drying
SiO_2-NP	EtOH	1/3 of the stock solution	30 s 2000 rpm	100°C 10min
PMMA	ACN	0.6 mg/mL	30 s 6000 rpm	100°C 10min

3.1.2 Post-doping of perovskite layer by selenium vapor

Post-doping of the $Cs_3Bi_2I_9$ perovskite absorbers with selenium in chapter 5 is carried out in a selenium-containing nitrogen atmosphere. The process is done in a homemade halogen-lamp-heated chamber with an elongated sample holder out of graphite, providing containers for selenium at both ends. The setup is schematically illustrated in figure 3.3. The chamber's pure nitrogen atmosphere is realized by evacuating and refilling the chamber with nitrogen up to 1000 mbar for several times. The post-doping is executed by first pre-heating the chamber for around 20 minutes before introducing the sample holder into the chamber. The temperature is tracked with sensors at the samples and selenium containers. Processes are typically carried out with a temperature ramp of 1 Ks^{-1} and process temperature between 340 to 350° C, which results in evaporating the selenium and forming a selenium vapor in the sample holder. After 20 to 60 minutes, the sample holder is withdrawn from the hot chamber. Before opening the system, the chamber is cooled down to room temperature over several hours.

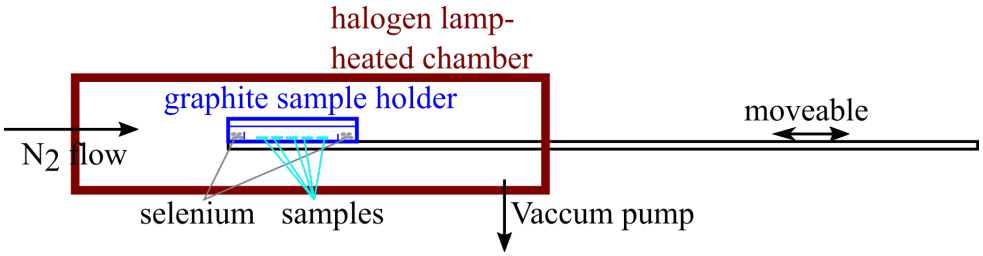

Figure 3.3: Schematic illustration of the homemade setup for post doping the perovskite layer by selenium vapor.

3.1.3 Synthesis of bismuth xanthate

The synthesis of bismuth xanthate is followed by the description of Vigneshwaran et al. [137]. For this bismuth (III) nitrate pentahydrate (2.06089 g, 4.2 mmol) is solved in 48 mL deionized water and 5.32 mL hydrochloric acid (HCl) (32%), resulting in a clear solution. In a second solution, potassium ethyl thiocyanate (2.18090 g, 16.7 mmol) is solved in 6.66 mL deionized water. The potassium ethyl thiocyanate solution is added to the bismuth (III) nitrate pentahydrate solution under continuous stirring. A yellow precipitation is immediately obtained. The observed solution is stirred for one hour at room temperature. The resulted dispersion is filtered, and the resulting yellow powder is dried in a desiccator. The dried powder is further purified by again adding deionized water to redissolve the educt materials. For drying, the dispersion is again filtered and dried in a desiccator. Successful synthesis is verified by elemental analysis.

3.1.4 Physical vapor deposition for contact layer preparation

The back electrode of solar cells is deposited by physical vapor deposition through a mask defining an active area of 0.24 cm^2. Gold (chapter 5) or silver (chapter 4) are used as electrode materials. The process is carried out at a base pressure of 5×10^{-6} mbar by subsequently increasing the evaporation rate from 0.5 to 3.5 Å/s until a layer thickness of 120 nm for silver or 60 nm for gold is achieved.

3.1.5 Fabricating the transparent conductive layer via sputtering

The TCO layers ITO and FTO deposited on glass were bought commercially. These TCO layers are generally fabricated by a sputter deposition process. Specified data of the TCO samples are summarized in table 3.6.

Table 3.6: Specified parameters of the commercial bought ITO and FTO coated glasses.

TCO	manufacturing company	glass typ	TCO thickness / nm	sheet resistance / Ω/□	transmission
ITO	Visiontek	1.1 mm soda lime glass	150	12	89% at 550 nm
FTO	Sigma	2.2 mm soda lime glass	400-450 nm	15	83.4%

The TCO glass samples were cut either in 15×15 mm^2 or 30×30 mm^2 pieces and laser scribed as illustrated in figure 3.2 for solar cell preparation.

3.2 Characterization methods for perovskite solar cells

In the following an overview of applied characterization methods for thin-film analysis (subchapter 3.2.1), chemical properties (subchapter 3.2.2), and studying electro-optical properties (subchapter 3.2.3) of perovskite absorbers and perovskite solar cells are given.

3.2.1 Thin film characterization

In this paragraph, techniques for characterizing thin films by their morphology and crystal phase are outlined.

The morphology of thin film can be analyzed by taking top-view images with an optical 3D-microscope[1] and scanning electron microscopy (SEM)[2].
An overview of layer surface coverage can be easily observed with the optical microscope by taking top-view images. Additionally, scanning the surface with the integrated laser can estimate the surface roughness ($R_a = \frac{1}{l}\int_0^l |z(x)|\,dx$ with l the measured length, and $z(x)$ the height at point x) [170]. Since optical microscope measurements are restricted to their optical limit, only details with a minimum size in the order of 1 µm can be visualized.
Since most of the morphology characteristics are smaller than 1 µm, like film homogeneity, grains characteristics, e.g. size and structure, and pinholes, these can not be featured with an optical microscope. Thus further analysis of the top-view is done by SEM measurements. Grain sizes are characterized with the *imageJ* software. Additionally, cross-section images on freshly broken samples are performed to obtain film thicknesses, roughness, and possible cavities to the layer underneath. At optimal conditions, a resolution of around 1 nm is achieved with our SEM setup. The measurements were performed by Tina Wahl and Daniela Müller.

The crystal phase of thin films can be analyzed by X-ray diffraction (XRD)[3] measurements. The used setup has a copper K_α X-ray tube with a wavelength of λ = 1.54 Å. Two measurement configurations are used to determine the crystal phase of thin films, Bragg-Brentano and gracing incidence (see figure 3.4).
The Bragg-Brentano method is typically used to analyze the bulk phase of a sample. For this, the divergence incident X-ray beam excites the fixed sample at a moving angle ω. Scattered diffracted X-rays are detected at an angle $\theta = \omega$ according to the sample. Since analyzed film stacks in this work generally have a maximum film thickness of 1 µm, complete solar stacks are generally depicted in Bragg-Brentano XRD measurements. With the grazing incidence method, sample surfaces of few nanometers can be characterized. Here monochromatic X-rays hit the sample at a fixed angle ω lower than 3°. The detector is moved by the angle θ according to the fixed sample. The penetration depth of the X-rays depends on the incident angle ω and the analyzing material. For higher angles ω the x-ray penetration depth in the sample are deeper, thus higher bulk information can be observed.
The resulting XRD pattern provides information about the structure and lattice parameters by analyzing the peak position. By comparing the known XRD patterns of crystalline materials with the measured ones, the phase compositions of the measured sample can be identified. The peak width can estimate crystallite size, strain, and defects. The preferred facet orientation is characterized by analyzing the peak area or height ratio. The peak intensities can provide information on the weight fraction in multiple phase samples.
XRD measurements are characterized with the *highscore+* software. The underground is defined using the granularity (values between 10 to 30) and the bending factor (values between 0 to 2). Further, diffraction peaks are fitted with the pseudo-Voigt function and, if necessary, considering their asymmetric type. All other parameters are kept unchanged.

[1] *Color 3D laser Microscope VK-9700K* setup from *Keyence*
[2] *Zeiss Crossbeam 550* setup from *Zeiss*
[3] *PANalytical Empyrian* setup from *Malvern Panaytical*

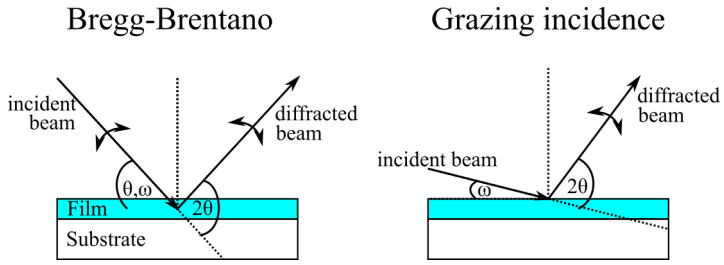

Figure 3.4: Schematic illustration of the Bragg-Brentano and grazing incidence measuring setup with XRD.

3.2.2 Chemical properties analysis of perovskite absorbers

The chemical properties of perovskite films and solar cells are characterized according to the elemental distribution in the bulk and molecular interactions with their chemical surrounding. Elemental analysis in films can be analyzed by X-ray fluorescence (XRF), energy-dispersive X-ray spectroscopy (EDX), and Time of Flight - Secondary Ion Mass Spectronomy (ToF-SIMS) measurements. A short overview of the measurement techniques and their main differences are outlined in more detail in the following. Hard x-ray photoelectron spectroscopy (HAXPES) and X-ray photoelectron spectroscopy (XPS) measurements can provide additional molecular interaction of molecules. The main differences of all named techniques is their resolution.

The XRF technology is based on exciting the sample with X-rays, which ionizes the material by releasing electrons from inner orbitals. Left holes are filled up with electrons from higher orbitals, releasing their excess energy by photons. These photon energies are detected being characteristic for each element due to their specific orbital energies. The used setup[4] excites the sample with an X-ray spot on an area of $1 \times 2\,\mathrm{mm}^2$. The penetration depth of those X-rays into the sample is 300 µm. Thus for our thin-films, being thinner than 1µm, complete sample stacks are analyzed. So spatial as well as depth resolution is therefore limited. However, this method is facile and fast, giving a first impression of present elements in the sample and being non-destructive. The XRF measurements were performed by Philipp von Bismarck.

EDX[5] measurements achieve higher spatial resolution. Here, in contrast to the XRF technology, the sample is exposed to an electron beam. Again the sample is ionized by releasing electrons from inner orbital. The left holes are filled with electrons from upper orbitals releasing photons with characteristic energy for each element. Since these electron beams are highly focused, a higher spatial resolution of the surface can be achieved. However, spatial and depth resolution is limited by electron scattering in the sample and emitted photons in all directions. The resolution is thus limited to some µm. This technique is processed in vacuum conditions making it more time-consuming, but providing a defined and oxygen-free atmosphere. The EDX measurements were performed by Daniela Müller.

[4] *Orbis Micro-XRF* setup from *Edax*
[5] *Zeiss Crossbeam 550* setup from *Zeiss*

ToF-SIMS[6] measurements can provide a high resolution of elemental distribution in a sample. The sample surface is sputtered with Bi_3^+ or Bi^+ ions. By using the Bi_3^+ ions reduced molecular fragmentation compared to Bi^+ is observed [171]. The released ions are then characterized by mass spectroscopy. Since the primary ion beam can be precisely focused, a spatial resolution of up to 70 nm in optimal conditions can be realized. Additional depth information of a sample can be observed by eroding the sample surface with a secondary ion beam of Cs^+ or oxygen-clusters$^+$ ions. Two measurements modes can be performed for obtaining either high mass resolution (spectrometry mode) or high spatial resolution (imaging mode) [171]. The delayed-extraction mode combines the advantages of the spectrometry and imaging mode, however reduced mass signals are observed. As this technology is based on sputtering, this method is destructive as well as time-consuming. Further interpretation difficulties can arise due to preferential sputtering of hybrid mixed organic and inorganic samples. Again this technique is processed in vacuum conditions providing an inert and standardized condition. The ToF-SIMS measurements were performed by Dr. Jonas Hanisch.
Elemental concentrations in specific sample depths are analyzed by integrating the signal in the area of interest over a time normalized depth profile. The F^- amount in figure 4.15g are determined by normalizing the sample layer thickness to the sputtering time with highest S^- signal (t_{100}) of the shown depth profiles in figure A.5. The normalized F^- values are integrated over 0-10 % t_{100}, 10-90,% t_{100} and 90-100 % t_{100} for the PEDOT:PSS/perovskite interface, perovskite bulk and perovskite surface F^- amounts. Further, the F^- values are normalized to $I_2{}^-$ plateau.
The analyzed element amounts in figure 4.44c, 4.51c are determined by normalizing the sample layer thickness to the Ag^+ signal and integrating the elemental signals of interest from the sample surface to the ETL layer.

HAXPES and XPS measurements[7] can provide additional information about molecule interactions. Similar to XRF measurements, the samples are excited by X-rays which release electrons. In contrast to the XRF technology, the released electron energy is directly detected, which is specific due to their orbitals. By chemical interaction with surrounding molecules, the binding energies can be slightly shifted and detected by this method. Since the X-rays are usually not focused, spatial resolution is limited. For XPS measurements, the penetration of the X-rays are some nanometers, thus only giving surface information of a sample. However, the penetration for hard X-rays in HAXPES measurements is much higher, which results in depth information of up to 100 nm depending on the sample material. Also, this technique is processed in vacuum conditions. The HAXPES and XPS were performed by Prof. Dr. Hand-Gerd Boyen and Derese Desta.

3.2.3 Study of electro-optical properties

In this paragraph, methods for analyzing the electro- and optical properties, like band-gap energies, charge charier dynamics, the conversion of light into charges, and solar cell performance are presented.

[6] *TOF-SIMS 5* setup from *ION-TOF GmbH*
[7] setup from *Scienta Omicron*

Perovskite film characterization

Absorptance A[8] of a thin film can be obtained by measuring the transmittance T and reflectance R of a sample (A=1-R-T). This provides a insight into the absorptance onset and strength of absorptance of a thin film, e.g. perovskite layer. Further, the band-gap energy (E_g) of semiconductors can be obtained by fitting the absorptance onset in a tauc-plot. In a tauc-plot plots the absorptance to the photon energy is plotted according to ($f(h\nu) = (Ah\nu)^2$) based on $(Ah\nu)^2 = B(h\nu - E_g)$ for direct electron transition with h the Planck constant, ν the photon's frequency and B a constant [172].

Transient resolved photoluminescence (TRPL) and steady-state PL measurements are used to analyze charge carrier characteristics and the quality of the perovskite layer. By TRPL, the lifetime of charge carriers can be calculated, thus giving a hint for good perovskite absorber film applicable for solar cell devices. Further analyzing the quenching behavior by comparing photoluminesce (PL) intensities of different sample stacks, like modified charge carrier extraction layers, provides insight into charge extraction and/or quality of the perovskite layer. The PL measurements were performed by Dr. Philip Schulz and Dr. Géraud Delport.

Perovskite solar cell characterization

The solar cell performance is characterized by measuring current-density–voltage dependency curves ($J(V)$-curves) [9] in the dark and illuminated by AM 1.5G sun spectra in forward and reverse bias scan direction. A 2-lamp sun simulator[10] realizes the sun spectrum. Since for tin-containing perovskite solar cell the Sn^{2+} oxidation in ambient atmosphere is highly critical, all measurements for these perovskite solar cells are performed in a home-made N_2-Box. This N_2-Box provides an inert atmosphere by a constant nitrogen flow. The $J(V)$-curves are analyzed according to their solar cell parameters short-circuit current density (J_{SC}), V_{OC}, fill factor (FF), and power conversion efficiency (PCE) as illustrated in Figure 3.5. The PCE gives the ratio of the generated power of the solar cell ($P_{\text{solar cell}}$) to the applied power of the light (P_{light}) and is calculated by the following equation:

$$PCE = \frac{P_{\text{solar cell}}}{P_{\text{light}}} = \frac{J_{\text{mpp}} \cdot V_{\text{mpp}}}{P_{\text{light}}} = FF\frac{J_{\text{SC}} \cdot V_{\text{OC}}}{P_{\text{light}}} \tag{3.1}$$

Further maximum power point (MPP) tracking is carried out by applying the V_{MPP} for several minutes under illumination extracting the PCE at MPP to observe an authentic solar cell performance and performance stability.

[8] UV-Vis spectrometer*Lambda 900* from *Perkin Elmer* or
XWS-30 light source from *MountainPhotonic* with the *ULS2048CL-EVO* UV-Vis spectrometer and *NIR-HSC-EVO* NIR-spectrometer from *Avaspec*

[9] *2400* measuring source unit from *Keithley* or
X200 setup from *Ossila*

[10] *WXS-90S-L2 Super Solar Simulator* setup from *WACOM*

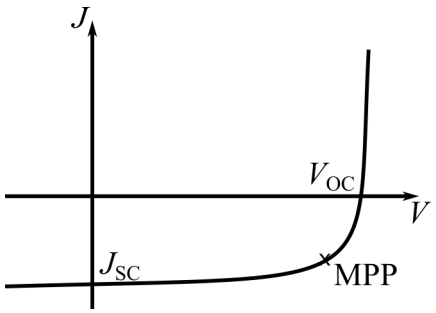

Figure 3.5: Exemplary illustration of a $J(V)$-curves with analyzed solar cell parameters.

External quantum efficiency (EQE)[11] is used to analyze wavelength-dependent conversion of light into charges. The maximum current in a solar cell can be calculated by integrating the spectra over the solar spectrum. Additionally, the E_g energy can be estimated by the onset of the spectra in a tauc-plot simultaneously to the absorptance investigation ($f(h\nu) = (EQE h\nu)^2$).

[11] *Bentham PVE 300* setup from *Bentham*

4 Development of tin-containing perovskites with improved sustainability

Highly efficient perovskite solar cells are commonly based on perovskite compositions containing lead. The presence of lead raises environmental and human health concerns, possibly hindering the wide acceptance of perovskite solar cells. Therefore, lead substitution is a critical issue for the practical implementation and acceptance of perovskite solar cells and alternatives should be explored in foresight [29, 61, 69]. A detailed literature review of alternative perovskite absorbers was presented in chapter 2.2.

This chapter investigates tin as a lead-alternative to reduce the impact on human health and improve environmental sustainability. Besides this, tin has a similar electronic configuration as lead [59, 60]. This leads to the same oxidation state [61], which makes the lead replacement by tin straightforward. Further the highest efficiencies are so far achieved by these lead-alternative tin-containing perovskite absorbers [8, 9].

Tin-lead mixed perovskite absorbers will be investigated in the first subchapter 4.1 by only partially replacing the lead with tin. The amount of lead is further reduced by perovskite absorber with entirely substituted lead by tin. These will be explored in subchapter 4.2. As the stability of tin-containing perovskite absorbers is challenging due to the fast tin oxidation, the stability will be studied in subchapter 4.3. The investigations made for each perovskite composition and the stability are motivated and described separately at the beginning of each subchapter.

The tin-containing perovskite solar cells are prepared in the p-i-n architecture, as for n-i-p the commonly used charge layers are inappropriate for these perovskite absorbers. The ETL, like SnO_2 and TiO_2, are metal oxides providing oxygen vacancies highly critical for these absorbers [74, 173]. Further, Spiro-OMeTAD used as HTL is also unfeasible for tin-containing perovskite absorber, as the typically used dopants damage the perovskite [74, 174] and the Spiro-OMeTAD have to be oxidized at air for high performance [174].

4.1 Exploring tin-lead mixed perovskite absorbers with increased sustainability

In this chapter tin-lead mixed perovskite absorbers will be investigated having an reduced harm on human health and improved environmental sustainability, solar cell efficiency and stability. Their impact on human health and the environment is in between the risk for pure lead and pure tin perovskites. These absorbers achieve over 21 % [8] efficiency and higher ambient stability than pure tin perovskites [104]. Besides this, they can be applied as a bottom cell in tandem solar cells because of their very low band-gap energies down to 1.2 eV [106].

PEDOT:PSS is highly hydroscopic [128] and acidic [127, 128]. Hence an unstable interface is expected, limiting the solar cell performance stability of tin-lead mixed perovskite solar cells [118] and perovskite solar cells in general [116, 128, 129]. Further, thermally unstable MAI is thought to limit the stability in tin-lead mixed perovskite solar cells [119] and perovskite solar cells in general [120–126]. However, in literature these strategies are rarely addressed for tin-lead mixed perovskite solar cells [116].
Thus, a strategy to replace PEDOT:PSS (see subchapter 4.1.1) and MA^+ in the perovskite composition (see subchapter 4.1.2) is explored. The optimization strategy is schematically illustrated in figure 4.1.

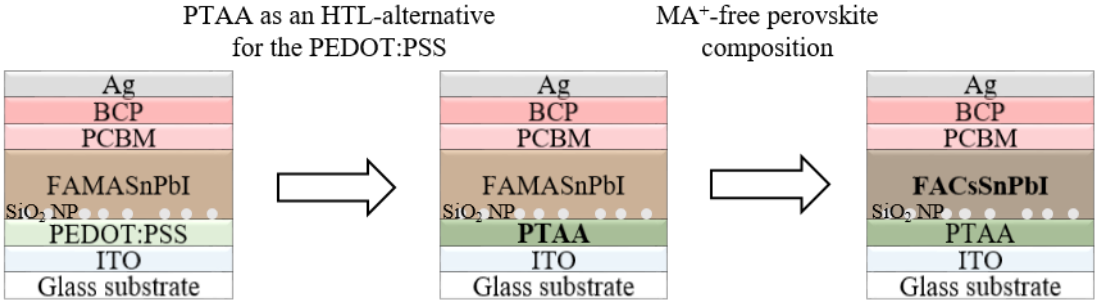

Figure 4.1: Schematic overview of the optimization strategy in chapter 4.1.

The 1:1 tin-lead mixed perovskite are deposited from a stochiometric perovskite solution by spin coating. A solvent mixture of dimethylformamide (DMF) with added DMSO to retard the crystallization of the perovskite and thus achieve a higher control of perovskite film formation is used [108]. An anti-solvent dripping initializes the nucleation to start perovskite film growth. The solar cell studied have an inverted solar cell stack as outlined in figure 3.1. ITO is used as TCO, PEDOT:PSS or the PEDOT:PSS-HTL-alternative as HTL, SiO_2-NP for improved perovskite growth and wetting [175], a combination of PCBM and BCP as ETL and Ag as back electrode. More details about the sample preparation are presented in chapter 3.1.

4.1.1 Investigating PTAA as an HTL-alternative for the PEDOT:PSS

In this subchapter, a PEDOT:PSS-HTL-alternative made from PTAA is explored.

PEDOT:PSS substitution has been rarely explored for tin-lead mixed perovskite solar cells [116]. Even though detrimental effects of the PEDOT:PSS/perovskite interface for tin-lead mixed perovskite solar cells were already reported [119]. It is expected that the hygroscopicity of the PEDOT:PSS [129] attracts water initiating the perovskite decomposition. Moreover, the acidity destroys the underlying ITO [127, 128]. Thus both aspects are expected to limit the stability of the solar cell devices [116, 129] and thus PEDOT:PSS as an HTL should be replaced.

In this work, PTAA is applied as a PEDOT:PSS alternative. PTAA can be easily fabricated from wet solution deposition via spin-coating and using it in lead perovskite solar cell devices accomplished promising solar cell performances [176]. As the perovskite coverage on PTAA is challenging as it has a hydrophobic surface [177], SiO_2-NP are used to improve perovskite wetting [175]. The overall aim of this chapter is to substitute PEDOT:PSS with PTAA and realize working solar cell devices.

For this investigation, the commonly used $FA_{0.75}MA_{0.25}Sn_{0.5}Pb_{0.5}I_3$ perovskite composition from literature [100] is chosen.
The impact of the PEDOT:PSS substitution by PTAA is first characterized in respect to the perovskite film growth followed by the phase analysis and solar cell performance.

The perovskite film growth is similar on the PEDOT:PSS and PTAA surface. The top-view SEM images show a complete coverage without pinholes and only slightly larger perovskite grains by using PTAA as HTL (PEDOT:PSS $(0.12 \pm 0.07)\,\mu m^2$, PTAA: $(0.13 \pm 0.09)\,\mu m^2$) (see figure 4.2). The images of the PTAA sample show brighter areas, suggesting an additional phase.
It seems that the perovskite morphology is less influenced by the used HTL. The use of SiO_2-NP as a porous interlayer between HTL and perovskite layer is expected to lead to similar perovskite growth.

Further, XRD studies are performed to characterize the impact of the HTL on the perovskite crystalline morphology (see figure 4.3). Both XRD diffractograms matches to a cubic perovskite phase. Since peak intensities are similar for all perovskite peaks, no changes in crystal orientation are observed. A peak at 12.7° indicate a small amount of lead iodide (PbI_2) for the PTAA sample. Excess of PbI_2 is controversially discussed in terms of its positive or negative impact on solar cell performance [62, 178–183]. On the one hand, excess of PbI_2 is often considered to reduce the defect density [62, 178] by passivating the perovskite surface and grain boundaries [62]. This is thought to be beneficial for the solar cell efficiency [62, 178, 179]. On the other hand, an excess of PbI_2 is reported to be detrimental [180–183], especially in terms of its long-term stability [182, 183].

As the perovskite morphology was characterized and minor impact by the used HTL, solar cell performance is studied in the following. Solar cells with a median efficiency of 11.5 % in reverse bias scan direction for PTAA devices compared to 13.0 % for the PEDOT:PSS ones are demonstrated (with the highest solar cell efficiency of 13.1 % for tin-lead mixed perovskite solar cell in this work) (see figure 4.4a). For the PTAA, a high median V_{OC} of 780 mV is achieved,

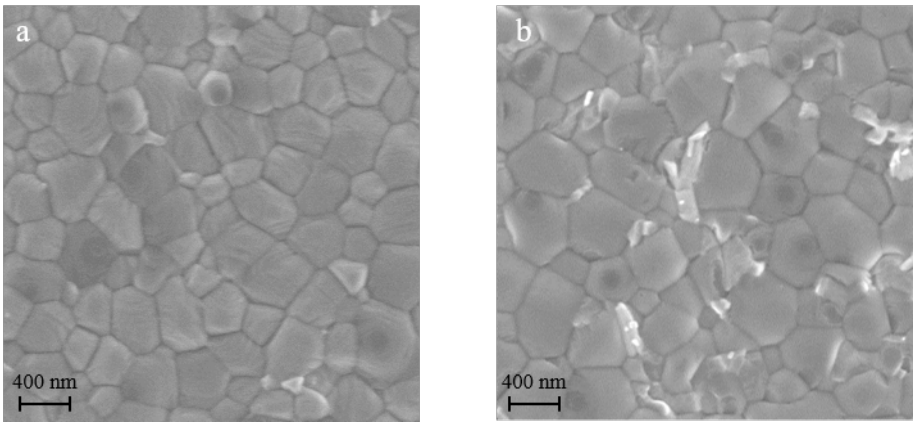

Figure 4.2: Top-view SEM images of ITO/HTL/SiO_2-NP/$FA_{0.75}MA_{0.25}Sn_{0.5}Pb_{0.5}I_3$ samples to characterize the impact of PEDOT:PSS (a) and PTAA (b) as HTL on the perovskite growth.

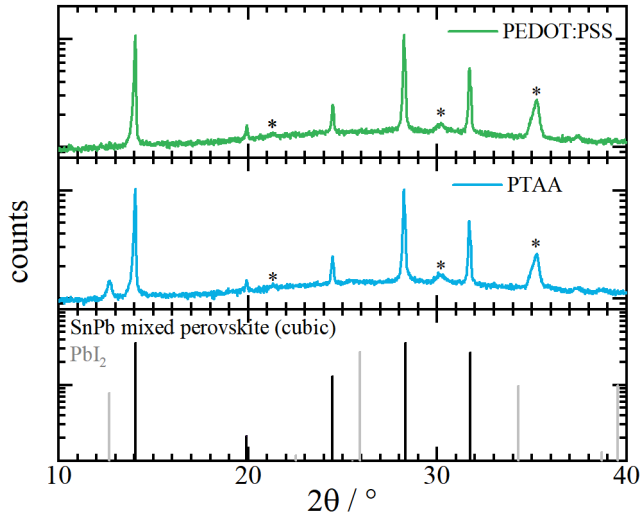

Figure 4.3: XRD diffractograms of ITO/HTL/SiO_2-NP/$FA_{0.75}MA_{0.25}Sn_{0.5}Pb_{0.5}I_3$ samples to characterize the influence of the HTL PEDOT:PSS or PTAA on the perovskite bulk phase. These are compared to XRD pattern of a cubic tin-lead mixed perovskite [184], PbI_2 [185] and ITO phase (marked as '*').

whereas these for PEDOT:PSS only reached a median V_{OC} of 710 mV. This is consistent with the general observed higher V_{OC} values for PTAA solar cells [176]. However, lower J_{SC} and FF are accomplished with the PTAA devices (22.6 vs. 23.5 mA cm^{-2} and 66 vs. 74 %; median values in reverse scan direction) (see figure 4.4b).

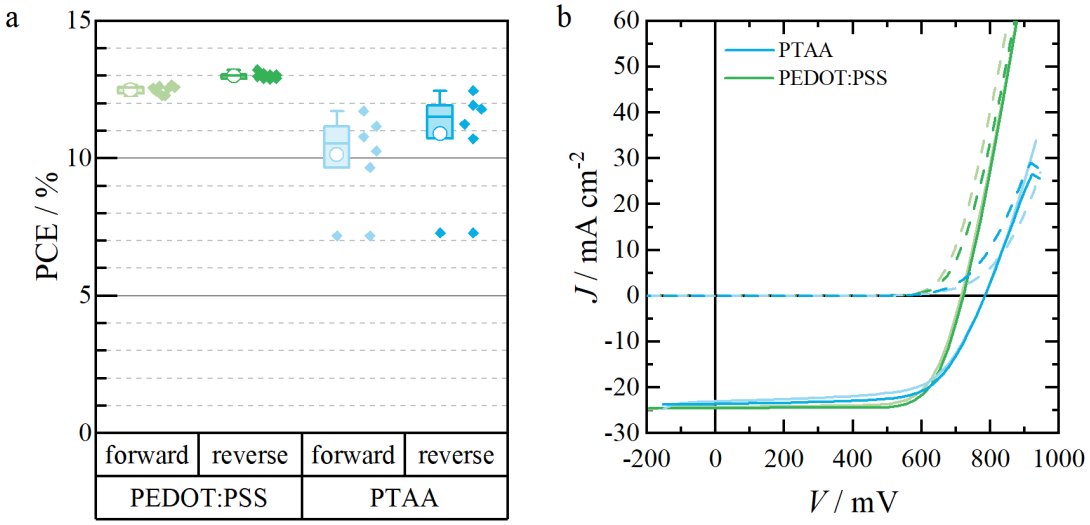

Figure 4.4: Impact of substituting the PEDOT:PSS by PTAA on the solar cell performance of tin-lead mixed $FA_{0.75}MA_{0.25}Sn_{0.5}Pb_{0.5}I_3$ perovskite devices (ITO/HTL/SiO_2-NP/$FA_{0.75}MA_{0.25}Sn_{0.5}Pb_{0.5}I_3$/PCBM/BCP/Ag). a: Overview of the achieved PCE displayed in box plots. b: Exemplary $J(V)$-curves for both HTL used. The lighter colored curve displays the forward bias scan direction, the darker one the reverse direction. Further dashed curves are dark measurements, while the solid lines represent illuminated ones.

In summary, replacing PEDOT:PSS with PTAA was successful. Fully covered perovskite growth on the HTL surface and a cubic perovskite phase are determined for both HTL samples by using SiO_2-NP as wetting agent. The PTAA solar cells have moderately lower PCE values with a median of 11.5 % compared to ones with PEDOT:PSS of 13.0 % (backward scan direction). Since this is a pre-step for the optimization strategy towards PEDOT:PSS-free and MA^+-free devices, no more in-depth characterization on these devices are performed.

4.1.2 Exploring a MA^+-free perovskite composition

Since MA^+ is considered to limit the long-term stability of the solar cells, a strategy to substitute this ion is presented in the following subchapter.

MA^+ should be eliminated as it limits the stability of tin-lead mixed perovskite solar cells [119]. For lead perovskite absorbers the MA^+ is generally eliminated in the perovskite composition due to its thermal instability [120–123], favoring ion migration [124, 125], and enhancing intrinsic self-degradation [126].

The MA^+ is replaced by Cs^+ and FA^+, two commonly used A- site cations in hybrid organic-inorganic perovskite compositions. In the following, the new standard HTL PTAA is used. PEDOT:PSS devices are utilized for comparison. A perovskite composition with 8.5 % Cs^+ (correlating to the total number of A cations) is chosen based on the experience on pure tin and pure lead perovskite solar cells and literature screening [45, 116, 119, 186–189]. For pure tin perovskites it will be shown that $FASnI_3$ results in reliable working devices (see chapter 4.2). For pure lead perovskites an amount of 17 % Cs^+ is discovered to be a good compromise in our research group. This leads to the chosen 8.5 % Cs^+ for a 50:50 mixed tin-lead perovskite composition also in regard of the reported Cs^+ amount between 0 to 25 % [45,116,119,186–189].

The achieved solar cell performance using the MA^+-free perovskite composition $FA_{0.915}Cs_{0.085}Sn_{0.5}Pb_{0.5}I_3$, and PTAA as HTL is very low (3.3 % in median) due to a strong S-shape in their $J(V)$-curves is observed(see figure 4.5). Solar cell devices with the same perovskite composition but using PEDOT:PSS as HTL, achieve median efficiencies of 12.9 % in reverse bias scan. Comparable perovskite growth and crystal bulk phase for both HTL samples, indicate no morphology alteration induced by the underlying HTL (see figure A.1, A.2). Thus the worse solar cell performance is expected to be caused by inappropriate interface properties.

An S-shape in a $J(V)$-curves generally indicate an energy barrier in the electronic device [190], so either the electron or holes are hindered from being efficiently transported through the device. It is assumed that this barrier is caused by the HTL, because appropriate solar cell performance is observed with PEDOT:PSS as HTL. Consequently, hole transport is thought to be hindered, by either (i) an unfavorable interface of the PTAA due to a reaction with the perovskite or (ii) an intrinsic unfavorable band structure of PTAA forming an energy barrier for the holes at the perovskite interface.

Unfavorable interface effects are analyzed by inserting a thin interlayer in between the HTL and the perovskite layer. This interlayer has to be sufficiently thin limiting insulating characteristics. PMMA is chosen as an interlayer material for this matter. Solar cells with PEDOT:PSS as HTL are analyzed as a reference system.

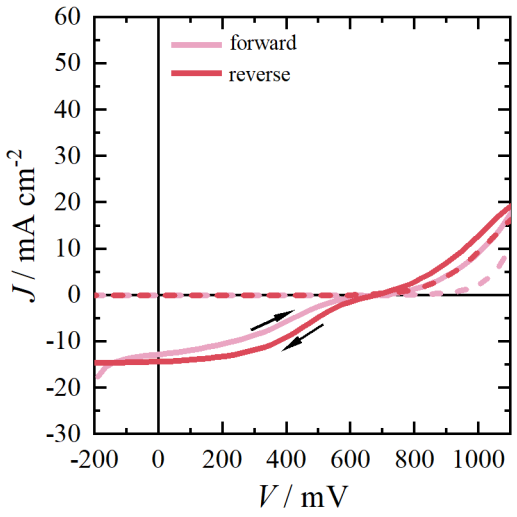

Figure 4.5: Exemplary $J(V)$-curves of a solar cell (ITO/PTAA/SiO_2-NP/perovskite/PCBM/BCP/Ag) using PTAA and the MA^+-free perovskite composition $FA_{0.915}Cs_{0.085}Sn_{0.5}Pb_{0.5}I_3$ illustrating the strong S-shape. The lighter colored curve displays the forward bias scan direction, the darker one the reverse scan. Dashed curves are dark measurements, while the solid lines represent measurements under illumination.

The inserted PMMA interlayer has a minor impact on the solar cell performance for the reference devices(see figure 4.6a), demonstrating a suitably chosen PMMA interlayer thickness. However, the solar cells with PTAA have not improved by the inserted interlayer (see figure 4.6b). Consequently, it is assumed that an interface interaction of PTAA and perovskite is not causing the S-shape.

Based on the findings before, it is assumed that an intrinsic non-matching band structures of the PTAA and MA^+-free composition cause the energy barrier (see schematic illustration of the suggested band structure in figure 4.7b). This band mismatch can either result from a moderately lower PTAA valence band than the PEDOT:PSS one (see figure 4.7b1) or/and from an increased valence band of the MA^+-free perovskite composition compared to the MA^+-containing perovskite (see figure 4.7b2). Thus (i) the energy barrier offset can be reduced by either upshifting the HTL (see figure 4.7c1) or (ii) downshifting the perovskite valence band (see figure 4.7c2). Upshifting can not be realized as long as PTAA is kept as HTL. Downshifting the perovskite valence band can be accomplished by reducing the atomic orbital overlap via structural perovskite tuning. The strategy adopted here is based on octahedra tilting by using a smaller A cation (see also theoretical background review in chapter 2.1.1 section band structure) [43, 45]. The impact of the A cation size tuning on the crystal structure is examined followed by the solar cell performance.

The impact of varying the Cs^+ amount on the crystal structure is analyzed by XRD measurements (see figure 4.8). Cs^+ is the smallest A-cation compared to MA^+ and FA^+ [29]. For low Cs^+ concentrations of x=8.5 % and x=15 %, the perovskite bulk crystallizes in a cubic structure [184]. For higher Cs^+ concentration x=25 and x=35 % additional peaks at 22.4°, and 26.6° appear. Based on the work of Prasanna et al., these are assigned to the (210) and (211) peaks of the tetragonal perovskite phase [45]. Thus the perovskite crystal structure is slightly tilting with an

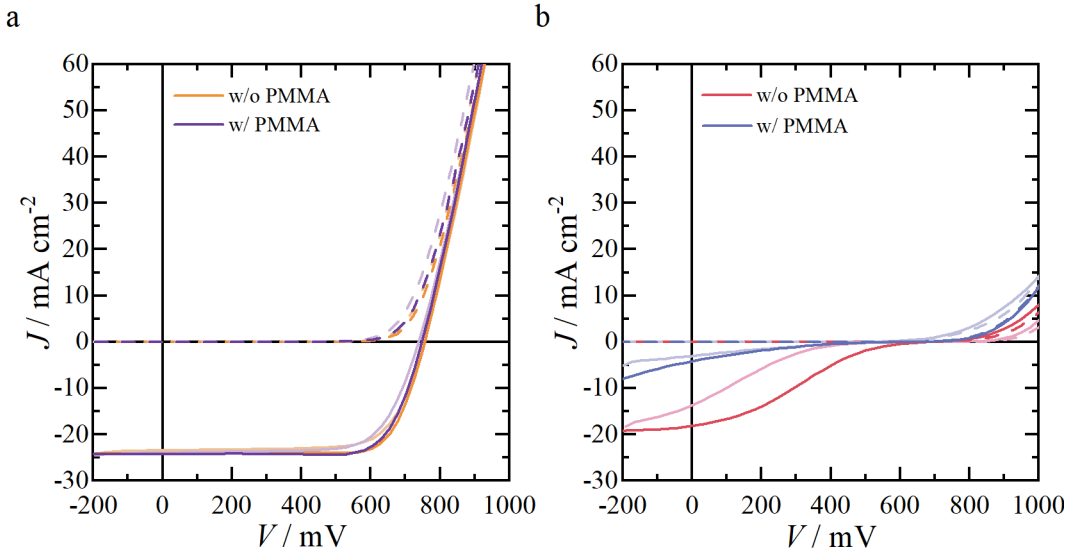

Figure 4.6: Analyzing the impact of interfacial properties of the HTL and perovskite on the solar cell performance by inserting PMMA in between the HTL and the perovskite layer (solar cell stack: ITO/HTL/PMMA/SiO_2-NP/$FA_{0.915}Cs_{0.085}Sn_{0.5}Pb_{0.5}I_3$/PCBM/BCP/Ag). a: used PEDOT:PSS and b: PTAA as HTL. Red colored lines show devices without and purple ones with. The lighter colored curve displays the forward bias scan direction, the darker one the reverse direction. Dashed curves are dark measurements, while the solid lines represent measurements under illumination.

increasing Cs^+ ratio. Thus it is expected that the atomic overlap of the tin and lead with the iodide is decreased lowering the energy of the formed perovskite valence band.
Enhancing the Cs^+ amount does not significantly change the perovskite morphology as indicated by SEM top-view images (see figure A.3).

Furthermore, the impact of the observed structural changes on the solar cell performance is examined. Exemplary $J(V)$-curves for solar cells with Cs^+ amounts of x=8.5 %, 15 %, 25 %, 35 %, and the stabilized median PCE value at MPP of these solar cells are shown in figure 4.9. As seen in the $J(V)$-curves, the S-shape decreases for higher Cs^+ amounts, and the overall efficiency enhances from 4 to 10 % in median.

As the S-shape reduces, improved band-alignment by downshifting the perovskite valence band is expected. This should also increase the band-gap energy, thus EQE measurements are performed.
EQE spectra show a slightly increased band-gap energy from 1.257 to 1.262 eV for the sample with increasing Cs^+ amount from x=8.5 to 35 % (see figure 4.10). However, the trend of increasing band-gap is not directly linear. The only slight valence-band shift is assumed to be too small for being accurate determined by EQE measurements.

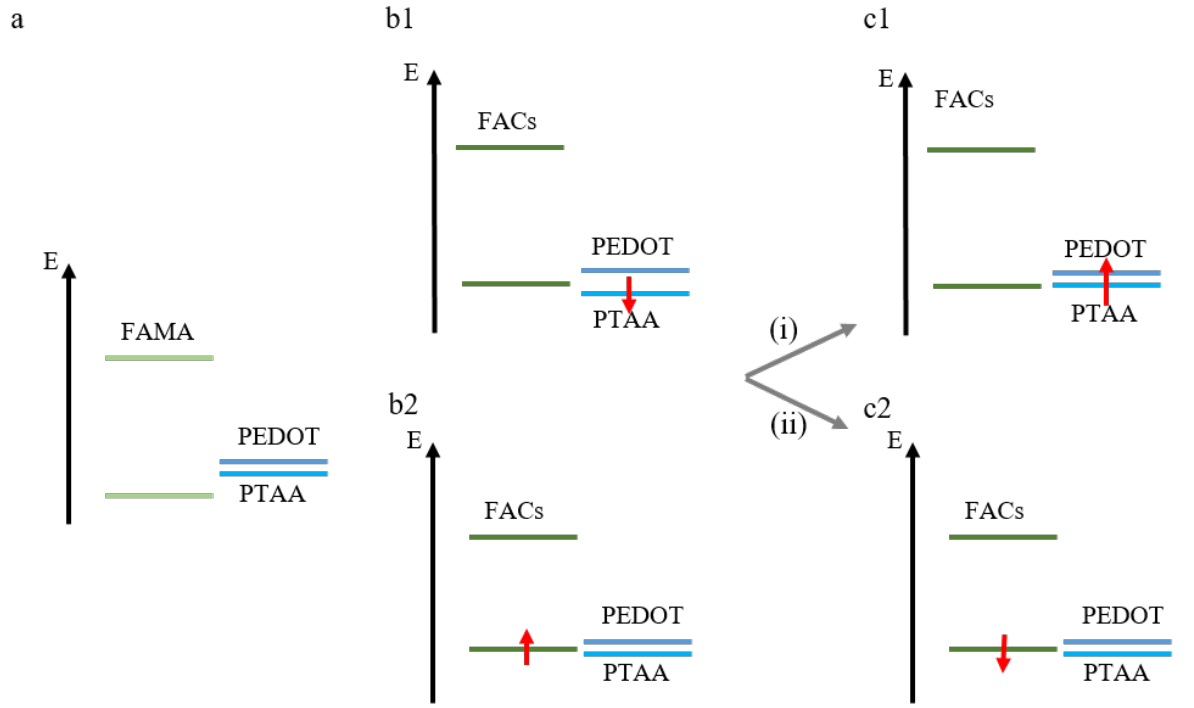

Figure 4.7: Schematic illustration of assumed band structure of the MA^+-containing $FA_{0.75}MA_{0.25}Sn_{0.5}Pb_{0.5}I_3$ (FAMA) (a) and MA^+-free $FA_{0.915}Cs_{0.085}Sn_{0.5}Pb_{0.5}I_3$ (FACs) (b) perovskite composition with the HTL PEDOT:PSS and PTAA. Additionally showing the suggested band mismatch (b) by either a lower valance band of the PTAA in comparison to PEDOT:PSS (b1) or the higher valence band of the FACs compared to the FAMA perovskite composition (b2). Present strategies to reduce the energy barrier between the FACs perovskite and the PTAA (c) by (i) upshifting the valence band of the PTAA (c1) or (ii) downshifting the valence band of the perovskite (c2).

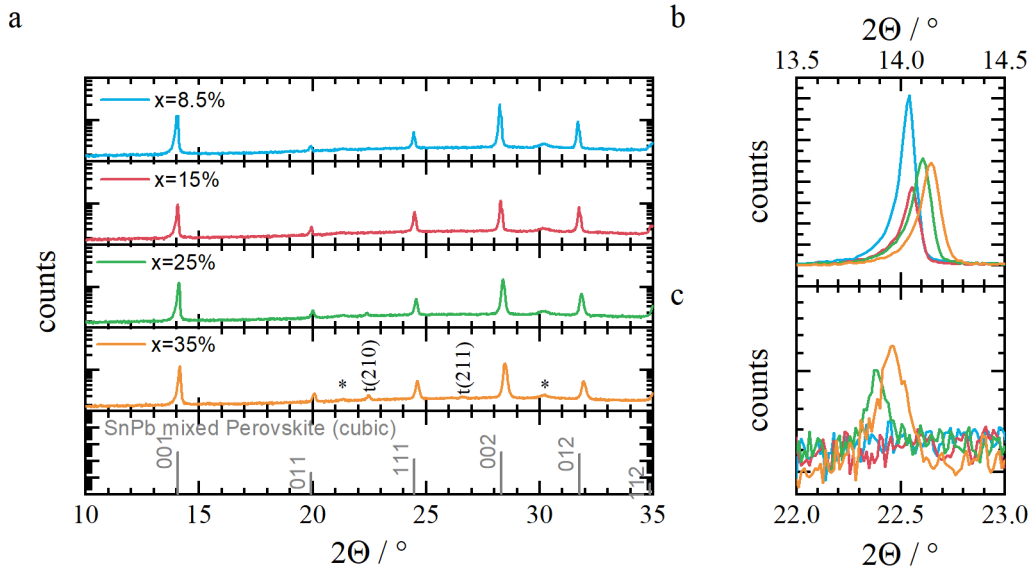

Figure 4.8: XRD measurements of ITO/PTAA/SiO_2-NP/$FA_{1-x}Cs_xSn_{0.5}Pb_{0.5}I_3$ samples with different Cs^+ amounts of x=8.5 %, 15 %, 25 %, 35 %. a: XRD diffratograms compared to a cubic tin-lead mixed perovskite [184] highlighting tetragonal reflexes t(210) and t(211) [45] and the ITO phase marked as '*'. b: Shift of the (001) reflexe to larger angles with increasing Cs^+ content. c: Appearing tetragonal (210) peak at 22.4° for increasing Cs^+ content.

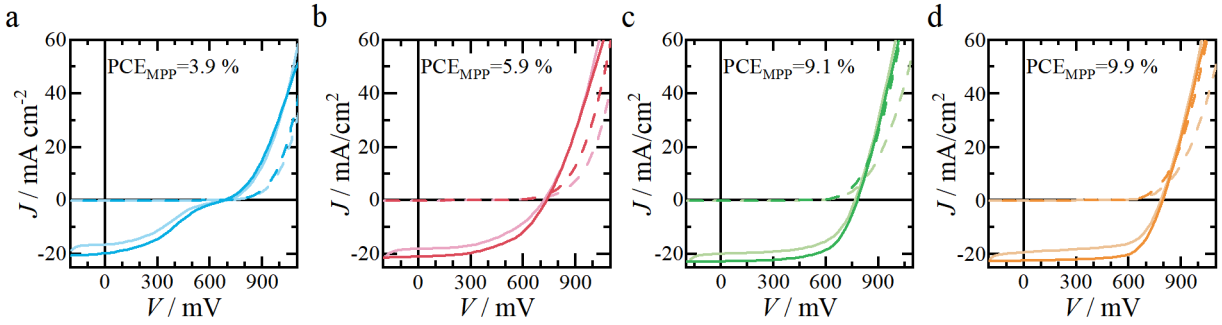

Figure 4.9: Exemplary $J(V)$-curves for increasing Cs^+ amounts in $FA_{1-x}Cs_xSn_{0.5}Pb_{0.5}I_3$ perovskite solar cells (ITO/PTAA/SiO_2-NP/$FA_{1-x}Cs_xSn_{0.5}Pb_{0.5}I_3$/PCBM/BCP/Ag) and their median PCE_{MPP} values of six solar cells. a: x=8.5 %, b: x=15 %, c: x=25 %, d: x=35 %. The lighter colored curve displays the forward bias scan direction, the darker one the reverse direction. Dashed curves are dark measurements, while the solid lines represent measurements under illumination.

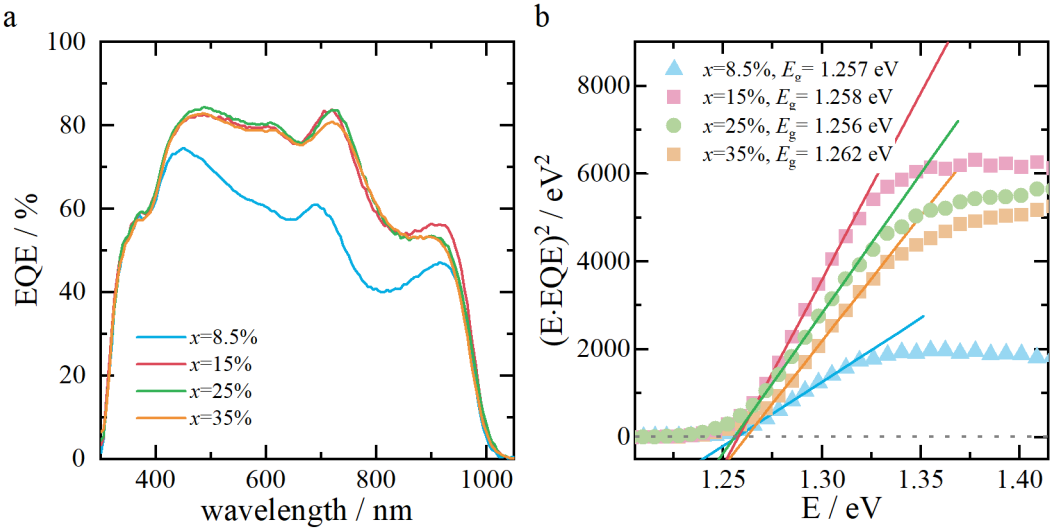

Figure 4.10: EQE spectra of MA^+-free tin-lead mixed perovskite solar cells (ITO/PTAA/SiO_2-NP/$FA_{1-x}Cs_xSn_{0.5}Pb_{0.5}I_3$/PCBM/BCP/Ag) using PTAA as HTL (a) and corresponding tauc-plot for extracting the band-gap energy (b). blue: x=0.085, red: x=0.15, green: x=0.25, orange: x=0.35.

In summary, MA^+-free $FA_{1-x}Cs_xSn_{0.5}Pb_{0.5}I_3$ perovskite solar cells with PTAA as a PEDOT:PSS-alternative were investigated. Low Cs^+ amounts results in poor solar cell performances due to a strong S-shape in their $J(V)$-curves. By adjusting the Cs^+ amount, the S-shape is reduced. This correlates to a slight tilting of the original cubic perovskite phase. By crystallographic perovskite modifications the perovskite band structure is expected to shift down in energy, resulting in an improved band-alignment of the HTL PTAA with the perovskite. This optimization strategy achieves an efficiency at MPP of 10 % in median with the MA^+-free $FA_{0.65}Cs_{0.35}Sn_{0.5}Pb_{0.5}I_3$ perovskite composition using the PEDOT:PSS alternative PTAA.

Summary and outlook: Exploring tin-lead mixed perovskite absorbers

The tin-lead mixed perovskite absorbers, as an example with improved environmental sustainability and reduced harm on human health, were investigated in the last chapter.
In detail a PEDOT:PSS-alternative in MA^+-free perovskite solar cells was explored. This was realized by first replacing PEDOT:PSS with PTAA in solar cell devices with an MA^+-containing perovskite composition. Comparable perovskite morphologies and crystal phase structures were obtained. Similar solar cell efficiencies were observed with PEDOT:PSS (PCE=13.0 %) and PTAA (PCE=11.5 %). Additionally, the MA^+ is replaced by an optimized mixture of FA^+ and Cs^+ for improved band alignment of the PTAA with the perovskite to yield maximal power conversion efficiencies of 10 % (median MPP).
These optimization strategies enqueue in a limited number of publications using an alternative to PEDOT:PSS in MA^+-free tin-lead mixed perovskite solar cells [116]. MA^+-free tin-lead mixed perovskite compositions are less frequently explored; the record for tin-lead mixed perovskite is still based on an MA^+-containing composition [8]. Using alternative HTL is also less common for tin-containing perovskite solar cells. NiO_x as HTL is less favorable, as metal oxides are suspected to insert oxygen vacancies [74,116]. Further perovskite coverage on PTAA is challenging as it has a hydrophobic surface [177]. This is solved by using SiO_2-NP to improve perovskite wetting [175]. The presented optimization approaches show how a PEDOT:PSS-alternative in MA^+-free tin-lead mixed perovskite solar cells can be realized. Nevertheless, further optimization approaches, as interfacial and perovskite morphology engineering, should be done to reduce unfavorable charge recombination and surpass the maximum solar cell efficiency in this work of 13.1 % for the MA^+-containing perovskite solar cells with PEDOT:PSS as HTL.

Regarding the relevance of tin-lead mixed perovskite absorbers for the perovskite solar cell technology, three main benefits can be drawn from those absorbers.
One is the reduced risk of lead due to the partial substitution by tin.
Moreover, the challenging tin oxidation is reported to be minimized in lead environment, thus mitigating the general stability concerns of tin-based perovskite absorbers (the stability will be investigated in detail in chapter 4.3).
Thus, tin-lead mixed perovskite absorbers can be an alternative to pure lead absorbers in perovskite solar cell technology, due to their improved sustainability, and high solar cell efficiency. Further, these perovskite absorbers can be used as a bottom solar cell in perovskite-perovskite tandem solar cells. Low band-gaps of <1.3 eV are so far only achievable with tin-lead mixed perovskite absorbers. A first experiment was performed to evaluate the usability of the fabricated solar cells in perovskite-perovskite tandem solar cells, showing promising results (see figure A.4). A 1.77 eV band-edge filter was used to simulate a semitransparent top wide band-gap perovskite solar cell. The tin-lead perovskite solar cell still achieved 4.5 % with filtered light.

4.2 Investigating tin perovskite absorbers being sustainable

This chapter analyzes pure tin perovskite solar cells to reduce harm on human health improve environmental sustainability further compared to the tin-lead mixed perovskites. This class of lead-free perovskite absorbers achieves solar cell performances of up to 14 % [9]. Here a trade-off is made between high sustainability and reduced solar cell performance.

A short introduction to the tin-based perovskite solar is given in the following. A detailed review on tin-based perovskite was given in chapter 2.2.1. Those tin perovskite solar cells are the so-far most promising lead-free perovskite solar cells due to their high solar cell efficiencies of up to 14 % [9]. However, one of the biggest challenges is the rapid oxidation from Sn^{2+} to Sn^{4+} deteriorating the perovskite phase. To suppress and retard the oxidation the additive SnF_2 is commonly used [74, 75, 191]. Additionally an improved perovskite morphology is gained adding this additive [148, 192–194]. However, the SnF_2 distribution in the perovskite bulk and chemical interactions remain unclear. Moreover, the fast reaction of the precursor materials results in uncontrollable nucleation and crystallization of the perovskite film [13]. Thus it is challenging to control the perovskite film growth leading to unfavorable perovskite morphology in terms of incomplete film coverage and low crystallinity with many structural defects [13]. Furthermore, low V_{OC} values of around 600 mV are generally achieved for those perovskite solar cells [103] in comparison to their band-gap energy of around 1.2 eV for $MASnI_3$ [159], 1.3 eV for $CsSnI_3$ [159] and 1.4 eV for $FASnI_3$ [159]. This is attributed to unmatching charge transport band alignments and a high defect density in the perovskite bulk [13, 74].

The optimization strategies in this work are based on the outlined challenges in the paragraph before. The impact of the SnF_2 additive on the film formation of $FASnI_3$ absorbers and interfaces will be analyzed in detail (see subchapter 4.2.1). Further charge layer interfaces will be optimized to address the challenges of appropriate perovskite morphology, band alignment mismatches, and perovskite interface defects (see subchapter 4.2.2). In the last subchapter the perovskite crystallographic structure of the perovskite film will be modified and analyzed (see subchapter 4.2.3).

For these optimization strategies, the $FASnI_3$ perovskite composition is chosen. The A-cation MA^+ is less favored here due to its instability concerns [120–123]. Furthermore, the Cs^+ as A-cation is also less favorable due to its low tolerance factor of 0.87 in the pure $CsSnI_3$ perovskite. For $FASnI_3$, a nearly perfect tolerance factor of 1.01 is calculated (see chapter 2.1.1 for the theoretical background). Mixed A-cation perovskite compositions are complex in perovskite precursor solution preparation, thus less favorable.

The analyzed perovskite films are deposited from a stochiometric perovskite solution by spin coating. A solvent mixture of DMF with added DMSO is used, which retards the crystallization of the perovskite and thus a higher control of perovskite film formation is achieved [195]. An anti-solvent dripping initializes the nucleation to start perovskite film growth.
If not specified otherwise, the characterized solar cells are inverted p-i-n stacks with ITO as TCO, PEDOT:PSS as HTL, a combination of PCBM and BCP as ETL and silver as back electrode. Detailed fabrication protocols are presented in the preparation method chapter 3.1.

4.2.1 Impact of SnF_2 additives on the perovskite film formation and its interfaces

The fast tin oxidation of Sn^{2+} to Sn^{4+} is a critical stability issue and one of the biggest challenges of Sn-based perovskite solar cells. SnF_2 is a commonly used additive in the perovskite precursor solution to suppress tin oxidation by reducing tin vacancies generated during the perovskite layer formation [74, 75, 191] and thus prevent a high defect-density [147, 148, 192]. Moreover, improved perovskite film morphology is observed with optimal amounts of SnF_2 addition, such as reduced pinhole formation, less voids, and a larger crystal grain size [148, 192–194].

While the utilization of SnF_2 as an additive in Sn-based perovskite solar cells is reported frequently [9, 80, 96, 99, 196, 197], the SnF_2 distribution in the perovskite bulk and chemical interactions remains unclear. In this subchapter, we examine the impact of SnF_2 additives in the perovskite precursor solution on the $FASnI_3$ perovskite bulk formation. The amount of SnF_2 additives varies from $x = 0 - 0.20$ (added molar ration to the SnI_2 amount). The local SnF_2 distribution in the perovskite bulk is analyzed by ToF-SIMS measurements while its chemical impact in the perovskite bulk is investigated by hard- (HAXPES) and soft x-ray photoelectronspectroscopy (XPS).

These presented achievements were accomplished within the project *Percistand*. As corresponding first author I was responsible for the design of experiment, preparation of samples, solar cell measurements, XRD measurements and interpretation of data. Jonas Hanisch performed and interpreted the ToF-SIMS measurements. Prof. Dr. Hans-Gerd Boyen, Dr. Philip Schulz and Derese Desta contributed to the HAXPES and XPS measurements and interpretation. Lisa Eisele participated as a master student by sample preparation and solar cell characterization. The main results are under preparation for submission in [198].

Impact of SnF_2 additive on the solar cell performance

To study the optimal amount of SnF_2 in the $FASnI_3$ perovskite bulk, solar cells with different SnF_2 amounts are prepared and characterized. Their extracted PCE are visualized in a boxplot, and exemplary $J(V)$-curves measured in forward bias scan direction are shown in figure 4.11. The solar cell performances improve up to an SnF_2 amount of $x = 0.15$ (see figure 4.11a). A maxima efficiency of up to 2.5 % is achieved for the optimal SnF_2 amount of $x = 0.15$. For no and high amounts of SnF_2 lower solar cell performance with strong hysteresis are observed [198].

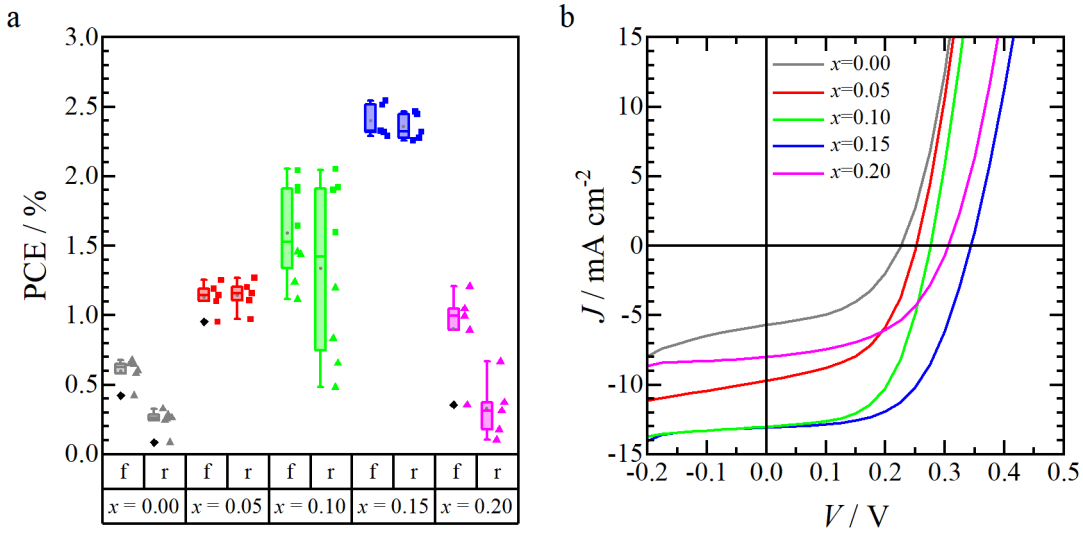

Figure 4.11: Impact of the SnF_2 amount in the $FASnI_3$ perovskite precursor solution on the solar cell performance adapted from [198]. a: Extracted PCE values visualized as boxplots for SnF_2 amounts from $x = 0$ to $x = 0.20$ measured in forward ('f') and reverse ('r') bias direction. Triangles show data values from batch one and squares from batch two. b: Exemplary $J(V)$-curves for each SnF_2 amount measured in the forward bias direction.

The impact on the perovskite morphology and its distribution in the perovskite bulk are analyzed, as the amount of SnF_2 additives strongly influences the solar cell performance.

Influence of the SnF_2 additive amount on the perovskite morphology

The impact of the SnF_2 additive amount on the perovskite morphology is investigated by analyzing its film properties and perovskite bulk phase.

A significantly homogeneous perovskite surface is achieved by adding SnF_2 into the perovskite precursor solution (see figure 4.12a,b). The top-view SEM images for the perovskite film without SnF_2 show a non-homogeneous layer surface. Adding precise amounts of SnF_2 into the perovskite solution, a uniform perovskite film is achieved. High amounts of SnF_2 ($x = 0.20$) leads to uniform perovskite, but with additional lighter areas. These are assumed to be SnF_2 crystals [198]. Improved perovskite morphology by adding optimal SnF_2 amounts is oftenly reported [148, 192–194, 199].
The non-homogeneous perovskite morphology for no added SnF_2 and high SnF_2 amounts are expected to be the reason for the lower solar cell performance with the observed strong hysteresis.

Additionally, XRD measurements are performed to characterize the perovskite phase (see figure 4.13). No significant differences in peak intensity and peak shift are observed for XRD pattern with different SnF_2 amounts. Thus the fluoride is not incorporated in the perovskite crystal structure, otherwise a peak shift would be expected [198]. These observations are consistent with other studies [32, 148, 200, 201]. The XRD pattern with high amounts of SnF_2 ($x = 0.20$) showed no additional peaks besides the perovskite phase and the ITO reflexes. The suggested additional crystalline SnF_2 phase discovered in the top-view SEM images cannot be verified. However, the amount of SnF_2 could be too small to be detectable via XRD measurements [198].

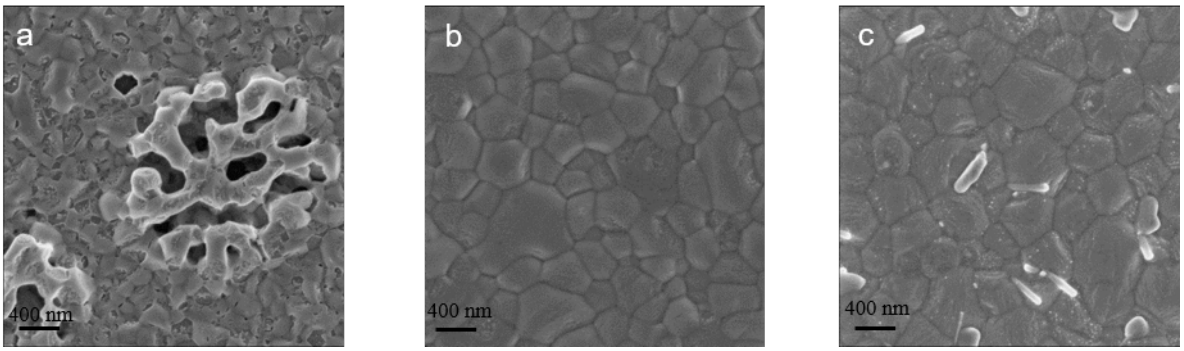

Figure 4.12: Impact of the SnF_2 additives on the $FASnI_3$ perovskite morphology displayed by top-view SEM images of ITO/PEDOT:PSS/perovskite samples adapted from [198] (a: $x = 0.00$, b: $x = 0.10$, c: $x = 0.20$).

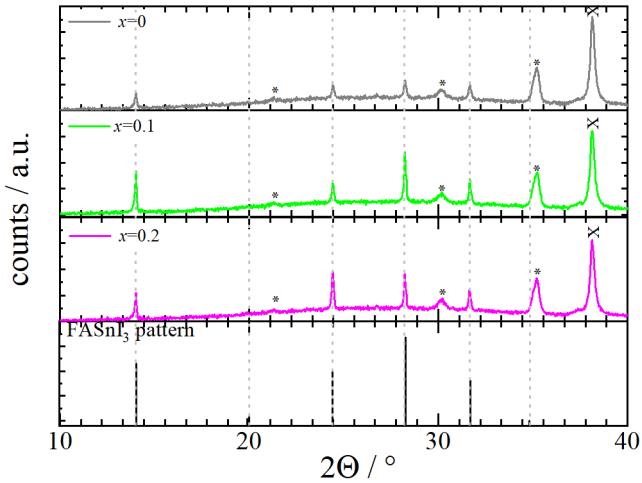

Figure 4.13: XRD pattern of $FASnI_3$ perovskite solar cells (ITO/PEDOT:PSS/perovskite/PCBM/BCP/Ag) with different SnF_2 amounts compared to a theoretical cubic $FASnI_3$ pattern adapted from [198]. ITO reflexes are marked as * and Ag reflexes as X.

In summary, the SnF_2 additive influences the perovskite film growth as an improved perovskite morphology is observed. For getting more insights into the impact of the SnF_2 addition on the perovskite film growth, the spatial distribution of the SnF_2 in the perovskite bulk is analyzed.

Spatial SnF_2 distribution in the $FASnI_3$ perovskite bulk

The SnF_2 distribution in the perovskite surface is investigated by ToF-SIMS measurements. For this, the fluoride F^- ion is tracked on the surface and perovskite bulk. The F^- is analyzed to visualize the SnF_2 distribution. The interpretation of Sn^{2+} ion distribution would be challenging as this ion is a superposition from the $FASnI_3$ perovskite, the SnF_2 additive, and the ITO. Thus, precise statements of the SnF_2 distribution would be difficult to be visualized via the Sn^{2+} distribution.

The lateral F^- distribution of the perovskite film surface for samples with $x = 0.00$, $x = 0.10$ and $x = 0.20$ are shown in figure 4.14. Adding no SnF_2 in the perovskite film reveals no detectable F^- signal, as expected. The observed signal intensity of up to two counts is regarded to be the background noise. For SnF_2 amounts of $x = 0.10$ a homogeneous F^- signal is observed. This suggests a uniform lateral SnF_2 distribution with no lateral SnF_2 accumulation. Adding high

amounts of SnF_2 $x = 0.20$ leads to uniform F^- distribution with additional areas of high F^- concentration. The areas with high F^- concentration are comparable to the size and form of the lighter parts visualized in the SEM top-view images. So the observed findings corroborate the assumption that SnF_2 crystals are formed in the perovskite film with high SnF_2 amounts [198].

For further specify the spatial SnF_2 additive in the perovskite bulk, ToF-SIMS depth profiles are performed. The F^- signal is visualized in 3D cubes to display the spatial distribution (see figure 4.15). A scheme illustrates the characterized sample stack consisting of the perovskite-, PEDOT:PSS-, and ITO-layer, as a guide to the eye (see figure 4.15a). As expected the perovskite film without added SnF_2 show negligible amounts of F^- (see figure 4.15b). Whereas three principle observation are made analyzing the F^- amount at the PEDOT:PSS/perovskite interface, perovskite bulk and perovskite surface in samples with added SnF_2 (see figure 4.15c-g)[1]: (i) high and constant F^- signals at the PEDOT:PSS/perovskite interface; (ii) negligible, but increasing F^- amounts in the perovskite bulk with enhancing SnF_2 concentration; (iii) small F^- amounts at the perovskite surface with strong increasing trend for higher SnF_2 concentration (x>0.10). Thus SnF_2 seems to preferably accumulate at the PEDOT:PSS/perovskite interface independently of the SnF_2 concentration (see figure 4.15g, orange dataset). The increasing amount of F^- in the perovskite bulk is nearly linear to the added SnF_2 concentration in the perovskite precursor solution (see figure 4.15g, gray dataset). Whereas, the increase of F^- at

[1] Detailed procedure for determining the F^- amounts is described in chapter 3.2.2.

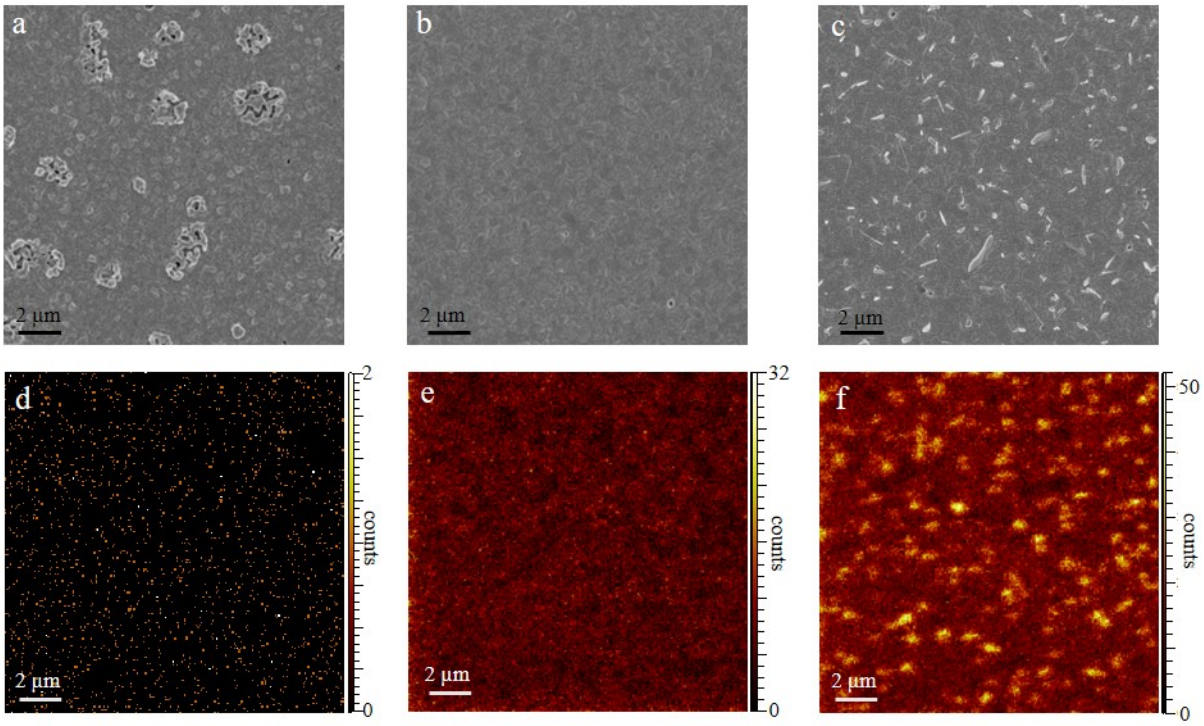

Figure 4.14: Characterization of the SnF_2 distribution by analyzing the fluoride (F^-) distribution on the $FASnI_3$ perovskite surface by ToF-SIMS (d-f) and corresponding SEM top-view images (a-c) for ITO/PEDOT:PSS/$FASnI_3$ samples with different SnF_2 amounts of $x = 0.00$ (a,d), $x = 0.10$ (b,e) and $x = 0.20$ (c,f) adapted from [198]. Measurements were performed in the delayer-extraction-mode using Bi^+ ions as the analysis beam and Cs^+ for sputtering.

the perovskite surface is stronger than the added SnF_2 concentration in the perovskite precursor solution (see figure 4.15g, red dataset). The total amount of F^- in the perovskite bulk is largest as this summarizes the amount over the hugest sample thickness (80 % of the perovskite thickness). Inconsistent slight differences of the F^- amounts are considered being due to statistic sample variation in two batches. For the sample with the highest SnF_2 amount ($x = 0.20$) the local lateral accumulations are visible here, too, as already observed in the surface study. Moreover, these local F^- accumulations continue vertically in the perovskite bulk, forming F^- channels throughout the perovskite bulk. It is assumed that SnF_2 crystals grow vertically from the PEDOT:PSS/ perovskite interface throughout the perovskite bulk, if the SnF_2 concentration is too high.
2D depth profiles further corroborate the F^- accumulation at the PEDOT:PSS interface as illustrated in figure A.5. These show, besides the F^- ions, additional ions representing the different layers in the sample stack. Here, the focus is on the S^- ions as those visualize the PEDOT:PSS layer. Accumulation at the PEDOT:PSS interface is verified as the maximum F^- signal is shortly before the S^- [198].

To sum up, spatial F^- distribution suggests a preferable accumulation of the SnF_2 at the PEDOT:PSS/ perovskite interface [198]. Consequently, the PEDOT:PSS/perovskite interface is investigated in more detail.

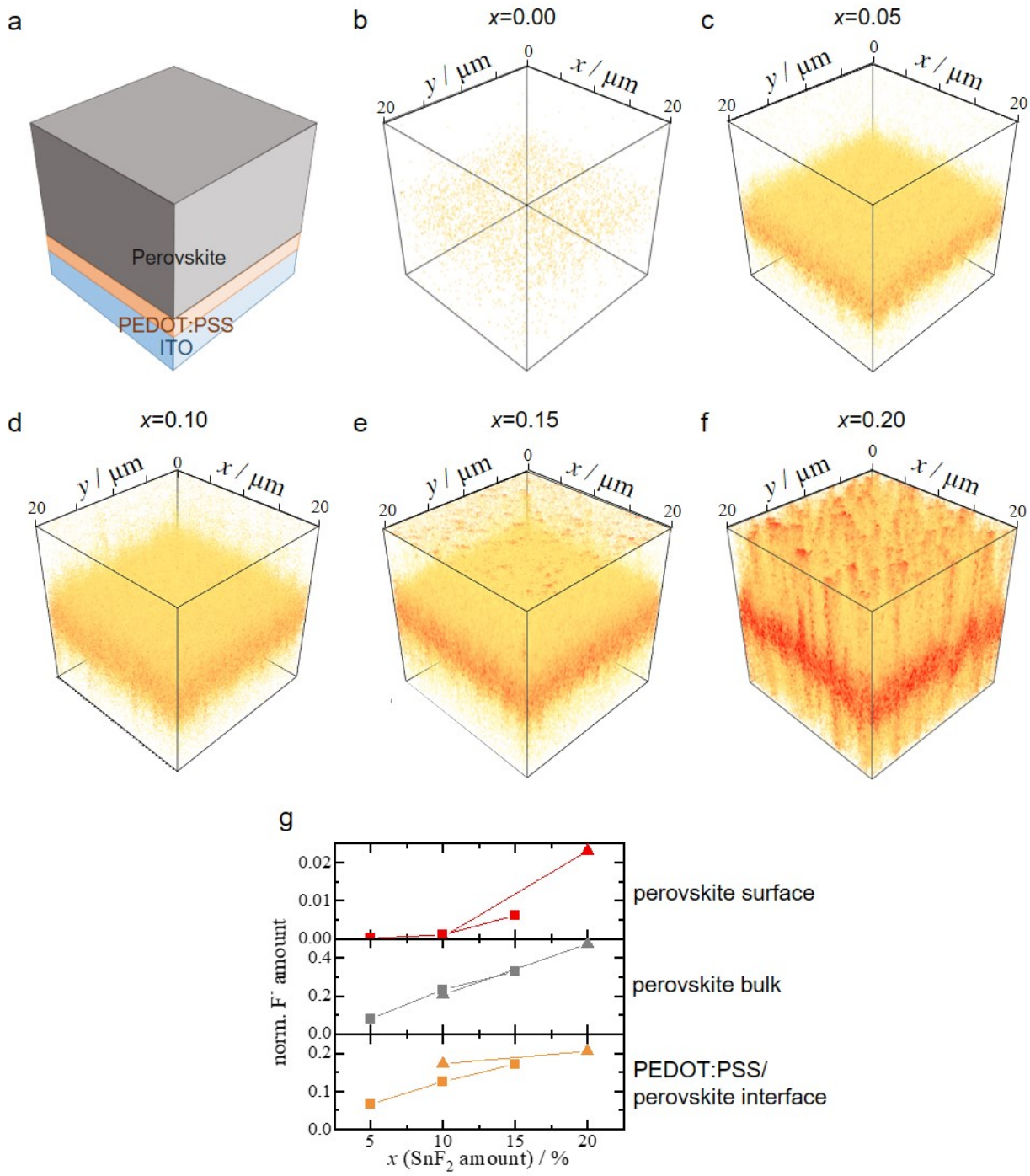

Figure 4.15: Characterization of SnF_2 bulk distribution by analyzing the fluoride (F^-) distribution in the $FASnI_3$ perovskite bulk (b-f) for different SnF_2 amounts x = 0.00 (b), x = 0.05 (c), x = 0.10 (d), x = 0.15 (e), x = 0.20 (f) with the corresponding device stack (a) taken from [198]. Color change from light yellow to dark orange indicate increasing F^- signal. Measurements were performed in the delayer-extraction-mode using Bi^+ ions as the analysis beam and Cs^+ for sputtering. (g): Evaluation of the (F^-) at the PEDOT:PSS/perovskite interface (orange dataset), perovskite bulk (gray dataset) and perovskite surface (red dataset) for two batches indicated as triangles and squares.

Impact of SnF_2 additive on the PEDOT:PSS/perovskite interface

For investigating the impact of the accumulated SnF_2 on the chemical nature of the PEDOT:PSS/perovskite interface, a combination of hard- and soft X-ray photoelectron spectroscopy (HAXPES, XPS) is performed. HAXPES supports depth information of up to 100 nm, whereas XPS is very surface sensitive.

Since these measurements are very time-consuming, only samples without and with the optimal amount for the solar cell performance of SnF_2 ($x = 0.15$) are investigated. For these measurements, semi-finished samples without deposited ETL and back electrode are fabricated with a maximal nominal perovskite layer thickness of 100 nm ($c_{perovskite}$=0.4 M). The thinner perovskite film does also provide significant thickness fluctuations with pinholes (see figure A.6). This makes it possible to analyze the PEDOT:PSS/perovskite interface also by XPS.

Some general findings are outlined, before illustrating the findings of the PEDOT:PSS/perovskite interface characterization. Those provide comparability of our study to other researchers.

To verify that fluor is incorporated in the perovskite film, we crosschecked the binding energy for such core levels (see figure 4.16). For the sample with SnF_2 addition, a clear signal at 685 eV is detected, which can be attributed to the fluor 1s core level [202]. The sample without SnF_2 revealed no signal at this binding energy. Consequently, no cross-contamination is observed, and only the sample with added SnF_2 contains fluoride.

Furthermore, the tin oxidation for this set of samples is analyzed. SnF_2 should retard and prevent the oxidation from Sn^{2+} to Sn^{4+}. Thus the 3d-$_{5/2}$ tin core level of the as-grown samples are investigated on behalf of their Sn^{2+} and oxidized Sn^{4+} fractions (see figure 4.17). For the sample without SnF_2 addition, the measured signal at 486 eV can be fitted by one peak. This binding energy is assigned to a pure Sn^{2+} contribution [203]. However, for the sample with

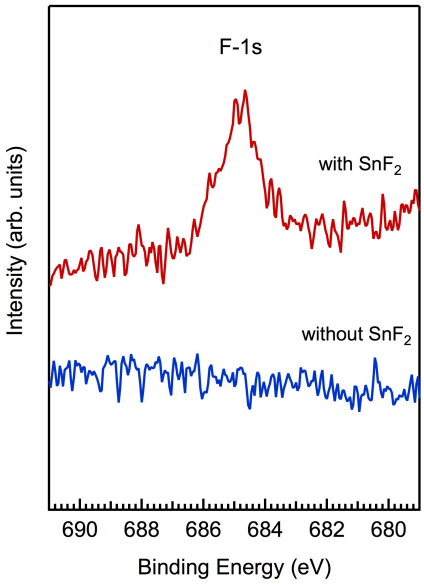

Figure 4.16: HAXPES measurement of perovskite samples (ITO/PEDOT:PSS/$FASnI_3$) without and with SnF_2 additive analyzing the F-1s core level.

SnF_2, the signal has to be fitted by two contributions. A second small signal at 487 eV is present corresponding to the Sn-$3d_{5/2}$ core level of Sn^{4+} [203]. Since a portion of Sn^{4+} is only detected for the sample with SnF_2 addition, we assume that the SnF_2 precursor material includes minor contaminations of Sn^{4+} ions. Soft aging these samples in a nitrogen atmosphere with circa 300 ppm oxygen for 60 days increases the Sn^{4+} portion. This is more prominent for the sample without SnF_2 (see figure 4.17c). The addition of SnF_2 does retard the oxidation from Sn^{2+} to Sn^{4+}.

In the following, the PEDOT:PSS/perovskite interface will be investigated.
Investigating the PEDOT:PSS interaction with the perovskite, a PEDOT:PSS film as a reference sample is characterized first. The sulfur S-1s and S-2p core levels are characterized by HAXPES and XPS measurements (see figure 4.18 black line). For the bulk related HAXPES measurements, signals at binding energies of 2477 eV and 2472 eV are observed. This can be attributed to the SO_3^-, and SO_3H groups of PSS and C-S-C molecular units of the PEDOT polymers in the HTL. These signals have intensity ratios of PEDOT to PSS of 1:4.2 consistent with the provider specification. The intensity ratio of the PEDOT:PSS films changes for the surface-sensitive XPS measurement. Doublets at binding energies of 163.8 eV and 168 eV are detected corresponding to the PEDOT and PSS polymers in the PEDOT:PSS film. The PEDOT fraction is reduced to a ratio of 1 to 6.5 compared to the PSS [198]. The observed findings are consistent with the chemical nature of PEDOT:PSS polymers in which the PEDOT:PSS core is surrounded by a PSS shell as illustrated in figure 4.19a. Thus the PEDOT:PSS film surface consists of a higher PSS ratio than the film bulk, as was also observed by other researchers [204]. The observed intensity ratios are summarized in table 4.1.

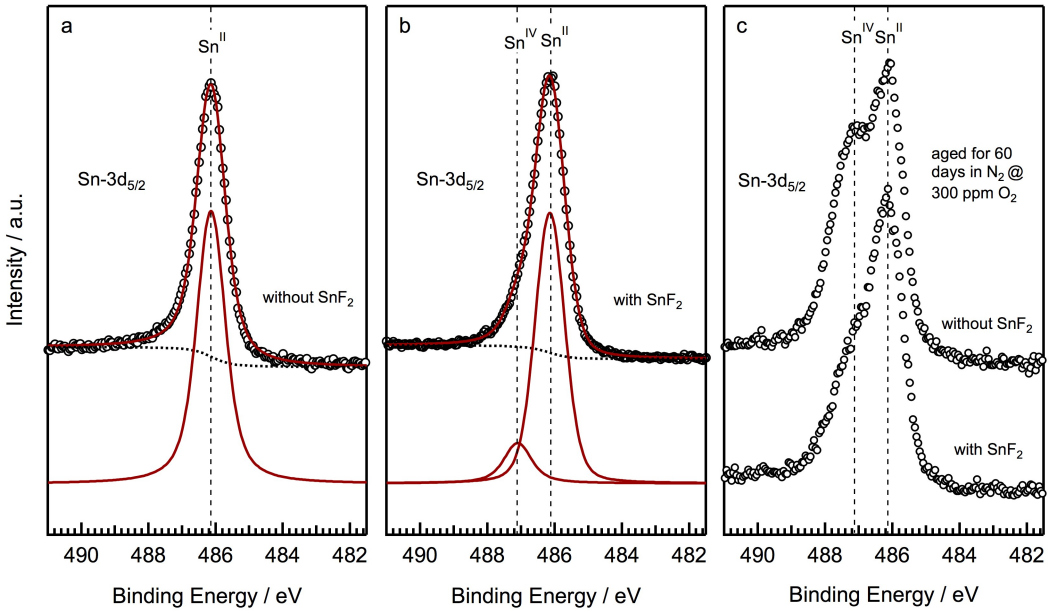

Figure 4.17: HAXPES measurement of perovskite samples (ITO/PEDOT:PSS/$FASnI_3$) without (a) and with (b) SnF_2 additive analyzing the Sn-$3d_{5/2}$ core level of as-grown and aged for 60 days in nitrogen atmosphere with 300 pm of oxygen (c). Circles are measured data, whereas solid lines are their fits.

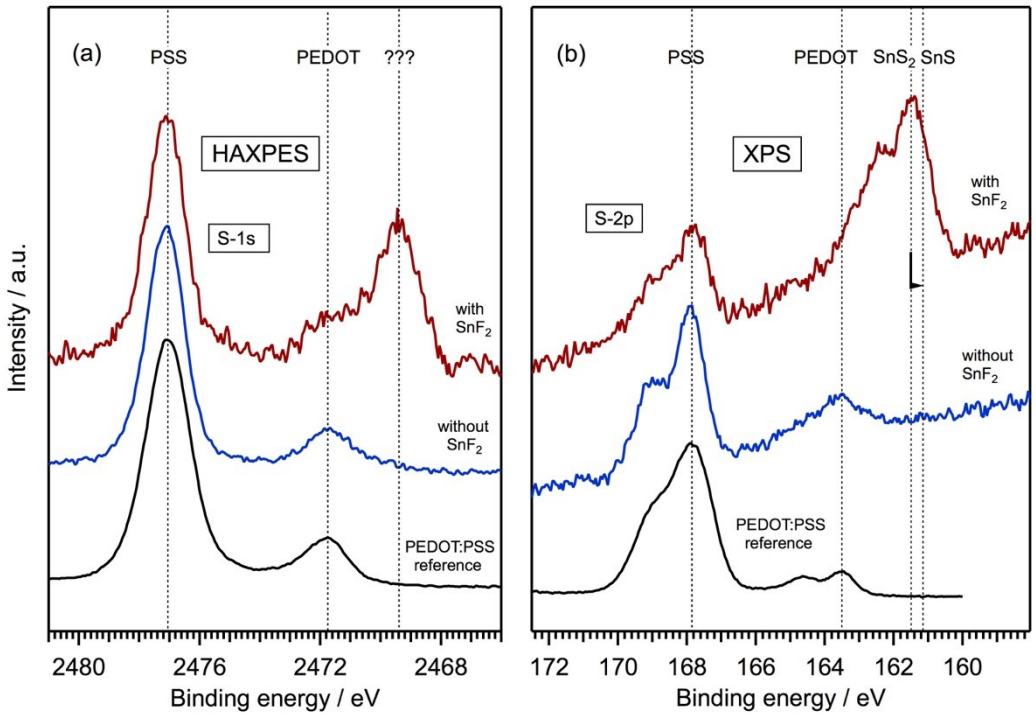

Figure 4.18: HAXPES (left) and XPS (right) measurements for analyzing the PEDOT:PSS/perovskite interface of ITO/PEDOT:PSS/($FASnI_3$) samples by their sulfur S-1s and S-2p core levels taken from [198]. Measured data of the PEDOT:PSS reference film are shown as a black, perovskite film without SnF_2 as a blue and perovskite film with SnF_2 as a red line. Literature values of PSS, PEDOT, SnS_2 and SnS are inserted as vertical lines [202].

Table 4.1: Summarized intensity ratios of the sulfur contributions S-1s (HAXPES) and S-2p (XPS) core levels assigned to the polymers PEDOT, PSS and the interlayer SnS for the PEDOT:PSS film as well as perovskite film with and without SnF_2 additive adapted from [198].

method	PEDOT:PSS film	PEDOT : PSS ratio of perovskite film without SnF_2	PEDOT : PSS : SnS ratio of perovskite film with SnF_2
HAXPES	1:4.2	1:3.9	1:4.0:2.5
XPS	1:6.5	1:4.1	1:4.1:9.1

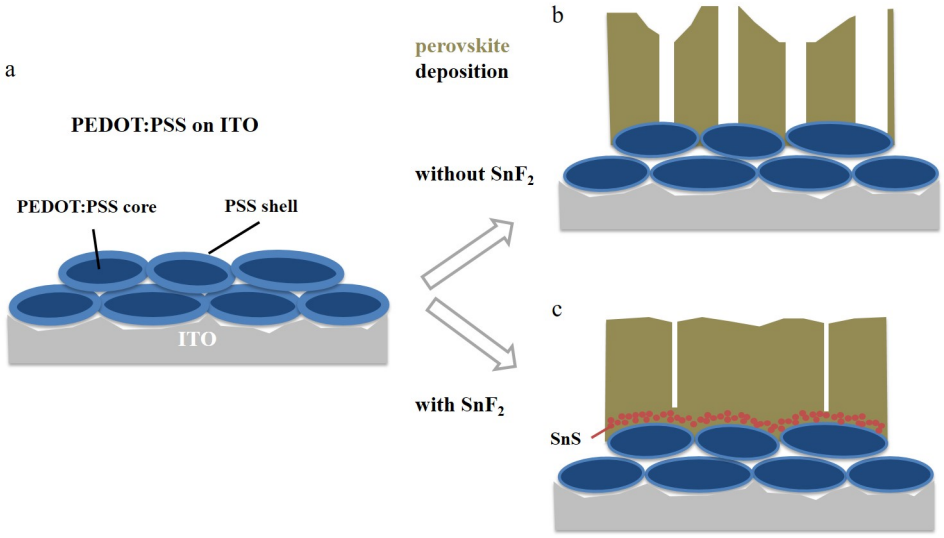

Figure 4.19: Schematic illustration of the as-grown PEDOT:PSS on ITO (a), deposited perovskite film without SnF_2 additive (b) and with SnF_2 (c) adapted from [198].

As a next step the samples with deposited perovskite on top of the PEDOT:PSS film are investigated.
First, the perovskite sample without added SnF_2 is characterized. Because the perovskite morphology without SnF_2 reveals inhomogeneous layer deposition with many pinholes (see figure 4.12a and A.6a), the PEDOT:PSS/perovskite interface can be easily analyzed by HAXPES as well as XPS measurements. Analyzing the sulfur contributions of this interface reveals observations similar to the pristine PEDOT:PSS film regarding the chemical species. No additional peaks are detected, which can be assigned to new chemical interactions. So the PEDOT and PSS polymers are not interacting with the perovskite absorber. However, the intensity ratio of the PEDOT and PSS polymers changes. For the bulk analysis via HAXPES measurements the PEDOT:PSS intensity ratio of 1:3.9 is unchanged from the pure PEDOT:PSS film (1:4.2). In contrast, the surface-sensitive XPS measurement reveals a lower PSS intensity compared to the PEDOT:PSS film. The intensity ratio changes to 1:4.1 for the PEDOT:PSS interface. It is assumed that the perovskite precursor solution DMF:DMSO is de-washing some of the PSS shells, resulting in a decreased PSS amount on the PEDOT:PSS film surface [198]. The finding of perovskite deposition without SnF_2 additive on the PEDOT:PSS is illustrated in figure 4.19b. A similar observation of de-washing was already reported in the literature [204].
Now, the observed results are compared to the perovskite film with SnF_2 additive. XPS and HAXPES measurements can be performed to analyze the PEDOT:PSS/perovskite interface, as the thinner inhomogeneous perovskite layer provides thickness fluctuations with pinholes. Since the pinholes density is still low, a low signal intensity of the interface in XPS measurements are gained. Thus measurements with integration time of several days are performed to achieve a sufficient signal to noise ratio. The sulfur core levels drastically changed with the SnF_2 additive in the perovskite bulk. The intensity ratio of the polymer PEDOT and PSS for both measurement techniques are consistent with the ones observed without SnF_2 in the perovskite bulk. In contrast an additional contribution appears at the 2469.4 eV for the HAXPES and a doublet at 162 eV for the XPS measurements with a weight fraction of 2.5 to 5 for the HAXPES and 9.1 to 5 for the XPS measurement compared to PEDOT:PSS [198]. The detailed fitting

of these curves is illustrated in figure A.7. Published XPS data suggest a SnS_x compound for the XPS measurements [205]. For this compound, an effective interlayer thickness of 1.2 nm is observed [198]. This is calculated by the Strohmeier equation [206] with inelastic mean pathways of 3.6 nm in PEDOT:PSS and 2.4 nm in the interlayer (see detailed calculation in the appendix) [202]. The SnS_x compound can be assigned to either tin(IV)sulfide (SnS_2) (binding energy of 161.5 eV) or tin(II)sulfide (SnS) (binding energy of 161.1 eV) [205]. Since a very low thickness of 1.2 nm is observed for the interlayer, it is assumed that the layer does not consist of a homogeneous layer rather than of accumulated nanograins/nanoparticle. Thus, the electrons are attracted to the residual positive charged SnS_x nanograin/nanoparticle, during the electron release of the photoelectron-spectroscopy measurements [198]. This leads to a kinetic energy loss of 0.4 eV for the released photoelectrons due to coulomb interaction [202, 205–210]. Considering this energy loss, the observed contribution in the XPS measurements now matches to SnS [198]. The perovskite formation with the SnS interlayer is depicted in figure 4.19.

For verifying the formed SnS by a chemical reaction of the SnF_2 with PEDOT:PSS an additional set of experiment are performed with deposited SnF_2 on PEDOT:PSS. Therefore, three samples with different SnF_2 concentrations were analyzed by XPS and HAXPES (see figure 4.20). Chosen SnF_2 concentrations were the same, double and quadrupled amount as in the original experiment before.
Consistent results of PEDOT and PSS S-1s and S-2p sulfur core levels as in figure 4.18 are observed. Further the SnS can be verified at 2469.4 eV (HAXPES) and 162.4 eV (XPS). The stronger signal in the XPS than the HAXPES measurements confirm the deposition of SnS on the sample surface. The overall lower signal compared to the one with deposited perovskite is suggested to be due to different deposition kinetics. It is assumed that a stronger accumulation of the SnF_2 is observed in the perovskite deposition procedure.

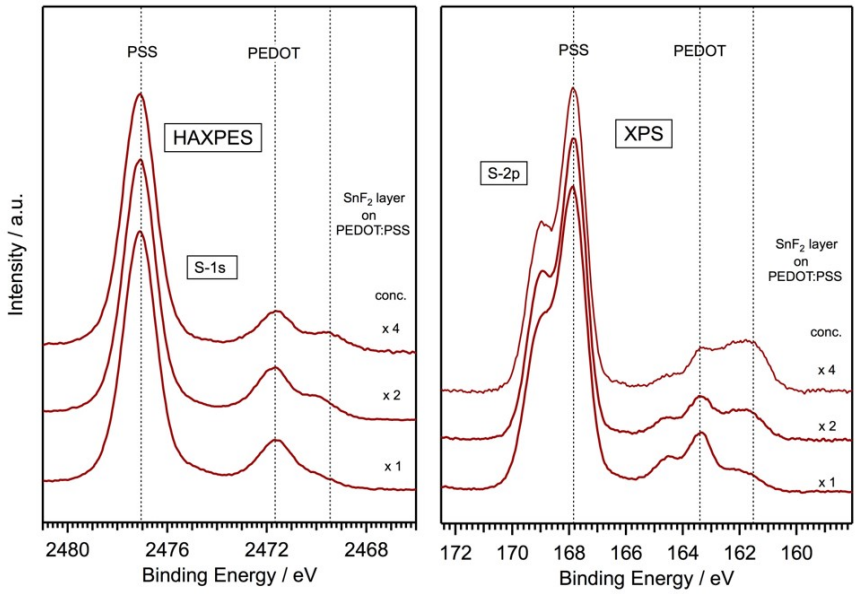

Figure 4.20: HAXPES (left) and XPS (right) measurements of deposited SnF_2 on PEDOT:PSS taken from [198]. Three SnF_2 concentrations were used for the deposition from DMF:DMSO: original, double and quadrupled concentration. Literature values of PSS, PEDOT, SnS_2 and SnS are inserted as vertical lines [202].

Consequently, by analyzing the PEDOT:PSS/perovskite interface, two principle findings are observed. The perovskite precursor solution de-washes the surface of the PEDOT:PSS film, resulting in a decreased PSS fraction on the PEDOT:PSS film surface. More importantly, the perovskite with SnF_2 addition reacts with the sulfur of the PEDOT:PSS film forming a 1.2 nm SnS interlayer [198].

Summary and outlook of the characterized SnF_2 additive impact on the perovskite absorber properties

Besides the well-known improved perovskite morphology and retarded Sn^{2+} oxidation, new (additional) unique observations of SnF_2 additives' impact on the perovskite bulk properties were discovered. These are (i) the preferable accumulation of SnF_2 additive at the PEDOT:PSS/perovskite interface and (ii) an ultrathin SnS interlayer formation at the PEDOT:PSS/perovskite interface. It is assumed that the accumulated SnF_2 additive contributes to the formed SnS interlayer.
The hygroscopic and acidic PEDOT:PSS [116, 127–129] is commonly not favored as an HTL in lead perovskite solar cells, but is often used in tin perovskite solar cells. The new finding of the formed SnS interlayer by interacting of the SnF_2 with the PEDOT:PSS could give a hint towards the reason why the combination of PEDOT:PSS as HTL and the SnF_2 additive are crucial components for high efficient Sn-based solar cells [9, 80, 96, 99, 196, 197]. As SnS is a p-type semiconductor [211], it is assumed that the formed interlayer supports the hole extraction in the solar cell device, improving the solar cell performance. This can be corroborated to the principle improved solar cell efficiency with increasing SnF_2 amount.

4.2.2 Interfacial engineering for improved solar cell performance

Further optimization strategies have to be considered, as the observed solar cell performance of 2.5 % by optimizing the SnF_2 amount is still relatively low.

Unappropriate charge layer interfaces are known to limit solar cell performances [13, 74, 103]. Three challenges commonly arise from unsuitable charge layer interfaces in the literature:
(i) unfavorable perovskite film formation [13] due to inappropriate interfacial properties of the underlying layer with the perovskite precursor solution. This generally results in perovskite morphologies with pinholes, cave structures, and high surface roughness. To cope with this, chemical engineering is preferred in the literature to control the perovskite film formation [80, 82–85, 98]. More easily, the HTL is modified to tune the perovskite film formation by the wetting behaviour of the perovskite precursor solution on the HTL surface. The perovskite coverage is strongly dependent on matching HTL surface properties to the perovskite precursor solution [175].
(ii) band offsets [13, 103]. The conduction and valence bands should be aligned more suitable to tin perovskite. The principal solar cell architecture is generally adopted from the lead-based perovskites for tin ones. However, tin perovskites have a different band structure. Thus commonly used charge layers for lead perovskite solar cells do not perfectly match to tin ones. Literature reports strategies for aligning the HTL [98, 212] and ETL [99] to the perovskite.
(iii) perovskite surface defects [72, 74, 103]. PCBM besides effectively withdraw electron charges is known for his passivation of perovskite surface defects [51].

Interfacial engineering is performed in the following subchapter to address the named challenges. The underlying charge layer interface, here the HTL, is modified to improve perovskite morphology. As we expect that PEDOT:PSS is a crucial component in tin perovskite solar cells (subchapter 4.2.1), this HTM is maintained. The HTL/perovskite is solely modified by depositing SiO_2-NP on top, forming a non-completely covering layer so that physical device properties are negligibly effected by these SiO_2-NP. Further the ETL interface is altered to align the conduction band and to passivate perovskite surface defects. A huge conduction band mismatch of the used ETL PCBM and perovskite is expected [103, 213]. Shifting the ETL conduction band to higher energies should reduce this mismatch. This is done by substituting the PCBM with other C_{60} derivatives with higher-lying LUMO levels. According to the results presented in organic solar cells, the C_{60} derivative ICBA and bis-PCBM are promising materials. They provide LUMO levels shifted to higher energies of 170 mV and 100 mV compared to PCBM [214].
An overview of the interfacial engineering strategy is schematically summarized in figure 4.21.

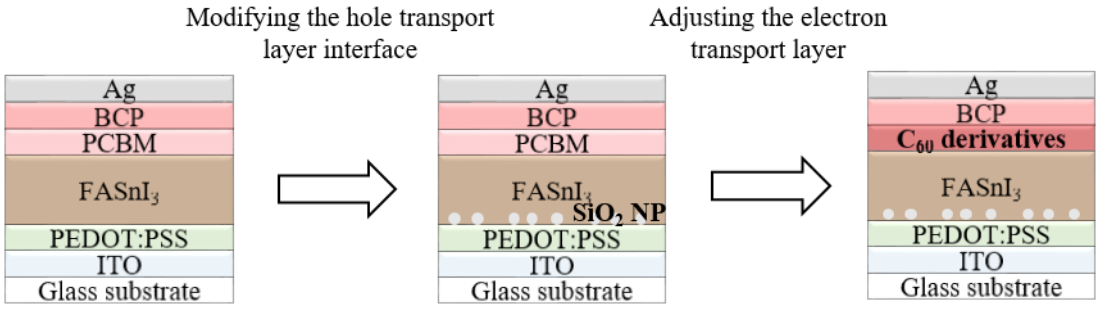

Figure 4.21: Schematic overview of the interfacial engineering strategy in chapter 4.2.2.

The solar cells preparation is basically unchanged from the ones presented in the subchapter before and illustrated in the preparation protocol (chapter 3.1). Differences are the deposited SiO_2-NP between the HTL and perovskite and the altered ETL materials ICBA and bis-PCBM besides PCBM.

The mainly presented results were accomplished within the project *Percistand* and are prepared for submission. As corresponding first author I was responsible for the design of experiment, preparation of samples, solar cell, UV-Vis, XRD and internal quantum efficiency (IQE) measurements and interpretation of data. Dr. Philip Schulz and Dr. Géraud Delport support the work by PL measurements and their interpretation.

Modifying the hole transport layer interface

The perovskite film growth is altered by modifying the HTL interface depositing an optimal amount of SiO_2-NP on top.
The perovskite film is characterized on semi-finished samples (ITO / PEDOT:PSS / (SiO_2-NP) / $FASnI_3$). The impact on the perovskite morphology, optical properties, and crystal morphology are analyzed by SEM, optical, and XRD measurements.

The top-view SEM measurements revealed improved perovskite coverage on the HTL using SiO_2-NP in the layer stack (see figure 4.22). The pinhole density is drastically reduced. The crystal grain size seems to be unaffected by this optimization approach. Moreover, the perovskite roughness is smoothed. The observed roughness R_a decreased from 36 nm without to 33 nm with SiO_2-NP.
The crystal morphology analysis obtained a comparable XRD pattern for both samples (see figure 4.23). No significant differences in peak intensities and full width at half maximum (FWHM) are observed, indicating no changes in crystal orientation, crystalline sizes, and phase.
Thus it seems that the modified HTL improves the perovskite morphology in terms of reduced pinholes but without affecting the crystal morphology.

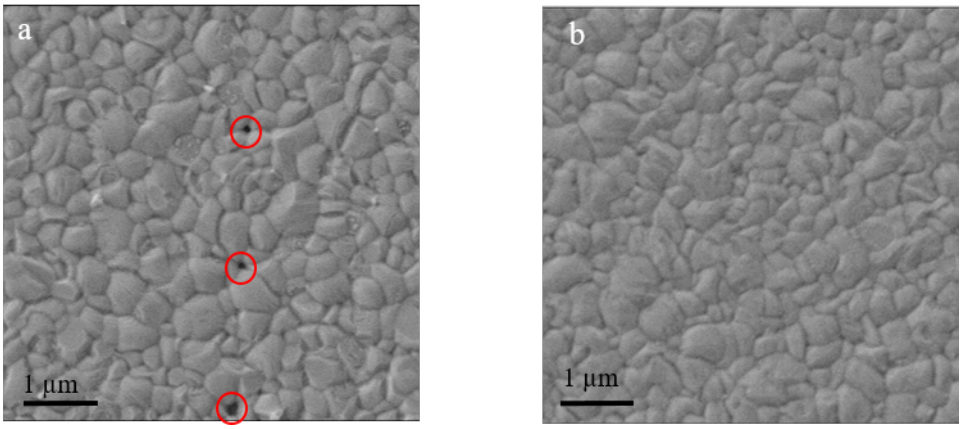

Figure 4.22: Impact of SiO_2-NP used in the device stack on the perovskite film characterized by top-view SEM images of ITO/PEDOT:PSS/(SiO_2-NP)/$FASnI_3$ samples. a: without SiO_2-NP, b: with SiO_2-NP. Red circles highlights the pinholes in the perovskite film.

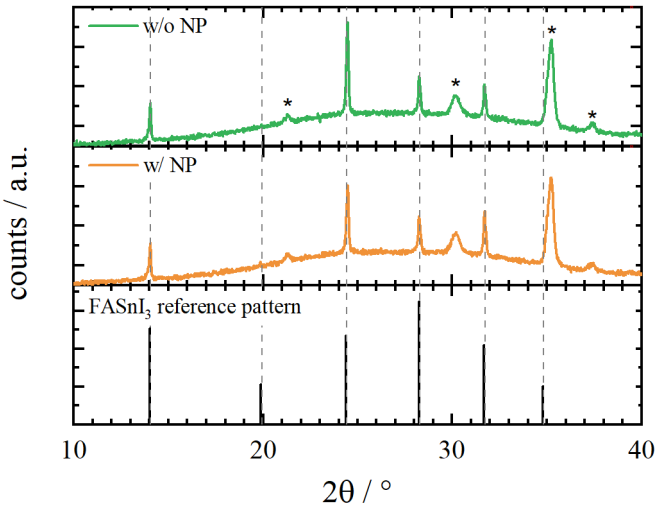

Figure 4.23: XRD pattern for analyzing the impact of inserting nanoparticle (NP) in the device stack on the perovskite crystal morphology compared to a reference $FASnI_3$ pattern [215]. ITO reflexes are marked as *.

The perovskite film is further analyzed by its defects properties combining transient resolved and steady-state PL measurements (see figure 4.24). These are performed on semi-finished encapsulated samples illuminating these from the substrate and encapsulation.
As the normalized steady-state PL spectra are comparable, it is expected that the perovskite defect energies are unaltered. The PL intensity of these spectra is unreliable since precise sample adjustment is challenging in this setup.
Thus the PL intensities are examined by integrating the TRPL spectra (see figure 4.24b). These revealed comparable integrated PL intensities for the samples illuminated via the encapsulation ($3.8 \cdot 10^4$ vs. $2.9 \cdot 10^4$, see figure 4.24c), whereas the integrated PL intensities are significantly enhanced from $2.1 \cdot 10^4$ to $5.6 \cdot 10^4$ using SiO_2-NP illuminated via the substrate. This behavior suggests increased radiative recombination at the HTL interface.
Fast and comparable lifetimes (τ) are observed illuminating from the same direction unaffected by the SiO_2-NP (see figure 4.24c). Meanwhile, slightly shorter lifetimes are observed illuminating the sample via the substrate (1 ns vs. 2 ns). This agrees with the expected faster quenching of charges by extracting holes via the hole transport layer. Thus it is expected that the radiative recombination occurs from similar energetic states for both sample types.

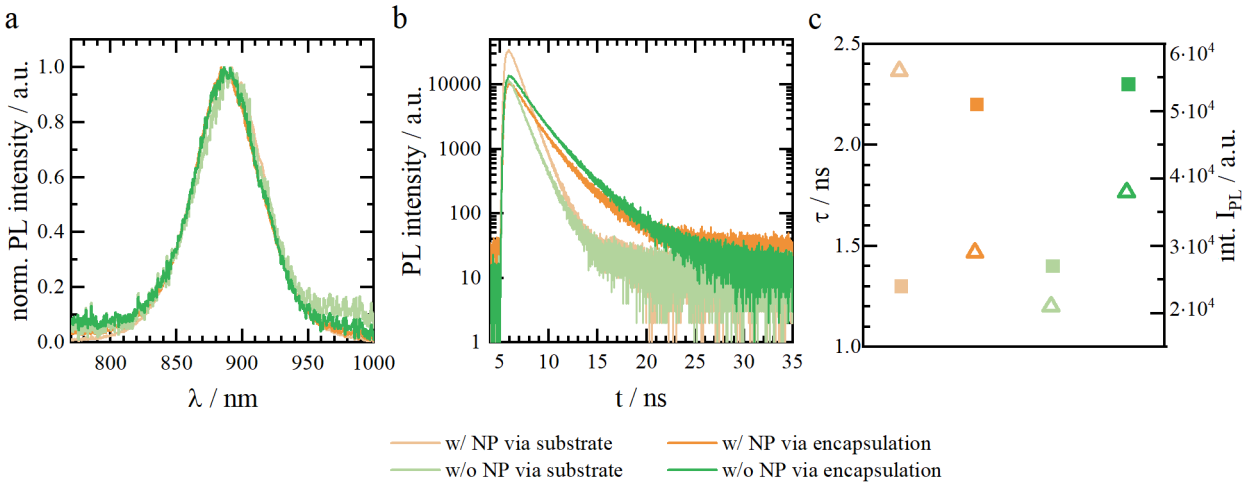

Figure 4.24: Impact of used SiO_2-NP on the perovskite defects analyzed by PL measurements. The measurements are performed on encapsulated semi-finisher stacks (ITO / PEDOT:PSS / (SiO_2-NP) / $FASnI_3$) illuminating these via the substrate (lighter color) or the encapsulation (darker color). Results of samples wihtout SiO_2-NP are displayed in green and with in orange. a: steady state PL, b: TRPL. c: calculated lifetime τ and integrated PL intensity (int. I_{PL}) from the TRPL.

To sum up the PL results, using SiO_2-NP for improved perovskite morphology results in no energetic variation of radiative states (steady state PL,τ), but a higher density of radiative states is observed (integrated PL intensity). Thus it is suggested that the density of non-radiative states is reduced in favor of higher contribution of radiative states' without affecting their energetic distribution.
This behavior is consistent with the observed improved perovskite film morphology without altered crystal morphology using SiO_2-NP.

Solar cells without and with SiO_2-NP are fabricated and analyzed, to verify the positive effect of improved perovskite morphology on solar cell performance. The PCE, V_{OC}, J_{SC} in the forward bias scan direction and $J(V)$-curves of best devices are shown in figure 4.25.
An improved solar cell efficiency with reduced spreading from median 3 % to 4 % is observed by using SiO_2-NP. The V_{OC} and J_{SC} is increases from 380 mV to 420 mV and 13.3 mA cm^{-2} to 15.3 mA cm^{-2}.
The gain in V_{OC} and J_{SC} is attributed to the reduced dark recombination due to the improved perovskite morphology.

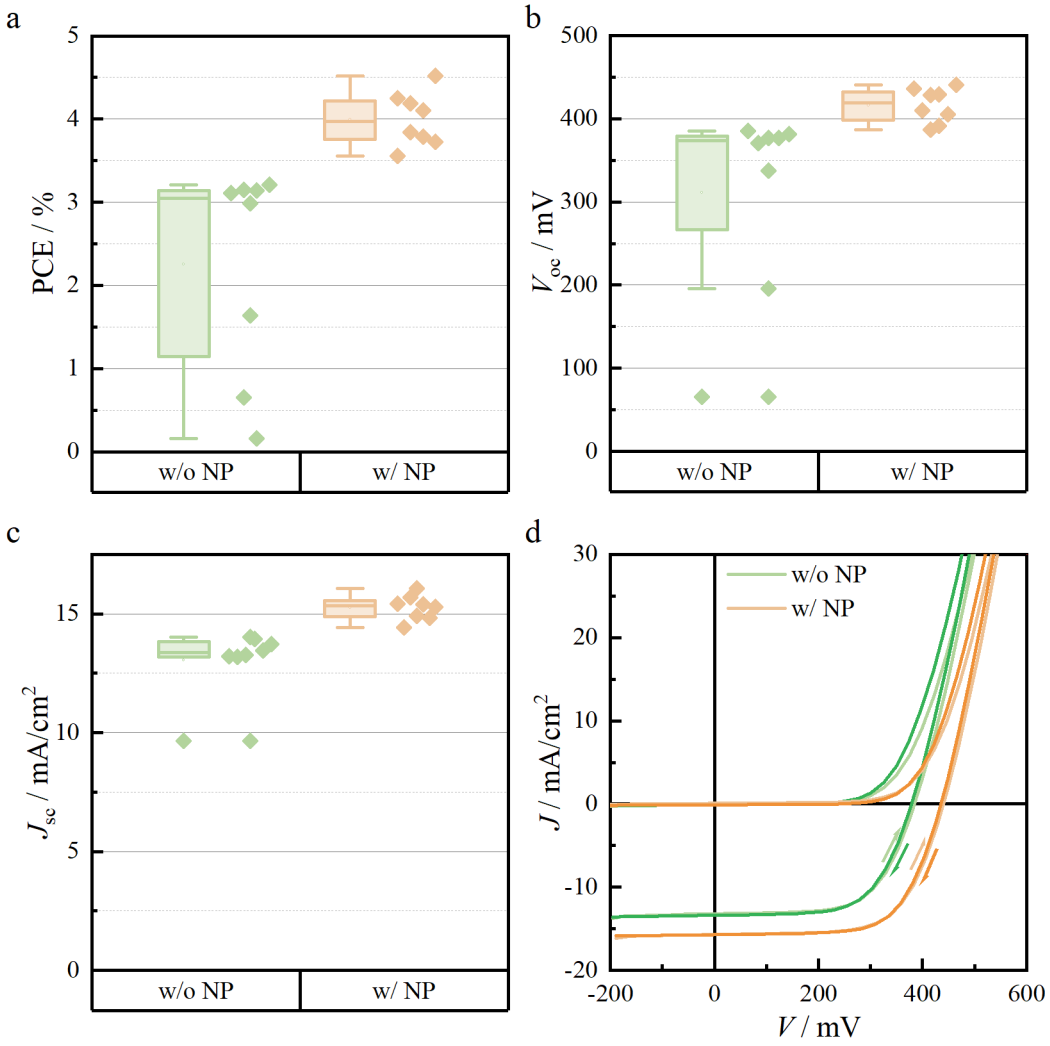

Figure 4.25: Impact of SiO_2-NP used in the device stack (ITO / PEDOT:PSS / (SiO_2-NP) / $FASnI_3$ / PCBM / BCP / Ag) on the solar cell performance. a: PCE, b: V_{OC}, c: J_{SC}, d: $J(V)$-curves of the best devices of each parameter.

Nevertheless, the impact of inserted SiO_2-NP on absorption properties of the layer stack and IQE of the solar cells are investigated.
The transmittance and reflectance are measured on the semi-finished stack. The examined spectra, including the absorptance, show no significant differences (see figure 4.26a). A slightly reduced reflection using SiO_2-NP is observed, resulting in an increased absorption from 300 to

650 nm.
Moreover, IQE measurements revealed similar spectra shapes with only differences in the IQE level (see figure 4.26b).
So the SiO_2-NP seems to have a negligible impact on the optical properties of the solar cell.

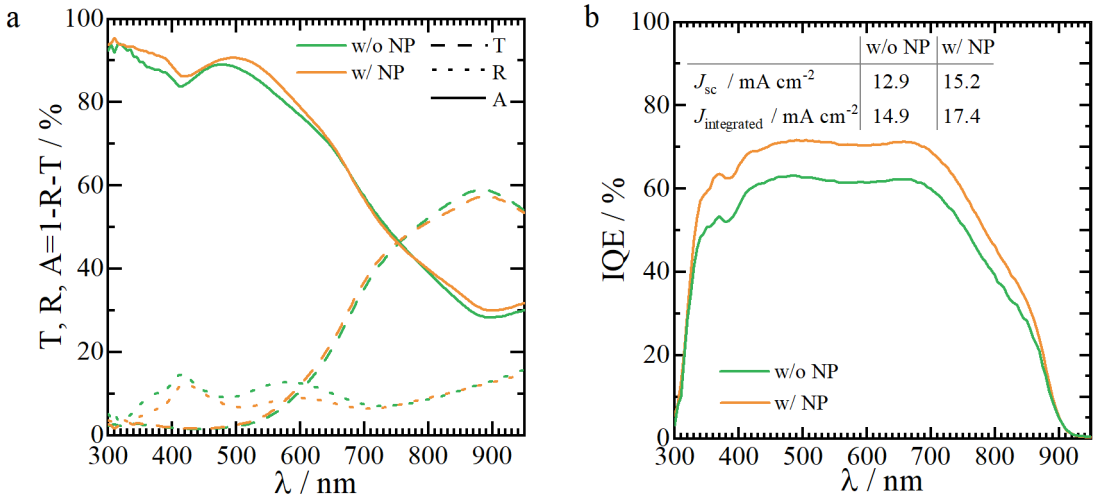

Figure 4.26: a: Impact of used NP on the optical properties of 601.23171670516 72.055427251732 601.23171670516 94.842186297152 samples (dotted line: reflectance R, dashed line: transmittance T, solid line: absorptance A, orange: without NP, green: with NP.) b: Impact of inserted NP on the IQE spectra.

In summary, HTL interfacial engineering was performed to control perovskite film formation. A pinhole-free perovskite film with reduced dark recombination was achieved. This improves the solar cell performance by around 33 %.

Adjusting the electron transport layer by using different fullerene derivatives

As introduced at the beginning of this subchapter, two additional fullerene derivatives are investigated to the commonly used PCBM. The aim is to align the conduction bands of the electron transport material to the perovskite to improve the solar cell performance.
As a band mismatch is expected between the perovskite and PCBM, alternative ETL have to be discovered with higher lying conduction band. As these ETL should be easily fabricated from solution, alternative C_{60} derivatives with higher lying lowest unoccuppied molecular orbital (LUMO) levels are chosen. Increased LUMO levels can be achieved by a contraction of the original 58π-electron-conjugated system of PCBM to a 56π one. This is accomplished by C_{60} derivatives with two side chains. Common ones are the ICBA and bis-PCBM (see chemical formula in figure 4.27) [214]. They provide LUMO levels shifted to higher energies of 170 mV and 100 mV compared to PCBM [214].

The three different C_{60} derivatives do significantly impact the solar cell performance (see figure 4.28). By substituting the PCBM by ICBA results in a median efficiency increase from 3.6 % to 5.6 %. However, unexpectedly an efficiency drop to 2.4 % in median is observed for the bis-PCBM devices.
The conduction band alignment is analyzed by characterizing the achieved V_{OC} values. Losses in V_{OC} are among others correlated to band mismatches of the perovskite with the charge layers [217]. As expected, the V_{OC} increases for both PCBM alternatives. The V_{OC} improves

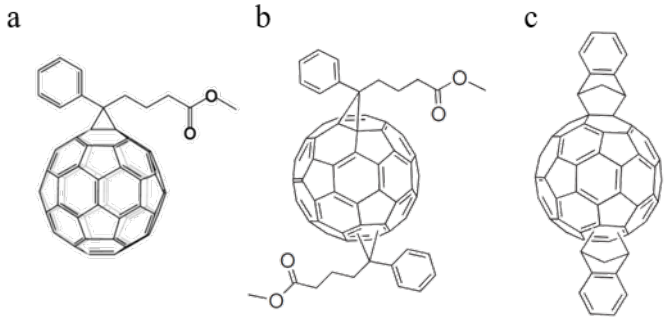

Figure 4.27: Chemical formula of PCBM (a) adapted with permission from [216], ICBA(b) and bis-PCBM(c) adapted from [214].

from 380 mV for the commonly used PCBM to 480 mV for bis-PCBM and further to 650 mV for ICBA devices (median values) (see figure 4.28a). The increasing V_{OC} trend correlates to the higher lying LUMO of bis-PCBM and ICBA. Thus, it is assumed that the conduction band of the perovskite is more suitably aligned using the PCBM alternatives.
Nevertheless, improved solar cell performance is only achieved for the ICBA devices. Thus additional effects besides conduction band alignment are suggested to impact the solar cell performance using the three ETL. The V_{OC} gain of the bis-PCBM devices is compensated by low FF (46 vs. 56 %) and J_{SC} (11.1 vs. 17.1 mA/cm^2) values compared to PCBM devices (median values) (see figure 4.28b). Also, for the ICBA devices, the J_{SC} reduces to 14.0 mA/cm^2 in median.

As especially PCBM is known for its passivation of perovskite surface defects [51], it is expected that due to different attached side groups to the buckyball the passivation is altered. Passivated perovskite surface defects can positively impact the FF [218–220]. The passivation of surface defects is analyzed by PL measurements, as a high density of defects are suspected to enhance the probability of dark recombination. Thus the PL intensity is analyzed to get insights into the passivation capacity of these ETL materials. Analogous to the SiO_2-NP investigation, steady-state and transient measurements are performed on encapsulated devices without back electrode illuminated from the encapsulation. Again similar spectra shapes are accomplished (see figure 4.29 a), suggesting a comparable energetic distribution of radiative states. As before, no interpretation of the PL intensity is made, as an appropriate sample adjustment is challenging for this setup. The PL intensity is therefore characterized by the integration of the TRPL signal (see figure 4.29 b). The ICBA devices reaches the highest PL intensity of 65000. The integrated PL intensity of PCBM (11000) and bis-PCBM (2000) are significantly lower (see figure 4.29 c). The passivation of perovskite surface defects seems to be much higher for ICBA than for the two other ETL. It can be assumed that the indene side group of the ICBA passivates the perovskite defects more effectively than the ester-groups of PCBM and bis-PCBM.
Comparable short lifetimes in the range of 0.70 to 0.85 ns are observed. This suggests fast charge extractions by the ETL (see figure 4.29 c).
The observed FF approximately follows the trend of PL intensity. However, the increase of PL intensity is much stronger than the FF gain for ICBA and reduced J_{SC} values can rarly be explained by the passivation.

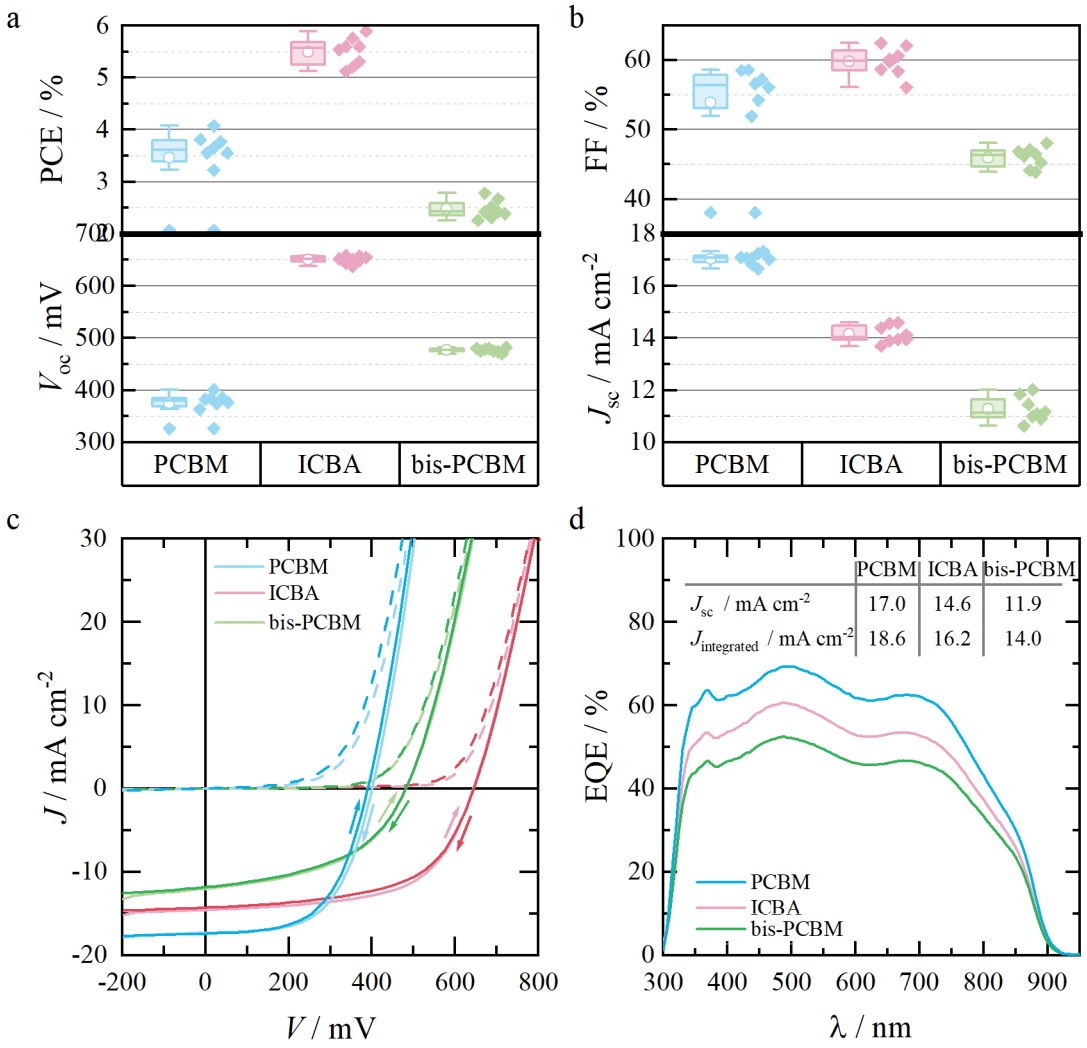

Figure 4.28: Impact of different C_{60}-fullerene derivatives on the solar cell performance (Solar cell stack: ITO / PEDOT:PSS / SiO_2-NP / $FASnI_3$ / C_{60}-fullerene derivatives / BCP / Ag)). a: PCE and V_{OC}, b: FF and J_{SC}, c: $J(V)$-curves of the best devices of each parameter and d: EQE spectra.

Consequently, it is suspected that a third effect can limit solar cell performance. A significantly reduced electron mobility is reported for the two PCBM alternative materials [221, 222]. Thus, these can lower the FF [223] and J_{SC} [224] as well. The limited electron mobility can not be compensated by reducing the ETL thickness, as this minimal thickness is needed for complete coverage of the perovskite surface.

To sum up, an improved solar cell performance from 3.6 % to 5.6 % is achieved altering the ETL. Three effects are accomplished by using the three ETL materials PCBM, ICBA, and bis-PCBM. The usage of the PCBM alternatives ICBA and bis-PCBM are expected to align more suitably with the conduction band. This increases the V_{OC} from 380 mV (PCBM) to 480 mV (bis-PCBM) and 650 mV (ICBA) due to assumed improved band alignment at the perovskite/ETL interface. However, V_{OC} gains are compensated by the lower intrinsic mobility for both PCBM alternatives resulting in FF and J_{SC} losses. For ICBA an improved perovskite defect passivation is observed, which is thought to partially compensate the losses from the intrinsic mobility.

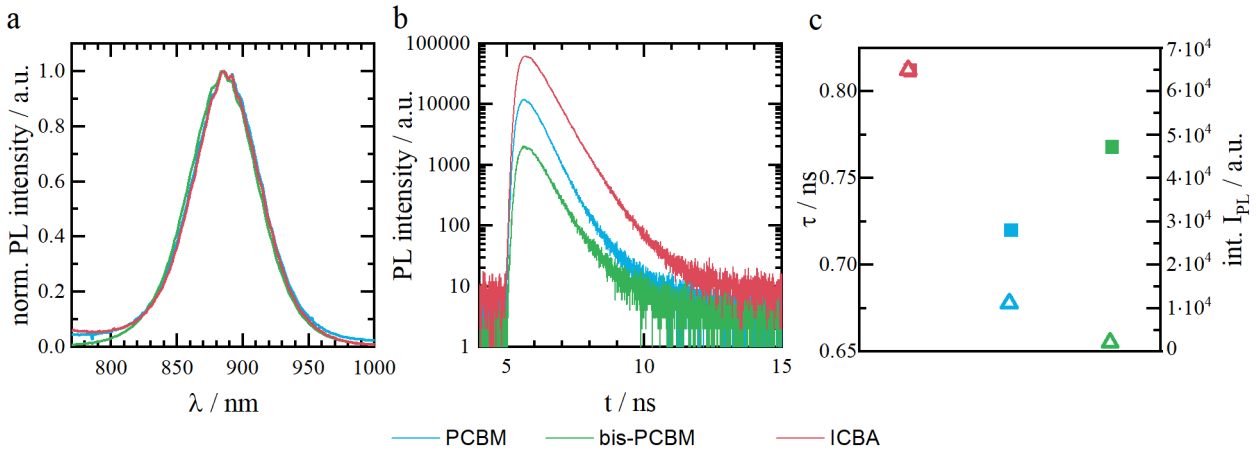

Figure 4.29: Analysis of perovskite defects by steady-state (a) and TR PL (b) measurements of encapsulated samples (ITO / PEDOT:PSS / (SiO_2-NP) / $FASnI_3$ / ETL) with different C_{60}-fullerene derivatives. Determined lifetime (τ, filled square) and integrated PL intensity (int. I_{PL}, unfilled triangle) from the TRPL are visualized in c. (blue: PCBM, green: bis-PCBM, red: ICBA).

Summary and outlook of interfacial engineering for improved solar cell performance

In summary, by interfacial engineering, the solar cell performance of $FASnI_3$ perovskite solar cells can be improved from 3.0 % to 5.5 % in median. A pinhole-free perovskite morphology with reduced dark recombination is accomplished by modifying the HTL/perovskite interface. This is realized by inserting SiO_2-NP in between these two layers. An overall increased efficiency from 3 % to 4 % in median is observed. Furthermore, the conduction band, of perovskite and ETL is assumed to be aligned by using the PCBM alternatives ICBA and bis-PCBM, because significant V_{OC} gains from 380 mV (PCBM) to 480 mV (bis-PBCM) and 650 mV (ICBA) are revealed. Despite the conduction band these also have various passivation capacities and limited intrinsic electron mobilities. Especially the V_{OC} gains in the bis-PCBM devices seem to be compensated by these. Nonetheless, the solar cell efficiency could be pushed from 3.6 % for PCBM devices to 5.5 % for ICBA devices in median. A high solar cell efficiency of up to 5.9 % is achieved.

For further improvements, a focus on the limited intrinsic ETL mobility should be placed. For this, reducing the ETL thicknesses should be favored. This can be done by smoother perovskite surface, or evaporating the ETL as surface roughness is less crucial for these processes.

4.2.3 Tuning the crystalline ordering of the perovskite film

As we focused on interfacial engineering by charge layer modification before, now improved perovskite morphology by texturing the crystallographic structure via 2D/3D mixed perovskite is explored.

2D/3D mixed perovskite films general achieve an improved perovskite morphology compared to their 3D analogue [82–87]. The 2D perovskite influences the crystal growth resulting in improved crystal ordering by enhanced crystallinity and packing with reduced defects [12]. The bulky cations hereby suppress the random bulk nucleation and crystallization in the wet layer

in favor for the nucleation and crystallization from the solution surface, leading to oriented growth and thus to highly oriented crystallites [93]. This enhances the solar cell performance and stability, as a reduced defects density decreases the probability for both non-radiative recombination [217] and initial sites for degradation processes [12]. Moreover, if the quasi-2D layers are arranged parallel to the substrate, the hydrophobic quasi-2D layers prevent oxygen and moisture infiltration [74]. However, charge transport can be hindered by these quasi-2D slices [74]. Figure 4.30 illustrates 2D layers aligned parallel and perpendicular to the substrate. More details about 2D/3D mixed perovskite films are outlined in subchapter 2.2.1.

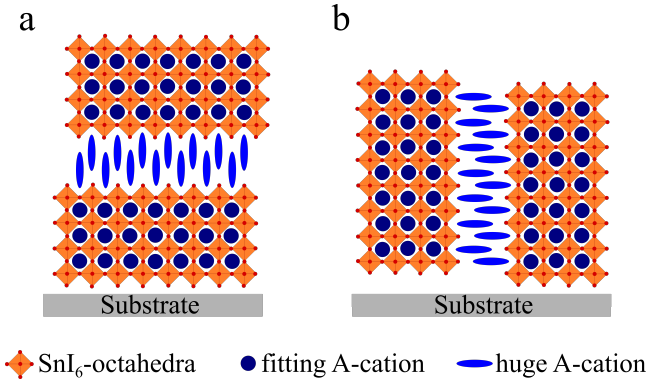

Figure 4.30: Schematic illustration of parallel (a) and perpendicular (b) arranged quasi-2D layers in 2D/3D mixed perovskites.

In this work, PEA^+ is used as a bulky cation to tune the crystalline perovskite structure. 2D/3D phenethylammonium tin iodide (PEA_2SnI_4)/$FASnI_3$ mixed perovskites are realized by mixing stoichiometric precursor solutions of PEA_2SnI_4 and $FASnI_3$. The given amounts are based on molar ratios of the 2D perovskite in comparison to the total molar ratio of the perovskite precursor solution. The overall perovskite solar cell fabrication and stack are kept unchanged to the subchapters before. Based on the optimization approaches in subchapter 4.2.2, SiO_2-NP are deposited for solar cell fabrication. Further, the fullerene derivative PCBM is compared to the ICBA one. Detailed information about deposition procedures are given in the subchapters 3.1.1 and 3.1.4.

In the beginning of this subchapter, the perovskite morphology will be analyzed by its crystallographic changes in dependency of the 2D perovskite ratio. Based on the observed results, the impact of structural changes on solar cell performance will be studied afterwards. The procedure is schematically illustrated in figure 4.31.

The content of this chapter was developed in cooperation with the master student Lisa Eisele writing her master thesis *Impact of hybrid 2D-Perovskites on the stability of Perovskite solar cells* [215] under my guidance.

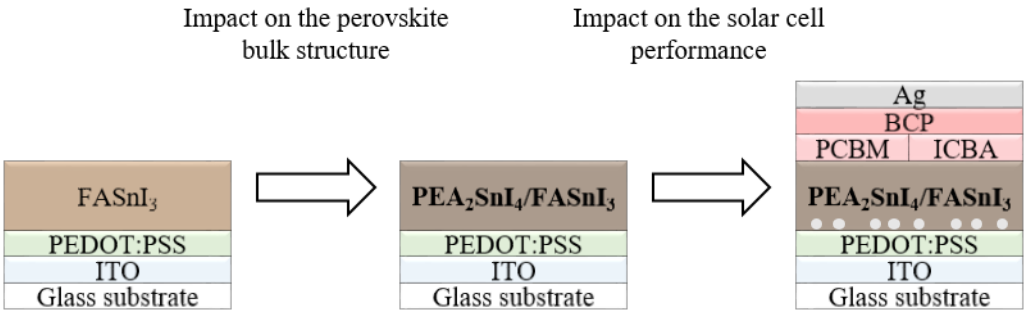

Figure 4.31: Schematic overview of the 2D/3D perovskite investigation in chapter 4.2.3.

Impact of the 2D PEA_2SnI_4 perovskite on the bulk structure

The following paragraph analyses the bulk properties of the perovskite film in dependency of the PEA_2SnI_4 amount.

The crystalline phase(s) are studied by XRD measurements (see figure 4.32). These are compared to XRD patterns of cubic $Pm\bar{3}m$ $FASnI_3$ and triclinic $P\bar{1}$ PEA_2SnI_4 crystals. These patterns were obtained from crystals synthesized and characterized by Lisa Eisele during her master thesis [215].
The 3D $FASnI_3$ perovskite film matches to the calculated $FASnI_3$ XRD pattern. The XRD pattern of the 2D PEA_2SnI_4 perovskite film suggest a highly oriented crystal with a {002} orientation. In these two organic (PEA^+) and inorganic layers based on the SnI_6 octahedra alternate. The 2D/3D perovskite film with 50 % $FASnI_3$ and 50 % PEA_2SnI_4 show a phase mixture of the 2D and 3D perovskite. However, it is dominated by the 2D PEA_2SnI_4 phase as a strong peak at 5.4° is observed. Reducing the 2D amount, the pattern is dominated by the 3D $FASnI_3$ peaks with strong texture effects. A strong orientation according to the {001}-planes is observed. The intensity ratio of the (001) to (111) peaks for different 2D/3D mixtures are examined in figure 4.32b. The strongest texture effect to the {001} orientation is observed for a PEA_2SnI_4 amount of 7.5 %. An enhanced (001)/(111) peak intensity ratio of 31 is accomplished. For the pure 3D perovskite, this ratio is smaller than 1.
Hence, an optimal amount of PEA_2SnI_4 results in a strong {001} facet crystal orientation. This suggests a strong impact of the 2D phase on the nucleation and crystallization process of the perovskite film.

Adding a PEA_2SnI_4 into a 3D system is reported to impact the nucleation and crystallization process significantly. In the 3D perovskite network nucleation and crystallization take place in the perovskite bulk and at the perovskite/air interface leading to a unstructured crystallization process [93]. This results in randomly oriented crystallites [93]. The XRD pattern of the pure 3D $FASnI_3$ with multiple crystal-oriented peaks and low peak intensities compared to the other XRD patterns support this hypothesis.
The nucleation and crystallization of the 2D PEA_2SnI_4 perovskite is thought to predominantly start at the solution/air interface and further crystallizes to the bottom of the substrate [93]. A highly oriented perovskite film is observed due to the suppressed undesirable bulk crystallization [93]. Again the observed results of the pure 2D PEA_2SnI_4 perovskite corroborate the supposed crystallization process.

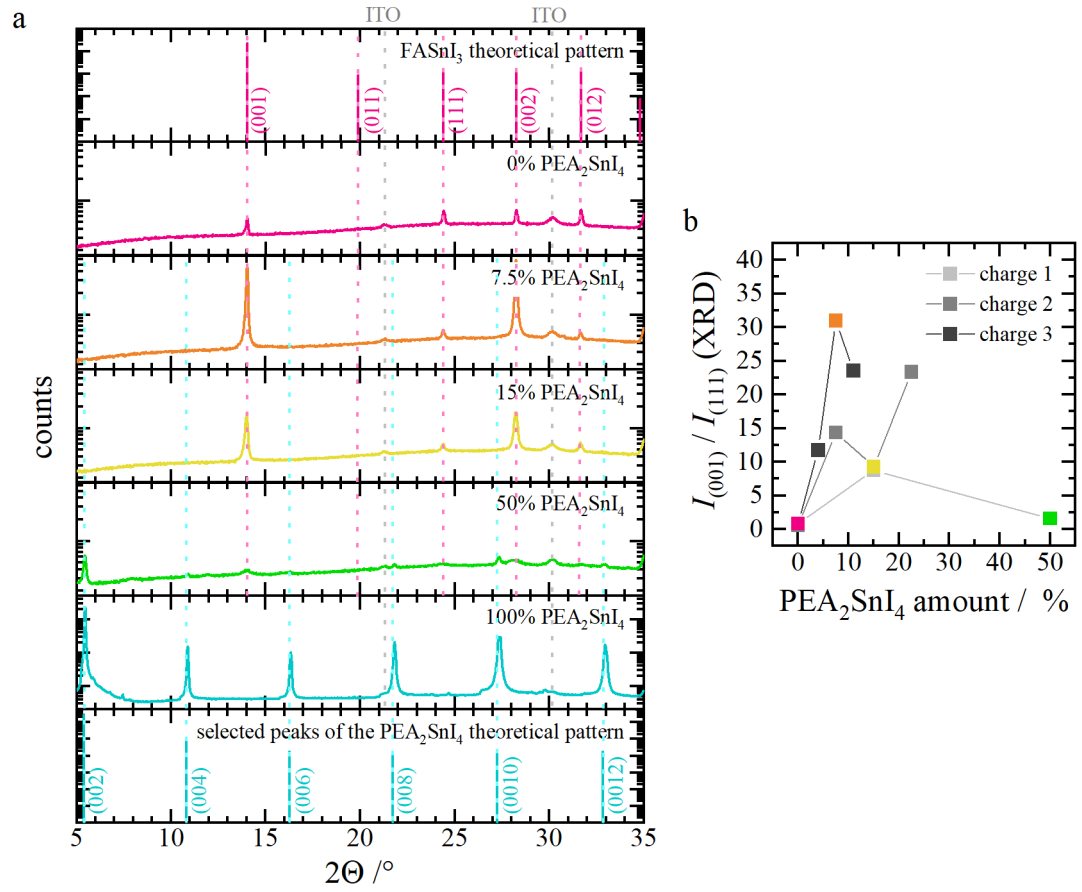

Figure 4.32: Impact of different 2D PEA_2SnI_4 perovskite amounts on the crystal structure of the perovskite layer. a: exemplary measured XRD pattern of 3D $FASnI_3$, multiple 3D/2D $FASnI_3$/PEA_2SnI_4 and 2D PEA_2SnI_4 compared to calculated 3D $FASnI_3$ and 2DPEA_2SnI_4 pattern, showing only the {002}-plane peaks. The given amounts refer to the total molar perovskite concentration. b: Analysis of crystal texturing in the 2D/3D mixed $FASnI_3$/PEA_2SnI_4 perovskite films by comparing the peak intensities of the (001) to the (111) 3D $FASnI_3$ peak.

Mixing a 2D and 3D perovskite is suggested to suppress the random bulk crystallization [93]. The perovskite nucleation and crystallization thus starts from the surface further crystallizing to the bottom, resulting in highly oriented crystallites [93]. The observed highly orientated perovskite film in the 2D/3D mixed perovskite again verify the proposed mechanism of [93].

To analyze, where the 2D phase(s) are located in the 2D/3D perovskite bulk, the spatial distribution of the PEA_2SnI_4 in the perovskite bulk is specified by grazing incidence X-ray diffraction (GIXRD) and ToF-SIMS measurements. A similar work observed a quasi-2D phase formed at the bottom of the perovskite bulk [88]. Here, analysis is carried out on samples having the highest crystallite orientation (7.5% PEA_2SnI_4).
GIXRD measurements with small ω angles (ω=0.15) and larger ω angles (ω=0.7) are carried out to compare the perovskite surface to the perovskite bulk (see figure 4.33a). The observed peaks at 12.5° are assigned to a SnI_4 phase [225] and the peak at 14.1° to the 3D $FASnI_3$ perovskite phase. No significant phase differences are observed, as no additional peaks are detected. Furthermore, no additional peaks are observed at smaller 2θ angles, e.g. 5.4° for the 2D perovskite, it is expected that no 2D phase is formed at the perovskite surface. However, for

the measurement with higher bulk sensitivity, the ratio of a 2D phase could be too small to be detectable via XRD measurements. Thus, the GIXRD study revealed no 2D phase formation at the perovskite surface, but 2D phases in the perovskite bulk (or at the HTL interface) can-not be specified appropriately.
ToF-SIMS measurements are performed to gain insight into whether the 2D perovskite preferable accumulates at the HTL interface or not. A sample fabricated without back electrode is analyzed (see figure 4.33b). The PEA^+ distribution in the 2D/3D perovskite bulk is analyzed by ToF-SIMS measurements. The PEA^+ (represented by $C_6H_5C_2H_4NH_3^+$ ions in the plot) distribution follows the FA^+ (represented by $CH_5C_2H_4^+$ ions in the plot) one. Thus, it seems that the PEA^+ is uniformly distributed in the perovskite bulk. Slight depth differences of the intensity maxima for the perovskite ions (Sn^+, CsI^+) are suggested to be either due to preferred accumulation of I^- at the HTL interface and/or preferential sputtering of organic and inorganic species common in ToF-SIMS measurements. So the PEA^+ seems to be homogeneously distributed in the perovskite bulk.

In summary, the GIXRD and ToF-SIMS measurements show a uniform distribution of the PEA^+ in the perovskite bulk with no preferred 2D phase built up at the perovskite surface. Thus, three scenarios are possible according to these observations: (i) no 2D phase is formed at all, which is not expected as a 2D phase is verified by BB-XRD for higher PEA^+ amounts (see figure 4.32);

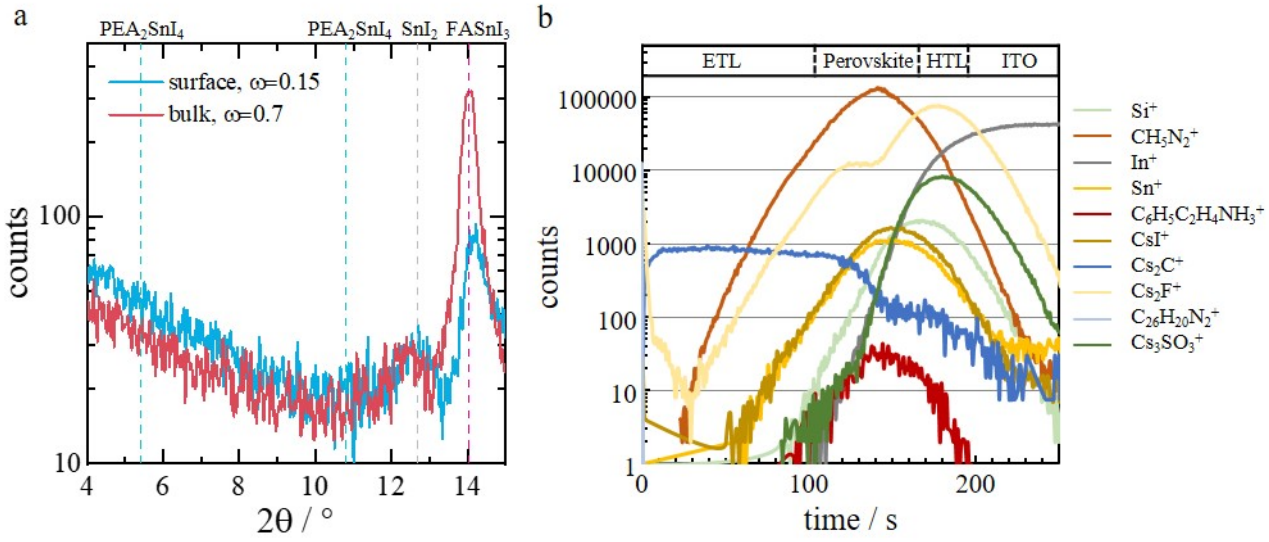

Figure 4.33: Analysis of the spatial PEA_2SnI_4 and PEA^+ distribution in the 2D/3D PEA_2SnI_4/$FASnI_3$ perovskite bulk with 7.5% PEA_2SnI_4. a: GIXRD pattern of the perovskite surface (ω=0.15) compared to the perovskite bulk (ω=0.7) measurement of semi-finished samples up to the perovskite layer.
b: ToF-SIMS depth profile of a sample prepared without back electrode (ITO / PEDOT:PSS / (SiO_2-NP) / $FASnI_3$ / PCBM / BCP). The $C_{26}H_{20}N_2^+$ corresponds to the BCP layer, the Cs_2C^+ mainly to the PCBM layer, the Sn^+, CsI^+, Cs_2F^+, $CH_5N_2^+$, $C_6H_5C_2H_4NH_3^+$ to the perovskite layer, the Si^+ to the SiO_2-NP, the $Cs_2SO_3^+$ to the PEDOT:PSS layer, and the In^+ to the ITO layer. Measurements were performed in the spectrometry-mode using Bi_3^+ ions as the analysis beam and Cs^+ for sputtering.

(ii) 2D phases are formed perpendicular to the substrate, which would fit to the non-formed parallel 2D phase at the perovskite surface and the uniform PEA^+ distribution in the perovskite bulk or (iii) the 2D phases are formed parallel to the substrate with multiple uniformly distributed layers inside the perovskite bulk.

The 2D PEA_2SnI_4 addition in the 3D $FASnI_3$ perovskite bulk observed a highly oriented crystalline layer for optimized 2D amounts. The distribution of the 2D PEA_2SnI_4/PEA^+ in the perovskite bulk can not be specified for sure. The BB-XRD measurement, together with reported findings in literature [88], indicates parallel 2D layers to the substrate. It is expected that multiple 2D slices are formed parallel to the substrate with no preferential 2D phase built at the perovskite interfaces.

Impact of PEA_2SnI_4 addition on the solar cell performance

As the highest pronounced crystal orientation is observed for the 2D amount of 7.5 %, the impact of improved perovskite morphology on solar cell performance is analyzed. Solar cells with a PEA_2SnI_4 amount of 7.5 % are compared to ones with a pure $FASnI_3$ perovskite with PCBM as ETL. For the 2D/3D mixed perovskite, the impact of the ETL by replacing PCBM with ICBA is further examined based on the results in subchapter 4.2.2.

The solar cell efficiency enhances from a median of 2.8 % to 4.3 % with negligible hysteresis by using a 2D/3D mixed perovskite instead of a pure 3D one (see figure 4.34a,b). All solar cell parameters contribute to this improved solar cell performance (see figure 4.34b). The FF is enhanced from 55 to 60 %, the V_{OC} from 350 to 420 mV, and the J_{SC} from 15.4 to 17.3 mA cm^{-2} in median (forward bias scan direction). Improved solar cell parameters are considered to be due to the crystallite orientation leading to reduced structural defects and thus dark recombination states.
The ETL variation results in a comparable trend as observed in subchapter 4.2.2. The PCE can be further enhanced to a median of 5.2 % due to a significantly improved V_{OC} of 670 mV. It is expected that an improved band alignment at the perovskite/ETL interface leads to the high V_{OC} and so to the PCE as analyzed in detail in subchapter 4.2.2.

Furthermore, the impact of the 2D perovskite addition in the perovskite bulk on the band structure is investigated. Figure 4.35a shows the measured EQE spectra for solar cells with a 2D/3D and a 3D perovskite. No significant differences in spectra shape and intensity can be observed. Thus, it seems that the absorption and wavelength-dependent conversion of photons into charges are similar. Further, the band-gap is extracted by plotting the data in a tauc-plot (see figure 4.35b). The fitting reveals slightly higher band-gap energy for the sample with the 2D/3D perovskite of 1.41 eV compared to the 3D perovskite of 1.40 eV. This is consistency with the theory of perovskite band-structure formation. By inserting the bulky cations, the atomic overlap of iodine and tin is lowered, resulting in a downshift of the valence band (see also theoretical derivation in paragraph *band-structure* in the subchapter 2.1.1).

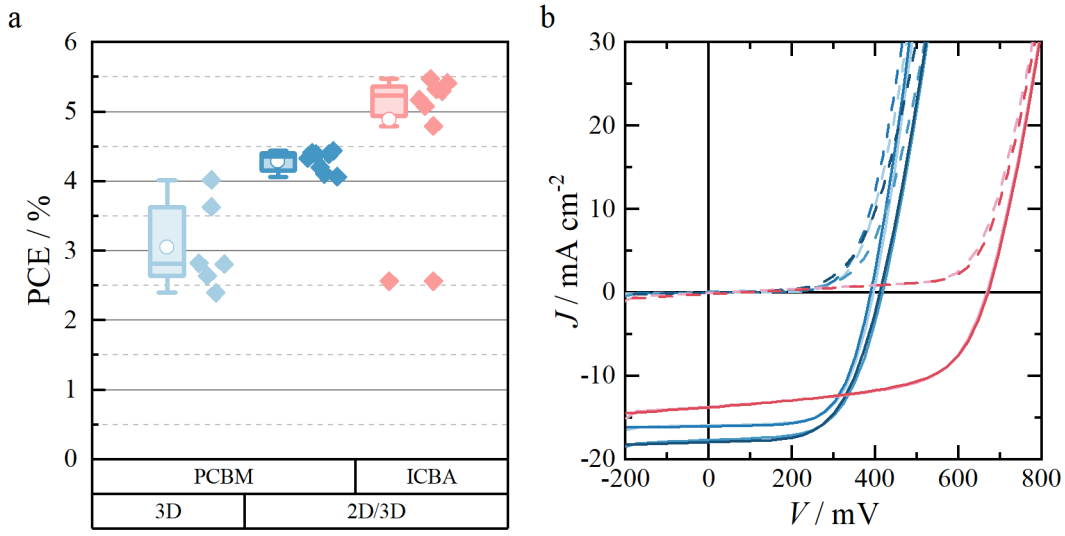

Figure 4.34: Solar cell performance of pure 3D $FASnI_3$ and 2D/3D $PEA_2SnI_4/FASnI_3$ mixed perovskite absorbers with 7.5 % PEA_2SnI_4 and a ETL variation for the 2D/3D mixed perovskite. a: Boxplot of the extracted PCE measured in the forward bias direction. b: Exemplary $J(V)$-curves for the named perovskite stacks in both bias scan directions. The lighter colored curve displays the forward bias scan direction, the darker one is the reverse direction. Further dashed curves are dark measurements, while the solid lines represent illuminated ones.

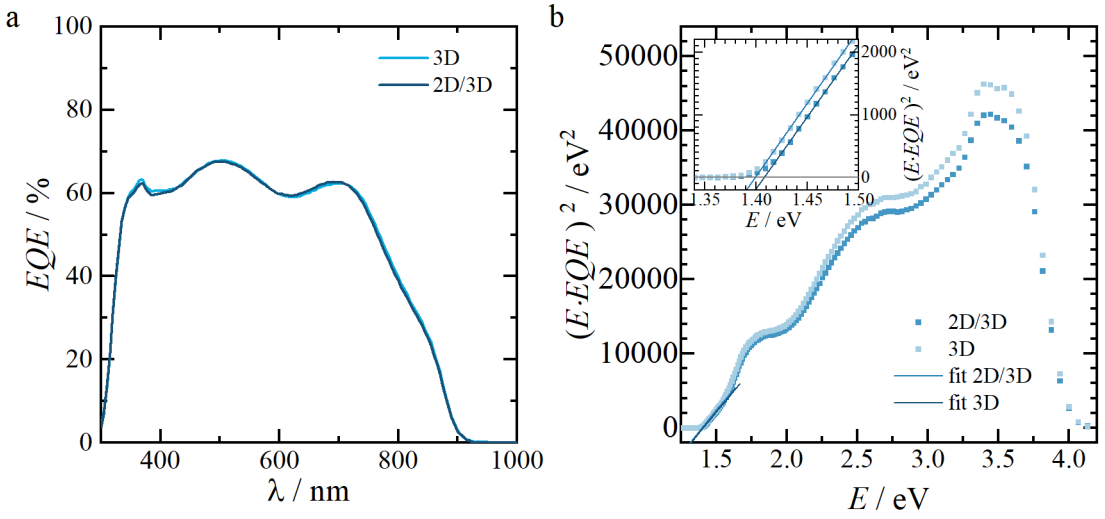

Figure 4.35: a: EQE spectra of 2D/3D $PEA_2SnI_4/FASnI_3$ mixed perovskite to pure 3D $FASnI_3$ perovskite solar cells (ITO / PEDOT:PSS / (SiO_2-NP) / $PEA_2SnI_4/FASnI_3$ / PCBM / BCP / **Ag!** (**Ag!**)). b: Tauc-plot of the EQE to extract the band-gap energy (b) with an inset illustrating the band-gap fit.

Summary and outlook of tuning the crystalline ordering of the perovskite film

To sum up, the perovskite morphology is tuned by adding 2D PEA_2SnI_4 perovskite to the 3D $FASnI_3$ perovskite. A significant texturing effect by a {001} crystallite orientation is observed for the 2D/3D mixed $PEA_2SnI_4/FASnI_3$ perovskite with optimized 2D PEA_2SnI_4 amounts. The strong perovskite phase orientation indicates a suppressed bulk nucleation and crystallization by favoring the perovskite/surface one. Multiple 2D slices parallel to the substrate are expected

to be formed without accumulation at the perovskite interfaces. The improved crystallographic morphology goes along with an improved solar cell performance. The efficiency and V_{OC} enhances from 2.8 %, 350 mV to 4.4 %, 420 mV in median. This is assumed to be due to reduced structural defect density, thus decreasing unfavorable charge recombination in the perovskite layer. The efficiency was further improved by using ICBA as ETL instead of the PCBM resulting in high median efficiency of 5.2 % with a V_{OC} of 670 mV. The solar cell efficiency even improved with dark storage in nitrogen atmosphere to a maximum efficiency of 6.6 % after 28 days of storage.

Summary and outlook: Investigating tin perovskite absorbers

Tin perovskite absorbers were investigated motivated by their improved sustainability than the tin-lead mixed perovskite absorbers explored in the previous subchapter.

This work accomplished a PCE of up to 6.6% for $FASnI_3$ based perovskite solar cells by optimizing the perovskite film and solar cell layer stack.
The commonly used SnF_2 additives in tin-containing perovskite absorbers were explored to access its mechanism enhancing the solar cell performance. Besides the well-known effects of improved perovskite film morphology and retarded Sn^{2+} oxidation, I made new findings in collaboration with colleagues. The SnF_2 preferably accumulates at the underlying PEDOT:PSS interface. Simultaneously, a thin 1.2 nm SnS interlayer is detected at this interface. It is expected that the accumulated SnF_2 reacts with the PEDOT:PSS to form this Sns interlayer. As SnS is a p-type semiconductor, it is assumed that the interlayer improves the hole extraction at the PEDOT:PSS interface, thus enhancing the solar cell performance as observed. The discovery could give a hint for the well-known experimental benefit of using PEDOT:PSS as HTL and SnF_2 additives for tin perovskite solar cells.
Strategies following interfacial and structural engineering were focused on further improving the solar performance addressing recombination and V_{OC} losses with optimized SnF_2 amount.
A pinhole-free perovskite film was achieved by controlling the perovskite film formation. This was achieved by modifying the HTL PEDOT:PSS interface introducing a porous SiO_2-NP layer. Furthermore, the conduction band of ETL and perovskite is aligned, and perovskite surface defects are effectively passivated by altering the ETL interface, replacing the commonly used PCBM with another C_{60} derivative ICBA. By these interfacial engineering techniques, a PCE of nearly 6 % is demonstrated by reduced V_{OC} losses and dark recombination processes.
Based on these results, the perovskite crystallographic morphology is improved by realizing 2D/3D mixed $PEA_2SnI_4/FASnI_3$ perovskites assumed to reduce recombination losses in the perovskite bulk. A strong texturing to the {001} planes correlating to enhanced solar cell performance is revealed by optimized 2D fractions. Combining the crystal texturing with the optimized interfaces, a high PCE of up to 6.6 % is observed.

In the following, tin perovskite absorbers' toxic and environmental impact is discussed concerning their solar cell performance.
Decreased solar cell performance is achieved by the pure tin perovskite solar cells compared to the tin-lead mixed ones. However, perovskite absorbers have a improved sustainability. This dilemma reflects the compromise that has to be made between solar cell performance and human health and environmental impact.
However, the remarkable solar cell improvements in this work and in literature are promising

for further increases in solar cell performance. To improve the tin perovskite solar cell performances, passivation strategies, and alternative HTL, ETL should be explored to further reduce recombination losses. Moreover, the degradation mechanism has to be explored and understood to prevent fast degradation of the solar cell devices and thus performance losses.

4.3 Stability analysis of tin-containing perovskite solar cells

Tin as a lead-alternative in perovskite absorbers was studied in the subchapter before, mainly focusing on the device efficiencies. This subchapter will investigate the stability of these tin-containing absorbers, as tin easily oxidizes from Sn^{2+} to Sn^{4+}, leading to the deterioration of the perovskite structure and thus limit solar cell performance. This oxidation process can be slowed down in tin-lead mixed perovskite absorbers [104, 105]. A literature review on the stability of perovskite solar cells, in general, was presented in chapter 2.3. The stability of tin-containing absorbers stressed by oxygen and moisture was reviewed in detail in subchapter 2.3.2. However, limited studies report a systematical stability study of tin-containing perovskites.

The efficiency of tin and tin-lead mixed perovskite solar cells stored dark in an inert atmosphere were tested over a time of 280 and 160 days (see figure 4.36, 4.37). These observed non-significant performance losses. Thus devices seem to be at least intrinsically stable.

Nevertheless, further studies need to be performed to get insights into critical preparation conditions and stress factors in operation.
These critical preparation conditions for perovskite solar cells are oxygen, moisture, high vacuum, and elevated temperature. These can impact the quality of the layers and thus the overall stability of the device afterwards.
Further, conditions affecting the solar cell operation stability leading to device deterioration are, for example, external stress factors like light, voltage, current, elevated temperature, contact to ambient atmosphere.

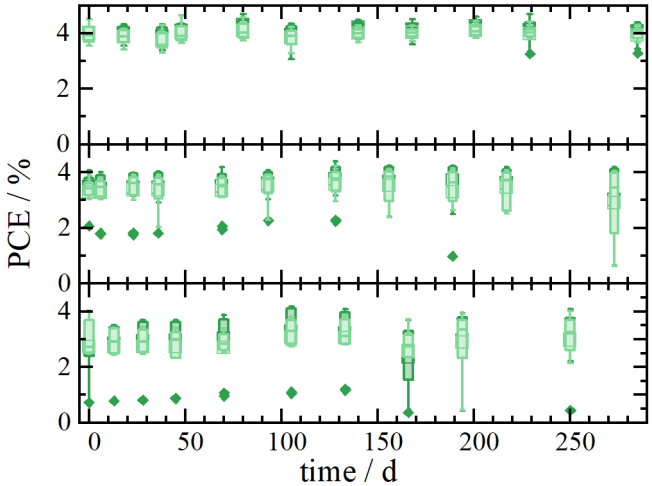

Figure 4.36: Solar cell performance of tin perovskite solar cells (ITO / PEDOT:PSS / SiO_2-NP / $FASnI_3$ / PCBM / BCP / Ag) of three batches with eight solar cells each stored dark in nitrogen atmosphere. Lighter color indicate forward and darker color indicate reverse measurements.

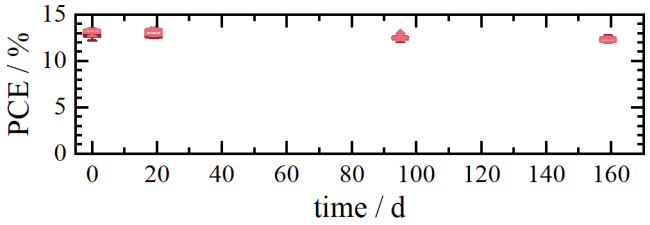

Figure 4.37: Solar cell performance of six tin-lead mixed perovskite solar cells (ITO / PEDOT:PSS / SiO_2-NP / $FA_{0.65}Cs_{0.35}Sn_{0.5}Pb_{0.5}I_3$ / PCBM / BCP / Ag) stored dark in nitrogen atmosphere. Lighter color indicate forward and darker color indicate reverse measurements.

For addressing the preparation and operation stability, two sets of experiments are performed. As ambient atmosphere contact is highly critical for tin-containing perovskites, due to the fast tin oxidation, its reactivity is explored. This should provide insight into the necessity of tin-containing perovskite solar cells preparation and encapsulation in inert atmosphere. Further first investigations on the operation stability are explored. Therefore, the samples are stressed at elevated temperature (85°C) in an inert atmosphere (nitrogen) based on the suggested testing conditions for first tests presented in a consensus statement for perovskite stability [138]. The 85°C thermal stress is used to analyze the thermal degradation, like chemical and structural phase instabilities, and accelerate the inert atmosphere's degradation process.

Thus in chapter 4.3.1, the (tin) reactivity is explored by ambient atmosphere stress, and in chapter 4.3.2, the samples are aged by thermal stress.
In both chapters, two sample categories are analyzed to distinguish between the degradation mechanism of the perovskite material itself and the perovskite device. These are pure perovskite films deposited on glass and complete solar cell stacks. For the pure perovskite film deposition, the glass surface is coated with SiO_2-NP, as illustrated in chapter 3.1.1, to achieve better wetting and comparable perovskite film formation as in solar cells. For the solar cell devices, identical stacks are chosen for both perovskite compositions to achieve comparability of the devices, as illustrated in figure 3.1. For these solar cell stacks, PEDOT:PSS is used as an HTL, a combination of PCBM and BCP as ETL, and silver as the back electrode. Analogously, comparable perovskite compositions without supplementary additive than SnF_2 were chosen. Thus, for the tin perovskite the $FASnI_3$ absorber from subchapter 4.2, and for the tin-lead mixed perovskite absorber the $FA_{0.65}Cs_{0.35}Sn_{0.5}Pb_{0.5}I_3$ absorber from subchapter 4.1 will be investigated.

T_{80} is extracted to achieve comparability of the different degradation time scales of multiple measurement techniques. The T_{80} corresponds to the time where the analyzed value achieves 80 % of the original unaltered sample value.

4.3.1 Exploring the reactivity of tin-containing perovskite in ambient atmosphere

The reactivity of tin-containing perovskite in the ambient atmosphere (22±1°C and 30-45 rH%) will be investigated in the following chapter to clarify if an inert atmosphere during perovskite solar cell preparation is mandatory. The impact of the ambient atmosphere on the perovskite film solely will be compared to complete solar cell devices is analyzed. The dominant degradation mechanism of either the perovskite layer or other device layers resulting in device deterioration will be distinguishable by comparing these.

Reactivity of tin-containing perovskite films in ambient atmosphere

The following section will analyze the stability of tin and tin-lead mixed perovskite films deposited on glass. The aim is to gain insights into the degradation mechanisms of the perovskite absorbers themselves. The focus is set on characterizing the optical and material stability investigating the degradation kinetics. Hereby, the phase stability is explored to characterize the deterioration of the ABX_3 perovskite structure due to tin oxidation in the ambient atmosphere. Additionally, optical properties are studied as appropriate absorption is needed for a good solar cell absorber. In this work, morphology changes are investigated by SEM top-view images, the absorption behavior by UV-Vis spectrometry, and phase changes by XRD and ToF-SIMS studies.

The fast degradation of the tin perovskite absorber in air is visible by a color change from black to yellow-brownish after two hours. In contrast, no significant color change is observed for the tin-lead mixed perovskite (see insets in figure 4.38). The SEM top-view images show a morphological transition of the tin perovskite film (see figure 4.38a, b). Pinholes and an additional phase seem to be preferably formed at the grain boundaries after a stress periode of two hours. Thus it is expected that the degradation process preferably starts at the grain boundaries as these are areas with high defect density. Lanzetta et al. reported similar observations [12]. After 26 hours of stress, the as-grown morphology is completely destroyed (see figure A.10).
The morphology of the tin-lead mixed perovskite film seems to be less influenced by the ambient atmosphere stress for two hours. No significant differences in the top-view SEM images are observed, like grain size, additional phases, and pinholes (see figure 4.38c, d).

An evident color change of the tin perovskite absorber indicates a variation of the absorption, which is analyzed in more detail in the following (see figure 4.39). Suitable light absorption is substantial for a solar cell absorber. The ability to convert photons into charges is analyzed by integrating the absorption spectrum folded by the AM 1.5G sun spectrum and assuming 100 % quantum efficiency to determine a hypothetical current density.
The absorptance of the tin perovskite film is already drastically decreasing after some hours (see figure 4.39a). Also, the spectral shape is changing from a broad absorption with a band-gap energy of 1.46 eV (see tauc-plot in figure A.11) to spectra with two characteristic peaks at 570 and 400 nm after 25 hours. The calculated current density decreases to 80 % of the original value after 9 hours (T_{80}) (see figure 4.39c).
The absorption change of the tin-lead mixed perovskite film is much slower (see figure 4.39b). Here the spectra shape is changing by a decreasing intensity of the 900 nm shoulder. After 9 hours, no significant changes of the calculated current density can be observed, and still 89% of the original value after 168 hours can be achieved (see figure 4.39c).

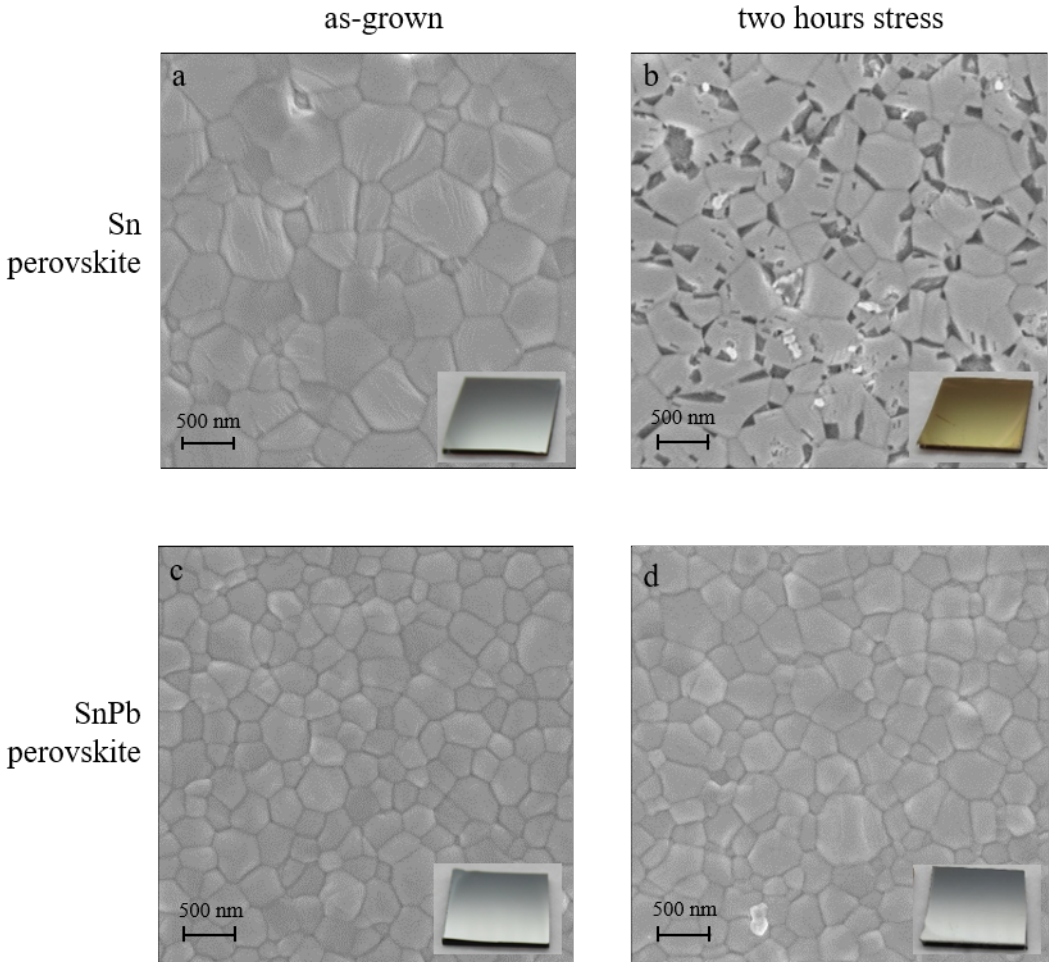

Figure 4.38: Morphological study of perovskite layers degraded in air for two hours. SEM top-view images and their corresponding photographs of 15 × 15 mm^2 samples as insets of fresh (a, c) and degraded samples (b, d) of tin (a, b) and tin-lead mixed (c, d) perovskite films deposited on glass.

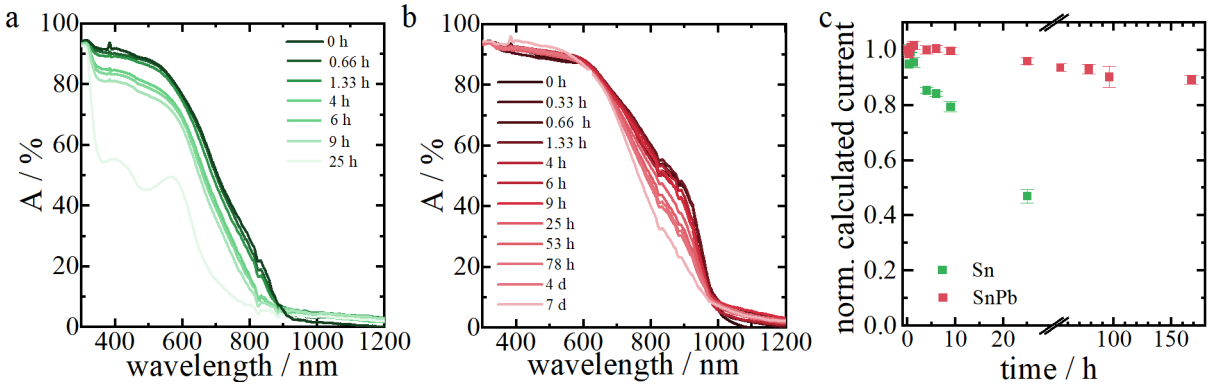

Figure 4.39: Degradation process of perovskite absorbers in air visualized by their absorption changes. Absorptance (A) of tin (a) and tin-lead mixed (b) perovskite films as well as (c) calculated conversion of photons into charges visualized as a normalized current density.

Since the absorption changes of the tin perovskite suggest a formed degradation product, the phase changes over time are studied by XRD measurements(see figure 4.40). The (001)-perovskite peak is chosen to illustrate the crystal phase changes (see figure 4.40c) since this peak has the highest intensity. Similar behavior is observed for all other perovskite-related peaks if not named differently.
For the tin perovskite film, the peak intensity is decreasing quickly (see figure 4.40a). The T_{80} is one hour. As no distinct additional diffraction reflexes are detected, the crystalline perovskite phase is mainly converted into an amorphous degradation product. Small reflexes are observed for the XRD pattern after 26 hours, similar to described Sn^{2+} oxidation in literature (see figure A.12) [82, 226]. It is assumed that the possibly oxidation product is di-formamidinium tin hexa-iodide (FA_2SnI_6).
Again phase changes of the tin-lead mixed perovskite film are different from the pure tin perovskite one. Three findings are observed: a decrease in peak intensity and a peak shift for the perovskite phase, and a strong decrease of the tetragonal (210) peak intensity (see figure 4.40b). The T_{80} is around seven hours observed by analyzing the (001)-perovskite peak intensity. A phase change could explain the peak shift and the vanishing tetragonal phase peak by converting the as-grown slightly tilted tetragonal phase to a crystalline cubic phase. As in chapter 4.1.2 a cubic phase was observed for a $FA_{>0.75}Cs_{<0.25}Sn_{0.5}Pb_{0.5}I_3$ perovskite composition, it can be assumed that an amorphous $CsSnPbI_3$ perovskite and crystalline $FA_{>0.75}Cs_{<0.25}Sn_{0.5}Pb_{0.5}I_3$ perovskite product is formed.

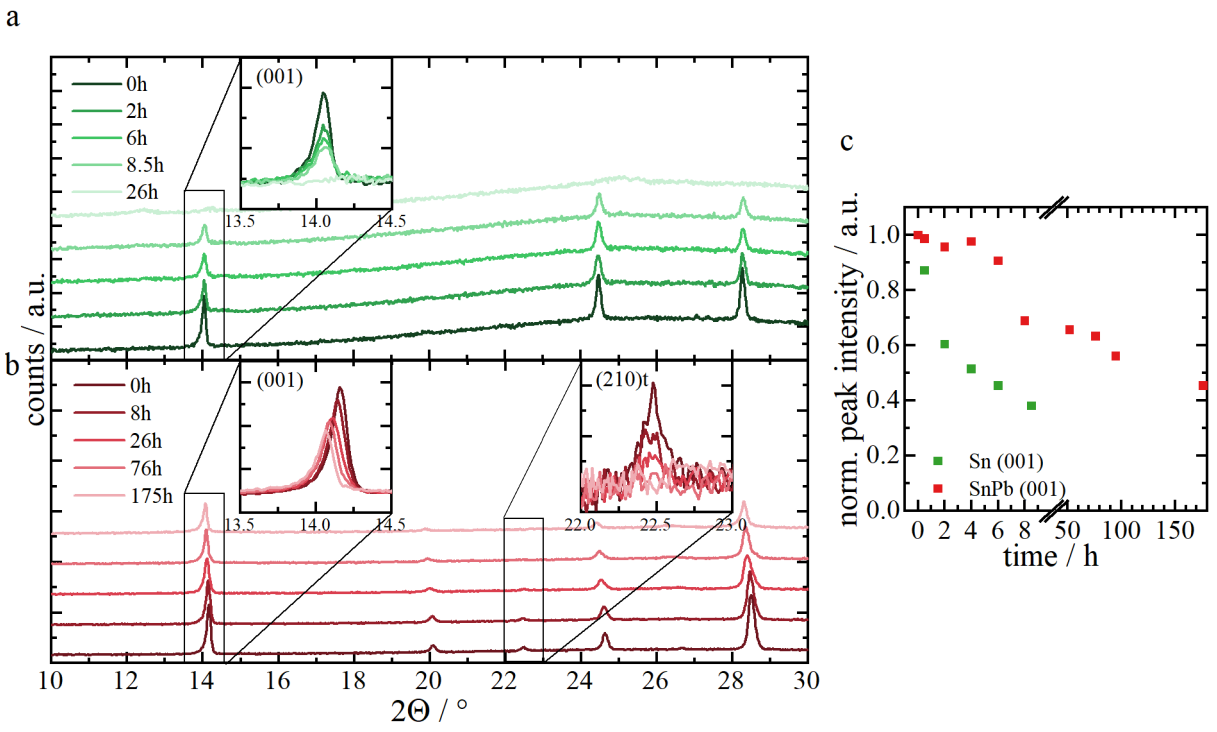

Figure 4.40: Degradation process of perovskite absorbers in air visualized in their crystal phase changes by XRD measurements. XRD patterns for the tin (a) and (b) tin-lead mixed perovskite at different time scales with insets to highlight significant changes. Extracted (001)-peak intensities (c) shown in a and b for visualizing the degradation process.

As differences in the crystal phase structure are observed, changes of element distribution by for example ion migration in the perovskite bulk are analyzed by ToF-SIMS measurements. Depth profiles of as-grown and altered ones for 30 minutes are shown in figure 4.41. These showed negligible changes in the elemental distribution. Thus, ion migration is not observed for the perovskite films as well as phase segregation in the perovskite bulk depth.

In summary, the tin perovskite films seem to degrade quite fast. Extracted T_{80} values lie between 1 hour for the perovskite phase and 9 hours for the absorption properties. Hypothetically it is suggested that a mainly amorphous decomposition product FA_2SnI_6 is formed. A two-step reaction scheme was supposed by Lanzetta et al. [146] and would support the observed findings:
$2\,FASnI_3 + O_2 \longrightarrow 2\,FAI + SnO_2 + SnI_4$
$SnI_4 + 2\,FAI \longrightarrow FA_2SnI_6$.
The tin perovskite first decomposes into SnO_2 and SnI_4 in air. The SnI_4 further reacts with the FAI to form FA_2SnI_6. The degradation process seems to be dominated by the oxygen environment rather than moisture, as the main degradation product is FA_2SnI_6. In a humid environment, a higher amount of SnO_2 would be expected based on the degradation process presented in figure 2.9.
The decomposition of the tin-lead mixed perovskite absorber is much slower, as suggested by Leijtens et al. [104]. Still, about 89% of the initially calculated current can be generated by absorption after 168 hours. For the as-grown perovskite phase, a T_{80} stability of seven hours is suggested. Hypothetically, the XRD patterns indicate phase changes of the slightly tilted $FA_{0.65}Cs_{0.35}Sn_{0.5}Pb_{0.5}I_3$ perovskite into a cubic system with reduced Cs-amount $FA_{>0.75}Cs_{<0.25}Sn_{0.5}Pb_{0.5}I_3$ and an amorphous CsSnPbI product.

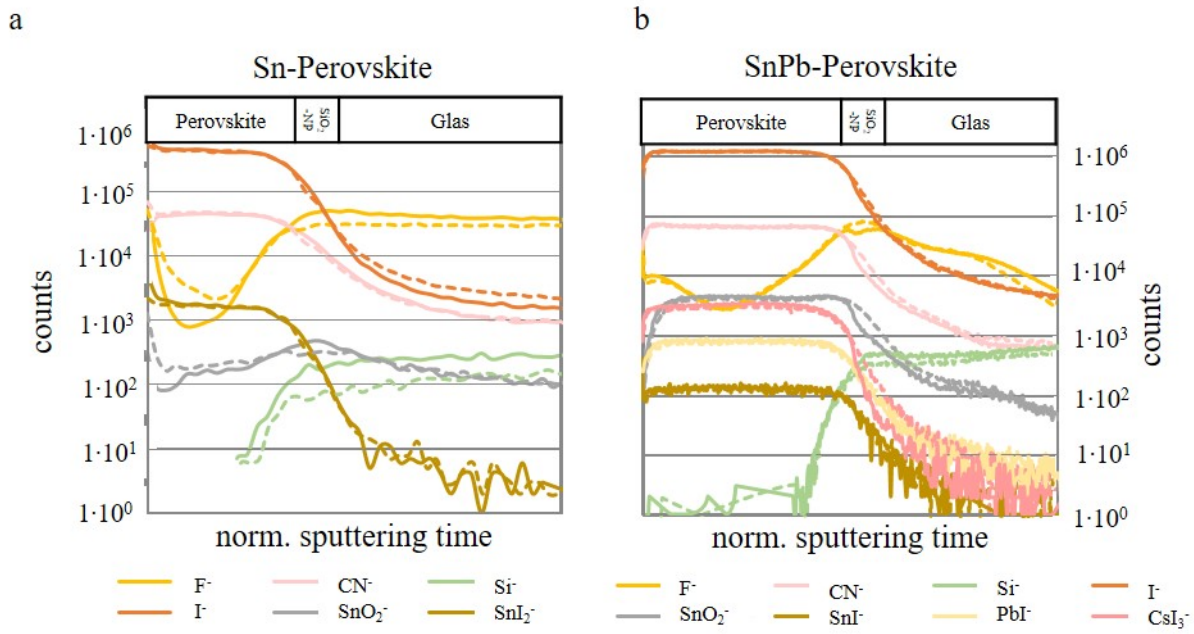

Figure 4.41: Tin (a) and tin-lead mixed (b) perovskite films' elemental distribution of as-grown (solide line) and aged samples for 30 minutes in the ambient atmosphere (dashed lines) investigated by ToF-SIMS. Measurements were performed in the spectrometry-mode using Bi_3^+ ions as the analysis beam and oxygen-clusters$^+$ for sputtering.

Reactivity of tin-containing perovskite solar cells in ambient atmosphere

Subsequently, the influence of ambient atmosphere on perovskite devices is investigated by their solar cell performance and perovskite bulk changes. The solar cell performances are analyzed as this is the central property of solar cells. Further phase changes are examined as these are influenced by the tin oxidation and ion migration in perovskite solar cells.

The solar cell performance over time in ambient atmosphere is summarized in figure 4.42, summarizing the PCE of each solar cell (see figure 4.42a). For illustrating the $J(V)$-curves shape changes over time, exemplary ones are illustrated at different time scales (see figure 4.42b,c). Since no significant hysteresis is observed for the measured solar cells, the solar cell performances over time are illustrated only by their reverse bias direction measurement.

In general, the efficiency of the perovskite solar cells decreases with increasing storage time in the ambient atmosphere. However, the efficiency seems to be constant during the first ten hours. A concrete T_{80} value for the degradation process is difficult to be determined as solar cells behave slightly differently depending on their measurement frequency. Some tin perovskite solar cells have a T_{80} value of minimum 68 hours with low measurement frequency, whereas others only achieve a T_{80} value of 14.5 hours with higher measurement frequencies. Similar T_{80} values are reported in literature for tin based perovskite solar cells [82, 88, 98, 226–230].
Likewise, some tin-lead mixed perovskite solar cells still have half of their original PCE after 66 hours with a lower measurement frequency. In contrast, others only show a quarter of their original efficiency after 37 hours measured with higher frequencies. The T_{80} value is around 13.5 hours. T_{80} of some days are generally achieved for comparable tin-lead mixed perovskite solar cells [231, 232].
For both perovskite solar cell stacks, performance decrease due to a generated S-shape in their $J(V)$-curves (see figure4.42b,c). In general, an S-shape indicates an energy barrier in the solar cell stack [190].

For getting more insights into the degradation process, structural changes of the perovskite absorber are analyzed by XRD measurements (see figure 4.43). Relevant alterations of the XRD pattern of the perovskite phase are highlighted by illustrating their changes in the (001)-peak in figure 4.43 and further observed findings like additional phase arising.

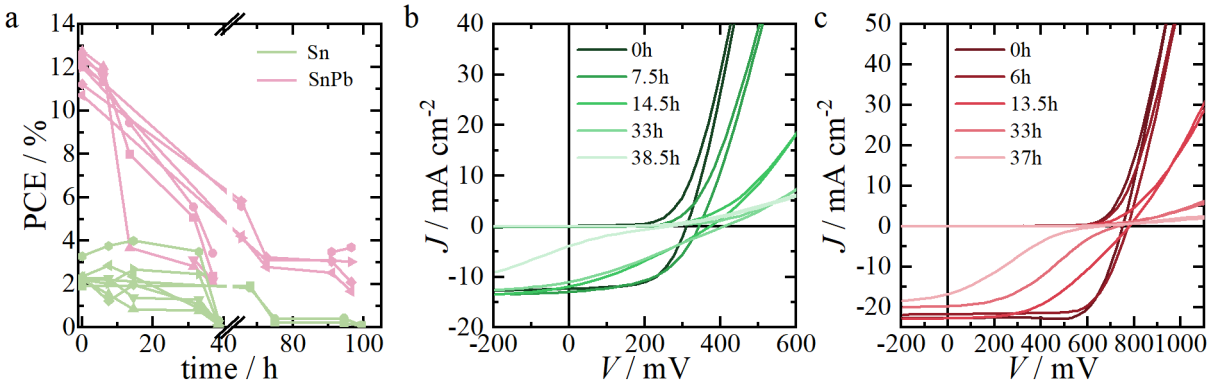

Figure 4.42: Impact of ambient conditions on the solar cell performance measured in reverse bias scan direction of tin and tin-lead mixed perovskite solar cells. a: Solar cell efficiency displayed over time. Exemplary $J(V)$-curves measured at different time scales for a tin (b) and tin-lead mixed (c) perovskite solar cell.

The peak intensity decreases with increasing stress time for tin perovskite devices, suggesting a phase decomposition (see figure 4.43a). After 15 hours (T_{80}), the peak intensity is lowered by 20 % of its original value (see figure 4.43a,c). Besides this, an additional peak at 26.8° arises after 15 hours of air stress (see inset in figure 4.43a). This peak is assumed to be the degradation product tin dioxide (SnO_2) (fitted by the *highscore+* software of our XRD-setup; see therefore the comparison of multiple possible degradation product patterns to the experimental pattern in figure A.13). This observation is in contrast to the perovskite film study, where this peak was not observed in the XRD pattern, and the degradation product is suggested to be FA_2SnI_6. In the literature (also see chapter 2.3.2) FA_2SnI_6 is assumed to be a degradation product in dry oxygen and SnO_2 in a moisture atmosphere with only slight amounts of oxygen [146]. Based on this, it seems that the perovskite phase deterioration is mainly triggered by oxygen in the perovskite film and moisture in the perovskite solar cell. The highly hygroscopic PEDOT:PSS [116, 128] could be the detrimental water source in the perovskite solar cell.
The decomposition is less pronounced for the tin-lead mixed perovskite solar cells (see figure 4.43b). The peak intensity is relatively decreased by approximately 20 % during the testing time of 100 hours (see figure 4.43c). In contrast to the perovskite film study (see figure 4.40) the peak at 22.5° corresponding to the tilted tetragonal perovskite structure does not change (see figure 4.43b). It seems that the perovskite absorber is protected from the ambient atmosphere by the ETL and back electrode layer on top.

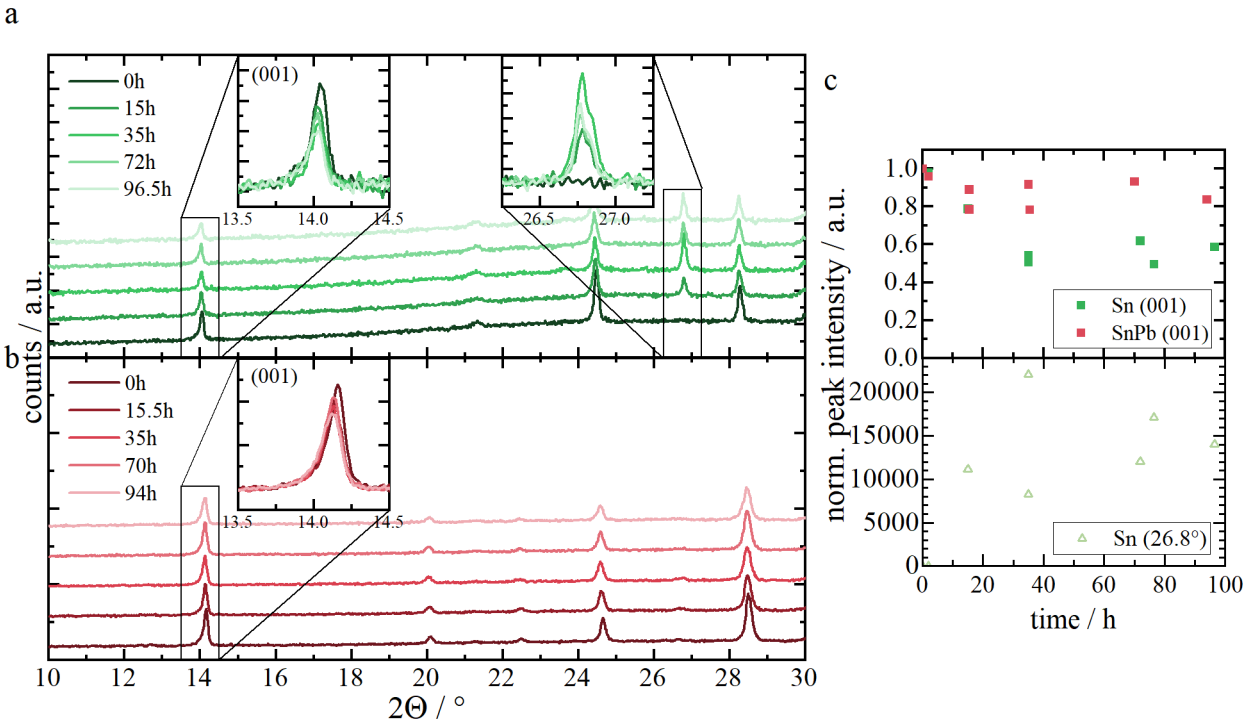

Figure 4.43: Impact of the ambient atmosphere on the crystal phase structure of tin (a) and tin-lead (b) mixed perovskite solar cells by exemplary measured XRD pattern with insets to highlight significant changes. c: Extracted normalized (001)-perovskite (filled squares) and 26.8° (unfilled triangles) peak intensities shown in a and b for visualizing the degradation process.

Besides structural modifications, ion migration is another prone phenomenon of perovskite solar cells. This is analyzed by comparing ToF-SIMS measurements of as-grown and aged samples for 40 hours in air. Depth profiles and analyzed ions' amount by integrating their signal[2] of relevant positives ions are shown in figure 4.44 and additional depth profiles of ions representing each layer in the perovskite solar cell stack in figure A.14. Negative ions are shown as a compound with Cs since Cs^+ was used as the sputtering beam. In principle, similar distributions are observed for most detected ions. Thus no drastic morphology changes seem to be caused by stressing the samples. If the sample morphology varies too drastically by e.g. pinholes, sputtered ions would be mixed from the surface and the underlying layer at pinholes, making statements of ion migration difficult.
For both perovskite solar cell stacks, oxygen diffuses into the silver electrode. The oxygen amount (integrated signal) increases from around 9000 (13000) to 46000 (35000) in the silver and ETL layer for tin (tin-lead) perovskite devices. However, the oxygen amount in the perovskite layer does not change, suggesting oxygen infiltration from the surface only until the ETL layer. Additionally, fluoride migrates to the electrode, increasing the fluoride concentration in the ETL, at the ETL/electrode interface, and in the back electrode. In these layers, the fluoride concentration (integrated signal) is enhanced in tin (tin-lead mixed) perovskite devices from 150 000 (100 000) to 1 900 000 (1 500 000). Further, only relatively slight enhanced iodine concentration is observed for the perovskite devices in the ETL. The amount of iodine in the silver and ETL layer is enhanced from 350 000 (17 000 000) to 570 000 (29 000 000) for the tin (tin-lead) devices.

In summary, the solar cell performance for both perovskite compositions suffers from enhanced S-shape with increased storage time in air. As comparable trends are observed, it is suggested that similar degradation mechanisms result in device losses. The S-shape is a hint to a formed energetic barrier in the solar cell stack.
The crystalline phase study gave no explicit explanation for a formed insulating material for both perovskite solar cells, as different findings were observed. The crystalline tin perovskite has a T_{80} stability of around 15 hours, and a new crystalline phase, presumably SnO_2, is formed. Whereas the tin-lead mixed perovskite absorber decomposes more slowly. The crystalline perovskite phases only decompose by approximately 20 % in the testing time scale of 100 hours, and no crystalline degradation phases are formed. Thus, perovskite structural phase alterations are less likely the reason behind solar cell performance losses, as different crystal bulk phase evolution are accomplished for both solar cell types. Further time scales of phase deterioration and devices losses do not correlate.
In both perovskite solar cells, similar oxygen infiltration and fluoride ion migration occurs independently of the perovskite composition. Interestingly the ion migration only takes place in solar cell devices. Thus, it seems that internal electric fields are needed for ion migration.
As illustrated in chapter 2.3, ion migration from the perovskite to the back electrode is known from literature [141–143, 166, 167]. However, this ion migration is mainly reported for the iodide ion, which often reacts with the back electrode, deteriorating it. It can be expected that fluoride migration can lead to a similar reaction with the PCBM, BCP, and silver, too. A reaction would deteriorate the original material properties as well as lead to new reaction products. A chemical reaction of fluoride can alter the transport properties of the ETL and back electrode layer, resulting in an energy barrier in a device leading to the observed S-shape in $J(V)$-curves.

[2] Detailed procedure for determining the F^- amounts is described in chapter 3.2.2.

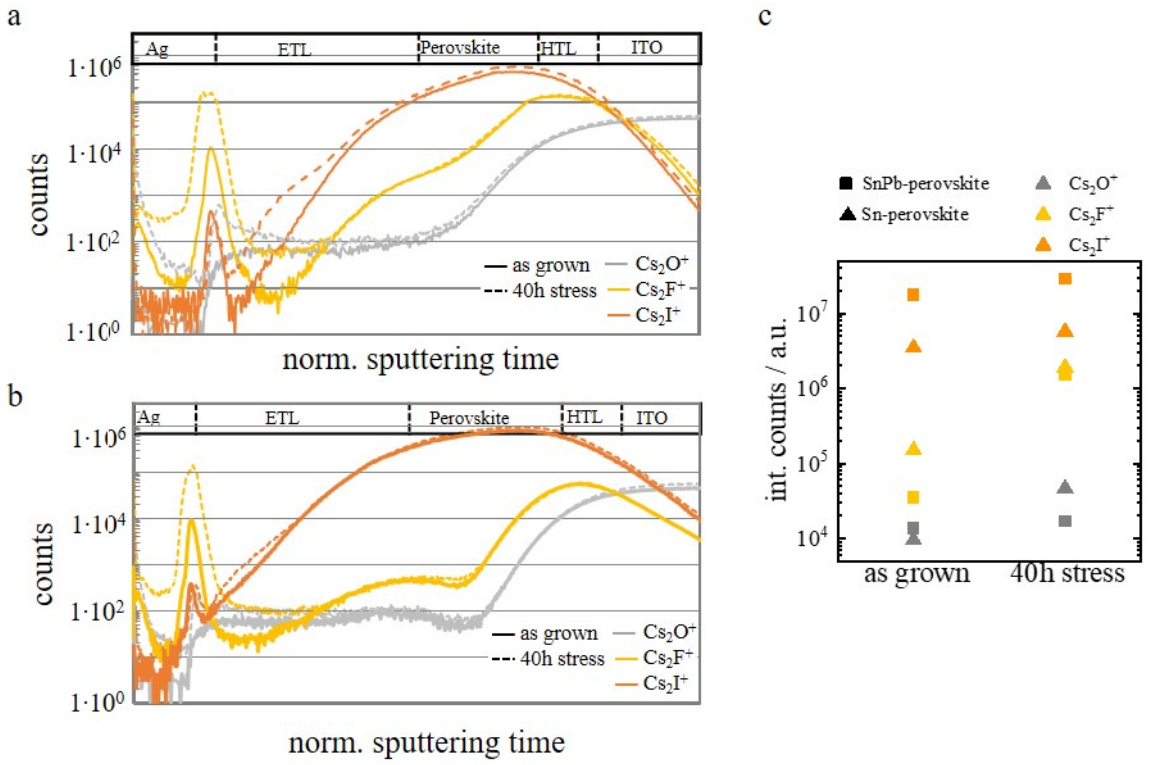

Figure 4.44: Impact of ion migration on perovskite solar cells stressed by the ambient atmosphere for 40 hours measured by ToF-SIMS. Comparative depth profile of tin (a) and tin-lead mixed (b) perovskite solar cells of fresh (solid line) and stressed (dashed line) samples. Measurements were performed in the spectrometry-mode using Bi_3^+ ions as the analysis beam and Cs^+ for sputtering. Signals of shown ions are integrated as a parameter for their amount in the relevant range of the silver and ETL layer and summarized in c.

Besides suggested ion migration destroying the transport properties of the ETL and/or electrode, by a degradation of the PCBM by oxygen and water inflation can result in decreased solar cell performance and would fit to the oxygen infiltration observed by ToF-SIMS measurements. Jiang et al. [233] and You et al. [234] reported degradation of perovskite solar cells in air, which they attributed to the unstable PCBM in air. This is caused by water and oxygen adsorption of this electron transport material (ETM) [235].
Consequently, it is assumed that either ion migration of the fluoride subsequently reacting with the silver electrode or PCBM leads to the degradation of the solar cell. Additionally, the instability of the PCBM in the ambient atmosphere can also negatively impact the solar cell stability.

Summary of the tin-containing perovskite reactivity study in ambient atmosphere

The following section summarizes the main observed findings of the perovskite film and device stability analysis in the ambient atmosphere. The main observations are summarized in table 4.2.

Table 4.2: Summarizing the main observations of tin-containing perovskite samples stressed in the ambient atmosphere.

perovskite	film properties	device properties
tin	Absorbance: T_{80} = 9 h phase morphology: T_{80} = 1 h; FA_2SnI_6 formation layer morphology: decomposition at grain boundaries	PCE: T_{80} = 14.5-68 h; S-shape phase morphology: T_{80} = 15 h; SnO_2 formation ToF-SIMS: O_2 infiltration, F^-, I^- migration
tin-lead	Absorbance: T_{80} > 168 h phase morphology: T_{80} = 7 h; phase segregation layer morphology: T_{80} > 2 h	PCE: T_{80} = 37-66 h; S-shape phase morphology: $T_{80} \sim 100$ h ToF-SIMS: O_2 infiltration, F^-, I^- migration

In the ambient atmosphere, the tin-lead mixed perovskite film seems to be more stable than the pure tin composition, as it was also shown by [104]. The perovskite phase stability is prolonged by a factor of seven considering their T_{80} value.
For the devices stressed in the ambient atmosphere, improved stability of the tin-lead mixed perovskite devices is not observed. Similar characteristics in the performance losses for both perovskite compositions are observed (S-shape). It is expected that the performance losses could be related to the fluoride migration towards the back electrode, deteriorating the ETL or back contact by reacting with these. Additionally, the degradation of the PCBM in the ambient atmosphere by oxidation or water infiltration can lead to solar cell efficiency losses. Thus it seems that performance losses are dominated by charge- or electrode-layer deterioration rather than perovskite absorber degradation.

The following will discuss the aspect of tin-containing perovskite reactivity in the ambient atmosphere.
The study showed a fast decomposition of tin-containing perovskite films. Additionally, oxygen- and moisture-free interface layers are essential for the device stability, as shown by the tin perovskite deterioration assumed to be initiated by the hygroscopic PEDOT:PSS layer. The pure tin perovskite absorber has shown higher sensitivity to oxygen and moisture than the tin-lead mixed ones. As the reactivity to oxygen and moisture seems to be high, moisture- and oxygen-free preparation and operation are needed for high tin-containing perovskite stability.
An operation in inert atmosphere can be easily realized by a mechanic barrier via device encapsulation. Nevertheless, the preparation must be carried out in an inert atmosphere until encapsulation with low oxygen and moisture concentration. Further, all used materials for the solar cell preparation should be at best water- and oxygen-free and non-attractive to water. Especially, PEDOT:PSS as HTL should be replaced by another material, as it seems that its hygroscopic nature deteriorates the perovskite (even if its impact on device failure was not

proven). Moreover, comparing the observed ambient stability to reports in literature, the tin perovskite solar cell stability is comparable, however, the tin-lead ones lag behind the literature. Thus, it seems, that there is still room for improvements for tin-lead mixed perovskite solar cells. Perovskite composition optimization is expected to enhance their stability.

4.3.2 Investigation of tin-containing perovskite solar cells under thermal stress

This chapter examines the impact of thermal stress on the tin and tin-lead mixed perovskite absorbers in inert atmosphere. It is a prerequisite for usage in real conditions where solar modules can reach temperatures up to 85°C in the field under full sunlight. Therefore, the samples are heated at 85°C in a nitrogen atmosphere. By these insights into the thermal stability, e.g., the perovskite bulk phase stability and chemical stability, are observed, and the aging in an inert atmosphere is accelerated. Analogously to the study in ambient atmosphere, the impact on perovskite films is investigated initially, followed by the analysis of the solar cell devices. The dominant degradation mechanism of either the perovskite layer or other layers resulting in device deterioration will be distinguishable by comparing the observed results.

Tin-containing perovskite films under thermal stress

In the following, the impact of thermal stress on solely perovskite films is analyzed to get insights into the thermal stability and accelerate the inert aging of the perovskite film it-selves.

Analogously to the study in ambient condition, the focus is set on analyzing the material and optical properties. The morphological phase stability is examined by characterizing the layer and phase morphology via SEM top-view images, XRD and ToF-SIMS studies. Further the optical properties are investigated by UV-Vis spectrometry.

Thermal stress seems to have a minor effect on the perovskite morphology. After six hours of thermal stress, no significant changes of the perovskite layer morphology can be observed in the SEM top-view images (see figure 4.45).

The impact of thermal stress on the optical properties is analyzed by its absorption. The absorption of the tin and tin-lead mixed perovskite films is not significantly changing in spectra shape and in the absorptance intensity (see figure 4.46a, b). As the spectra are not changing, the calculated generated current by integrating the spectra are basically constant (see figure 4.46c).

Thermal stress seems to have a minor impact on the perovskite crystal phase as well. The crystal phase analysis is performed by measuring XRD at different time scales for the tin and tin-lead mixed perovskite films (see figure 4.47). Again the (001)-peak of the perovskite phase for tin and tin-lead mixed perovskite layers are depicted as an example for analyzing the perovskite phase (see figure 4.47c). A slight decrease in the peak intensity, and no significant changes in peak position are observed. Inconsistent slight differences of the XRD pattern are considered being due to statistic sample variations. Similar observations were made by Meng et al. for tin based perovskite absorbers [236].

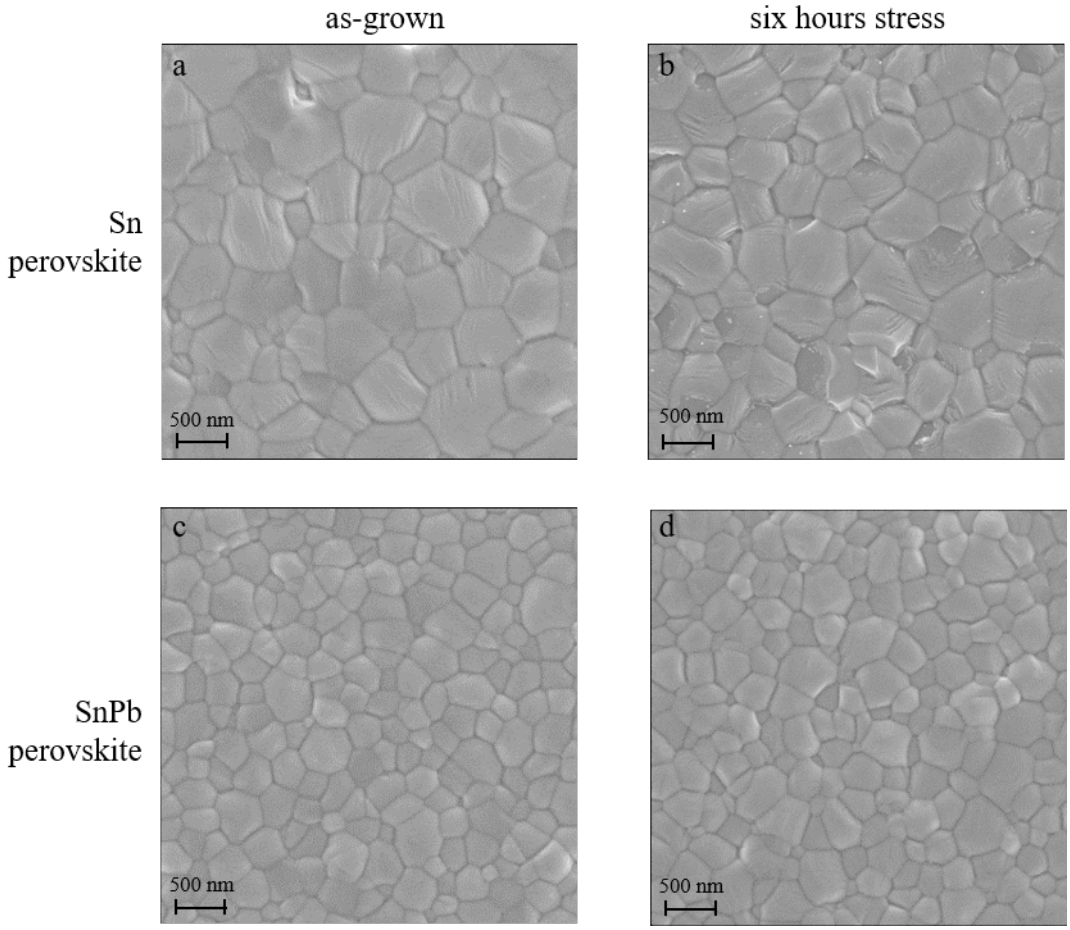

Figure 4.45: Illustration of morphology changes by SEM top-view images of fresh (a, c) and stressed samples at 85°C for six hours (b, d) of tin (a,b) and tin-lead mixed (c.d) perovskite films deposited on glass.

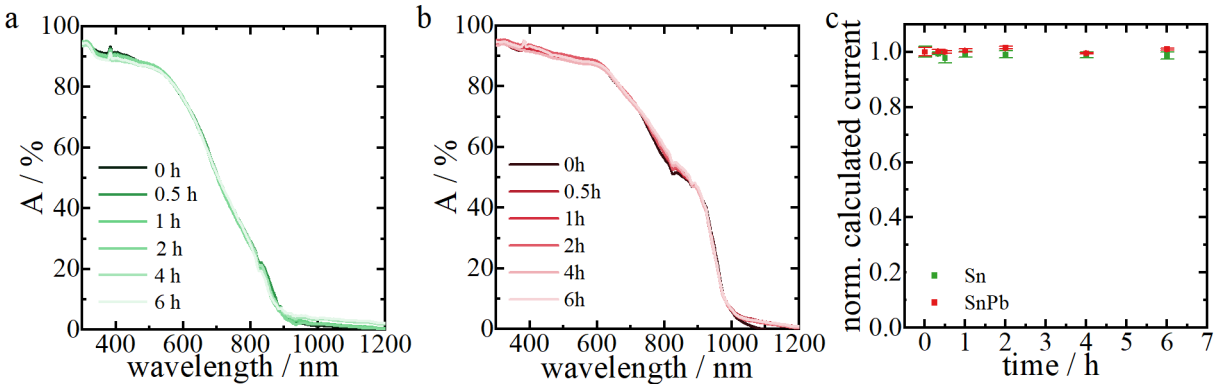

Figure 4.46: Absorptance (A) of tin (a) and tin-lead mixed (b) perovskite absorbers stressed at 85°C for different time scales. c: Calculated conversion of photons into charges visualized as a norm. current density.

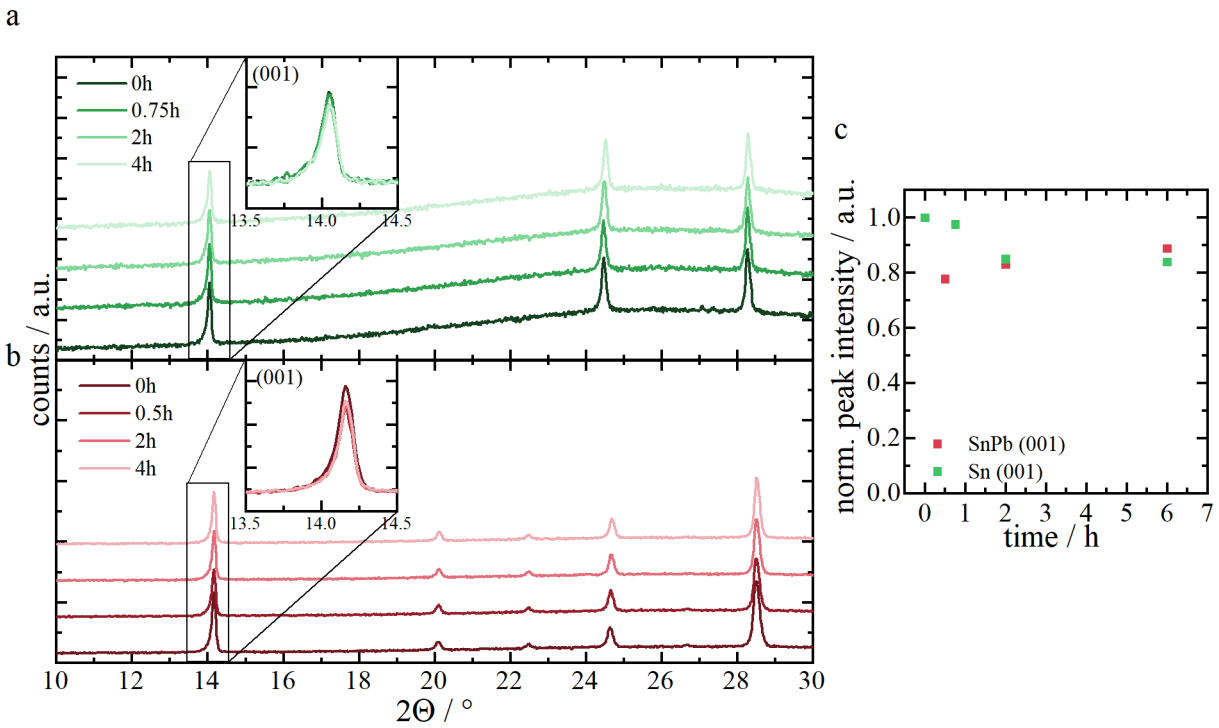

Figure 4.47: Investigation of the perovskite crystal structure by analyzing XRD-patterns of perovskite films stressed by 85°C in inert atmosphere. XRD patterns for the tin (a) and (b) tin-lead mixed perovskite at different time scales with insets to highlight significant changes. Extracted (001)-peak intensities (c) shown in a and b for visualizing the degradation process.

Analogously, to the reactivity study in the ambient atmosphere, possible ion migration activated by heat is investigated by ToF-SIMS depth profiles (see figure 4.48). Stressing the tin and tin-lead mixed perovskite films for six hours at 85°C, does not change the elemental distribution in the perovskite films. Thus, ions seem not to migrate in these perovskite films.

In summary, stressing the perovskite absorber layers by heat for two or six hours in nitrogen atmosphere does not cause any significant changes in the perovskite morphology, absorption capacity, crystalline perovskite phase and elemental distribution in the perovskite bulk. It seems that the tin and tin-lead mixed perovskite films are stable against heating in inert conditions at least in a short time range of six hours. This suggests a stable perovskite phase without phase transitions in the analyzed temperature range. Similar observations were already made for tin perovskite films by Meng et al. [236] and Leijtens et al. for tin-lead mixed perovskite films [104].

Tin-containing perovskite solar cells under thermal stress

As the stability of perovskite films in thermal stress were studied before, these results are correlated to the degradation in perovskite solar cell devices.

The impact of thermal stress is analyzed by investigating their solar cell performance and perovskite phase changes. The solar cell performances are analyzed as this is the central property of solar cells. Further phase changes are examined as these are influenced by the tin oxidation and ion migration in perovskite solar cells.

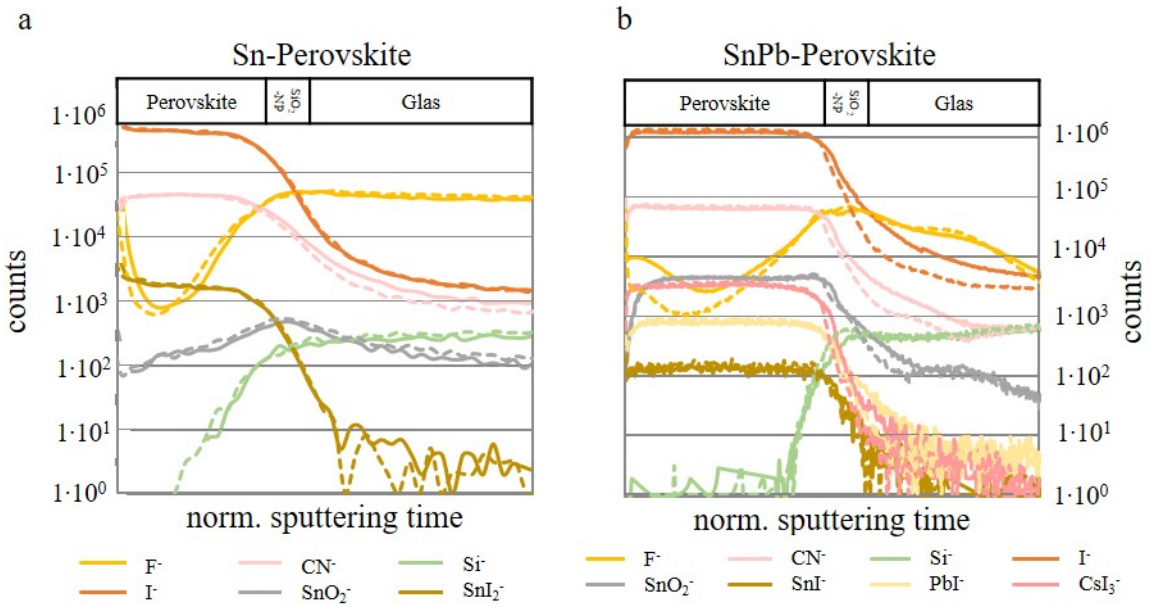

Figure 4.48: Tin (a) and tin-lead mixed (b) perovskite films' elemental distribution of as-grown (solide line) and thermal stressed samples for two hours (dashed lines) investigated by ToF-SIMS. Measurements were performed in the spectrometry-mode using Bi_3^+ ions as the analysis beam and oxygen-clusters$^+$ for sputtering.

The solar cell performance is summarized in figure 4.49, illustrating the PCE changes of each solar cell over time (see figure 4.49a) and exemplary $J(V)$-curves of one tin (see figure 4.49b) and one tin-lead mixed (see figure 4.49c) perovskite solar cell.
The different perovskite compositions seem to be affected differently by the thermal stress. After 30 minutes of heating, the efficiency of tin devices abruptly decreases from 2.2% in mean to around half of the original value, 1.3% in mean. So, the T_{80} is less than 30 minutes. Afterwards, no more significant decrease in efficiency appears. The shape of the $J(V)$-curves is not changing significantly. Wang et al. reported a T_{80} value of 100 minutes for already the unoptimized device, however using nickeloxide as HTL [83].
For tin-lead mixed perovskite solar cells, the efficiency decreases with prolonging heating time. Moreover, the hysteresis rolls over. In the beginning, the reverse bias measurements achieve a higher PCE value, whereas, after two hours of heating, the forward bias measurements achieve higher PCE values. The T_{80} stability time is roughly two hours. The overall PCE decreases from around 11% to 6%, stressing the samples for four hours. Besides the hysteresis, the overall shape of the $J(V)$-curves are similar. A stable tin-lead mixed perovskite solar cells for a 3 hours stress is reported by Han et al., also using nickeloxide as HTL [237].

XRD measurements are performed at different time scales of heating to get insight into the degradation mechanism (see figure 4.50). Again changes of the XRD patterns are discussed focusing on the (001)-perovskite peak.
For both perovskite compositions, similar trends are observed. The perovskite phase seems to be basically unchanged by the temperature stress since no intensity change nor shift of the (001)-peaks are observed (see figure 4.50a, b). However, a peak at 26.8° is arising for both perovskite compositions (see figure 4.50a, b). The intensity of this peak is not following any

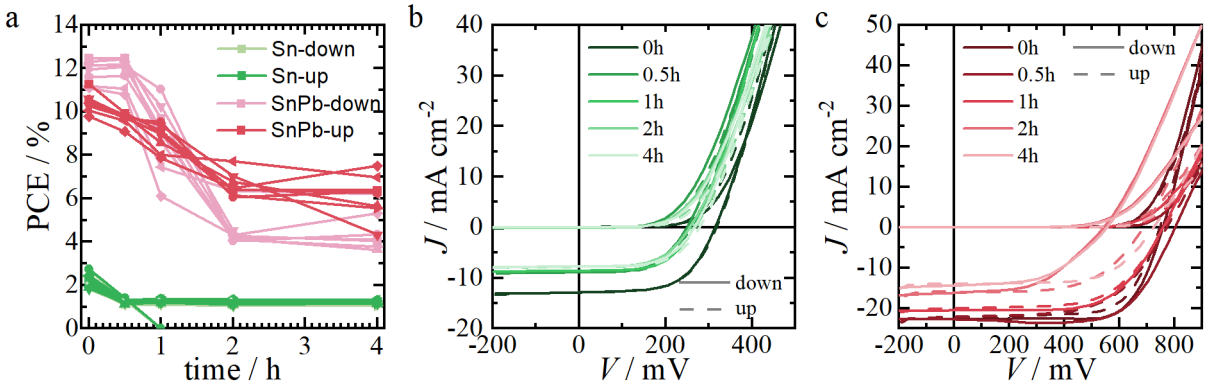

Figure 4.49: Impact of temperature stress on the solar cell performance of tin and tin-lead mixed perovskite solar cells. a: Solar cell efficiency displayed over time. Exemplary $J(V)$-curves measured at different time scales for a tin (b) and tin-lead mixed (c) perovskite solar cell.

trend with increasing heating time for the tin perovskite solar cells (see figure 4.50c). Whereas for the tin-lead mixed perovskite solar cells, the peak intensity increases with prolonging heating time. Analogously to the interpretation of the tin devices stressed in ambient conditions, it is assumed that this peak correlates to a SnO_2 phase. Surprisingly, since the thermal stress is performed in an inert atmosphere. It is expected that residual water in the used hygroscopic PEDOT:PSS [116, 128] is the source of primary moisture but also oxygen. Already small amounts of moisture and oxygen are assumed to be sufficient to decompose a tin-lead mixed perovskite absorber by thermal activation [238].

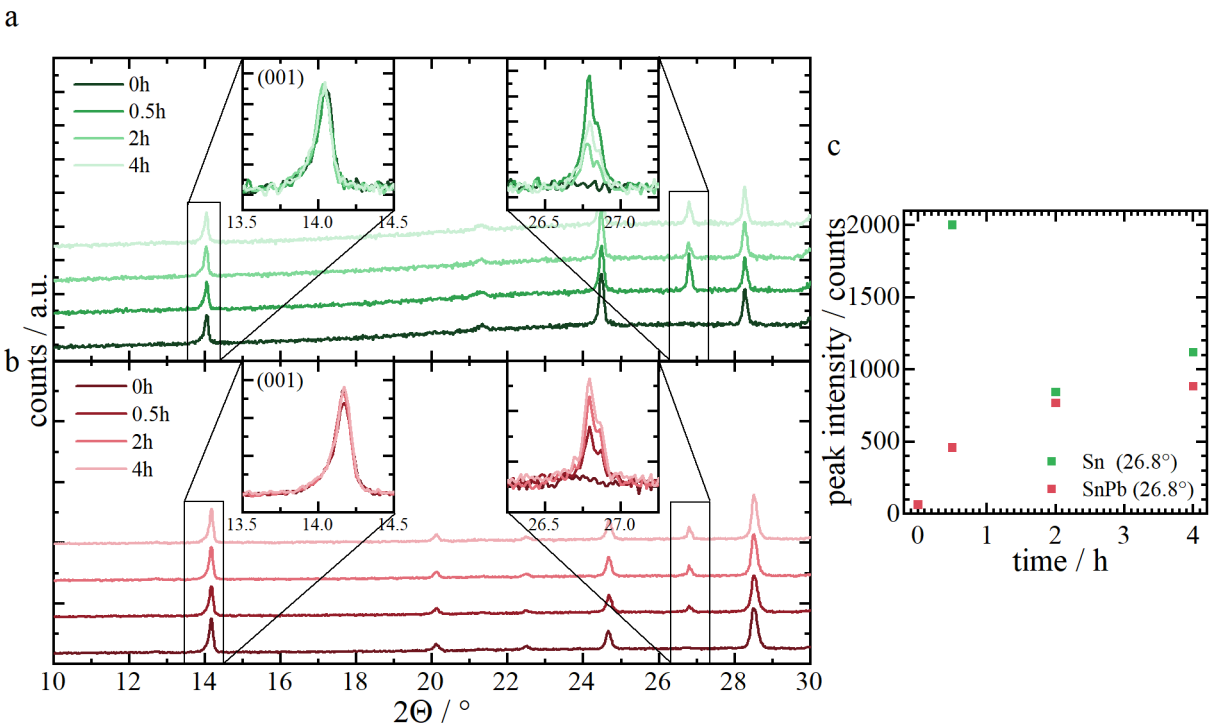

Figure 4.50: Impact of thermal stress on the crystal phase structure of tin (a) and tin-lead (b) mixed perovskite solar cells by measured XRD patterns with insets to highlight significant changes. c: Extracted peak intensity of the 26.8°-reflex to visualize the degradation process.

ToF-SIMS depth profiles of as-grown and stressed perovskite solar cells are compared for further insights into the ion migration (see figure 4.51). Again the displayed depth profiles highlight only the relevant ions, whom ions' amount by integrating their signal[3] are shown in figure 4.51c. All ions representing each layer in the solar cell stack are shown in figure A.15 in the appendix. The iodine seems to be mobilized by thermal stress, thus migrating from the perovskite bulk to the surface. The iodine concentration enhances in the ETL and at the ETL/ silver interface from 350 000 (17 000 000) to 590 000 (28 000 000) in tin (tin-lead) perovskite solar cells. Analogously to the ambient test, the fluoride concentration in the ETL, especially in the tin perovskite solar cell, is increased. However, the amount accumulated directly at the Ag/ETL interface seems to decrease. It seems, that fluoride from the Ag/ETL interface migrates into the ETL. The overall amount of fluoride in the silver electrode and ETL is constant for tin perovskite devices (150 000) or even decreased for the tin-lead mixed perovskite devices (100 000 to 60 000). The amount of oxygen is only slightly enhanced from 9 000 (13 000) to 12 000 (17 000) for tin (tin-lead) perovskite devices in silver and ETL layer.

[3] Detailed procedure for determining the F^- amounts is described in chapter 3.2.2.

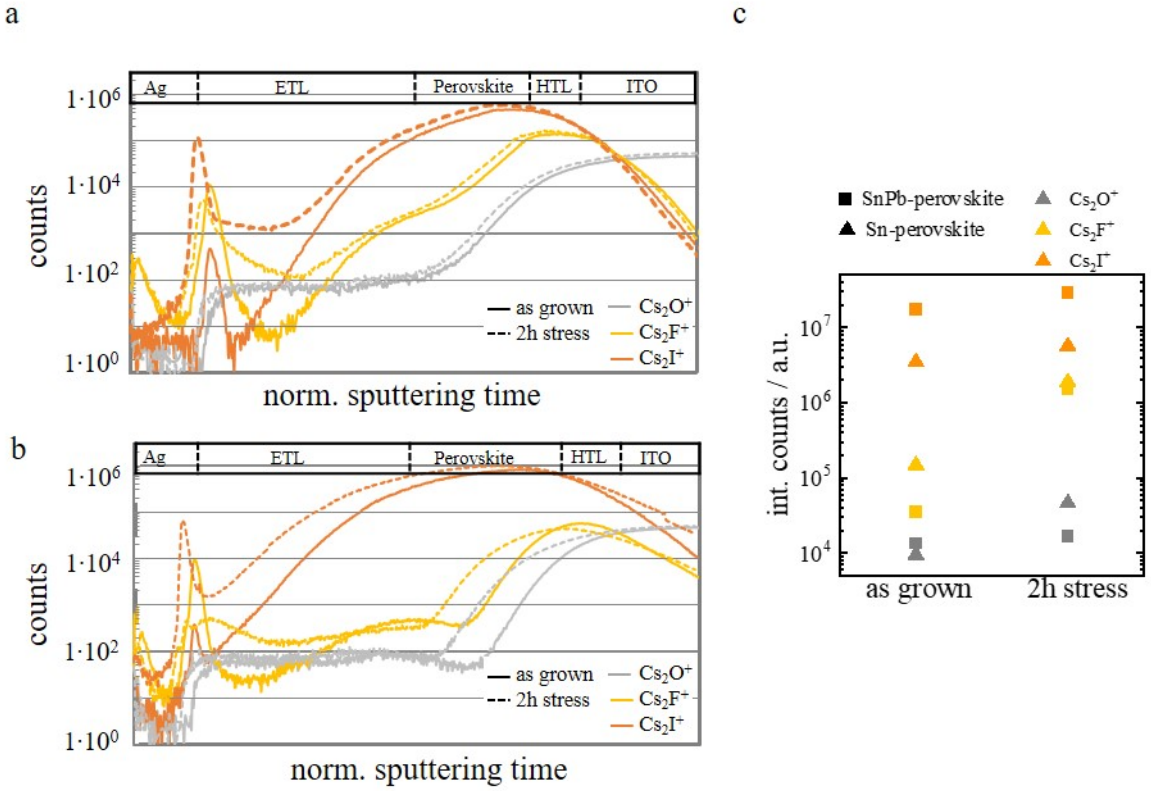

Figure 4.51: Impact of two hours temperature stress on ion migration in the perovskite solar cell stack measured by ToF-SIMS measurements. Comparative depth profiles of tin (a) and tin-lead mixed (b) perovskite solar cells of fresh (solid line) and stressed (dashed line) samples. Measurements were performed in the spectrometry-mode using Bi_3^+ ions as the analysis beam and Cs^+ for sputtering. Signals of shown ions are integrated as a parameter for their amount in the relevant range of the silver and ETL layer and displayed in c.

The impact of thermal stress on solar cell performance can be correlate to perovskite material changes. The amount of SnO_2 phase corresponds to the PCE losses. For the tin perovskite solar cells, an abrupt efficiency decline after 30 minutes of heating is observed, which would fit to the new phase already significantly arising after 30 minutes of heating. For the tin-lead mixed perovskite solar cells, the decrease in efficiency with longer heating time can be correlated to the increased amount of the new phase. However, the increased iodine, fluoride migration can also be the reason for the decline in solar cell performance. Analogously, it seems that the ion migration is triggered by an internal field, as for the pure perovskite film no ion migration was observed. The consequences of these ion migrations were discussed in detail in the previous subchapter.

Summary of investigated tin-containing perovskite absorbers under thermal stress

The following section summarizes the main observed findings of the perovskite films and devices stability analysis under thermal stress. The main observations are summarized in table 4.3.

Table 4.3: Summarizing the main observations of the aged samples by thermal stress.

perovskite	film properties	device properties
tin	Absorbance: $T_{80} > 6$ h	PCE: $T_{80} > 0.5$ h; abrupt losses
	phase morphology: $T_{80} > 6$ h	phase morphology: $T_{80} > 4$ h; SnO_2 formation
	layer morphology: $T_{80} > 2$ h	ToF-SIMS: F^-, I^- migration
tin-lead	Absorbance: $T_{80} > 6$ h	PCE:$T_{80} = 2$ h
	phase morphology: $T_{80} > 6$ h	phase morphology: $T_{80} > 4$ h; SnO_2 formation
	layer morphology: $T_{80} > 2$ h	ToF-SIMS: F^-, I^- migration

The perovskite films seem to be stable under thermal stress in nitrogen atmosphere. This suggests a stable perovskite phase for the studied tin and tin-lead mixed perovskite composition in the analyzed temperature range.
Whereas devices losses are determined for both perovskite compositions with different trends. Performance losses of tin devices are abruptly observed already after 30 minutes of stress. However, these remained static after the abrupt loss. The performance of tin-lead devices decreased linearly. These losses are correlated either to a formed degradation material, assumed to be SnO_2, or iodide migration. However, it is expected that iodide migration dominates the performance losses. If formed SnO_2 is the dominant reason for performance losses, the tin perovskite solar cell stressed in ambient condition with also formed SnO_2 in a comparable amount, need to have a similar trend in their $J(V)$-curves. However, the $J(V)$-curves of ambient stressed tin solar cells have very characteristic S-Shapes, whereas the thermally stressed ones have not.

As no changes in the tin-containing perovskite films are detected under thermal stress, and the devices seem to deteriorate, the performance losses are assumed to be dominated by charge or electrode-layer degradation rather than perovskite absorber deterioration. Thus device stacks have to be optimized, to gain improved thermal resistance.
Studies reporting on similar stability testing achieved significantly lower PCE losses [83, 237].

They used nickeloxide as HTL instead of PEDOT:PSS [83, 237]. This can be an additional hint, that PEDOT:PSS is unfavorable for stable devices.
However, as ion migration seems to be the most dominant degradation mechanism here, these should be prevented by using different charge transport and electrode material. Charge layers with diminished probability for reactions with mitigated ions, leading to deteriorating these need to be investigated. Guerrero et al. used a Cr_2O_3/Cr electrode to prevent the iodine reaction with silver (see chapter 2.3.3) [166]. Moreover, interlayers can be inserted to prevent ion migration throughout the solar cell device. Besides modifying the solar cell stack, optimizing the perovskite layer by reducing its defects can limit ion migration, as ions favorably migrate at defects [29].

4.3.3 Summary and outlook of the tin-containing perovskite stability study

In the previous chapters, the stability of tin-containing perovskite solar cells was investigated. The main findings will be summarized in the following.

The stability analysis highlights the high reactivity of tin-containing perovskite absorbers in the ambient atmosphere and their low thermal resistance in devices.
The ambient atmosphere study in this work emphasized the necessity of inert atmosphere preparation and encapsulation of tin-containing perovskite devices. Additional oxygen- and moisture-free materials for solar cell preparation should be favored. However, the solar cell losses seemed to be dominated by the degradation of the device rather than the perovskite film itself. The first initial short-term aging test by elevated temperature (85°C) in an inert atmosphere observed stable perovskite films at least for a six hours stress. However, the perovskite devices have low thermal resistance unstable due to assumed high ion migration.

This work gave a first insight into the short-term stability of tin-containing perovskite absorbers. Based on the observed results, especially strategies for a PEDOT:PSS alternative and thermal resistance device stacks need to be explored. Exploring PEDOT:PSS-alternatives is not trivial as shown for tin-lead perovskite solar cells in chapter 4.1 and its assumed beneficial impact in combination with SnF_2 (see chapter 4.2.1.) Furthermore, intermixing of material seems to be crucial, as ion migration for the devices stressed in ambient atmosphere and by heat was verified. So in-depth analysis of charge layer interfaces is needed to understand the degradation mechanism. So that specific optimization can be performed to limit ion migration and charge layer deterioration yielding in an stability of perovskite solar cells.
Nevertheless, the high stability of tin-containing devices in an inert atmosphere is very encouraging (see figure 4.36 and 4.37), as tin oxidation by oxygen and moisture in inert conditions can be prevented and thus in future applications by sample encapsulation.

For an overall understanding of dominant degradation mechanism, additional aging test and longer tests have to be performed beyond the ambient and thermal stress. Procedures for perovskite solar cell stability were presented by perovskite specialists in [138]. They suggested to explore the dark, bias, light, outdoor and thermal stability with at least the common experiment duration of 1000 hours [138]. Based on these recommendations, this work was a first short test of ambient and thermal stability for tin-containing perovskites.
For future investigating tin-containing perovskite, systematic stability test on the thermal and

light stability of perovskite films, unencapsulated and encapsulated devices should be performed. Additionally, the bias stability of unencapsulated and encapsulated devices should be explored. Further, test conditions should be combined, because accelerated degradation of lead-perovskite was reported by combining oxygen and light [152]. A very common test for solar cells is the 'damp heat' with an testing atmosphere of 85°C and 85 rH% [138]. So far these were only minor considered by the research interests [140]. However, such detailed characterizations were beyond the scope of this work.
Nevertheless, already important findings could be revealed with the short-term annealing experiments as the devices degraded fast - in contrast to non-visible changes within the perovskite layer itself.

Summary and outlook: Development of tin-containing perovskite with improved sustainability

In this chapter, tin-containing perovskite absorbers were investigated as lead-alternatives being advantageous when considering human health and environmental aspects.

Tin-lead mixed perovskite absorbers were explored as high performing lead-alternative solar cells with mitigated toxic and environmentally impact.
PEDOT:PSS and MA^+-containing perovskite composition are generally not favored for perovskite solar cells [120–128, 128], but have been less considered for tin-lead mixed perovskite solar cells [116]. Thus a strategy to replace these was examined. Therefore, PEDOT:PSS was replaced by PTAA as the first step with still MA^+-containing tin-lead mixed perovskite solar cells. For both solar cell stacks comparable efficiencies of 13.0 % with PEDOT:PSS and 11.5 % with PTAA are reached. By targeted optimizing the FA^+ and Cs^+ ratio to replace the MA^+ in the tin-lead mixed perovskite composition the PTAA/perovskite interface is adjusted and an efficiency of 10 % at MPP for MA^+-free and PEDOT:PSS-free tin-lead mixed perovskite solar cells is realized.

To further reduce the lead content, pure tin perovskite absorbers were examined making compromises in the solar cell performance.
In this work, a new mechanism behind the commonly used SnF_2 additive was discovered. A preferable accumulation of the SnF_2 at the PEDOT:PSS/perovskite was discovered. Moreover, an ultrathin SnS interlayer is formed as a result of a reaction of the accumulated SnF_2 with the underlying PEDOT:PSS. As SnS is a p-type semiconductor [211], this interlayer is assumed to improve the solar cell performance, as observed. The new finding of the formed SnS interlayer can give a hint towards the reason why PEDOT:PSS as HTL and the SnF_2 additive are crucial components for highly efficient Sn-based solar cells [9, 80, 96, 99, 196, 197].
Interfacial engineering of the HTL and ETL was performed for $FASnI_3$ perovskite absorbers to reduce recombination and band mismatch losses in the solar cell device. A facile strategy was implemented to observe pinhole-free perovskite film growth by altering the underlying HTL surface, covering it with an optimal amount of SiO_2-NP. This reduces structural defect and accordingly non-radiative recombination in the perovskite film. The solar cell performance improved from 3.0 to 4.0 % in the median. To reduce conduction band mismatch and in consequence V_{OC} losses, ETL with higher conduction bands were investigated. Substituting the commonly used PCBM by ICBA or bis-PCBM with a LUMO of higher energy is assumed to improve conduction band alignment to the perovskite layer, as increased V_{OC} values are accomplished. However, the reduced intrinsic electron mobility of the ICBA and bis-PCBM is assumed to limit the solar cell efficiency increase. The improved interfaces increases the solar cell efficiency from 3.0 % to 5.6 % in the median, nearly doubling the V_{OC} to 650 mV.
Further higher crystalline ordering and thus assumed reduced defect states in the perovskite bulk is achieved by 2D/3D mixed perovskite absorbers improving the solar cell performance. The impact of different 2D PEA_2SnI_4 : 3D $FASnI_3$ on the perovskite film crystalline phase was unraveled. The highest crystalline ordering is observed for a 2D ratio of 7.5 % (2D molar to the total perovskite molarity). The strong crystal perovskite texturing indeed enhances the perovskite solar cells' efficiency and V_{OC} from 2.8 %, 350 mV for the 3D perovskite to 4.3 %, 420 mV for the 2D/3D mixed perovskite in the median. Replacing the PCBM by ICBA to

additionally align the band structure and passivate perovskite defects, the efficiency improves further to 5.2 % with a V_{OC} of 670 mV.
In total, the optimization strategies lead to a solar cell performance of up to 6.6 % for the $FASnI_3$-based perovskite solar cells in this work.

Stable tin-containing perovskite solar cells is one of the main challenges as tin oxides fast. A systematically stability analysis in ambient condition and under thermal stress was performed.
A high reactivity for tin-containing perovskite films in the ambient atmosphere was verified with faster degradation for pure tin perovskites. However, the efficiency losses of the solar cells are assumed to be dominated by charge and electrode deterioration rather than the perovskite itself due to material intermixing by ion migration. Nevertheless, preparation - and encapsulation processes and all used materials for solar cell preparation should be at best oxygen- and moisture-free for tin-containing perovskite solar cells. Especially the used hygroscopic PEDOT:PSS as HTL seems to negatively influence the stability.
Aging by thermal stress (85°C) in an inert atmosphere was performed to achieve insights into the thermal operation stability and accelerate the degradation in inert conditions. Even if no degradation for tin-containing perovskite films was observed for six hours, their analogous devices deteriorate fast by assumed ion migration.
As for both stress conditions, material intermixing due to ion migration from the perovskite is assumed to limit their stability, optimized device stacks should be explored in the future, preventing ion migration. This work provided a first insight into the short-term stability of tin-containing perovskites.

This investigation demonstrates, that tin-containing perovskite absorbers are very promising lead-alternatives, even if they have only a reduced toxicity and environmental impact. Future developments should focus on needed aspects for commercializing these perovskite solar cells. One of these are needed improved solar cell performance to be comparative to lead-based perovskite solar cells and other solar cell technologies. Moreover, further studies should address the mechanism behind the stability issues to prevent degradation processes. Furthermore, encapsulation techniques in inert atmosphere have to be explored to achieve appropriate stability. Lastly, larger area deposition of the tin-containing perovskite solar cells and module fabrication should be investigated.

5 Exploring bismuth-based perovskite absorbers with high sustainability

As the environmental and human health impact of tin perovskites is still controversial reported [10, 11], a further lead-free alternative being non-toxic and environmentally friendly is explored. Therefore, the bismuth-based $A_3Bi_2I_9$ (ABI) compound is studied with additional promising ambient material stability in the following chapter.

The optimization strategies are based on challenges of ABI compounds outlined in the theoretical chapter 2.2.2.
These compounds suffer from an unfavorable perovskite morphology (pinholes and low crystallinity of the perovskite film) [29, 132]. This will be addressed at the beginning of this chapter (see subchapter 5.1). Furthermore, ABI compounds have huge band-gap energies of around (1.8-2.9 eV) [15], which is not ideal for single-junction cells. Thus strategies to reduce these band-gaps will be considered in subchapter 5.2 by integrating selenium and sulfur in the absorber compound as calculations showed promising results [136] .

In this work the fully inorganic $Cs_3Bi_2I_9$ perovskite composition is chosen, as a high PCE of 3 % [16] is reported for this $Cs_3Bi_2I_9$ absorber, and the unfavorable MA^+ is eliminated [120–123].

5.1 Morphology optimization of the $Cs_3Bi_2I_9$ film

In this subchapter a strategy for a homogeneous $Cs_3Bi_2I_9$ perovskite film deposition is explored, which is further modified to tune the perovskite morphology. Additionally, the impact of the modified perovskite film morphology on the solar cell performance is investigated.

Deposition and characterization of $Cs_3Bi_2I_9$ perovskite films

The $Cs_3Bi_2I_9$ perovskite films are prepared from a stoichiometric perovskite solution by spin coating and drying the wet-layer at a heat plate. Details about the perovskite film preparation are described in chapter 3.1.

A gas quenching deposition method was implemented to yield homogeneous perovskite deposition. A strong nitrogen gas stream (gas quenching) during spin coating enhances the number of nucleation sides for the crystal growth by a sudden increase of the wet-layer precursor concentration. With this method dense homogeneous perovskite films can be accomplished (see figure 5.1b), whereas without gas quenching isolated small crystals are observed (see figure 5.1a).

For verifying that the deposition method yields the desired $Cs_3Bi_2I_9$ perovskite phase, XRD measurements are performed (see figure 5.2). As the measured XRD pattern is comparable to the reference one, a phase pure perovskite deposition is assumed. Thus, the carried out deposition method is suitable for synthesizing a $Cs_3Bi_2I_9$ perovskite film.

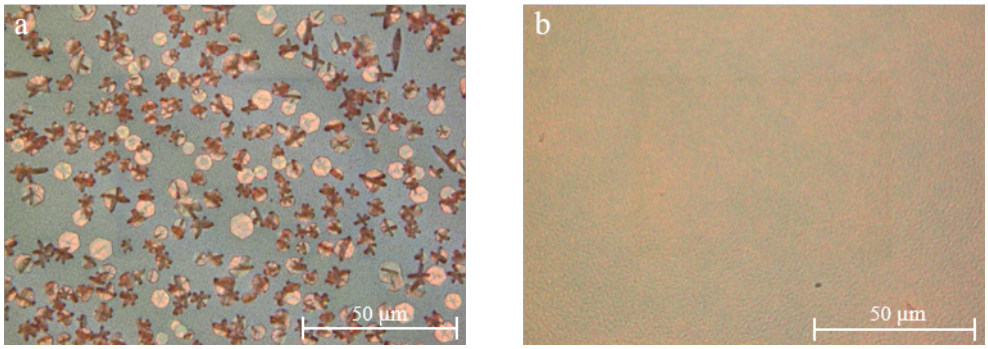

Figure 5.1: Optical microscope surface images of $Cs_3Bi_2I_9$ perovskite deposition on FTO/TiO_2 samples without (a) and (b) with gas quenching.

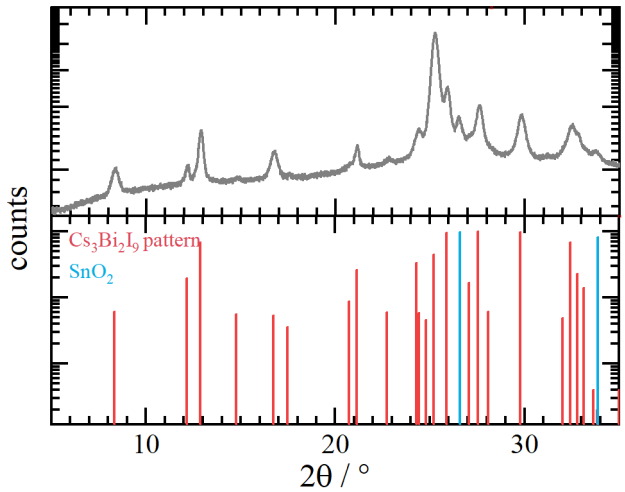

Figure 5.2: XRD pattern of deposited $Cs_3Bi_2I_9$ on a FTO/TiO_2 sample compared to a $Cs_3Bi_2I_9$ reference pattern [239].

Furthermore, the impact of the annealing temperature on the perovskite film morphology is analyzed.
Therefore, perovskite films, deposited on the ETL and annealed at varying temperatures between 100 and 300 °C, are investigated by SEM cross-section images (see figure 5.3). With increasing annealing temperature increased grain sizes are observed. The grain size rises from a non-definable size smaller than 100 nm for an annealing temperature of 100°C to grain sizes of 200-300 nm for 300°C. Huge grains are generally favored for perovskite films in solar cells, as they guarantee fewer grain boundaries which are considered to enhance non-radiative recombination losses [240–242].

Since drastic grain size alterations are observed, these perovskite films are further characterized in terms of its crystalline phase properties by measuring XRD pattern. Two general findings are observed analyzing the XRD patterns (see figure 5.4). By increasing the temperature, the peak intensity of {001} planes are significantly enhanced in comparison to other peak planes. The intensity ratio of the (002)-peak to the (101)-peak is rising from below 1 to more than 50. This indicates a preferred crystal orientation to the {001} crystal planes with higher annealing temperatures. Accurate crystal facet orientation can positively effect solar cell

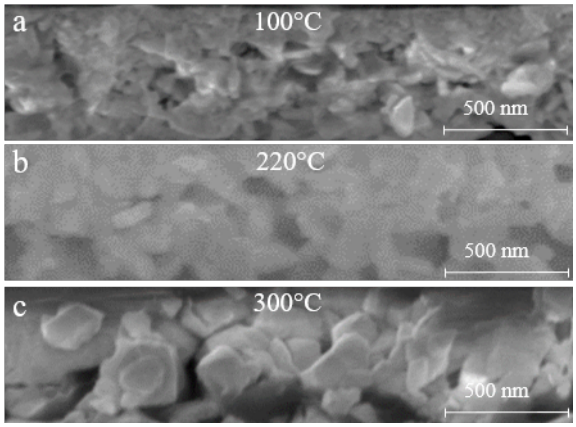

Figure 5.3: SEM cross-section images of $Cs_3Bi_2I_9$ perovskite layer deposited on FTO/TiO_2 sample and annealed at different temperatures (a: 100°C, b: 220°C, c: 300°C). The images only show the perovskite layer.

performance [243, 244]. Besides this, the FWHM of the (002) peaks decreases from around 0.43 to 0.05° with an increasing temperature from 100 to 300°C. Two parameters principally leads to a reduced FWHM: increased crystalline size and reduced microstrain in the crystal. Both are thought being beneficial for solar cells [245–252].

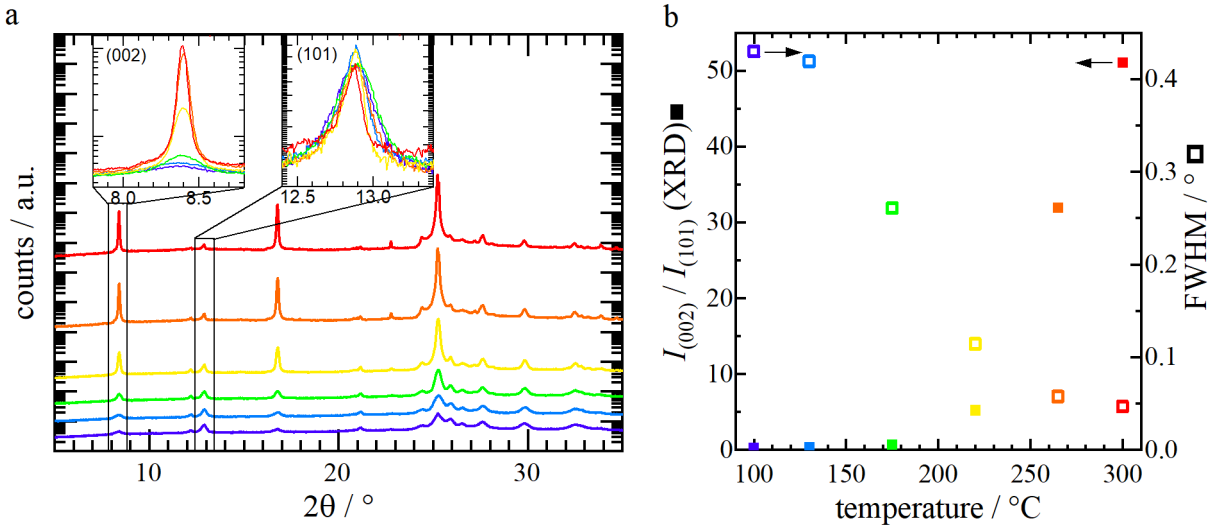

Figure 5.4: Modification of $Cs_3Bi_2I_9$ perovskite micro-crystallinity by the annealing temperature. a: Influence of annealing temperature on the XRD pattern. b: The analyzed peak intensity ratios of the (002) to (101) peaks are illustrated as filled squares and FWHM of the (002) peak displayed as open squares.

Improved micro-crystalline layers are expected to have fewer defects, reducing non-radiative recombination. This hypothesis is corroborated by a steady-state PL study, in which higher PL intensity is observed for samples with higher annealing temperature (see figure A.16). Higher PL intensity suggests less non-radiative recombination, which are unfavorable losses in solar cell devices [217, 253].

Impact of improved perovskite film morphology on the solar cell characteristics

The experimental findings and postulated interpretation are confirmed by studying their solar cell performances. The used solar cell stack is a standard n-i-p stack with FTO as TCO layer, TiO_2 as ETL, Spiro-OMeTAD as HTL, and gold as back electrode. Details about the solar cell fabrication are described in chapter 3.1.
An exemplary SEM cross-section images visualizes the morphology of the solar cell stack (see figure 5.5).

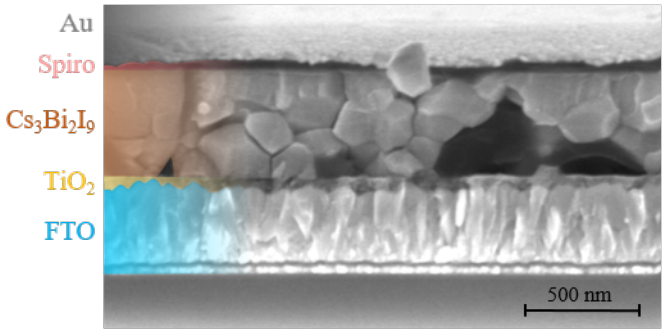

Figure 5.5: SEM cross-section image of a FTO/TiO_2/$Cs_3Bi_2I_9$/Spiro-OMeTAD/Au solar cell.

The measured $J(V)$-curves are evaluated according to their solar cell parameters. Exemplary $J(V)$-curves measured in reverse bias scan direction are shown in figure 5.6a. The observed J_{SC} and PCE values for reverse scans are depicted in figure 5.6b.
As seen by the $J(V)$-curves, the current in the solar cells increases with higher annealing temperature. The J_{SC} is enhanced by nearly one order of magnitude from an average of 0.015 to 0.12 mA cm^{-2} increasing the temperatures from 100 to 300°C. This is attributed to reduced charge carrier recombination by improved perovskite film morphology due to a decreased grain boundary concentration and better micro-crystallinity. The solar cell efficiency increased from an average value of 0.002 to 0.023 %.

To sum up, the gas-quenching method was implemented to yield dense, homogeneous $Cs_3Bi_2I_9$ films. The perovskite morphology is further modified by increasing the annealing temperature resulting in highly oriented crystallites and huger grain sizes. By the improved perovskite morphology, the solar cell efficiency could be enhanced by one order of magnitude. However, the efficiencies are still very low presumably assigned to the very high exciton binding energies [15] and high band-gap energies (see figure A.17). Thus, additional optimization strategies are necessary.

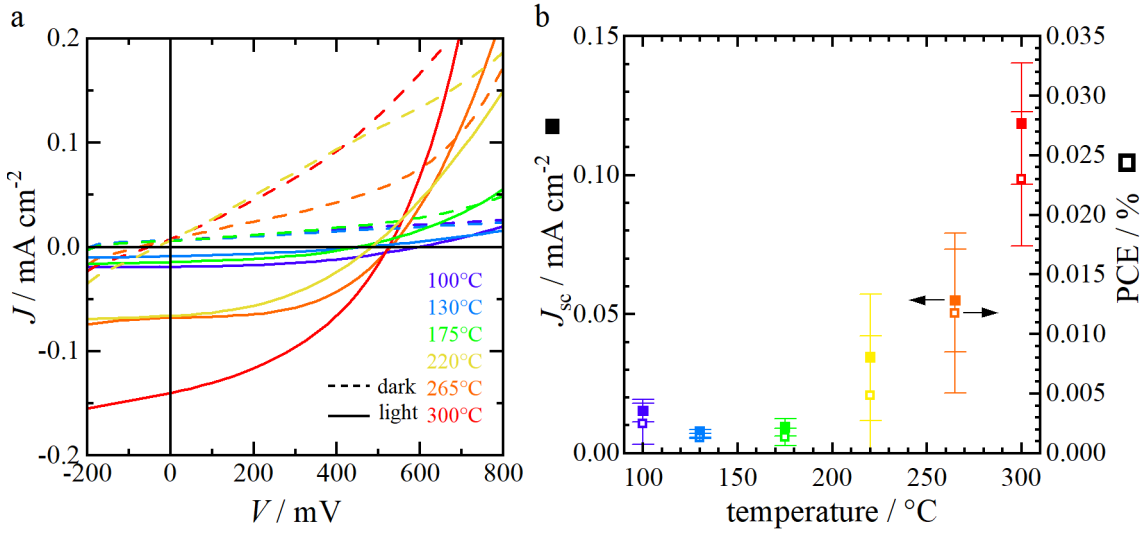

Figure 5.6: Impact of perovskite annealing temperature on the solar cell performance (solar cell stack: FTO/TiO_2/$Cs_3Bi_2I_9$/Spiro-OMeTAD/Au). a: $J(V)$-curves of typical solar cell devices measured in reverse bias scan direction prepared at different annealing temperature.
b: Extracted J_{SC} (visualized as filled squares) and PCE (visualized as unfilled squares) values of reverse bias measured solar cells.

5.2 Strategies for adjusting the band-gap energy of bismuth-based perovskite absorbers

Since the too wide band-gap of the $Cs_3Bi_2I_9$ perovskite is assumed to be one of the main issues limiting the solar cell performance, optimization strategies on lowering the band-gap energies are explored. As illustrated in the theoretical part of this work (see chapter 2.2.2), Sun et al. calculated promising reduced band-gap energies by incorporating selenium or sulfur via a split-anion approach with iodide [136]. Thus in the following subchapter, methods considering the incorporation of sulfur and selenium are presented.

Strategy to insert sulfur in $Cs_3Bi_2I_9$ perovskite absorbers to reduce the absorber band-gap energy

Reducing the band-gap energy of ABI perovskite absorber by incorporating sulfur seems to be an auspicious approach. Sun et al. estimated a suitable band-gap energy of 1.38 eV for the $MABiI_2S$ perovskite composition with split anions of iodide and sulfur [136]. Furthermore, Vigneshwaran et al. presented a strategy by using bismuth xanthate ($Bi(xt)_3$) (see chemical formula in equation 5.1) as a sulfur source to dope the $MA_3Bi_2I_9$ perovskite. A reduced band-gap energy of 1.45 eV [137] is achieved for this composition, being suitable for single-junction solar cells. Inspired by those results, this doping technique is studied here for the $Cs_3Bi_2I_9$ perovskite.

$Bi(xt)_3$ is synthesized according to the synthesis illustrated by Vigneshwaran et al. [137] in chapter 3.1.3. The molecule consists of three ethyl xanthate functional groups attached to one bismuth atom. Due to its organic side chains, this molecule is soluble in multiple organic solvents [137,254]. Furthermore, it decomposes at temperatures between 100 to 200°C to Bi_2S_3 and volatile organic residues, as illustrated in equation 5.1 [137, 254].

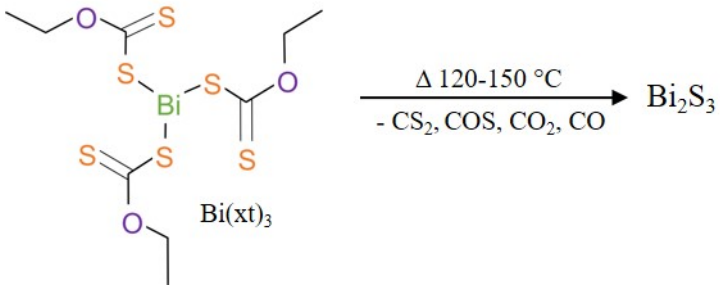

(5.1)

By mixing the $Bi(xt)_3$ with BiI_3 and cesium iodide (CsI) the sulfur shall be incorporated in the crystal structure resulting in the preferred $CsBiI_2S$ compound (see reaction scheme 5.2).

$$2\ Bi(xt)_3 + BiI_3 + 3\ CsI \xrightarrow[-\ CS_2, COS, CO_2, CO]{\Delta\ 120\text{-}150\ °C} 3\ CsBiI_2S \tag{5.2}$$

Thus a precursor solution with a stoichiometry based on the illustrated reaction is prepared, and thin films are deposited.

The fabricated thin films showed a color change from bright red for the undoped $Cs_3Bi_2I_9$ compound to black for the doped one (see figure 5.7a). This was further qualified by obtaining the absorption (see figure 5.7b), which shows a lowered absorptance on-set for the film prepared with the added $Bi(xt)_3$. The band-gap energy reduces from 2.1 eV to 1.4 eV estimated by a tauc-plot (see inset in figure 5.7b).

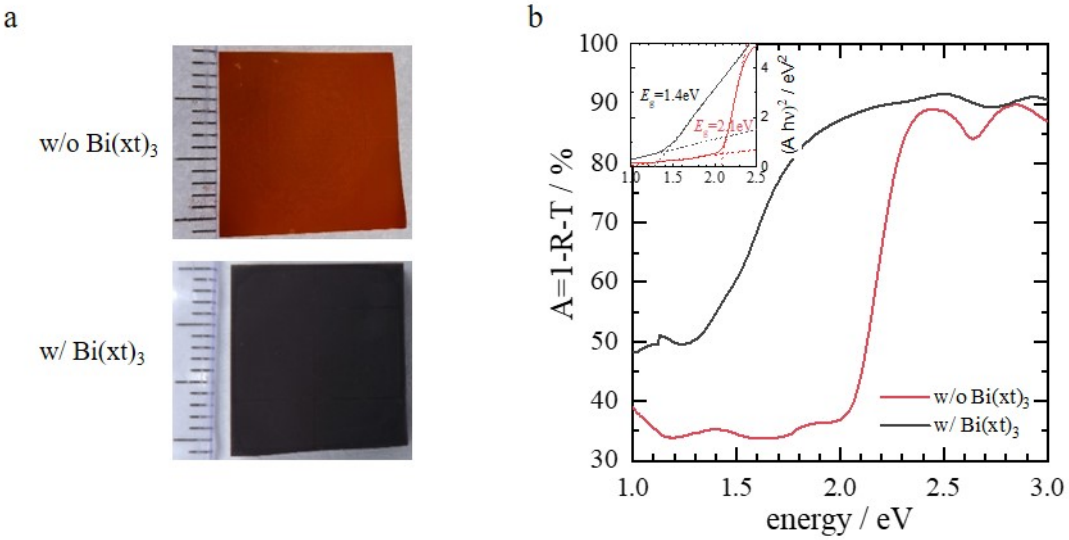

Figure 5.7: Absorption modification by adding $Bi(xt)_3$ into the perovskite precursor solution. a: Top-view photographs of $15 \times 15\ mm^2$ samples without and with added $Bi(xt)_3$. b: Compared absorptance of samples (FTO/TiOx/perovskite) made without and with $Bi(xt)_3$. The inset shows the tauc-plot for determining the band-gap energy.

For further specifying the observed material phases, XRD studies are performed on the deposited films (see figure 5.8). The observed XRD pattern without and with $Bi(xt)_3$ are comparable to the theoretical $Cs_3Bi_2I_9$ pattern without peak shifts (see figure 5.8b). Additional peaks at 23.8° and 39.4° are observed by added $Bi(xt)_3$, which can not be attributed to the $Cs_3Bi_2I_9$, FTO, or Au phase. In order to identify this compound(s), the observed pattern is compared to reference patterns of various phases that could appear as by-products of the reaction 5.2, focusing on the two additional significant peaks at 23.8° and 39.4° (see figure A.18). The peaks fit best to a Cs phase, which indicates a too high concentration of CsI in the layer. Even when reducing the CsI amount in an unstoichiometric precursor solution, the Cs phase can still be observed (see figure 5.8a).

It is assumed that the desired $CsBiI_2S$ material is not formed, as neither a peak shift (being expected when iodine is replaced by sulfur) nor significant differences in the XRD pattern are observed. Thus an alternative reaction is proposed for the postulated process in reaction 5.2, in which the $Cs_3Bi_2I_9$ perovskite-like phase with excess CsI and amorphous Bi_2S_3 material is formed. Additionally, it is assumed that the CsI decomposes into Cs and amorphous I_2. A reaction scheme for the postulated process is illustrated as follows:

$$4\ Bi(xt)_3 + 2\ BiI_3 + 6\ CsI \xrightarrow[-\ CS_2, COS, CO_2, CO]{\Delta\ 120\text{-}150\ °C} 2\ Bi_2S_3 + Cs_3Bi_2I_9 + 3\ CsI\ (3Cs{+}1.5\ I_2) \tag{5.3}$$

The observed darker color of the films with $Bi(xt)_3$ is attributed to the absorption behavior of Bi_2S_3 with a band-gap of 1.3-1.7 eV [255–257].

Therefore it is concluded that doping the $Cs_3Bi_2I_9$ perovskite with sulfur by using $Bi(xt)_3$ was not successful. Thus, further characterization of these films in solar cells is not considered.

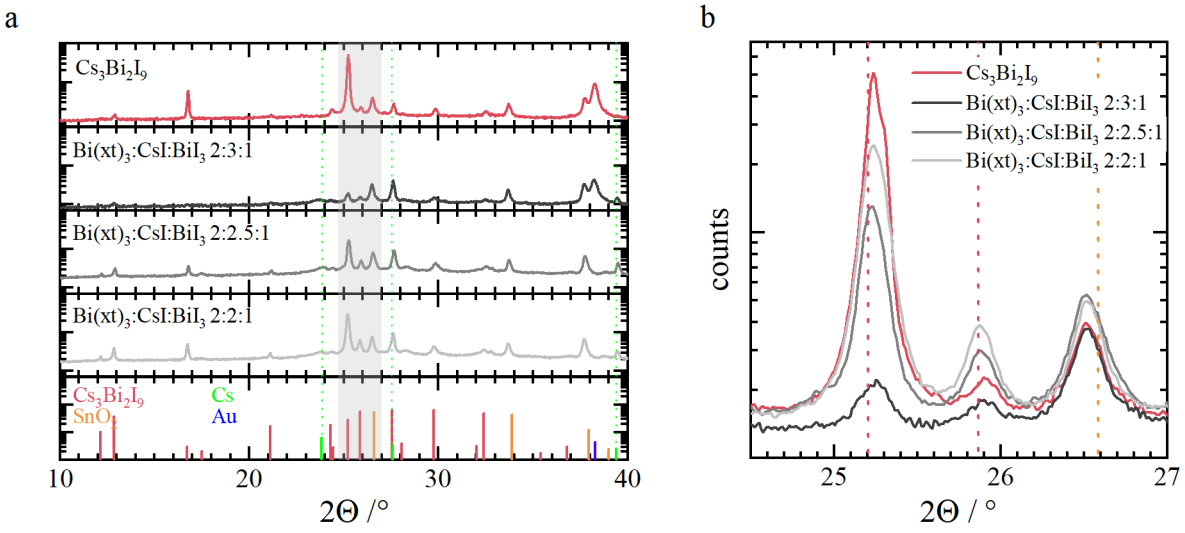

Figure 5.8: a: XRD pattern of samples with added $Bi(xt)_3$ compared to an experimental (top pattern) and reference pattern (bottom pattern) of $Cs_3Bi_2I_9$. Further, XRD patterns with different stoichiometric are shown to vary the CsI amount. b: (006) reflex at 25.2° (marked in red) of the XRD pattern normalized to the FTO peak at 26.5° (marked in orange) (SnO_2 is the reference for the FTO).

Strategy to insert selenium in the $Cs_3Bi_2I_9$ perovskite absorbers to reduce the absorber band-gap energy

Besides incorporating sulfur, Sun et al. presented selenium as another anion for the split-anion approach to reduce the band-gap of $MA_3Bi_2I_9$ to 1.29 eV by forming the $MABiI_2Se$ absorber [136].

Here, a post-treatment procedure of $Cs_3Bi_2I_9$ films by selenium vapor is applied to incorporate selenium to form the preferable $CsBiISe_2$ absorber. The method of post-treatment is described in the methodical section in chapter 3.1.2 and was successfully used at the Zentrum für Sonnenenergie- und Wasserstoff-Forschung Baden-Württemberg (ZSW) to dope $Cu_2ZnSn(S, Se)_4$ absorbers with selenium [258].

Two batches at processing temperatures of 340°C and 350 °C for 20 minutes are carried out. Additionally to the $Cs_3Bi_2I_9$ films, pristine FTO-TiO_2- substrates are post-treated with selenium as reference samples. The deposition of selenium is studied by XRF measurements and sample color changes for a first impression of lowered band-gap energy. In figure 5.9a the elemental composition before and after the post-treatment is analyzed by XRF measurements. As indicated by the orange-colored data in figure 5.9a, the amount of selenium is enhanced for all samples after the post-treatment. So the selenium deposition was successful. All other elements referring to the $Cs_3Bi_2I_9$ perovskite-like phase are constant, indicating no overall decomposition of the perovskite layer. The color of the $Cs_3Bi_2I_9$ films did not change, whereas slightly brown-grey colored samples were observed for the reference sample (see figure 5.9b). Thus, the expected color change to black by a reduced band-gap energy is not observed.

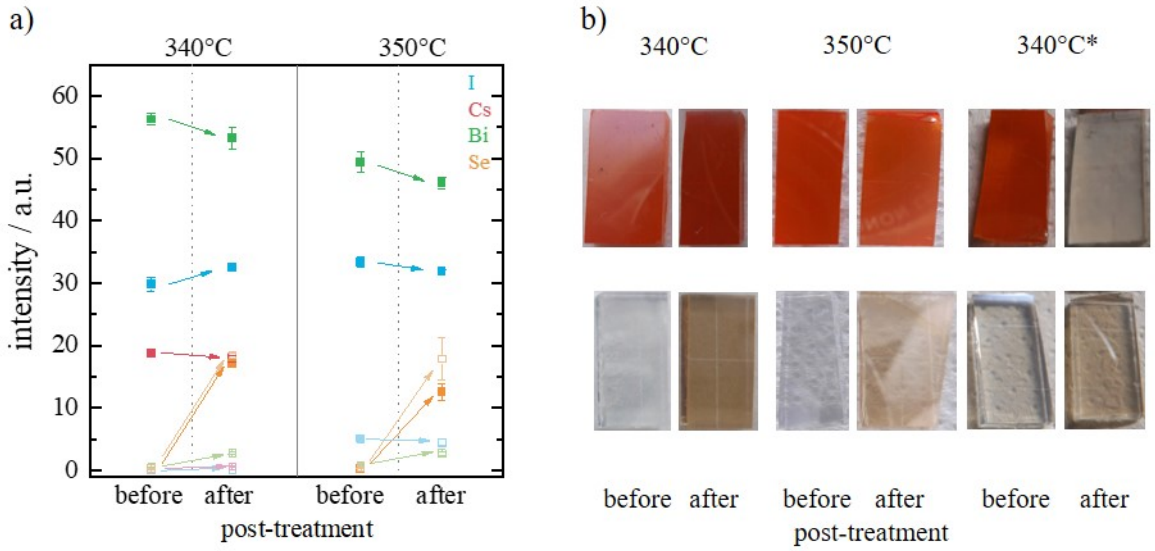

Figure 5.9: a: Uncalibrated XRF intensity, reflecting changes in the composition of selenized $Cs_3Bi_2I_9$ perovskite samples (filled squares) and pristine FTO/TiO_2- samples (unfilled squares) at two post-treatment temperatures for 20 minutes. Data values show two measurements on different sample areas of one sample. b: Top-view photos of those samples before and after the post-treatment and samples of a more prolonged post-treatment of 60 minutes at 340°C (named 340°C*). Samples with deposited $Cs_3Bi_2I_9$ are illustrated in the top row and pristine FTO substrates in the bottom row.

Again, XRD studies are performed to check if the desired material is formed (see figure 5.10). The observed XRD pattern suggests that $Cs_3Bi_2I_9$ perovskite-like phase was formed by comparing these to the reference pattern of $Cs_3Bi_2I_9$ independently on the post-treatment (see figure 5.10a). Moreover, no peak shift is observed as exemplarily illustrated by the (004)-peak, which is expected when selenium would be incorporated in the perovskite crystal structure (see figure 5.10b). The increased peak intensities of {002}-planes are expected to be due to the thermal annealing during the selenium process. The thermal annealing effect on the perovskite crystal morphology was investigated in detail in the previous subchapter.

Thus it is assumed that selenium is deposited on top of the $Cs_3Bi_2I_9$ films. However, the selenium does not significantly incorporate into the perovskite crystal, as no changes of the perovskite film color and the XRD pattern are observed. It is expected that either the amount of selenium is too low to be significantly inserted in the perovskite structure, or the selenium diffusion process into the perovskite layer is hindered. Thus a higher process temperature and longer process are suggested to potentially improve the selenium incorporation into the $Cs_3Bi_2I_9$ structure as the selenium supply would be higher.
A prolonged post-treatment for 60 minutes results in an overall decomposition of the original $Cs_3Bi_2I_9$ layer. This gets apparent in the pale color of the films after post-treatment (see figure 5.9b). Higher temperatures of 410 °C also lead to an overall decomposition (see figure A.19). The decomposed $Cs_3Bi_2I_9$ layers for the longer process (340°C, 60 minutes) and the process with higher temperature (410°C, 20 minutes) suggest that the degradation temperature lays at temperature ranges of 340°C to 410 °C for the $Cs_3Bi_2I_9$ material. A thermogravimetric analysis is performed to verify the critical decomposition temperature (see figure A.20). This reveals a decomposition temperature of 340°C (see figure A.20), which is consistent with the findings of our selenium processes. So a higher temperature and longer process to enhance the amount of selenium are unsuccessful as the original process parameters are already in the critical decomposition temperature range of the $Cs_3Bi_2I_9$ material.

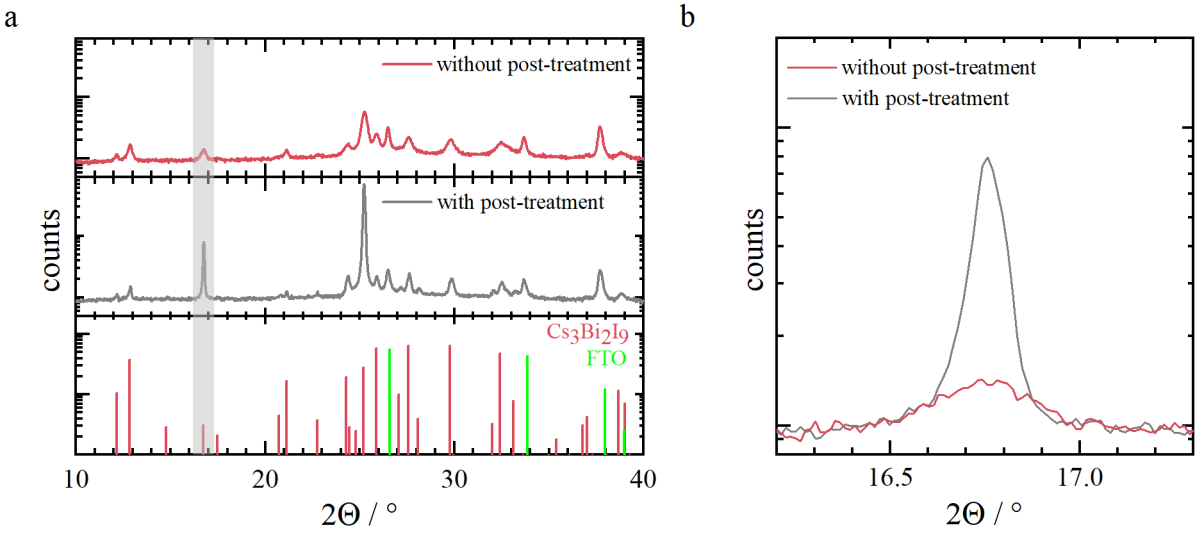

Figure 5.10: a: XRD pattern of samples with and without post-treatment compared to a theoretical $Cs_3Bi_2I_9$ pattern. b: (004) peak at 16.8°C of the XRD pattern for the two samples.

The incorporation of selenium by the presented selenium vapor was not feasible due to the relatively low process temperature and short process time needed to prevent $Cs_3Bi_2I_9$ perovskite decomposition. Thus, characterizing the observed films in solar cell devices is not considered any further.

Summary and outlook of investigating bismuth-based perovskite absorbers

$Cs_3Bi_2I_9$ perovskite absorbers as a lead-alternative with no impact on the environment and human health was investigated.
The gas quenching deposition method for $Cs_3Bi_2I_9$ films was successfully established. Further, this method was adapted to alter the perovskite film morphology. By increasing the annealing temperature, the perovskite grains were enlarged and higher crystallite ordering were observed. These improved perovskite films were further incorporated solar cell devices. Characterized solar cells yield solar cell characteristics which enhanced with improved perovskite morphology. Nevertheless, the obtained solar cell efficiencies of 0.04 % in maximum are still low due to suspected high exciton binding energies and high band-gap energies.
Based on the observed results, strategies to lower the band-gap energy by selenium or sulfur incorporation were presented. Unfortunately, the desired doped materials could not be synthesized.

Bismuth is a promising candidate for lead substitution in perovskite absorbers due to their high environmental sustainability and non-toxicity. However, their application in solar cell devices is challenging due to their high band-gap energy and resulting low power conversion efficiency. However, application in other technologies like photodetectors, memory devices, or photocatalysis should be considered as semiconductor properties were verified [15, 259].

6 Summary and Perspectives

Summary and Discussion

This work explores lead-alternative perovskite absorbers with the goal to improve solar cell performance and environmental sustainability as well as reduce the impact on human health. The suitability of two elements, tin and bismuth, was analyzed by preparation and characterization of perovskite films and solar cells.

Tin was examined as a possible candidate to substitute lead due to its low impact on human health and the environment. Two categories of tin-containing perovskite compositions, tin-lead mixed and pure tin perovskite, were investigated. Tin-lead mixed perovskites generally achieve higher solar cell performances and an improved ambient stability compared to pure tin ones. However, the lead is only partially replaced in these absorbers.

For tin-lead mixed perovskite solar cells realizing PEDOT:PSS-alternative HTL and MA^+-free perovskite composition seems challenging [116]. At the same time, the literature widely discusses the unfavorable hygroscopic, acidic PEDOT:PSS [127, 128], and thermally unstable MA^+ in the perovskite composition [120–126]. The commonly used PEDOT:PSS-alternatives are not suitable for tin-containing perovskites. Inorganic oxide-based HTL insert oxygen vacancies [74, 173], and organic HTL normally contains dopants, which both damage the perovskite [74, 174]. Further, perovskite coverage on the hydrophobic PTAA surface is also challenging in general [177].
In this work, a strategy to replace PEDOT:PSS and implement a MA^+-free perovskite absorber for 1:1 tin-lead mixed perovskite solar cells was pursued. SiO_2-NP as a universal wetting agent is therefore used to fully cover the PTAA surface with the perovskite. Comparable efficiencies of 13.0 % with PEDOT:PSS as HTL and 11.5 % with PTAA are obtained for a still MA^+-containing perovskite absorber. By targeted optimization of the FA^+ and Cs^+ ratio to replace the MA^+ in the tin-lead mixed perovskite composition, the PTAA/perovskite interface is adjusted and an efficiency of 10 % at MPP for MA^+-free and PEDOT:PSS-free tin-lead mixed perovskite solar cells is realized.

Furthermore, the lead content is further reduced by studying pure lead-free $FASnI_3$-based tin perovskite solar cells.
The SnF_2 additive is commonly used in tin-containing perovskite absorbers to improve solar cell performance. Here, the impact of the SnF_2 additive on the film formation and its distribution in the perovskite film is thoroughly investigated. A preferable accumulation of the SnF_2 at the PEDOT:PSS/perovskite interface was discovered by using ToF-SIMS measurements. An ultrathin SnS interlayer is formed as a result of a reaction of the accumulated SnF_2 with the underlying PEDOT:PSS, which has been verified the first time by combined detailed XPS and HAXPES studies. As SnS is a p-type semiconductor, this interlayer is assumed to improve the solar cell performance [211]. The new finding of the formed SnS interlayer could give a hint

towards the reason why PEDOT:PSS as HTL and the SnF_2 additive are crucial components for highly efficient Sn-based solar cells [9,80,96,99,196,197]. However, the hygroscopic and acidic PEDOT:PSS [116, 127–129] is commonly not favored as an HTL in lead perovskite solar cells. As the efficiency of 2.5 % with optimized SnF_2 amount is expected to be limited by unfavorable recombination and band mismatches [13, 103], HTL and ETL interfacial engineering was performed to optimize the solar cell device. Structural defects resulting from unfavorable perovskite growth are common for tin perovskite absorbers due to their fast crystallization [13]. This is generally addressed by applying challenging chemical engineering [80–84]. In this work, a simple strategy was implemented to observe pinhole-free perovskite film growth by altering the underlying HTL surface, covering it with an optimal amount of SiO_2-NP. This reduces defect states and thus non-radiative recombination in the perovskite film verified using comprehensive PL measurements. The median solar cell performance improved from 3.0 to 4.0 %. Furthermore, the conduction-band-mismatch at the perovskite/ETL interface is assumed to limit the V_{OC} in tin perovskite solar cells [13, 103]. Realizing V_{OC} values over 600 mV is still challenging for tin perovskite solar cells [103, 140]. Thus, aligning the conduction band to the perovskite band and, in consequence, yielding higher V_{OC} values, ETL with conduction bands of increased energy are investigated in this work. The ETL interface was modified by using multiple C_{60} derivatives to optimize the band alignment and to passivate the perovskite defects. Substituting the commonly used PCBM by ICBA and bis-PCBM with a LUMO of higher energy is assumed to improve conduction-band alignment to the perovskite layer because of accomplished increased V_{OC} values. Further, improved perovskite defect passivation is observed with ICBA as ETL. However, the reduced intrinsic electron mobility, especially of the bis-PCBM, is expected to limit the solar cell efficiency increase. The overall interface engineering increases the solar cell efficiency from 3.0 % to 5.6 % in the median, with nearly doubling the V_{OC} to 650 mV for the devices with SiO_2-NP and ICBA. Nonetheless, the V_{OC} losses are still high, considering that the $FASnI_3$ has band-gap energy of 1.4 eV. It is expected that recombination at interfaces and in the bulk is still dominant. Thus, alternative charge layers with suitable band alignment and sufficient intrinsic mobility should be explored. Further, a strategy to reduce the defect density in the perovskite bulk is a part of further investigations in this work.
A higher crystalline ordering and thus reduced crystal defects acting as dark recombination states are generally achieved by 2D/3D mixed perovskite absorbers, which improve the solar cell performance [9,74,77,82–93,96,97,150,196,213,260–264]. Thus in this work, the impact of different 2D PEA_2SnI_4 : 3D $FASnI_3$ on the perovskite crystalline phase was unraveled by XRD studies. The strongest phase texturing is observed for a 2D ratio of 7.5 % (compared to total perovskite molarity). The strong crystal perovskite texturing indeed results in an improved solar cell efficiency from 2.8 % for the 3D perovskite to 4.3 % for the 2D/3D mixed perovskite in the median with a slight increase of V_{OC} from 350 to 420 mV. Replacing of PCBM by ICBA resulted in a better band alignment and defect passivation. As a result, the efficiency improved further to 5.2 %.
In summary, the optimization strategies lead to a solar cell performance of up to 6.6 % for the $FASnI_3$-based perovskite solar cells in this work.

Realizing stable tin-containing perovskite solar cells is one of the main challenges as tin oxidizes fast. Nevertheless, only a few reports have systematically explored the stability of tin-containing perovskite absorbers to understand the dominant degradation mechanism. Especially, thermal stress has not been investigated in detail so far to the best of my knowledge [140]. In this work, the

degradation processes in the ambient atmosphere (22±1°C, 30-45 rH%) and under thermal stress (85°C, nitrogen atmosphere) for pure tin and tin-lead mixed perovskites were explored. Identical solar cell stacks were chosen to achieve comparability (ITO/PEDOT:PSS/SiO_2-NP/perovskite /PCBM/BCP/Ag).
A high reactivity for tin-containing perovskite films in the ambient atmosphere was verified. However, the efficiency losses of the solar cells are assumed to be dominated by charge and electrode deterioration, rather than the perovskite itself due to material intermixing by ion migration. Moreover, the sensitivity to oxygen and moisture is more critical for pure tin than tin-lead mixed perovskite absorbers. Nevertheless, the high reactivity highlights the necessity for oxygen- and moisture-free preparation and encapsulation, as well as for preparation materials for tin-containing perovskite solar cells. The hygroscopic PEDOT:PSS as HTL used in this work, seems to impact the stability negatively.
Aging by thermal stress (85°C) in an inert atmosphere was performed to achieve insights into the thermal operation stability and to accelerate the degradation in inert condition. Even if no degradation for tin-containing perovskite films was observed for six hours, their analogous devices deteriorate fast by material intermixing due to assumed ion migration.
As for both stress conditions, material intermixing due to ion migration from the perovskite seems to limit their stability, optimized device stacks should be explored in the future, preventing ion migration. This work provides a first insight into the short-term stability of tin-containing perovskites. However, further tests with additional stress parameters (light, electrical bias) and prolonged, cycled tests should be performed to gain an overview of the dominant degradation mechanism in tin-containing perovskite solar cells.

Based on investigating tin-containing perovskite solar cells, PEDOT:PSS as HTL seems to be controversial. PEDOT:PSS should be avoided in terms of its negative impact on device stability. It was also discovered that replacing PEDOT:PSS with other HTLs is not trivial, as shown for the tin-lead mixed perovskite solar cells. Moreover, the interaction of the PEDOT:PSS with the SnF_2 additive is crucial for the formation of the (beneficial) ultrathin SnS interlayer. Thus, substituting PEDOT:PSS is not straightforward, even though it seems to be necessary for stable devices.

As tin perovskite absorbers' human health and environmental impact are controversially reported [10, 11], a second substitution possibility for the lead was explored in this work. Bismuth perovskite-like absorbers were studied as being a non-toxic and environmentally friendly material example with high ambient stability.
A simple deposition method to yield dense and homogeneous $Cs_3Bi_2I_9$ films by gas quenching was implemented. Further, the procedure was modified by its post-treatment temperature tuning the film crystalline morphology. The deposited perovskite layers were incorporated into solar cell devices with confirmed solar cell characteristics. The developed perovskite morphology tuning improved solar cell performance.
As the high band-gap of 2.1 eV for the $Cs_3Bi_2I_9$ is unfavorable for single-junction devices, strategies to optimize the band-gap energy were explored. Theoretical calculations showed promising reduced band-gap energies of 1.5 eV (1.3 eV) by applying a split anion approach using sulfur (selenium) [136]. Unfortunately, the studied synthesis routes of these lower bang-gap materials did not reveal the desired products.

In this work, different strategies were examined to improve lead-alternative perovskite solar cells. The main highlights are shortly summarized below.
Device and perovskite composition optimization accomplished MA^+-free and PEDOT:PSS-alternative tin-lead mixed perovskite solar cells with a 10 % efficiency. A new (additional) unique mechanism of the commonly used SnF_2 was discovered by thoroughly investigating the $FASnI_3$ perovskite film and its interfaces. A high solar cell efficiency of up to 6.6 % was achieved for the $FASnI_3$-based perovskite solar cells by developing perovskite interfaces and perovskite crystal texturing. First stability analysis of tin-containing perovskite absorbers highlighted the necessity of oxygen- and moisture-free preparation and operation, especially PEDOT:PSS was verified to be detrimental. Further material intermixing by ion migration in and out of the perovskite seems to harm the solar cell devices in an ambient atmosphere and under thermal stress.
For the lead-alternative Bismuth, a deposition procedure for homogeneous and dense $Cs_3Bi_2I_9$ perovskite deposition was implemented and solar cell characteristics were verified for these perovskite films.

Conclusion

The studied lead-alternative perovskite absorbers demonstrate the compromise (up to now) made between the impact on human health and the environment, and solar cell performance.
Tin-containing perovskite absorbers are highly promising as lead-alternatives due to their high solar cell performances. However, for tin-lead mixed perovskite absorbers the lead content is only reduced. Further, the impact of tin perovskites on human health and the environment is controversially reported and has been poorly explored up to now, making their sustainability uncertain.
On the other hand, the alternative bismuth-based perovskite absorbers are highly sustainable, but achieve unsatisfying solar cell performance.

Nevertheless, tin-containing perovskite absorbers should be further investigated as these are the most promising lead-alternative perovskite absorbers (up to now) regarding their solar cell performances.
Tin-lead mixed perovskites combine the advantage of a decreased amount of lead and outstanding low band-gap energies for perovskite absorbers. Thus these absorbers can be used in perovskite-perovskite tandem devices with decreased lead content.
Tin-based perovskite solar cells are promising lead-free perovskite absorbers. As shown in this work, they achieve promising solar cell efficiency and seem to be intrinsically stable (dark storage in an inert atmosphere). Moreover, there has been an enormous progress in solar cell efficiency in the last few years [100] with a perspective for further improvements.
The challenging high reactivity in the ambient atmosphere can be solved by preparing and encapsulating tin-containing perovskite solar cells in an inert atmosphere.

Bismuth perovskite-like absorbers are promising as they are considered to have no impact on human health and the environment, and achieve a high ambient stability. However, solar cell performances still suffer from high exciton binding energies and high band-gap energies. Thus, application in solar cell devices has less relevance. Applications in other technologies like photodetectors, memory devices, or photocatalysis should be considered, too.

Outlook

The results of this work show that tin-containing perovskite absorbers are potential candidates for lead-alternative perovskites. Significant improvements have been made in realizing PEDOT:PSS-alternative and MA^+-free tin-lead mixed perovskite solar cells with 10 % efficiency, as well as using interfacial and perovskite engineering in tin perovskite solar cells accomplishing an efficiency of up to 6.6 %. Nevertheless, commercializing this technology will require further research and improvements in addition to this work.

As the main application for tin-lead mixed absorbers is assumed to be in tandem devices, perovskite composition tuning should be further explored to observe suitable band-gap energies. For tin perovskite solar cells, their PCE has to be further increased to be competitive in the solar market. The main limitations are expected to be recombination losses and rapid tin oxidation. Further, (long-term) stability tests need to be performed for tin-containing perovskite solar cells to understand the dominant degradation mechanism and to suppress tin oxidation. Based on the unraveled degradation mechanism, stable devices can be explored, including effective encapsulation techniques.

Besides these optimization strategies, for overall commercialization in the future, tin perovskite's impact on human health and the environment needs to be analyzed to estimate its risk.
Further, modules fabrication procedures need to be investigated for these lead-alternative perovskite absorbers. These would include large-area deposition and serial interconnection design. The general and also in this work used deposition process, spin coating, and the anti-solvent method cannot be scaled-up [265–267]. Thus, scaling-up deposition procedures, like blade- and slot-die coating, should be explored simultaneously with the overall optimization of lead-alternative perovskite solar cells on a small scale in order to solve challenges early and thus be time-efficient [265–267].

When these requirements are fulfilled, I expect lead-alternative perovskite solar cells to play a significant role in developing new, renewable energy sources.

A Appendix

Appendix referring to chapter 3.1

In the following table all used chemicals and materials are summarized with their production company and purity.

Table A.1: Overview of the used chemicals and materials with their relevant material properties.

chemical or material	purity	manufacturing company	miscellaneous
Acetonitrile (ACN)	99.8 %, anhydrous	Sigma Aldrich	–
Ammonia	–	VWR	25 %
Anisole	dehydrated 99.7 %	Sigma Aldrich	–
BCP	99.95 %	Sigma Aldrich	–
bis-PCBM	>99.5 %	Ossila	–
BiI_3	99.999 %	Sigma Aldrich	–
CsI	>99.999 %	Sigma Aldrich	–
Dichlorobenzene (DCB)	99 %, anhydrous	Sigma Aldrich	–
DMF	99.8 %	Sigma Aldrich	–
DMSO	>99.9 %	Sigma Aldrich	–
Ethanol (EtOH)	anhydrous[1]	VWR	–
Formamidiniumiodide (FAI)	anhydrous >99 %	Sigma Aldrich	–
FTO deposited on glass	15 Ω/□	Sigma Aldrich	400-450 nm
Gold	99.99 %	EVOCHEM	–
ICBA	99.9 %	Sigma Aldrich	–
Isopropanol	99.5 %, anhydrous	Sigma Aldrich	–
ITO deposited on glass	12 Ω/□	Visiontek	150 nm
PbI_2	>99.99 %	TCI	–
Leadthiocyanate (PbSCN)	99.5 %	Sigma Aldrich	–
PCBM	99 %	Solenne, Sigma Aldrich	–
Phenethylammoniumiodide (PEAI)	98 %	Sigma Aldrich	–
PMMA	–	Sigma Aldrich	–
PTAA	–	–	–

[1] water content <0.0003 %

MAI	–	GreatCell Solar	–
PEDOT:PSS	–	Hereaus	–
Titanium(IV)isopropoxide	99.999 %	Sigma Aldrich	–
Tetraelthylorthosilicate (TEOS)	99.999 %	Sigma Aldrich	–
Silver	99.99 %	Chempur	–
SnF_2	99 %	Sigma Aldrich	–
SnI_2	99.999 %	Alfa Aesar	–
Spiro-OMeTAD	99 %	Sigma Aldrich	–

Synthesis of SiO_2-NP

Siliconoxid nanoparticles are synthesized via the Stöber process [168]. Nanoparticles with a diameter of 30 to 40 nm are synthesized from a stirring solution of 2.717 mL ethanol, 0.027 mL water, 0.101 mL ammonia at 30°C by fast adding 0.114 mL TEOS [169]. Before usage the stock suspension is generally diluted with ethanol to one third of the original concentration.

Appendix referring to chapter 4.1

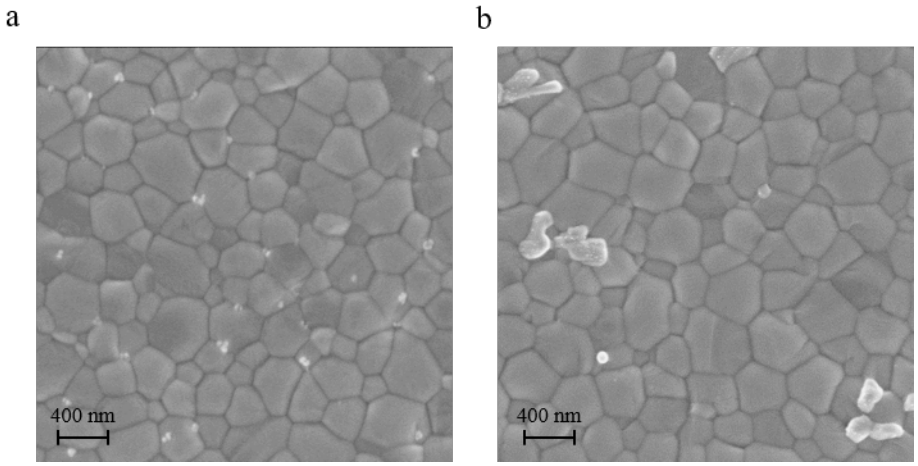

Figure A.1: SEM top-view images of MA^+-free tin-lead mixed perovskite ($FA_{0.915}Cs_{0.085}Sn_{0.5}Pb_{0.5}I_3$) films grown on PEDOT:PSS (a) and PTAA (b).

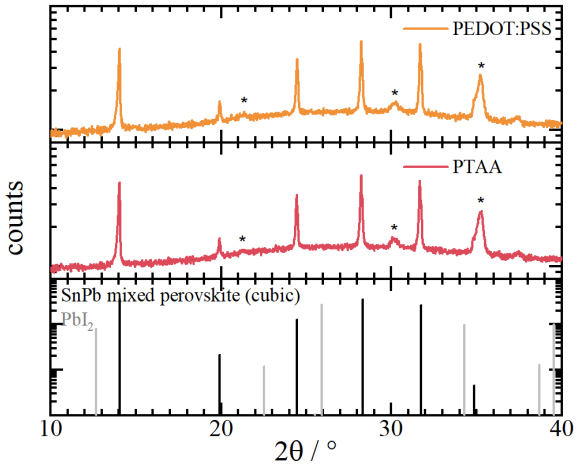

Figure A.2: XRD measurement of MA^+-free tin-lead mixed perovskite ($FA_{0.915}Cs_{0.085}Sn_{0.5}Pb_{0.5}I_3$) films grown on PEDOT:PSS and PTAA compared to XRD pattern of a cubic tin-lead mixed perovskite [184] and PbI_2 [185]. ITO reflexes are marked as *.

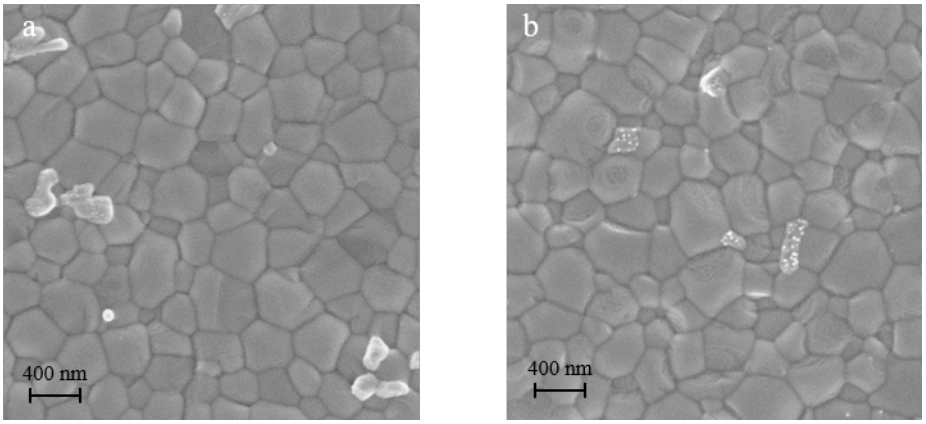

Figure A.3: SEM top-view images for analyzing the impact of Cs^+ amount on the perovskite morphology. a: $FA_{0.915}Cs_{0.085}Sn_{0.5}Pb_{0.5}I_3$ and b: $FA_{0.65}Cs_{0.35}Sn_{0.5}Pb_{0.5}I_3$ perovskite deposited on PTAA.

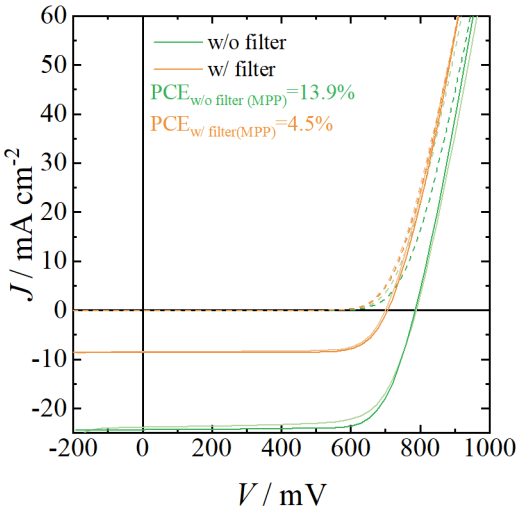

Figure A.4: Solar cell performance of a tin-lead mixed perovskite solar cells simulating it in a perovskite-perovskite tandem device. $J(V)$-curves of a tin-lead mixed perovskite solar cells measured without (green color) and with (orange color) filtered light intensity by 1.77 nm band-edge filter. The band-edge filter simulate a semitransparent top wide band-gap perovskite solar cell. The lighter colored curve displays the forward bias scan direction, the darker one the reverse direction. Dashed curves are dark measurements, while the solid lines represent measurements under illumination.

Appendix referring to chapter 4.2

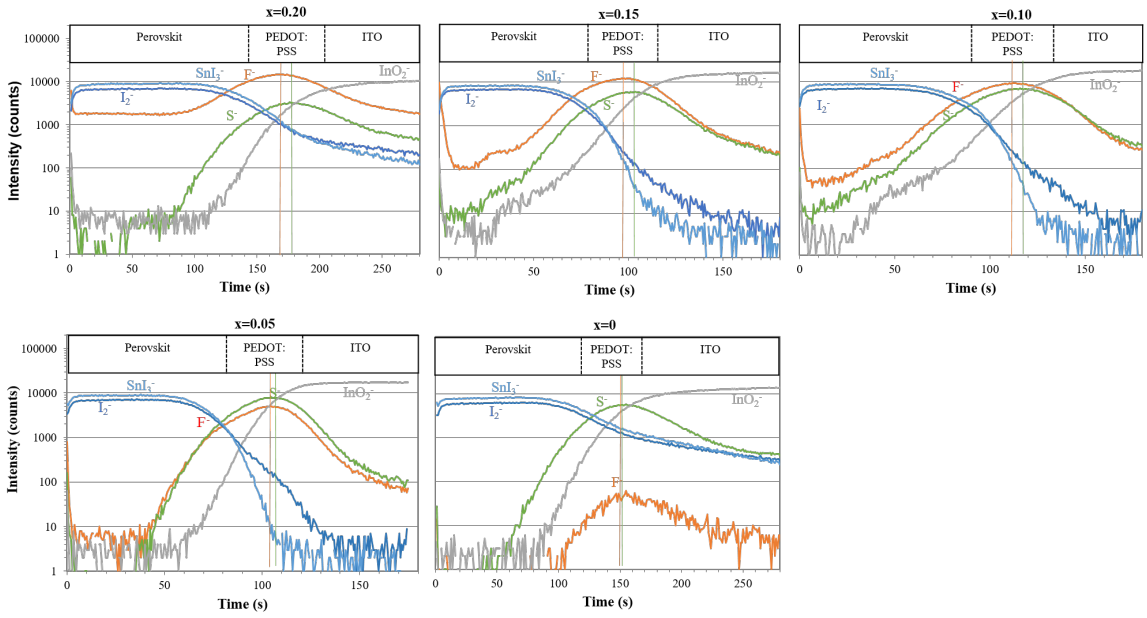

Figure A.5: ToF-SIMS depth profiles of ITO/PEDOT:PSS/$FASnI_3$ samples with different SnF_2 amounts (x = 0.00, x = 0.05, x = 0.10, x = 0.15, x = 0.20) modified from [198]. The layers (perovskite, PEDOT:PSS, ITO) are marked for enhanced clarity. The maxima of the ions F^- and S^- corresponding to the SnF_2 and PEDOT:PSS are highlighted by vertical lines. Measurements were performed in the delayed-extraction-mode using Bi^+ ions as the analysis beam and Cs^+ for sputtering.

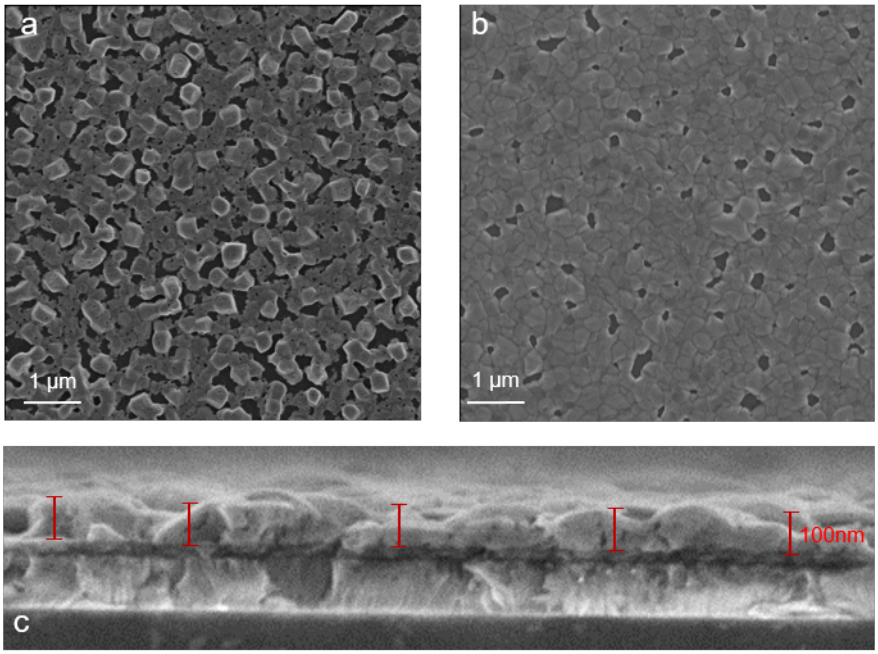

Figure A.6: SEM images of analyzed ITO/PEDOT:PSS/$FASnI_3$ samples by HAXPES and XPS taken from [198]. These were fabricated by a lower perovskite precursor solution ($c_{\text{perovskite}}$ = 0.4M). a: Top-view image of the sample without SnF_2 additive, b: Top-view image of the sample with SnF_2 additive. c: Cross-section images of the sample with SnF_2 additive, illustrating the maximal perovskite thickness of 100 nm and significant thickness fluctuations.

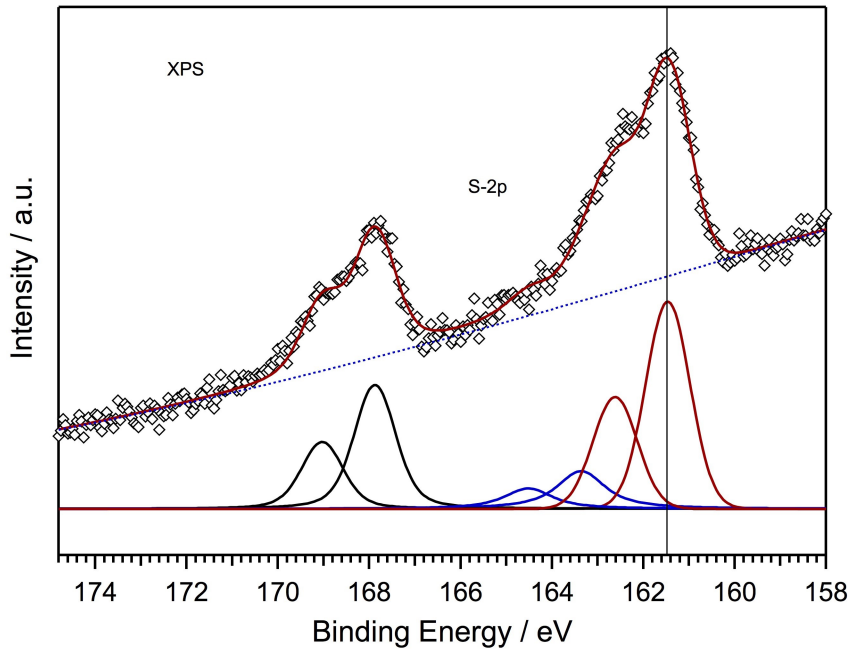

Figure A.7: Sulfur-2p core level fit of XPS data shown in figure 4.18. black: contribution of the PSS, blue: of the PEDOT and red: of the formed SnS interlayer.

Strohmeier equation for determining the 1.2 nm SnS interlayer thickness [206]:

$$d_{SnS} = \lambda_{SnS} \sin\Theta \log\left(\frac{I_{SnS}\,\lambda_{PEDOT:PSS}\,N_{PEDOT:PSS}}{I_{PEDOT:PSS}\,\lambda_{SnS}\,N_{SnS}} + 1\right) \tag{A.1}$$

with λ the inelastic mean free path, θ the electron take-off angle, N volume density, I intensity ratio of photoelectron peaks.

Table A.2: Values for determining the SnS layer thickness of 1.2 nm with the strohmeier equation.

material	density / g cm^{-3}	molar mass / g mol^{-1}	N / mol cm^{-3}	λ / nm	I
PEDOT:PSS (1:4.1)	1.44 [268]	171.52	0.0084	3.6 [202]	5.1
SnS	5.08 [211]	150.76	0.034	2.4 [202]	9.1

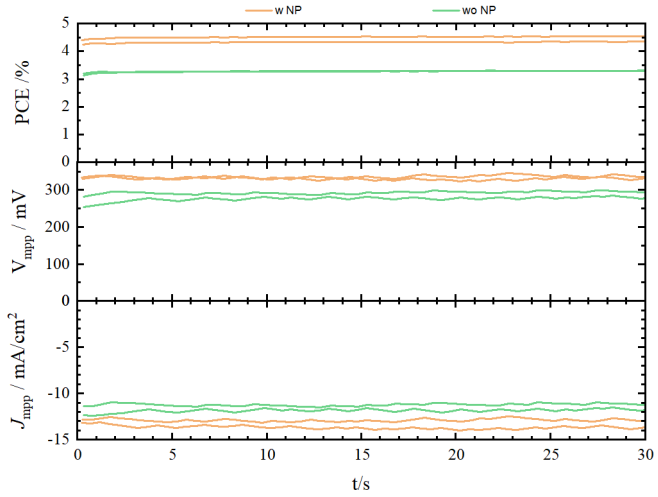

Figure A.8: Exemplary MPP tracking for two solar cells each with and without inserted NP in the device stack for characterizing the performance stability.

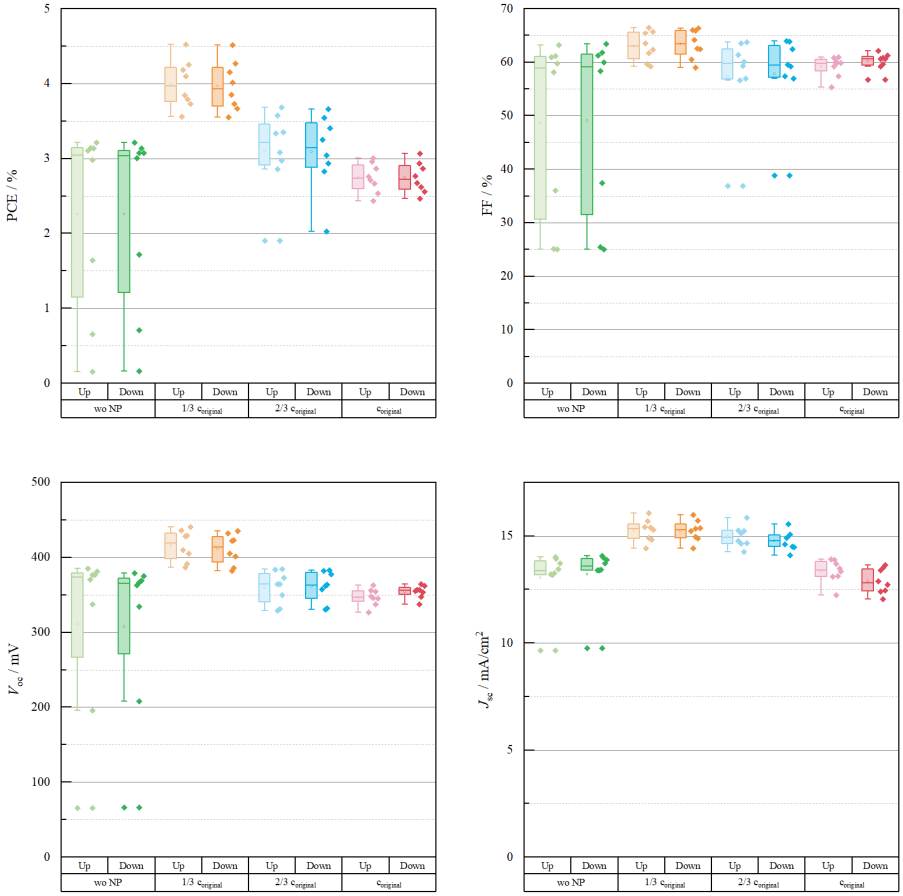

Figure A.9: Additional analysis of the NP solution concentration influencing the NP coverage density on the solar cell performance.

Appendix referring to chapter 4.3

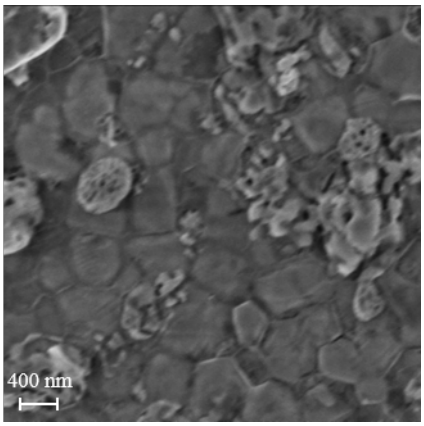

Figure A.10: SEM top-view image of a tin perovskite film degraded in ambient condition for 26 hours.

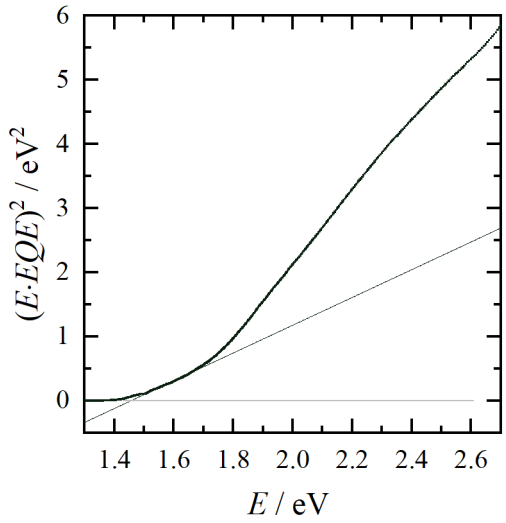

Figure A.11: Tauc-plot of the as-grown $FASnI_3$ perovskite film.

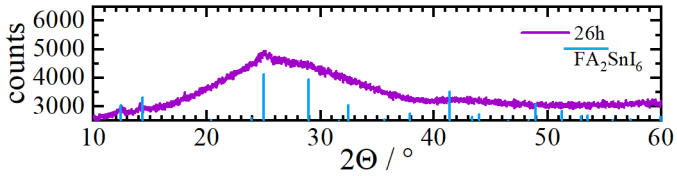

Figure A.12: XRD pattern of tin perovskite absorbers stored in ambient conditions for 26 hours compared to a FA_2SnI_6 reference pattern [269].

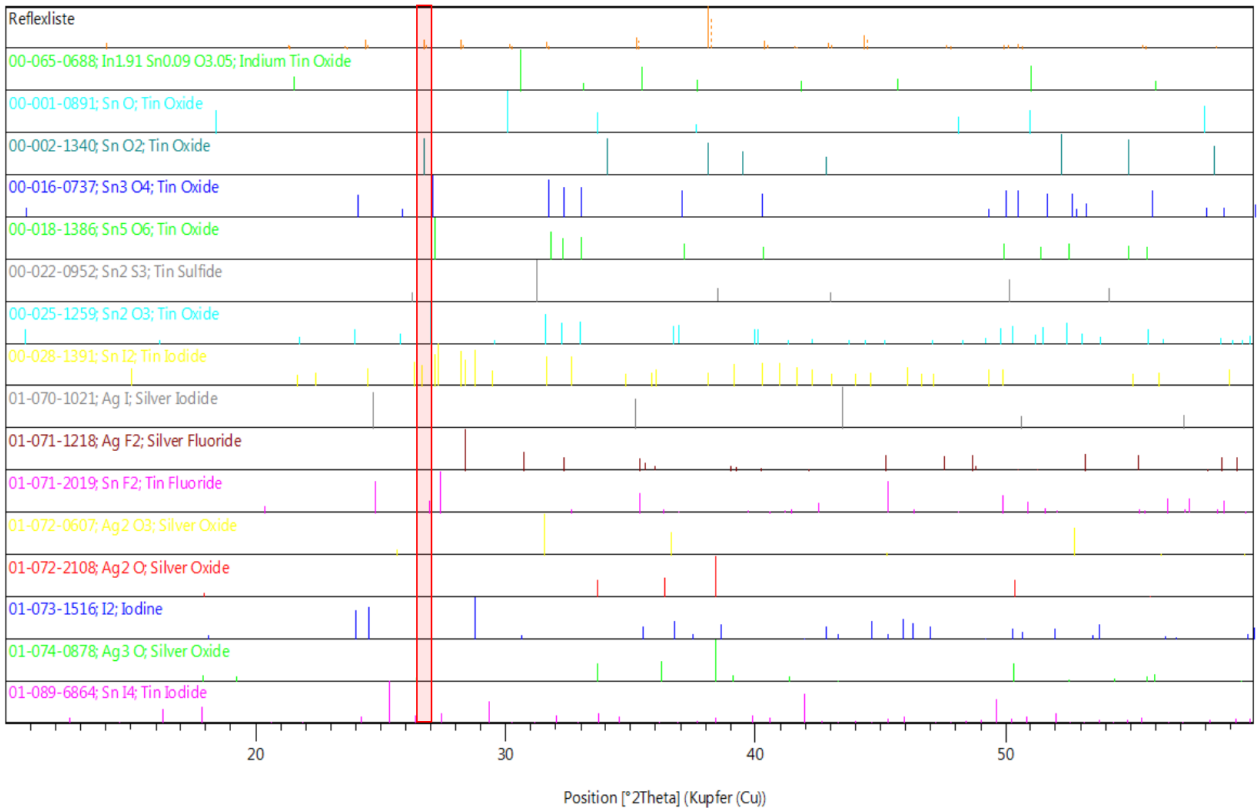

Figure A.13: Exemplary comparison of measured XRD of the tin perovskite solar cell stressed for 96.5 hours in ambient conditions to possible degradation product patterns (SiO_2, Sn_5O_6, SnF_2, SnI_4, SI_2, Sn_2S_3, AgI, AgF_2, Ag_2O_3, Ag_3O, Ag_2O, SnO_2, Sn_3O_4, Sn_2O_3, SnO, I_2).

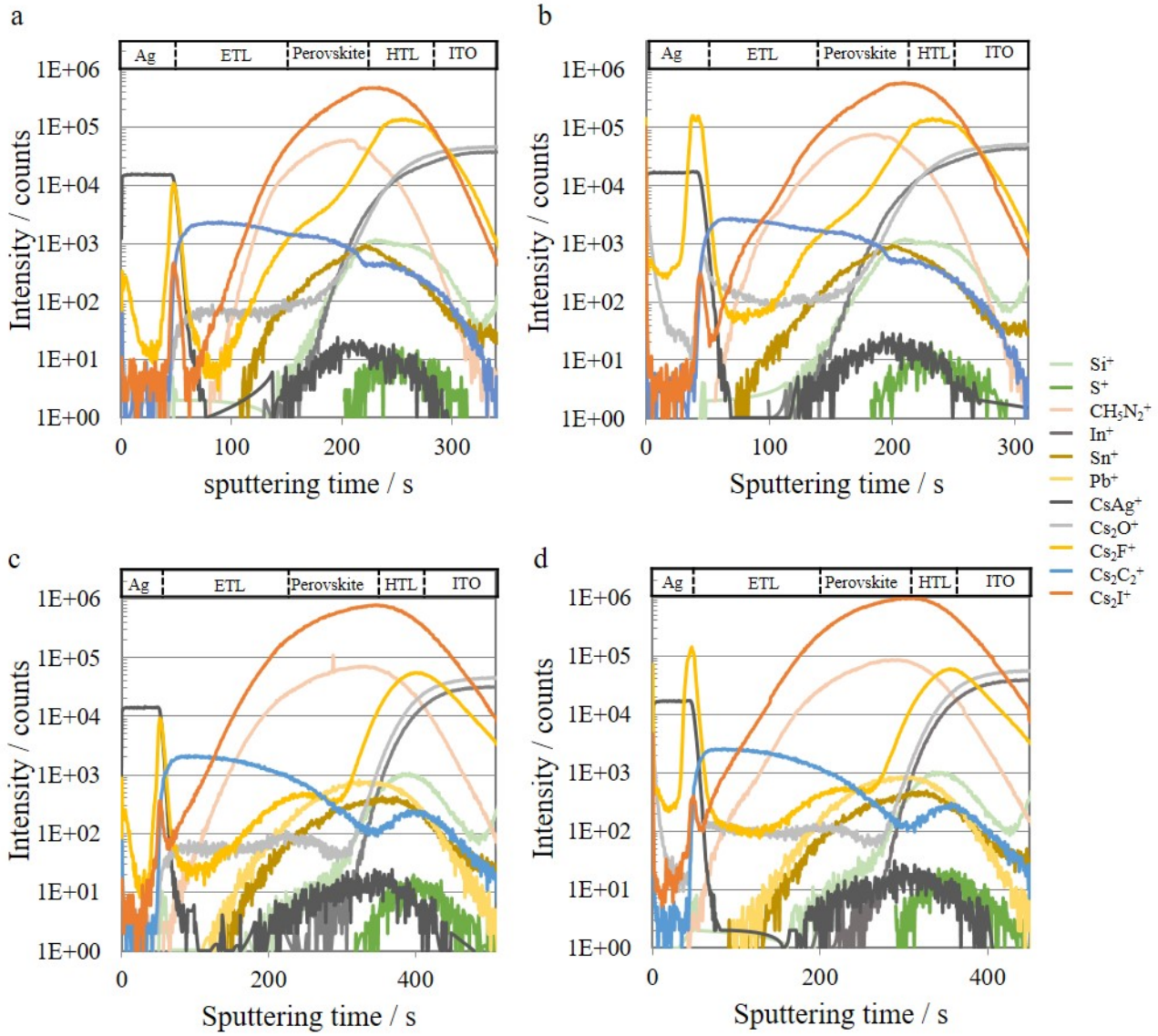

Figure A.14: Impact of degradation after 40 hours in ambient condition of perovskite solar cells on ion distribution throughout the full perovskite solar cell stack. Comparative ToF-SIMS depth profile of tin (a,b) and tin-lead mixed (c,d) perovskite solar cells of fresh (a,c) and stressed (b,d) samples. In difference to figure 4.44, here all relevant ions for displaying each layer in the solar cell stack are shown. Measurements were performed in the spectrometry-mode using Bi_3^+ ions as the analysis beam and Cs^+ for sputtering.

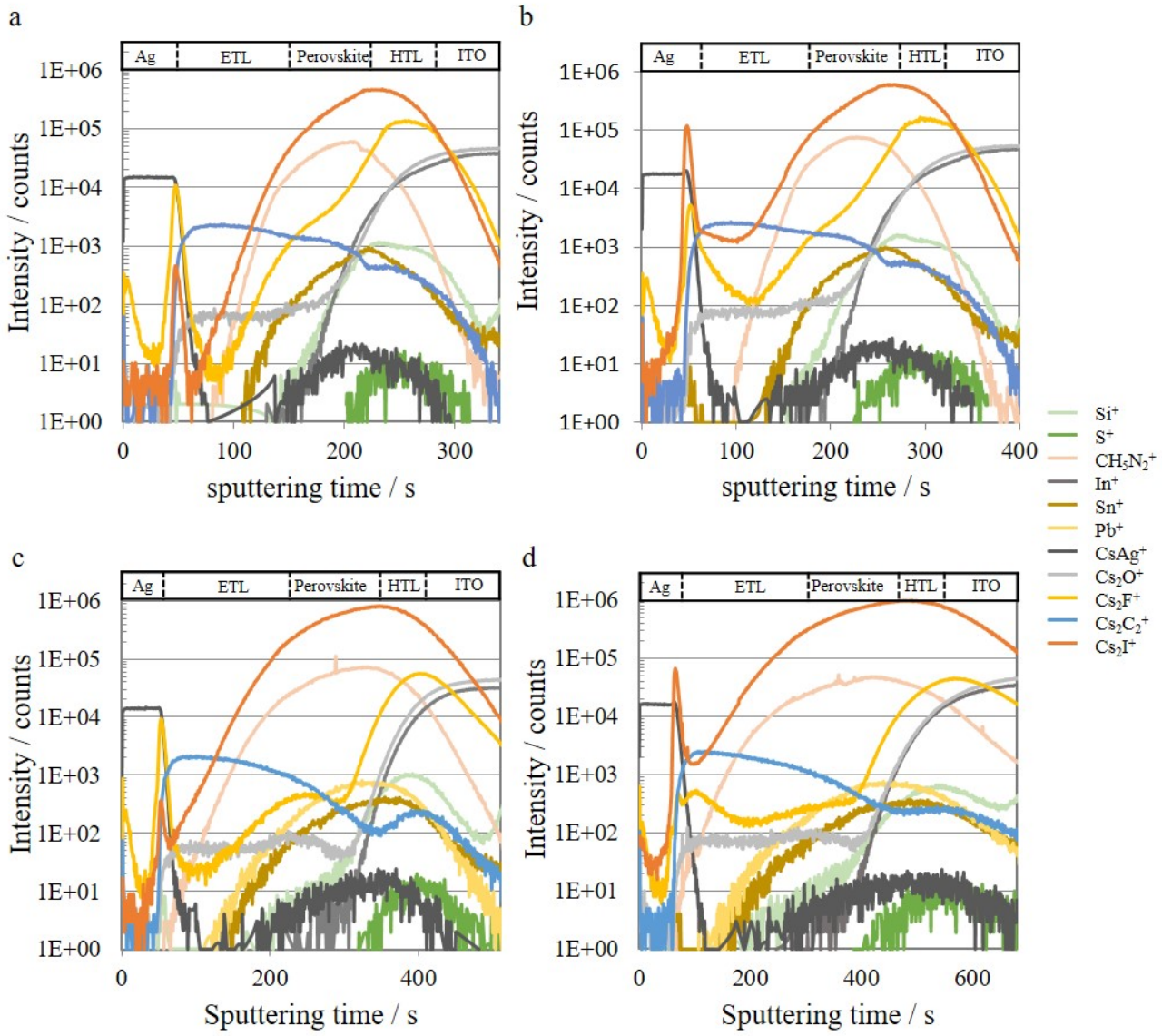

Figure A.15: Impact of temperature stress of 85°C for 2 hours on ion distribution throughout the full perovskite solar cell stack. Comparative ToF-SIMS depth profile of tin (a,b) and tin-lead mixed (c,d) perovskite solar cells of fresh (a,c) and stressed (b,d) samples. In difference to figure 4.51, here all relevant ions for displaying each layer in the solar cell stack are shown. Measurements were performed in the spectrometry-mode using Bi_3^+ ions as the analysis beam and Cs^+ for sputtering.

Appendix referring to chapter 5

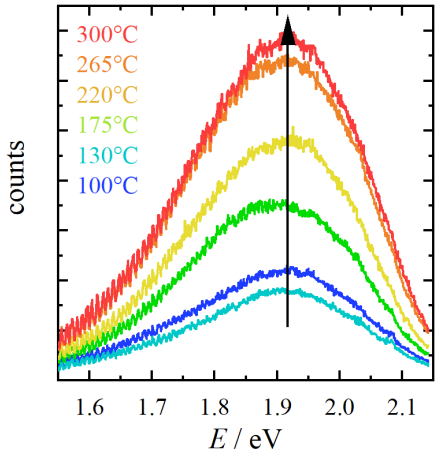

Figure A.16: PL study of $Cs_3Bi_2I_9$ perovskite absorbers deposited on FTO/TiO_2 samples annealed at different temperatures for 20 minutes.

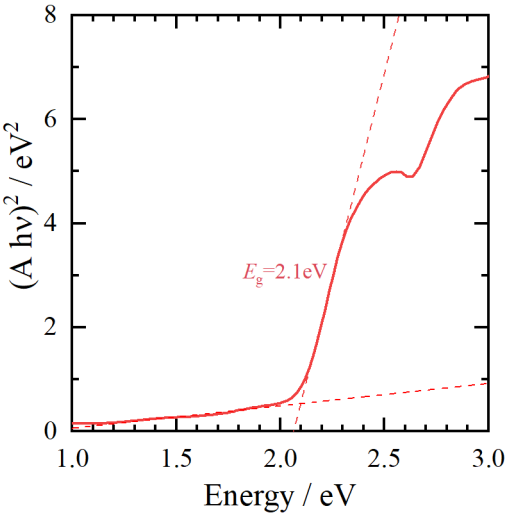

Figure A.17: Tauc-plot to illustrate the estimated band-gap energies for the $Cs_3Bi_2I_9$ perovskite films.

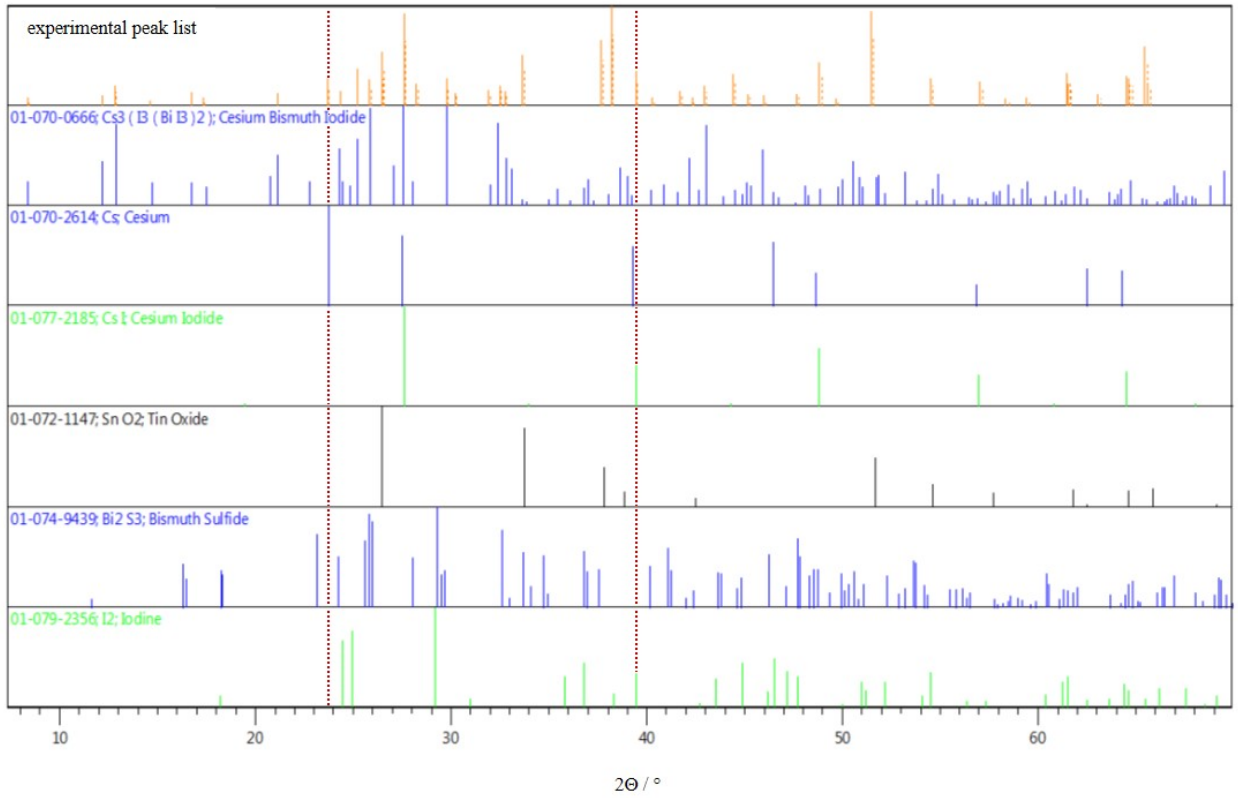

Figure A.18: Extracted peaks for the measured XRD pattern of the perovskite film with added $Bi(xt)_3$. The perovskite film here was fabricated in stoichiometric amounts of the precursor materials as suggested by the reaction equation 5.2 ($Bi(xt)_3$:BiI_3:CsI 2:1:3). The observed peak list is compared to the reference pattern of $Cs_3Bi_2I_9$, Cs, CsI, SnO_2, bismuthsulfide (Bi_2S_3) and I_2. The two peaks at 23.8° and 39.4°, which can not be assigned to the perovskite phase, are highlighted by vertical lines.

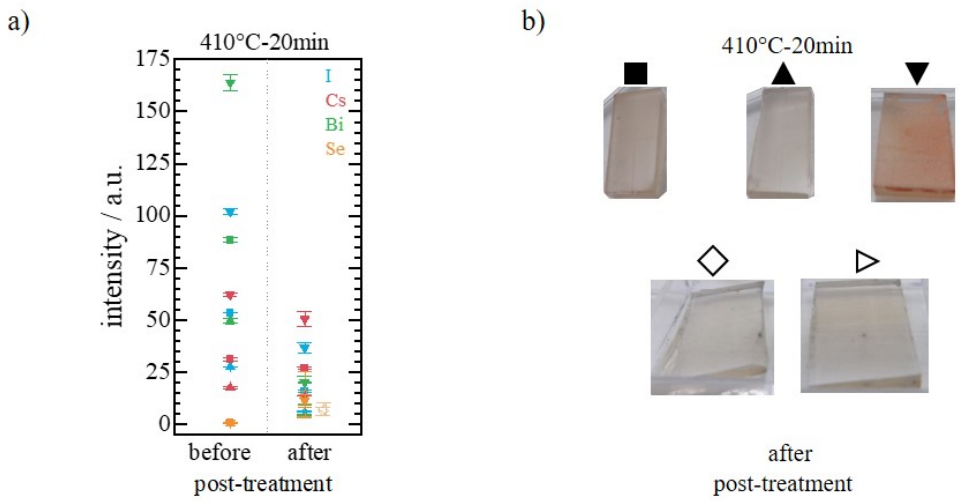

Figure A.19: a: Uncalibrated XRF intensity, reflecting changes in the composition of selenized $Cs_3Bi_2I_9$ perovskite samples (filled symbols) and pristine FTO/TiO_2- samples (unfilled symbols) at a post-treatment temperatures of 410°C for 20 minutes. b: Top-view images of the decomposed samples after the post-treatment at 410°C for 20 minutes for the perovskite samples (top row) and the pristine FTO substrates (bottom row).

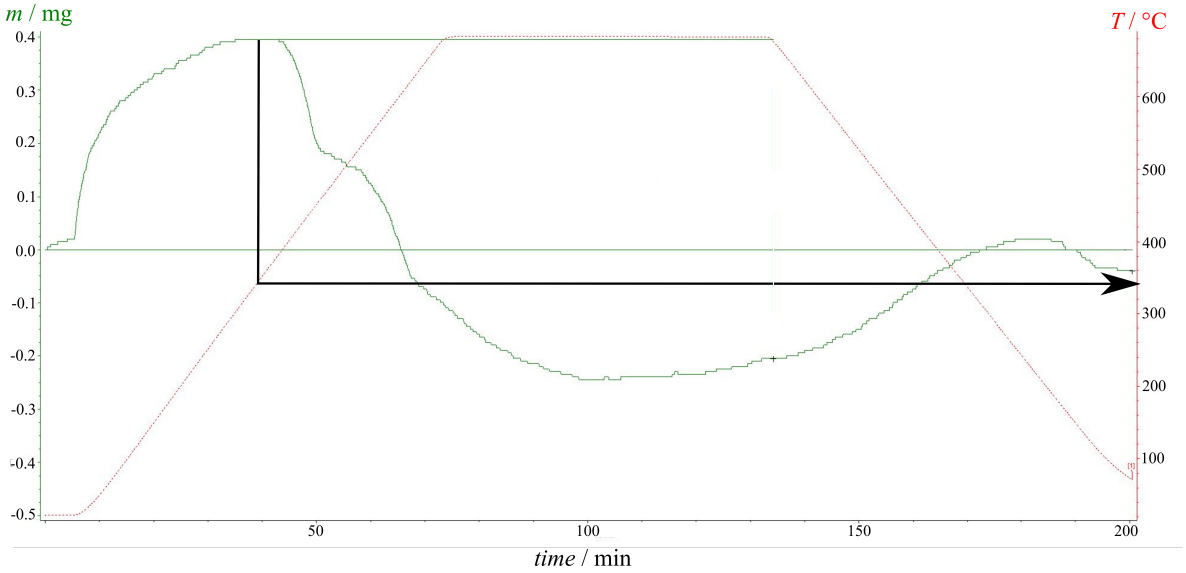

Figure A.20: Thermogravimetric analysis of a $Cs_3Bi_2I_9$ film for analyzing the decomposition temperature. Here shown are the mass loss in green and the temperature ramp in red during the measurement process. The black arrow highlights the mass loss of the sample after 38 minutes of heating at a temperature of 340°C. This indicates the decomposition process of the $Cs_3Bi_2I_9$ film starts at 340°C forming volatile products leading to a lighter mass of the sample.

Bibliography

[1] European Union, "Paris Agreement," https://ec.europa.eu/clima/policies/international/negotiations/paris_en#tab-0-0, accessed: 22 September 2021.

[2] European Union, "Proposal for a DIRECTIVE OF THE EUROPEAN PARLIAMENT AND OF THE COUNCIL amending Directive (EU) 2018/2001 of the European Parliament and of the Council, Regulation (EU) 2018/1999 of the European Parliament and of the Council and Directive 98/70/EC of the European Parliament and of the Council as regards the promotion of energy from renewable sources, and repealing Council Directive (EU)."

[3] National Renewable Energy Laboratory, "Best Research-Cell Efficiencies," https://www.nrel.gov/pv/assets/pdfs/best-research-cell-efficiencies-rev211117.pdf, accessed: 22 November 2021.

[4] M. Powalla, S. Paetel, E. Ahlswede, R. Wuerz, C. D. Wessendorf, and T. Magorian Friedlmeier, "Thin–film solar cells exceeding 22% solar cell efficiency: An overview on CdTe-, Cu(In,Ga)Se_2 -, and perovskite-based materials," *Applied Physics Reviews*, vol. 5, no. 4, p. 041602, 2018.

[5] A. L. Wani, A. Ara, and J. A. Usmani, "Lead toxicity: a review," *Interdisciplinary toxicology*, vol. 8, no. 2, pp. 55–64, 2015.

[6] European Union, "DIRECTIVE 2011/65/EU OF THE EUROPEAN PARLIAMENT AND OF THE COUNCIL of 8 June 2011 on the restriction of the use of certain hazardous substances in electrical and electronic equipment," 22.09.2021.

[7] A. Abate, "Perovskite Solar Cells Go Lead Free," *Joule*, vol. 1, no. 4, pp. 659–664, 2017.

[8] K. Xiao, R. Lin, Q. Han, Y. Hou, Z. Qin, H. T. Nguyen, J. Wen, M. Wei, V. Yeddu, M. I. Saidaminov, Y. Gao, X. Luo, Y. Wang, H. Gao, C. Zhang, J. Xu, J. Zhu, E. H. Sargent, and H. Tan, "All-perovskite tandem solar cells with 24.2% certified efficiency and area over 1 cm^2 using surface-anchoring zwitterionic antioxidant," *Nature Energy*, no. 1, pp. 1–11, 2020.

[9] B.-B. Yu, Z. Chen, Y. Zhu, Y. Wang, B. Han, G. Chen, X. Zhang, Z. Du, and Z. He, "Heterogeneous 2D/3D Tin-Halides Perovskite Solar Cells with Certified Conversion Efficiency Breaking 14," *Advanced Materials*, p. e2102055, 2021.

[10] A. Babayigit, D. Duy Thanh, A. Ethirajan, J. Manca, M. Muller, H.-G. Boyen, and B. Conings, "Assessing the toxicity of Pb- and Sn-based perovskite solar cells in model organism Danio rerio," *Scientific Reports*, vol. 6, p. 18721, 2016.

[11] J. Li, H.-L. Cao, W.-B. Jiao, Q. Wang, M. Wei, I. Cantone, J. Lü, and A. Abate, "Biological impact of lead from halide perovskites reveals the risk of introducing a safe threshold," *Nature Communications*, vol. 11, no. 1, p. 310, 2020.

[12] L. Lanzetta, N. Aristidou, and S. A. Haque, "Stability of Lead and Tin Halide Perovskites: The Link between Defects and Degradation," *The Journal of Physical Chemistry Letters*, vol. 11, no. 2, pp. 574–585, 2020.

[13] B. Li, B. Chang, L. Pan, Z. Li, L. Fu, Z. He, and L. Yin, "Tin-Based Defects and Passivation Strategies in Tin-Related Perovskite Solar Cells," *ACS Energy Letters*, pp. 3752–3772, 2020.

[14] H. Suzuki and Y. Matano, eds., *Organobismuth chemistry*. Amsterdam: Elsevier Science, 1. ed. ed., 2001.

[15] S. Attique, N. Ali, S. Ali, R. Khatoon, N. Li, A. Khesro, S. Rauf, S. Yang, and H. Wu, "A Potential Checkmate to Lead: Bismuth in Organometal Halide Perovskites, Structure, Properties, and Applications," *Advanced science (Weinheim, Baden-Wurttemberg, Germany)*, vol. 7, no. 13, p. 1903143, 2020.

[16] F. Bai, Y. Hu, Y. Hu, T. Qiu, X. Miao, and S. Zhang, "Lead-free, air-stable ultrathin $Cs_3Bi_2I_9$ perovskite nanosheets for solar cells," *Solar Energy Materials and Solar Cells*, vol. 184, pp. 15–21, 2018.

[17] M. B. Johnston and L. M. Herz, "Hybrid Perovskites for Photovoltaics: Charge-Carrier Recombination, Diffusion, and Radiative Efficiencies," *Accounts of Chemical Research*, vol. 49, no. 1, p. 146, 2016.

[18] L. M. Herz, "Charge-Carrier Mobilities in Metal Halide Perovskites: Fundamental Mechanisms and Limits," *ACS Energy Letters*, vol. 2, no. 7, pp. 1539–1548, 2017.

[19] F. Ruf, M. F. Aygüler, N. Giesbrecht, B. Rendenbach, A. Magin, P. Docampo, H. Kalt, and M. Hetterich, "Temperature-dependent studies of exciton binding energy and phase-transition suppression in (Cs,FA,MA)$Pb(I,Br)_3$ perovskites," *APL Materials*, vol. 7, no. 3, p. 031113, 2019.

[20] S. de Wolf, J. Holovsky, S.-J. Moon, P. Löper, B. Niesen, M. Ledinsky, F.-J. Haug, J.-H. Yum, and C. Ballif, "Organometallic Halide Perovskites: Sharp Optical Absorption Edge and Its Relation to Photovoltaic Performance," *The Journal of Physical Chemistry Letters*, vol. 5, no. 6, pp. 1035–1039, 2014.

[21] S. D. Stranks, G. E. Eperon, G. Grancini, C. Menelaou, M. J. P. Alcocer, T. Leijtens, L. M. Herz, A. Petrozza, and H. J. Snaith, "Electron-hole diffusion lengths exceeding 1 micrometer in an organometal trihalide perovskite absorber," *Science*, vol. 342, no. 6156, pp. 341–344, 2013.

[22] B.-W. Park, B. Philippe, S. M. Jain, X. Zhang, T. Edvinsson, H. Rensmo, B. Zietz, and G. Boschloo, "Chemical engineering of methylammonium lead iodide/bromide perovskites: tuning of opto-electronic properties and photovoltaic performance," *Journal of Materials Chemistry A*, vol. 3, no. 43, pp. 21760–21771, 2015.

[23] C. M. Sutter-Fella, Y. Li, M. Amani, J. W. Ager, F. M. Toma, E. Yablonovitch, I. D. Sharp, and A. Javey, "High Photoluminescence Quantum Yield in Band Gap Tunable Bromide Containing Mixed Halide Perovskites," *Nano Letters*, vol. 16, no. 1, pp. 800–806, 2016.

[24] F. Hao, C. C. Stoumpos, R. P. H. Chang, and M. G. Kanatzidis, "Anomalous band gap behavior in mixed Sn and Pb perovskites enables broadening of absorption spectrum in solar cells," *Journal of the American Chemical Society*, vol. 136, no. 22, pp. 8094–8099, 2014.

[25] G. Rose, "Beschreibung einiger neuen Mineralien des Urals," *Annalen der Physik*, vol. 124, no. 12, pp. 551–573, 1839.

[26] D. Weber, "$CH_3NH_3SnBr_xI_{3-x}$ (x = 0-3), ein Sn(II)-System mit kubischer Perowskitstruktur / $CH_3NH_3SnBr_xI_{3-x}$ (x = 0-3), a Sn(II)-System with Cubic Perovskite Structure," *Zeitschrift für Naturforschung B*, vol. 33, no. 8, pp. 862–865, 1978.

[27] A. Kojima, K. Teshima, Y. Shirai, and T. Miyasaka, "Organometal Halide Perovskites as Visible-Light Sensitizers for Photovoltaic Cells," *Journal of the American Chemical Society*, vol. 131, no. 7, pp. 6050–6051, 2009.

[28] K. Frohna and S. D. Stranks, "Hybrid perovskites for device applications," in *Handbook of Organic Materials for Electronic and Photonic Devices*, pp. 211–256, Elsevier, 2019.

[29] A. K. Jena, A. Kulkarni, and T. Miyasaka, "Halide Perovskite Photovoltaics: Background, Status, and Future Prospects," *Chemical Reviews*, vol. 119, no. 5, pp. 3036–3103, 2019.

[30] J. Y. Kim, J.-W. Lee, H. S. Jung, H. Shin, and N.-G. Park, "High-Efficiency Perovskite Solar Cells," *Chemical Reviews*, vol. 120, no. 15, pp. 7867–7918, 2020.

[31] V. M. Goldschmidt, "Die Gesetze der Krystallochemie," *Die Naturwissenschaften*, vol. 14, no. 21, pp. 477–485, 1926.

[32] Z. Xiao and Y. Yan, "Progress in Theoretical Study of Metal Halide Perovskite Solar Cell Materials," *Advanced Energy Materials*, vol. 7, no. 22, p. 1701136, 2017.

[33] Q. Xu, D. Yang, J. Lv, Y.-Y. Sun, and L. Zhang, "Perovskite Solar Absorbers: Materials by Design," *Small Methods*, vol. 2, no. 5, p. 1700316, 2018.

[34] G. Kieslich, S. Sun, and A. K. Cheetham, "Solid-state principles applied to organic-inorganic perovskites: new tricks for an old dog," *Chemical Science*, vol. 5, no. 12, pp. 4712–4715, 2014.

[35] Z. Li, M. Yang, J.-S. Park, S.-H. Wei, J. J. Berry, and K. Zhu, "Stabilizing Perovskite Structures by Tuning Tolerance Factor: Formation of Formamidinium and Cesium Lead Iodide Solid-State Alloys," *Chemistry of Materials*, vol. 28, no. 1, pp. 284–292, 2016.

[36] Q. Wang, B. Chen, Y. Liu, Y. Deng, Y. Bai, Q. Dong, and J. Huang, "Scaling behavior of moisture-induced grain degradation in polycrystalline hybrid perovskite thin films," *Energy & Environmental Science*, vol. 10, no. 2, pp. 516–522, 2017.

[37] Y. Takahashi, R. Obara, Z.-Z. Lin, Y. Takahashi, T. Naito, T. Inabe, S. Ishibashi, and K. Terakura, "Charge-transport in tin-iodide perovskite $CH_3NH_3SnI_3$: origin of high conductivity," *Dalton Transactions*, vol. 40, no. 20, pp. 5563–5568, 2011.

[38] T. Baikie, Y. Fang, J. M. Kadro, M. Schreyer, F. Wei, S. G. Mhaisalkar, M. Graetzel, and T. J. White, "Synthesis and crystal chemistry of the hybrid perovskite $(CH_3NH_3)PbI_3$ for solid-state sensitised solar cell applications," *Journal of Materials Chemistry A*, vol. 1, no. 18, pp. 5628–5641, 2013.

[39] M. T. Weller, O. J. Weber, P. F. Henry, A. M. Di Pumpo, and T. C. Hansen, "Complete structure and cation orientation in the perovskite photovoltaic methylammonium lead iodide between 100 and 352 K," *Chemical communications (Cambridge, England)*, vol. 51, no. 20, pp. 4180–4183, 2015.

[40] Y. Kawamura, H. Mashiyama, and K. Hasebe, "Structural Study on Cubic–Tetragonal Transition of $CH_3NH_3PbI_3$," *Journal of the Physical Society of Japan*, vol. 71, no. 7, pp. 1694–1697, 2002.

[41] S. Kahmann, O. Nazarenko, S. Shao, O. Hordiichuk, M. Kepenekian, J. Even, M. V. Kovalenko, G. R. Blake, and M. A. Loi, "Negative Thermal Quenching in $FASnI_3$ Perovskite Single Crystals and Thin Films," *ACS Energy Letters*, vol. 5, no. 8, pp. 2512–2519, 2020.

[42] E. C. Schueller, G. Laurita, D. H. Fabini, C. C. Stoumpos, M. G. Kanatzidis, and R. Seshadri, "Crystal Structure Evolution and Notable Thermal Expansion in Hybrid Perovskites Formamidinium Tin Iodide and Formamidinium Lead Bromide," *Inorganic Chemistry*, vol. 57, no. 2, pp. 695–701, 2018.

[43] S. Tao, I. Schmidt, G. Brocks, J. Jiang, I. Tranca, K. Meerholz, and S. Olthof, "Absolute energy level positions in tin- and lead-based halide perovskites," *Nature Communications*, vol. 10, no. 1, p. 2560, 2019.

[44] P. Schulz, E. Edri, S. Kirmayer, G. Hodes, D. Cahen, and A. Kahn, "Interface energetics in organo-metal halide perovskite-based photovoltaic cells," *Energy & Environmental Science*, vol. 7, no. 4, p. 1377, 2014.

[45] R. Prasanna, A. Gold-Parker, T. Leijtens, B. Conings, A. Babayigit, H.-G. Boyen, M. F. Toney, and M. D. McGehee, "Band Gap Tuning via Lattice Contraction and Octahedral Tilting in Perovskite Materials for Photovoltaics," *Journal of the American Chemical Society*, vol. 139, no. 32, pp. 11117–11124, 2017.

[46] P. Würfel, *Physik der Solarzellen*. Spektrum-Hochschultaschenbuch, Heidelberg: Spektrum Akad. Verl., 2. [vollst. überarb.] aufl. ed., 2000.

[47] M. Ye, C. He, J. Iocozzia, X. Liu, X. Cui, X. Meng, M. Rager, X. Hong, X. Liu, and Z. Lin, "Recent advances in interfacial engineering of perovskite solar cells," *Journal of Physics D: Applied Physics*, vol. 50, no. 37, p. 373002, 2017.

[48] D. Yang, X. Zhou, R. Yang, Z. Yang, W. Yu, X. Wang, C. Li, S. Liu, and R. P. H. Chang, "Surface optimization to eliminate hysteresis for record efficiency planar perovskite solar cells," *Energy & Environmental Science*, vol. 9, no. 10, pp. 3071–3078, 2016.

[49] Q. Fu, X. Tang, B. Huang, T. Hu, L. Tan, L. Chen, and Y. Chen, "Recent Progress on the Long-Term Stability of Perovskite Solar Cells," *Advanced science (Weinheim, Baden-Wurttemberg, Germany)*, vol. 5, no. 5, p. 1700387, 2018.

[50] P.-W. Liang, C.-C. Chueh, S. T. Williams, and A. K.-Y. Jen, "Roles of Fullerene-Based Interlayers in Enhancing the Performance of Organometal Perovskite Thin-Film Solar Cells," *Advanced Energy Materials*, vol. 5, no. 10, p. 1402321, 2015.

[51] Y. Fang, C. Bi, D. Wang, and J. Huang, "The Functions of Fullerenes in Hybrid Perovskite Solar Cells," *ACS Energy Letters*, vol. 2, no. 4, pp. 782–794, 2017.

[52] Z. Hawash, L. K. Ono, and Y. Qi, "Recent Advances in Spiro–MeOTAD Hole Transport Material and Its Applications in Organic–Inorganic Halide Perovskite Solar Cells," *Advanced Materials Interfaces*, vol. 5, no. 1, p. 1700623, 2018.

[53] W. Han, G. Ren, J. Liu, Z. Li, H. Bao, C. Liu, and W. Guo, "Recent Progress of Inverted Perovskite Solar Cells with a Modified PEDOT:PSS Hole Transport Layer," *ACS Applied Materials & Interfaces*, vol. 12, no. 44, pp. 49297–49322, 2020.

[54] X. Zheng, Y. Hou, C. Bao, J. Yin, F. Yuan, Z. Huang, M. Wei, A. Y. Alsalloum, P. Maity, B. Turedi, C. Yang, F. Gao, E. H. Sargent, O. M. Bakr, K. Song, J. Liu, J. Troughton, N. Gasparini, C. Zhou, Y. Lin, D.-J. Xue, B. Chen, A. K. Johnston, N. Wei, M. N. Hedhili, D. Baran, T. D. Anthopoulos, Y. Han, Z.-H. Lu, O. F. Mohammed, and N. Research, "Managing grains and interfaces via ligand anchoring enables 22.3%-efficiency inverted perovskite solar cells," *Nature Energy*, pp. 1–2, 2017.

[55] X. Zheng, B. Chen, J. Dai, Y. Fang, Y. Bai, Y. Lin, H. Wei, X. C. Zeng, and J. Huang, "Defect passivation in hybrid perovskite solar cells using quaternary ammonium halide anions and cations," *Nature Energy*, vol. 2, no. 7, 2017.

[56] W. Ke, C. C. Stoumpos, and M. G. Kanatzidis, ""Unleaded" Perovskites: Status Quo and Future Prospects of Tin-Based Perovskite Solar Cells," *Advanced Materials*, vol. 31, no. 47, p. e1803230, 2019.

[57] G. Kapil, T. Bessho, C. H. Ng, K. Hamada, M. Pandey, M. A. Kamarudin, D. Hirotani, T. Kinoshita, T. Minemoto, Q. Shen, T. Toyoda, T. N. Murakami, H. Segawa, and S. Hayase, "Strain Relaxation and Light Management in Tin–Lead Perovskite Solar Cells to Achieve High Efficiencies," *ACS Energy Letters*, vol. 4, no. 8, pp. 1991–1998, 2019.

[58] L. Ye, S. Zhang, D. Qian, Q. Wang, and J. Hou, "Application of Bis-PCBM in Polymer Solar Cells with Improved Voltage," *The Journal of Physical Chemistry C*, vol. 117, no. 48, pp. 25360–25366, 2013.

[59] H. Fu, "Review of lead-free halide perovskites as light-absorbers for photovoltaic applications: From materials to solar cells," *Solar Energy Materials and Solar Cells*, vol. 193, pp. 107–132, 2019.

[60] H.-y. Zhang, R. Li, W.-w. Liu, M. Zhang, and M. Guo, "Research progress in lead-less or lead-free three-dimensional perovskite absorber materials for solar cells," *International Journal of Minerals, Metallurgy, and Materials*, vol. 26, no. 4, pp. 387–403, 2019.

[61] W. Ke and M. G. Kanatzidis, "Prospects for low-toxicity lead-free perovskite solar cells," *Nature Communications*, vol. 10, no. 1, p. 965, 2019.

[62] M. Chen, M.-G. Ju, H. F. Garces, A. D. Carl, L. K. Ono, Z. Hawash, Y. Zhang, T. Shen, Y. Qi, R. L. Grimm, D. Pacifici, X. C. Zeng, Y. Zhou, and N. P. Padture, "Highly stable and efficient all-inorganic lead-free perovskite solar cells with native-oxide passivation," *Nature Communications*, vol. 10, no. 1, p. 16, 2019.

[63] A. E. Shalan, S. Kazim, and S. Ahmad, "Lead-Free Perovskites: Metals Substitution towards Environmentally Benign Solar Cell Fabrication," *ChemSusChem*, vol. 12, no. 18, pp. 4116–4139, 2019.

[64] K. M. Boopathi, P. Karuppuswamy, A. Singh, C. Hanmandlu, L. Lin, S. A. Abbas, C. C. Chang, P. C. Wang, G. Li, and C. W. Chu, "Solution-processable antimony-based light-absorbing materials beyond lead halide perovskites," *Journal of Materials Chemistry A*, vol. 5, no. 39, pp. 20843–20850, 2017.

[65] R. G. Cooper and A. P. Harrison, "The exposure to and health effects of antimony," *Indian journal of occupational and environmental medicine*, vol. 13, no. 1, pp. 3–10, 2009.

[66] R. Mohan, "Green bismuth," *Nature chemistry*, vol. 2, no. 4, p. 336, 2010.

[67] E. Greul, M. Petrus, A. Binek, P. Docampo, and T. Bein, "Highly stable, phase pure $Cs_2AgBiBr_6$ double perovskite thin films for optoelectronic applications," *Journal of Materials Chemistry A*, vol. 5, no. 37, pp. 19972–19981, 2017.

[68] F. Igbari, R. Wang, Z.-K. Wang, X.-J. Ma, Q. Wang, K.-L. Wang, Y. Zhang, L.-S. Liao, and Y. Yang, "Composition Stoichiometry of $Cs_2AgBiBr_6$ Films for Highly Efficient Lead-Free Perovskite Solar Cells," *Nano Letters*, vol. 19, no. 3, pp. 2066–2073, 2019.

[69] T. Miyasaka, A. Kulkarni, G. M. Kim, S. Öz, and A. K. Jena, "Perovskite Solar Cells: Can We Go Organic–Free, Lead–Free, and Dopant–Free?," *Advanced Energy Materials*, vol. 10, no. 13, p. 1902500, 2020.

[70] N. Pai, J. Lu, T. R. Gengenbach, A. Seeber, A. S. R. Chesman, L. Jiang, D. C. Senevirathna, P. C. Andrews, U. Bach, Y.-B. Cheng, and A. N. Simonov, "Silver Bismuth Sulfoiodide Solar Cells: Tuning Optoelectronic Properties by Sulfide Modification for Enhanced Photovoltaic Performance," *Advanced Energy Materials*, p. 1803396, 2018.

[71] M.-G. Ju, M. Chen, Y. Zhou, H. F. Garces, J. Dai, L. Ma, N. P. Padture, and X. C. Zeng, "Earth-Abundant Nontoxic Titanium(IV)-based Vacancy-Ordered Double Perovskite Halides with Tunable 1.0 to 1.8 eV Bandgaps for Photovoltaic Applications," *ACS Energy Letters*, vol. 3, no. 2, pp. 297–304, 2018.

[72] M. Chen, M.-G. Ju, A. D. Carl, Y. Zong, R. L. Grimm, J. Gu, X. C. Zeng, Y. Zhou, and N. P. Padture, "Cesium titanium(iv) bromide thin films based stable lead-free perovskite solar cells," *Joule*, vol. 2, no. 3, pp. 558 – 570, 2018.

[73] Xue-Ping Cui, Ke-Jian Jiang, Jin-Hua Huang, Qian-Qian Zhang, Mei-Ju Su, Lian-Ming Yang, Yan-Lin Song, and Xue-Qin Zhou, "Cupric bromide hybrid perovskite heterojunction solar cells," *Synthetic Metals*, vol. 209, pp. 247–250, 2015.

[74] E. W.-G. Diau, E. Jokar, and M. Rameez, "Strategies To Improve Performance and Stability for Tin-Based Perovskite Solar Cells," *ACS Energy Letters*, vol. 4, no. 8, pp. 1930–1937, 2019.

[75] S. Gupta, D. Cahen, and G. Hodes, "How SnF_2 Impacts the Material Properties of Lead-Free Tin Perovskites," *The Journal of Physical Chemistry C*, vol. 122, no. 25, pp. 13926–13936, 2018.

[76] T.-B. Song, T. Yokoyama, C. C. Stoumpos, J. Logsdon, D. H. Cao, M. R. Wasielewski, S. Aramaki, and M. G. Kanatzidis, "Importance of Reducing Vapor Atmosphere in the Fabrication of Tin-Based Perovskite Solar Cells," *Journal of the American Chemical Society*, vol. 139, no. 2, pp. 836–842, 2017.

[77] D. H. Cao, C. C. Stoumpos, T. Yokoyama, J. L. Logsdon, T.-B. Song, O. K. Farha, M. R. Wasielewski, J. T. Hupp, and M. G. Kanatzidis, "Thin Films and Solar Cells Based on Semiconducting Two-Dimensional Ruddlesden–Popper $(CH_3(CH_2)_3NH_3)_2(CH_3NH_3)_{n-1}Sn_nI_{3n+1}$ Perovskites," *ACS Energy Letters*, vol. 2, no. 5, pp. 982–990, 2017.

[78] M. E. Kayesh, T. H. Chowdhury, K. Matsuishi, R. Kaneko, S. Kazaoui, J.-J. Lee, T. Noda, and A. Islam, "Enhanced Photovoltaic Performance of $FASnI_3$ -Based Perovskite Solar Cells with Hydrazinium Chloride Coadditive," *ACS Energy Letters*, vol. 3, no. 7, pp. 1584–1589, 2018.

[79] W. Li, J. Li, J. Li, J. Fan, Y. Mai, and L. Wang, "Addictive-assisted construction of all-inorganic $CsSnIBr_2$ mesoscopic perovskite solar cells with superior thermal stability up to 473 K," *Journal of Materials Chemistry A*, vol. 4, no. 43, pp. 17104–17110, 2016.

[80] X. Liu, T. Wu, J.-Y. Chen, X. Meng, X. He, T. Noda, H. Chen, X. Yang, H. Segawa, Y. Wang, and L. Han, "Templated growth of $FASnI_3$ crystals for efficient tin perovskite solar cells," *Energy & Environmental Science*, vol. 13, no. 9, pp. 2896–2902, 2020.

[81] J. Liu, M. Ozaki, S. Yakumaru, T. Handa, R. Nishikubo, Y. Kanemitsu, A. Saeki, Y. Murata, R. Murdey, and A. Wakamiya, "Lead-Free Solar Cells based on Tin Halide Perovskite Films with High Coverage and Improved Aggregation," *Angewandte Chemie International Edition*, vol. 57, no. 40, pp. 13221–13225, 2018.

[82] M. E. Kayesh, K. Matsuishi, R. Kaneko, S. Kazaoui, J.-J. Lee, T. Noda, and A. Islam, "Coadditive Engineering with 5-Ammonium Valeric Acid Iodide for Efficient and Stable Sn Perovskite Solar Cells," *ACS Energy Letters*, vol. 4, no. 1, pp. 278–284, 2019.

[83] F. Wang, X. Jiang, H. Chen, Y. Shang, H. Liu, J. Wei, W. Zhou, H. He, W. Liu, and Z. Ning, "2D-Quasi-2D-3D Hierarchy Structure for Tin Perovskite Solar Cells with Enhanced Efficiency and Stability," *Joule*, vol. 2, no. 12, pp. 2732–2743, 2018.

[84] H. Kim, Y. H. Lee, T. Lyu, J. H. Yoo, T. Park, and J. H. Oh, "Boosting the performance and stability of quasi-two-dimensional tin-based perovskite solar cells using the formamidinium thiocyanate additive," *Journal of Materials Chemistry A*, vol. 6, no. 37, pp. 18173–18182, 2018.

[85] E. Jokar, C.-H. Chien, A. Fathi, M. Rameez, Y.-H. Chang, and E. W.-G. Diau, "Slow surface passivation and crystal relaxation with additives to improve device performance and durability for tin-based perovskite solar cells," *Energy & Environmental Science*, vol. 11, no. 9, pp. 2353–2362, 2018.

[86] Y. Liao, H. Liu, W. Zhou, D. Yang, Y. Shang, Z. Shi, B. Li, X. Jiang, L. Zhang, L. N. Quan, R. Quintero-Bermudez, B. R. Sutherland, Q. Mi, E. H. Sargent, and Z. Ning, "Highly Oriented Low-Dimensional Tin Halide Perovskites with Enhanced Stability and Photovoltaic Performance," *Journal of the American Chemical Society*, vol. 139, no. 19, pp. 6693–6699, 2017.

[87] H. Xu, Y. Jiang, T. He, S. Li, H. Wang, Y. Chen, M. Yuan, and J. Chen, "Orientation Regulation of Tin–Based Reduced–Dimensional Perovskites for Highly Efficient and Stable Photovoltaics," *Advanced Functional Materials*, vol. 29, no. 47, p. 1807696, 2019.

[88] S. Shao, J. Liu, G. Portale, H.-H. Fang, G. R. Blake, G. H. ten Brink, L. J. A. Koster, and M. A. Loi, "Highly Reproducible Sn-Based Hybrid Perovskite Solar Cells with 9% Efficiency," *Advanced Energy Materials*, vol. 8, no. 4, p. 1702019, 2018.

[89] J. Horn, M. Scholz, K. Oum, T. Lenzer, and D. Schlettwein, "Influence of phenylethylammonium iodide as additive in the formamidinium tin iodide perovskite on interfacial characteristics and charge carrier dynamics," *APL Materials*, vol. 7, no. 3, p. 031112, 2019.

[90] M. Liao, B.-B. Yu, Z. Jin, W. Chen, Y. Zhu, X. Zhang, W. Yao, T. Duan, I. Djerdj, and Z. He, "Efficient and Stable $FASnI_3$ Perovskite Solar Cells with Effective Interface Modulation by Low-Dimensional Perovskite Layer," *ChemSusChem*, vol. 12, no. 22, pp. 5007–5014, 2019.

[91] J. Qiu, Y. Xia, Y. Zheng, W. Hui, H. Gu, W. Yuan, H. Yu, L. Chao, T. Niu, Y. Yang, X. Gao, Y. Chen, and W. Huang, "2D Intermediate Suppression for Efficient Ruddlesden–Popper (RP) Phase Lead-Free Perovskite Solar Cells," *ACS Energy Letters*, vol. 4, no. 7, pp. 1513–1520, 2019.

[92] J. Qiu, Y. Xia, Y. Chen, and W. Huang, "Management of Crystallization Kinetics for Efficient and Stable Low-Dimensional Ruddlesden-Popper (LDRP) Lead-Free Perovskite Solar Cells," *Advanced science (Weinheim, Baden-Wurttemberg, Germany)*, vol. 6, no. 1, p. 1800793, 2019.

[93] J. Dong, S. Shao, S. Kahmann, A. J. Rommens, D. Hermida-Merino, G. H. ten Brink, M. A. Loi, and G. Portale, "Mechanism of Crystal Formation in Ruddlesden–Popper Sn–Based Perovskites," *Advanced Functional Materials*, vol. 30, no. 24, p. 2001294, 2020.

[94] Kohei Nishimura, Muhammad Akmal Kamarudin, Daisuke Hirotani, Kengo Hamada, Qing Shen, Satoshi Iikubo, Takashi Minemoto, Kenji Yoshino, and Shuzi Hayase, "Lead-free tin-halide perovskite solar cells with 13% efficiency," *Nano Energy*, vol. 74, p. 104858, 2020.

[95] C. Liu, J. Tu, X. Hu, Z. Huang, X. Meng, J. Yang, X. Duan, L. Tan, Z. Li, and Y. Chen, "Enhanced hole transportation for inverted tin-based perovskite solar cells with high performance and stability," *Advanced Functional Materials*, vol. 29, p. 1808059, feb 2019.

[96] T. Wu, D. Cui, X. Liu, X. Meng, Y. Wang, T. Noda, H. Segawa, X. Yang, Y. Zhang, and L. Han, "Efficient and Stable Tin Perovskite Solar Cells Enabled by Graded Heterostructure of Light–Absorbing Layer," *Solar RRL*, vol. 4, no. 9, p. 2000240, 2020.

[97] N. Zibouche and M. S. Islam, "Structure-Electronic Property Relationships of 2D Ruddlesden-Popper Tin- and Lead-based Iodide Perovskites," *ACS Applied Materials & Interfaces*, vol. 12, no. 13, pp. 15328–15337, 2020.

[98] X. Liu, Y. Wang, F. Xie, X. Yang, and L. Han, "Improving the Performance of Inverted Formamidinium Tin Iodide Perovskite Solar Cells by Reducing the Energy-Level Mismatch," *ACS Energy Letters*, vol. 3, no. 5, pp. 1116–1121, 2018.

[99] X. Jiang, F. Wang, Q. Wei, H. Li, Y. Shang, W. Zhou, C. Wang, P. Cheng, Q. Chen, L. Chen, and Z. Ning, "Ultra-high open-circuit voltage of tin perovskite solar cells via an electron transporting layer design," *Nature Communications*, vol. 11, no. 1, p. 1245, 2020.

[100] J. Cao and F. Yan, "Recent progress in tin-based perovskite solar cells," *Energy & Environmental Science*, vol. 14, no. 3, pp. 1286–1325, 2021.

[101] G. Nasti and A. Abate, "Tin Halide Perovskite ($ASnX_3$) Solar Cells: A Comprehensive Guide toward the Highest Power Conversion Efficiency," *Advanced Energy Materials*, vol. 10, no. 13, p. 1902467, 2020.

[102] W. Gao, C. Chen, C. Ran, H. Zheng, H. Dong, Y. Xia, Y. Chen, and W. Huang, "A–Site Cation Engineering of Metal Halide Perovskites: Version 3.0 of Efficient Tin–Based Lead–Free Perovskite Solar Cells," *Advanced Functional Materials*, vol. 30, no. 34, p. 2000794, 2020.

[103] F. Gu, Z. Zhao, C. Wang, H. Rao, B. Zhao, Z. Liu, Z. Bian, and C. Huang, "Lead–Free Tin–Based Perovskite Solar Cells: Strategies Toward High Performance," *Solar RRL*, vol. 3, no. 9, p. 1900213, 2019.

[104] T. Leijtens, R. Prasanna, A. Gold-Parker, M. F. Toney, and M. D. McGehee, "Mechanism of Tin Oxidation and Stabilization by Lead Substitution in Tin Halide Perovskites," *ACS Energy Letters*, vol. 2, no. 9, pp. 2159–2165, 2017.

[105] Y. Zong, N. Wang, L. Zhang, M.-G. Ju, X. C. Zeng, X. W. Sun, Y. Zhou, and N. P. Padture, "Homogenous Alloys of Formamidinium Lead Triiodide and Cesium Tin Triiodide for Efficient Ideal-Bandgap Perovskite Solar Cells," *Angewandte Chemie International Edition*, vol. 56, no. 41, pp. 12658–12662, 2017.

[106] C. Wang, Z. Song, C. Li, D. Zhao, and Y. Yan, "Low–Bandgap Mixed Tin–Lead Perovskites and Their Applications in All–Perovskite Tandem Solar Cells," *Advanced Functional Materials*, vol. 29, no. 47, p. 1808801, 2019.

[107] H. L. Zhu and W. C. H. Choy, "Crystallization, Properties, and Challenges of Low-Bandgap Sn-Pb Binary Perovskites," *Solar RRL*, vol. 2, no. 10, p. 1800146, 2018.

[108] H. L. Zhu, J. Xiao, J. Mao, H. Zhang, Y. Zhao, and W. C. H. Choy, "Controllable Crystallization of $CH_3NH_3Sn_{0.25}Pb_{0.75}I_3$ Perovskites for Hysteresis-Free Solar Cells with Efficiency Reaching 15.2%," *Advanced Functional Materials*, vol. 27, no. 11, p. 1605469, 2017.

[109] J. Tong, Z. Song, D. H. Kim, X. Chen, C. Chen, A. F. Palmstrom, P. F. Ndione, M. O. Reese, S. P. Dunfield, O. G. Reid, J. Liu, F. Zhang, S. P. Harvey, Z. Li, S. T. Christensen, G. Teeter, D. Zhao, M. M. Al-Jassim, M. F. A. M. van Hest, M. C. Beard, S. E. Shaheen, J. J. Berry, Y. Yan, and K. Zhu, "Carrier lifetimes of >1 μs in Sn-Pb perovskites enable efficient all-perovskite tandem solar cells," *Science*, vol. 479, no. May, p. eaav7911, 2019.

[110] Q. Chen, J. Wu, J. T. Matondo, L. Bai, D. M. Maurice, and M. Guli, "Optimization of Bulk Defects in Sn/Pb Mixed Perovskite Solar Cells Through Synergistic Effect of Potassium Thiocyanate," *Solar RRL*, vol. 4, no. 12, p. 2000584, 2020.

[111] Y. Zong, Z. Zhou, M. Chen, N. P. Padture, and Y. Zhou, "Lewis-Adduct Mediated Grain-Boundary Functionalization for Efficient Ideal-Bandgap Perovskite Solar Cells with Superior Stability," *Advanced Energy Materials*, vol. 8, no. 27, p. 1800997, 2018.

[112] X. Xu, C.-C. Chueh, Z. Yang, A. Rajagopal, J. Xu, S. B. Jo, and A. K.-Y. Jen, "Ascorbic acid as an effective antioxidant additive to enhance the efficiency and stability of Pb/Sn-based binary perovskite solar cells," *Nano Energy*, vol. 34, pp. 392–398, 2017.

[113] T. Jiang, Z. Chen, X. Chen, T. Liu, X. Chen, W. E. I. Sha, H. Zhu, and Y. Yang, "Realizing High Efficiency over 20% of Low–Bandgap Pb–Sn–Alloyed Perovskite Solar Cells by In Situ Reduction of Sn^{4+}," *Solar RRL*, vol. 4, no. 3, p. 1900467, 2020.

[114] Z. Zhu, N. Li, D. Zhao, L. Wang, and A. K.-Y. Jen, "Improved Efficiency and Stability of Pb/Sn Binary Perovskite Solar Cells Fabricated by Galvanic Displacement Reaction," *Advanced Energy Materials*, vol. 9, no. 7, p. 1802774, 2019.

[115] D. Ramirez, K. Schutt, Z. Wang, A. J. Pearson, E. Ruggeri, H. J. Snaith, S. D. Stranks, and F. Jaramillo, "Layered Mixed Tin–Lead Hybrid Perovskite Solar Cells with High Stability," *ACS Energy Letters*, vol. 3, no. 9, pp. 2246–2251, 2018.

[116] J. Werner, T. Moot, T. A. Gossett, I. E. Gould, A. F. Palmstrom, E. J. Wolf, C. C. Boyd, M. F. A. M. van Hest, J. M. Luther, J. J. Berry, and M. D. McGehee, "Improving Low-Bandgap Tin–Lead Perovskite Solar Cells via Contact Engineering and Gas Quench Processing," *ACS Energy Letters*, vol. 5, no. 4, pp. 1215–1223, 2020.

[117] Z. Shariatinia, "Recent progress in development of diverse kinds of hole transport materials for the perovskite solar cells: A review," *Renewable and Sustainable Energy Reviews*, vol. 119, p. 109608, 2020.

[118] R. Prasanna, T. Leijtens, S. P. Dunfield, J. A. Raiford, E. J. Wolf, S. A. Swifter, J. Werner, G. E. Eperon, C. de Paula, A. F. Palmstrom, C. C. Boyd, M. F. A. M. van Hest, S. F. Bent, G. Teeter, J. J. Berry, and M. D. McGehee, "Design of low bandgap tin–lead halide perovskite solar cells to achieve thermal, atmospheric and operational stability," *Nature Energy*, vol. 4, no. 11, pp. 939–947, 2019.

[119] T. Leijtens, R. Prasanna, K. A. Bush, G. E. Eperon, J. A. Raiford, A. Gold-Parker, E. J. Wolf, S. A. Swifter, C. C. Boyd, H.-P. Wang, M. F. Toney, S. F. Bent, and M. D. McGehee, "Tin–lead halide perovskites with improved thermal and air stability for efficient all-perovskite tandem solar cells," *Sustainable Energy & Fuels*, vol. 2, no. 11, pp. 2450–2459, 2018.

[120] B. Conings, J. Drijkoningen, N. Gauquelin, A. Babayigit, J. D'Haen, L. D'Olieslaeger, A. Ethirajan, J. Verbeeck, J. Manca, E. Mosconi, F. de Angelis, and H.-G. Boyen, "Intrinsic Thermal Instability of Methylammonium Lead Trihalide Perovskite," *Advanced Energy Materials*, vol. 5, no. 15, p. 1500477, 2015.

[121] E. J. Juarez-Perez, L. K. Ono, M. Maeda, Y. Jiang, Z. Hawash, and Y. Qi, "Photodecomposition and thermal decomposition in methylammonium halide lead perovskites and inferred design principles to increase photovoltaic device stability," *Journal of Materials Chemistry A*, vol. 6, no. 20, pp. 9604–9612, 2018.

[122] W. Tan, A. R. Bowring, A. C. Meng, M. D. McGehee, and P. C. McIntyre, "Thermal Stability of Mixed Cation Metal Halide Perovskites in Air," *ACS Applied Materials & Interfaces*, vol. 10, no. 6, pp. 5485–5491, 2018.

[123] S.-H. H. Turren-Cruz, A. Hagfeldt, and M. Saliba, "Methylammonium-free, high-performance, and stable perovskite solar cells on a planar architecture," *Science*, vol. 362, no. 6413, pp. 449–453, 2018.

[124] T. Zhang, X. Meng, Y. Bai, S. Xiao, C. Hu, Y. Yang, H. Chen, and S. Yang, "Profiling the organic cation-dependent degradation of organolead halide perovskite solar cells," *Journal of Materials Chemistry A*, vol. 5, no. 3, pp. 1103–1111, 2017.

[125] Y. Zhao, W. Zhou, H. Tan, R. Fu, Q. Li, F. Lin, D. Yu, G. Walters, E. H. Sargent, and Q. Zhao, "Mobile-Ion-Induced Degradation of Organic Hole-Selective Layers in Perovskite Solar Cells," *The Journal of Physical Chemistry C*, vol. 121, no. 27, pp. 14517–14523, 2017.

[126] S. Wang, Y. Jiang, E. J. Juarez-Perez, L. K. Ono, and Y. Qi, "Accelerated degradation of methylammonium lead iodide perovskites induced by exposure to iodine vapour," *Nature Energy*, vol. 2, no. 1, 2017.

[127] M. P. de Jong, L. J. van IJzendoorn, and M. J. A. de Voigt, "Stability of the interface between indium-tin-oxide and poly(3,4-ethylenedioxythiophene)/poly(styrenesulfonate) in polymer light-emitting diodes," *Applied Physics Letters*, vol. 77, no. 14, pp. 2255–2257, 2000.

[128] J. R. Manders, S.-W. Tsang, M. J. Hartel, T.-H. Lai, S. Chen, C. M. Amb, J. R. Reynolds, and F. So, "Solution-Processed Nickel Oxide Hole Transport Layers in High Efficiency Polymer Photovoltaic Cells," *Advanced Functional Materials*, vol. 23, no. 23, pp. 2993–3001, 2013.

[129] M. B. Islam, M. Yanagida, Y. Shirai, Y. Nabetani, and K. Miyano, "NiO_x Hole Transport Layer for Perovskite Solar Cells with Improved Stability and Reproducibility," *ACS Omega*, pp. 2291–2299, 2017.

[130] K. Eckhardt, V. Bon, J. Getzschmann, J. Grothe, F. M. Wisser, and S. Kaskel, "Crystallographic insights into $(CH_3NH_3)_3(Bi_2I_9)$: a new lead-free hybrid organic-inorganic material as a potential absorber for photovoltaics," *Chemical communications (Cambridge, England)*, vol. 52, no. 14, pp. 3058–3060, 2016.

[131] B.-W. Park, B. Philippe, X. Zhang, H. Rensmo, G. Boschloo, and E. M. J. Johansson, "Bismuth Based Hybrid Perovskites $A_3Bi_2I_9$ (A: Methylammonium or Cesium) for Solar Cell Application," *Advanced Materials*, vol. 27, no. 43, pp. 6806–6813, 2015.

[132] A. Kulkarni, T. Singh, M. Ikegami, and T. Miyasaka, "Photovoltaic enhancement of bismuth halide hybrid perovskite by N-methyl pyrrolidone-assisted morphology conversion," *RSC Advances*, vol. 7, no. 16, pp. 9456–9460, 2017.

[133] S. S. Shin, J. P. Correa Baena, R. C. Kurchin, A. Polizzotti, J. J. Yoo, S. Wieghold, M. G. Bawendi, and T. Buonassisi, "Solvent-Engineering Method to Deposit Compact Bismuth-Based Thin Films: Mechanism and Application to Photovoltaics," *Chemistry of Materials*, vol. 30, no. 2, pp. 336–343, 2018.

[134] D. B. Khadka, Y. Shirai, M. Yanagida, and K. Miyano, "Tailoring the film morphology and interface band offset of caesium bismuth iodide-based Pb-free perovskite solar cells," *Journal of Materials Chemistry C*, vol. 7, no. 27, pp. 8335–8343, 2019.

[135] K.-H. Hong, J. Kim, L. Debbichi, H. Kim, and S. H. Im, "Band Gap Engineering of $Cs_3Bi_2I_9$ Perovskites with Trivalent Atoms Using a Dual Metal Cation," *The Journal of Physical Chemistry C*, vol. 121, no. 1, pp. 969–974, 2017.

[136] Y.-Y. Sun, J. Shi, J. Lian, W. Gao, M. L. Agiorgousis, P. Zhang, and S. Zhang, "Discovering lead-free perovskite solar materials with a split-anion approach," *Nanoscale*, vol. 8, no. 12, pp. 6284–6289, 2016.

[137] M. Vigneshwaran, T. Ohta, S. Iikubo, G. Kapil, T. S. Ripolles, Y. Ogomi, T. Ma, S. S. Pandey, Q. Shen, T. Toyoda, K. Yoshino, T. Minemoto, and S. Hayase, "Facile Synthesis and Characterization of Sulfur Doped Low Bandgap Bismuth Based Perovskites by Soluble Precursor Route," *Chemistry of Materials*, vol. 28, no. 18, pp. 6436–6440, 2016.

[138] M. V. Khenkin, E. A. Katz, A. Abate, G. Bardizza, J. J. Berry, C. Brabec, F. Brunetti, V. Bulović, Q. Burlingame, A. Di Carlo, R. Cheacharoen, Y.-B. Cheng, A. Colsmann, S. Cros, K. Domanski, M. Dusza, C. J. Fell, S. R. Forrest, Y. Galagan, D. Di Girolamo, M. Grätzel, A. Hagfeldt, E. von Hauff, H. Hoppe, J. Kettle, H. Köbler, M. S. Leite, S. Liu, Y.-L. Loo, J. M. Luther, C.-Q. Ma, M. Madsen, M. Manceau, M. Matheron, M. McGehee, R. Meitzner, M. K. Nazeeruddin, A. F. Nogueira, Ç. Odabaşı, A. Osherov, N.-G. Park, M. O. Reese, F. de Rossi, M. Saliba, U. S. Schubert, H. J. Snaith, S. D. Stranks, W. Tress, P. A. Troshin, V. Turkovic, S. Veenstra, I. Visoly-Fisher, A. Walsh, T. Watson, H. Xie, R. Yıldırım, S. M. Zakeeruddin, K. Zhu, and M. Lira-Cantu, "Consensus statement for stability assessment and reporting for perovskite photovoltaics based on ISOS procedures," *Nature Energy*, vol. 5, no. 1, pp. 35–49, 2020.

[139] P. Holzhey and M. Saliba, "A full overview of international standards assessing the long-term stability of perovskite solar cells," *Journal of Materials Chemistry A*, vol. 6, no. 44, pp. 21794–21808, 2018.

[140] F. Hao, H. Tan, Z. Jin, and L. Ding, "Toward stable and efficient Sn-containing perovskite solar cells," *Science Bulletin*, vol. 65, no. 10, pp. 786–790, 2020.

[141] Y. Yuan, Q. Wang, Y. Shao, H. Lu, T. Li, A. Gruverman, and J. Huang, "Electric-Field-Driven Reversible Conversion Between Methylammonium Lead Triiodide Perovskites and Lead Iodide at Elevated Temperatures," *Advanced Energy Materials*, vol. 6, no. 2, p. 1501803, 2016.

[142] J. L. Minns, P. Zajdel, D. Chernyshov, W. van Beek, and M. A. Green, "Structure and interstitial iodide migration in hybrid perovskite methylammonium lead iodide," *Nature Communications*, vol. 8, p. 15152, 2017.

[143] C. Eames, J. M. Frost, P. R. F. Barnes, B. C. O'Regan, A. Walsh, and M. S. Islam, "Ionic transport in hybrid lead iodide perovskite solar cells," *Nature Communications*, vol. 6, p. 7497, 2015.

[144] T. Wu, M. Ahmadi, and B. Hu, "Giant current amplification induced by ion migration in perovskite single crystal photodetectors," *Journal of Materials Chemistry C*, vol. 6, no. 30, pp. 8042–8050, 2018.

[145] Y. Luo, P. Khoram, S. Brittman, Z. Zhu, B. Lai, S. P. Ong, E. C. Garnett, and D. P. Fenning, "Direct Observation of Halide Migration and its Effect on the Photoluminescence of Methylammonium Lead Bromide Perovskite Single Crystals," *Advanced Materials*, vol. 29, no. 43, 2017.

[146] L. Lanzetta, T. Webb, N. Zibouche, X. Liang, D. Ding, G. Min, R. J. E. Westbrook, B. Gaggio, T. J. Macdonald, M. S. Islam, and S. A. Haque, "Degradation mechanism of hybrid tin-based perovskite solar cells and the critical role of tin (IV) iodide," *Nature Communications*, vol. 12, no. 1, p. 2853, 2021.

[147] M. H. Kumar, S. Dharani, W. L. Leong, P. P. Boix, R. R. Prabhakar, T. Baikie, C. Shi, H. Ding, R. Ramesh, M. Asta, M. Graetzel, S. G. Mhaisalkar, and N. Mathews, "Lead-Free Halide Perovskite Solar Cells with High Photocurrents Realized Through Vacancy Modulation," *Advanced Materials*, vol. 26, no. 41, pp. 7122–7127, 2014.

[148] W. Liao, D. Zhao, Y. Yu, C. R. Grice, C. Wang, A. J. Cimaroli, P. Schulz, W. Meng, K. Zhu, R.-G. Xiong, and Y. Yan, "Lead-Free Inverted Planar Formamidinium Tin Triiodide Perovskite Solar Cells Achieving Power Conversion Efficiencies up to 6.22%," *Advanced Materials*, vol. 28, no. 42, pp. 9333–9340, 2016.

[149] K. P. Marshall, M. Walker, R. I. Walton, and R. A. Hatton, "Enhanced stability and efficiency in hole-transport-layer-free $CsSnI_3$ perovskite photovoltaics," *Nature Energy*, vol. 1, no. 12, 2016.

[150] M. Li, W.-W. Zuo, Y.-G. Yang, M. H. Aldamasy, Q. Wang, S. H. T. Cruz, S.-L. Feng, M. Saliba, Z.-K. Wang, and A. Abate, "Tin Halide Perovskite Films Made of Highly Oriented 2D Crystals Enable More Efficient and Stable Lead-free Perovskite Solar Cells," *ACS Energy Letters*, vol. 5, no. 6, pp. 1923–1929, 2020.

[151] M. Wei, K. Xiao, G. Walters, R. Lin, Y. Zhao, M. I. Saidaminov, P. Todorović, A. Johnston, Z. Huang, H. Chen, A. Li, J. Zhu, Z. Yang, Y.-K. Wang, A. H. Proppe, S. O. Kelley, Y. Hou, O. Voznyy, H. Tan, and E. H. Sargent, "Combining Efficiency and Stability in Mixed Tin-Lead Perovskite Solar Cells by Capping Grains with an Ultrathin 2D Layer," *Advanced Materials*, vol. 32, no. 12, p. e1907058, 2020.

[152] N. Aristidou, I. Sanchez-Molina, T. Chotchuangchutchaval, M. Brown, L. Martinez, T. Rath, and S. A. Haque, "The role of oxygen in the degradation of methylammonium lead trihalide perovskite photoactive layers," *Angewandte Chemie International Edition*, vol. 54, no. 28, pp. 8208–8212, 2015.

[153] D. Bryant, N. Aristidou, S. Pont, I. Sanchez-Molina, T. Chotchunangatchaval, S. Wheeler, J. R. Durrant, and S. A. Haque, "Light and oxygen induced degradation limits the operational stability of methylammonium lead triiodide perovskite solar cells," *Energy & Environmental Science*, vol. 9, no. 5, pp. 1655–1660, 2016.

[154] N. Aristidou, C. Eames, I. Sanchez-Molina, X. Bu, J. Kosco, M. S. Islam, and S. A. Haque, "Fast oxygen diffusion and iodide defects mediate oxygen-induced degradation of perovskite solar cells," *Nature Communications*, vol. 8, 2017.

[155] M. Kulbak, S. Gupta, N. Kedem, I. Levine, T. Bendikov, G. Hodes, and D. Cahen, "Cesium Enhances Long-Term Stability of Lead Bromide Perovskite-Based Solar Cells," *The Journal of Physical Chemistry Letters*, vol. 7, no. 1, pp. 167–172, 2016.

[156] M. Saliba, T. Matsui, J.-Y. Seo, K. Domanski, J.-P. Correa-Baena, M. K. Nazeeruddin, S. M. Zakeeruddin, W. Tress, A. Abate, A. Hagfeldt, and M. Gratzel, "Cesium-containing triple cation perovskite solar cells: improved stability, reproducibility and high efficiency," *Energy & Environmental Science*, vol. 9, no. 6, pp. 1989–1997, 2016.

[157] R. Wang, M. Mujahid, Y. Duan, Z.-K. Wang, J. Xue, and Y. Yang, "A Review of Perovskites Solar Cell Stability," *Advanced Functional Materials*, vol. 29, no. 47, p. 1808843, 2019.

[158] S. Pont, D. Bryant, C.-T. Lin, N. Aristidou, S. Wheeler, X. Ma, R. Godin, S. A. Haque, and J. R. Durrant, "Tuning $CH_3NH_3Pb(I_{1-x}Br_x)_3$ perovskite oxygen stability in thin films and solar cells," *Journal of Materials Chemistry A*, vol. 5, no. 20, pp. 9553–9560, 2017.

[159] C. C. Stoumpos, C. D. Malliakas, and M. G. Kanatzidis, "Semiconducting tin and lead iodide perovskites with organic cations: phase transitions, high mobilities, and near-infrared photoluminescent properties," *Inorganic Chemistry*, vol. 52, no. 15, pp. 9019–9038, 2013.

[160] M. Ha, A. Karmakar, G. M. Bernard, E. Basilio, A. Krishnamurthy, A. M. Askar, K. Shankar, S. Kroeker, and V. K. Michaelis, "Phase Evolution in Methylammonium Tin Halide Perovskites with Variable Temperature Solid-State 119 Sn NMR Spectroscopy," *The Journal of Physical Chemistry C*, vol. 124, no. 28, pp. 15015–15027, 2020.

[161] X. Zhou, W. Qi, J. Li, J. Cheng, Y. Li, J. Luo, M. J. Ko, Y. Li, Y. Zhao, and X. Zhang, "Toward Efficient and Stable Perovskite Solar Cells: Choosing Appropriate Passivator to Specific Defects," *Solar RRL*, vol. 4, no. 10, p. 2000308, 2020.

[162] B. Roose, Q. Wang, and A. Abate, "The Role of Charge Selective Contacts in Perovskite Solar Cell Stability," *Advanced Energy Materials*, p. 1803140, 2018.

[163] K. Y. Chiu, S. H. Chang, W.-C. Huang, H.-M. Cheng, H. Shaw, S.-C. Yeh, C.-T. Chen, Y. O. Su, S.-H. Chen, and C.-G. Wu, "Functional graded fullerene derivatives for improving the fill factor and device stability of inverted-type perovskite solar cells," *Nanotechnology*, vol. 29, no. 30, p. 305701, 2018.

[164] A. G. Boldyreva, I. S. Zhidkov, S. Tsarev, A. F. Akbulatov, M. M. Tepliakova, Y. S. Fedotov, S. I. Bredikhin, E. Y. Postnova, S. Y. Luchkin, E. Z. Kurmaev, K. J. Stevenson, and P. A. Troshin, "Unraveling the Impact of Hole Transport Materials on Photostability of Perovskite Films and p-i-n Solar Cells," *ACS Applied Materials & Interfaces*, vol. 12, no. 16, pp. 19161–19173, 2020.

[165] K. Domanski, J.-P. Correa-Baena, N. Mine, M. K. Nazeeruddin, A. Abate, M. Saliba, W. Tress, A. Hagfeldt, and M. Grätzel, "Not All That Glitters Is Gold: Metal-Migration-Induced Degradation in Perovskite Solar Cells," *ACS Nano*, vol. 10, no. 6, pp. 6306–6314, 2016.

[166] A. Guerrero, J. You, C. Aranda, Y. S. Kang, G. Garcia-Belmonte, H. Zhou, J. Bisquert, and Y. Yang, "Interfacial Degradation of Planar Lead Halide Perovskite Solar Cells," *ACS Nano*, vol. 10, no. 1, pp. 218–224, 2016.

[167] Y. Kato, L. K. Ono, M. V. Lee, S. Wang, S. R. Raga, and Y. Qi, "Silver Iodide Formation in Methyl Ammonium Lead Iodide Perovskite Solar Cells with Silver Top Electrodes," *Advanced Materials Interfaces*, vol. 2, no. 13, pp. n/a–n/a, 2015.

[168] W. Stöber, A. Fink, and E. Bohn, "Controlled growth of monodisperse silica spheres in the micron size range," *Journal of Colloid and Interface Science*, vol. 26, no. 1, pp. 62–69, 1968.

[169] G. H. Bogush, M. A. Tracy, and C. F. Zukoski, "Preparation of monodisperse silica particles: Control of size and mass fraction," *Journal of Non-Crystalline Solids*, vol. 104, no. 1, pp. 95–106, 1988.

[170] Keyence, "Manual: Color 3D Laser Microscope VK-9700K/VK-8700K."

[171] S. P. Harvey, J. Messinger, K. Zhu, J. M. Luther, and J. J. Berry, "Investigating the Effects of Chemical Gradients on Performance and Reliability within Perovskite Solar Cells with TOF-SIMS," *Advanced Energy Materials*, vol. 10, no. 26, p. 1903674, 2020.

[172] P. Makula, M. Pacia, and W. Macyk, "How To Correctly Determine the Band Gap Energy of Modified Semiconductor Photocatalysts Based on UV-Vis Spectra," *The Journal of Physical Chemistry Letters*, vol. 9, no. 23, pp. 6814–6817, 2018.

[173] S. J. Lee, S. S. Shin, J. Im, T. K. Ahn, J. H. Noh, N. J. Jeon, S. I. Seok, and J. Seo, "Reducing Carrier Density in Formamidinium Tin Perovskites and Its Beneficial Effects on Stability and Efficiency of Perovskite Solar Cells," *ACS Energy Letters*, vol. 3, no. 1, pp. 46–53, 2018.

[174] M. Konstantakou and T. Stergiopoulos, "A critical review on tin halide perovskite solar cells," *Journal of Materials Chemistry A*, vol. 5, no. 23, pp. 11518–11549, 2017.

[175] M. Schultes, N. Giesbrecht, J. Küffner, E. Ahlswede, P. Docampo, T. Bein, and M. Powalla, "Universal Nanoparticle Wetting Agent for Upscaling Perovskite Solar Cells," *ACS Applied Materials & Interfaces*, vol. 11, no. 13, pp. 12948–12957, 2019.

[176] D. B. Khadka, Y. Shirai, M. Yanagida, J. W. Ryan, and K. Miyano, "Exploring the effects of interfacial carrier transport layers on device performance and optoelectronic properties of planar perovskite solar cells," *Journal of Materials Chemistry C*, vol. 5, no. 34, pp. 8819–8827, 2017.

[177] S. Zhang, M. Stolterfoht, A. Armin, Q. Lin, F. Zu, J. Sobus, H. Jin, N. Koch, P. Meredith, P. L. Burn, and D. Neher, "Interface Engineering of Solution-Processed Hybrid Organohalide Perovskite Solar Cells," *ACS Applied Materials & Interfaces*, vol. 10, no. 25, pp. 21681–21687, 2018.

[178] M. Jiang, Y. Wu, Y. Zhou, and Z. Wang, "Observation of lower defect density brought by excess PbI_2 in $CH_3NH_3PbI_3$ solar cells," *AIP Advances*, vol. 9, no. 8, p. 085301, 2019.

[179] N. Ueoka, T. Oku, Y. Ohishi, H. Tanaka, and A. Suzuki, "Effects of Excess PbI_2 Addition to $CH_3NH_3PbI_{3-x}Cl_x$ Perovskite Solar Cells," *Chemistry Letters*, vol. 47, no. 4, pp. 528–531, 2018.

[180] F. Liu, Q. Dong, M. K. Wong, A. B. Djurišić, A. Ng, Z. Ren, Q. Shen, C. Surya, W. K. Chan, J. Wang, A. M. C. Ng, C. Liao, H. Li, K. Shih, C. Wei, H. Su, and J. Dai, "Is Excess PbI_2 Beneficial for Perovskite Solar Cell Performance?," *Advanced Energy Materials*, vol. 6, no. 7, pp. n/a–n/a, 2016.

[181] H.-y. Wang, M.-Y. Hao, J. Han, M. Yu, Y. Qin, P. Zhang, Z.-X. Guo, X.-c. Ai, and J.-p. Zhang, "Adverse Effects of Excess Residual PbI_2 on Photovoltaic Performance, Charge Separation, and Trap-State Properties in Mesoporous Structured Perovskite Solar Cells," *Chemistry (Weinheim an der Bergstrasse, Germany)*, vol. 23, no. 16, pp. 3986–3992, 2017.

[182] G. Tumen-Ulzii, C. Qin, D. Klotz, M. R. Leyden, P. Wang, M. Auffray, T. Fujihara, T. Matsushima, J.-W. Lee, S.-J. Lee, Y. Yang, and C. Adachi, "Detrimental Effect of Unreacted PbI_2 on the Long-Term Stability of Perovskite Solar Cells," *Advanced Materials*, vol. 32, no. 16, p. e1905035, 2020.

[183] Z. Hu, Q. An, H. Xiang, L. Aigouy, B. Sun, Y. Vaynzof, and Z. Chen, "Enhancing the Efficiency and Stability of Triple-Cation Perovskite Solar Cells by Eliminating Excess PbI_2 from the Perovskite/Hole Transport Layer Interface," *ACS Applied Materials & Interfaces*, vol. 12, no. 49, pp. 54824–54832, 2020.

[184] W. Ke, I. Spanopoulos, Q. Tu, I. Hadar, X. Li, G. S. Shekhawat, V. P. Dravid, and M. G. Kanatzidis, "Ethylenediammonium-Based "Hollow" Pb/Sn Perovskites with Ideal Band Gap Yield Solar Cells with Higher Efficiency and Stability," *Journal of the American Chemical Society*, vol. 141, no. 21, pp. 8627–8637, 2019.

[185] G. Wyckoff, "New york note: Cadmium iodide structure," 1963.

[186] A. M. Igual-Muñoz, J. Ávila, P. P. Boix, and H. J. Bolink, "$FAPb_{0.5}Sn_{0.5}I_3$: A Narrow Bandgap Perovskite Synthesized through Evaporation Methods for Solar Cell Applications," *Solar RRL*, vol. 4, no. 2, p. 1900283, 2020.

[187] G. E. Eperon, T. Leijtens, K. A. Bush, R. Prasanna, T. Green, J. T.-W. Wang, D. P. McMeekin, G. Volonakis, R. L. Milot, R. May, A. Palmstrom, D. J. Slotcavage, R. A. Belisle, J. B. Patel, E. S. Parrott, R. J. Sutton, W. Ma, F. Moghadam, B. Conings, A. Babayigit, H.-G. Boyen, S. Bent, F. Giustino, L. M. Herz, M. B. Johnston, M. D. McGehee, and H. J. Snaith, "Perovskite-perovskite tandem photovoltaics with optimized band gaps," *Science*, vol. 354, no. 6314, pp. 861–865, 2016.

[188] J. Liu, G. Wang, Z. Song, X. He, K. Luo, Q. Ye, C. Liao, and J. Mei, "$FAPb_{1-x}Sn_xI_3$ mixed metal halide perovskites with improved light harvesting and stability for efficient planar heterojunction solar cells," *Journal of Materials Chemistry A*, vol. 5, no. 19, pp. 9097–9106, 2017.

[189] S. Shao, Y. Cui, H. Duim, X. Qiu, J. Dong, G. H. ten Brink, G. Portale, R. C. Chiechi, S. Zhang, J. Hou, and M. A. Loi, "Enhancing the Performance of the Half Tin and Half Lead Perovskite Solar Cells by Suppression of the Bulk and Interfacial Charge Recombination," *Advanced Materials*, vol. 30, no. 35, p. e1803703, 2018.

[190] R. Saive, "S-Shaped Current–Voltage Characteristics in Solar Cells: A Review," *IEEE Journal of Photovoltaics*, pp. 1–8, 2019.

[191] J. Pascual, M. Flatken, R. Félix, G. Li, S.-H. Turren-Cruz, M. H. Aldamasy, C. Hartmann, M. Li, D. Di Girolamo, G. Nasti, E. Hüsam, R. G. Wilks, A. Dallmann, M. Bär, A. Hoell, and A. Abate, "Fluoride Chemistry in Tin Halide Perovskites," *Angewandte Chemie International Edition*, 2021.

[192] M. Xiao, S. Gu, P. Zhu, M. Tang, W. Zhu, R. Lin, C. Chen, W. Xu, T. Yu, and J. Zhu, "Tin-Based Perovskite with Improved Coverage and Crystallinity through Tin-Fluoride-Assisted Heterogeneous Nucleation," *Advanced Optical Materials*, vol. 6, no. 1, p. 1700615, 2018.

[193] T. M. Koh, T. Krishnamoorthy, N. Yantara, C. Shi, W. L. Leong, P. P. Boix, A. C. Grimsdale, S. G. Mhaisalkar, and N. Mathews, "Formamidinium tin-based perovskite with low E_g for photovoltaic applications," *Journal of Materials Chemistry A*, vol. 3, no. 29, pp. 14996–15000, 2015.

[194] Z. Zhao, F. Gu, Y. Li, W. Sun, S. Ye, H. Rao, Z. Liu, Z. Bian, and C. Huang, "Mixed-Organic-Cation Tin Iodide for Lead-Free Perovskite Solar Cells with an Efficiency of 8.12," *Advanced science (Weinheim, Baden-Wurttemberg, Germany)*, vol. 4, no. 11, p. 1700204, 2017.

[195] F. Hao, C. C. Stoumpos, P. Guo, N. Zhou, T. J. Marks, R. P. H. Chang, and M. G. Kanatzidis, "Solvent-Mediated Crystallization of CH3NH3SnI3 Films for Heterojunction Depleted Perovskite Solar Cells," *Journal of the American Chemical Society*, vol. 137, no. 35, pp. 11445–11452, 2015.

[196] E. Jokar, P.-Y. Cheng, C.-Y. Lin, S. Narra, S. Shahbazi, and E. Wei-Guang Diau, "Enhanced Performance and Stability of 3D/2D Tin Perovskite Solar Cells Fabricated with a Sequential Solution Deposition," *ACS Energy Letters*, pp. 485–492, 2021.

[197] K. Nishimura, M. A. Kamarudin, D. Hirotani, K. Hamada, Q. Shen, S. Iikubo, T. Minemoto, K. Yoshino, and S. Hayase, "Lead-free tin-halide perovskite solar cells with 13% efficiency," *Nano Energy*, vol. 74, p. 104858, 2020.

[198] J. Zillner, H.-G. Boyen, J. Hanisch, P. Schulz, D. Desta, J. Küffner, E. Ahlswede, and M. Powalla, "The Role of SnF_2 Additives on Interface and Film Formation in All Lead-Free $FASnI_3$ Perovskite Solar Cells," *in preparation for submission to Advanced Funtional Materials*, 2021.

[199] C. Hartmann, S. Gupta, T. Bendikov, X. Kozina, T. Kunze, R. Félix, G. Hodes, R. G. Wilks, D. Cahen, and M. Bär, "Impact of SnF_2 Addition on the Chemical and Electronic Surface Structure of $CsSnBr_3$," *ACS Applied Materials & Interfaces*, vol. 12, no. 10, pp. 12353–12361, 2020.

[200] R. Nishikubo, N. Ishida, Y. Katsuki, A. Wakamiya, and A. Saeki, "Minute-Scale Degradation and Shift of Valence-Band Maxima of $(CH_3NH_3)SnI_3$ and $HC(NH_2)_2SnI_3$ Perovskites upon Air Exposure," *The Journal of Physical Chemistry C*, vol. 121, no. 36, pp. 19650–19656, 2017.

[201] J. H. Heo, J. Kim, H. Kim, S. H. Moon, S. H. Im, and K.-H. Hong, "Roles of SnX_2 (X = F, Cl, Br) Additives in Tin-Based Halide Perovskites toward Highly Efficient and Stable Lead-Free Perovskite Solar Cells," *The Journal of Physical Chemistry Letters*, vol. 9, no. 20, pp. 6024–6031, 2018.

[202] "NIST Electron Inelastic-Mean-Free-Path Database: Version 1.2."

[203] K. P. Marshall, R. I. Walton, and R. A. Hatton, "Tin perovskite/fullerene planar layer photovoltaics: improving the efficiency and stability of lead-free devices," *Journal of Materials Chemistry A*, vol. 3, no. 21, pp. 11631–11640, 2015.

[204] S. Jäckle, M. Liebhaber, J. Niederhausen, M. Büchele, R. Félix, R. G. Wilks, M. Bär, K. Lips, and S. Christiansen, "Unveiling the Hybrid n-Si/PEDOT:PSS Interface," *ACS Applied Materials & Interfaces*, vol. 8, no. 13, pp. 8841–8848, 2016.

[205] T. J. Whittles, L. A. Burton, J. M. Skelton, A. Walsh, T. D. Veal, and V. R. Dhanak, "Band Alignments, Valence Bands, and Core Levels in the Tin Sulfides SnS, SnS_2, and Sn_2S_3: Experiment and Theory," *Chemistry of Materials*, vol. 28, no. 11, pp. 3718–3726, 2016.

[206] B. R. Strohmeier, "An ESCA method for determining the oxide thickness on aluminum alloys," *Surface and Interface Analysis*, vol. 15, no. 1, pp. 51–56, 1990.

[207] H.-G. Boyen, A. Ethirajan, G. Kästle, F. Weigl, P. Ziemann, G. Schmid, M. G. Garnier, M. Büttner, and P. Oelhafen, "Alloy formation of supported gold nanoparticles at their transition from clusters to solids: does size matter?," *Physical Review Letters*, vol. 94, no. 1, p. 016804, 2005.

[208] H. Hövel, B. Grimm, M. Pollmann, and B. Reihl, "Cluster-Substrate Interaction on a Femtosecond Time Scale Revealed by a High-Resolution Photoemission Study of the Fermi-Level Onset," *Physical Review Letters*, vol. 81, no. 21, pp. 4608–4611, 1998.

[209] H. Hövel, I. Barke, H.-G. Boyen, P. Ziemann, M. G. Garnier, and P. Oelhafen, "Photon energy dependence of the dynamic final-state effect for metal clusters at surfaces," *Physical Review B*, vol. 70, no. 4, 2004.

[210] G. K. Wertheim, S. B. DiCenzo, and S. E. Youngquist, "Unit Charge on Supported Gold Clusters in Photoemission Final State," *Physical Review Letters*, vol. 51, no. 25, pp. 2310–2313, 1983.

[211] J. A. Andrade-Arvizu, M. Courel-Piedrahita, and O. Vigil-Galán, "SnS-based thin film solar cells: perspectives over the last 25 years," *Journal of Materials Science: Materials in Electronics*, vol. 26, no. 7, pp. 4541–4556, 2015.

[212] C. Ran, J. Xi, W. Gao, F. Yuan, T. Lei, B. Jiao, X. Hou, and Z. Wu, "Bilateral interface engineering toward efficient 2d-3d bulk heterojunction tin halide lead-free perovskite solar cells," *ACS Energy Letters*, vol. 3, no. 3, pp. 713–721, 2018.

[213] X. Xu, K. Cao, W. Zhu, W. Gu, B. Ma, M. Qin, J. Qian, Y. Lu, Z. Liu, S. Chen, X. Lu, and W. Huang, "Improved Crystallization and Stability of Mixed-Cation Tin Iodide for Lead-Free Perovskite Solar Cells," *ACS Applied Energy Materials*, vol. 3, no. 6, pp. 5415–5426, 2020.

[214] Y. Matsuo, "Design Concept for High-LUMO-level Fullerene Electron-acceptors for Organic Solar Cells," *Chemistry Letters*, vol. 41, no. 8, pp. 754–759, 2012.

[215] Lisa Eisele, "Impact of hybrid 2D-Perovskites on the stability of Perovskite solar cells," 2020.

[216] L. Jia, M. Chen, and S. Yang, "Functionalization of fullerene materials toward applications in perovskite solar cells," *Materials Chemistry Frontiers*, vol. 4, no. 8, pp. 2256–2282, 2020.

[217] P. Chen, Y. Bai, and L. Wang, "Minimizing Voltage Losses in Perovskite Solar Cells," *Small Structures*, vol. 2, no. 1, p. 2000050, 2021.

[218] Z. Li, J. Dong, C. Liu, J. Guo, L. Shen, and W. Guo, "Surface Passivation of Perovskite Solar Cells Toward Improved Efficiency and Stability," *Nano-micro letters*, vol. 11, no. 1, p. 50, 2019.

[219] F. Tan, H. Tan, M. I. Saidaminov, M. Wei, M. Liu, A. Mei, P. Li, B. Zhang, C.-S. Tan, X. Gong, Y. Zhao, A. R. Kirmani, Z. Huang, J. Z. Fan, R. Quintero-Bermudez, J. Kim, Y. Zhao, O. Voznyy, Y. Gao, F. Zhang, L. J. Richter, Z.-H. Lu, W. Zhang, and E. H. Sargent, "In Situ Back-Contact Passivation Improves Photovoltage and Fill Factor in Perovskite Solar Cells," *Advanced Materials*, vol. 31, no. 14, p. e1807435, 2019.

[220] M. Wang, H. Wang, W. Li, X. Hu, K. Sun, and Z. Zang, "Defect passivation using ultrathin PTAA layers for efficient and stable perovskite solar cells with a high fill factor and eliminated hysteresis," *Journal of Materials Chemistry A*, vol. 7, no. 46, pp. 26421–26428, 2019.

[221] S. Roland, L. Yan, Q. Zhang, X. Jiao, A. Hunt, M. Ghasemi, H. Ade, W. You, and D. Neher, "Charge Generation and Mobility-Limited Performance of Bulk Heterojunction Solar Cells with a Higher Adduct Fullerene," *The Journal of Physical Chemistry C*, vol. 121, no. 19, pp. 10305–10316, 2017.

[222] M. A. Faist, P. E. Keivanidis, S. Foster, P. H. Wöbkenberg, T. D. Anthopoulos, D. D. C. Bradley, J. R. Durrant, and J. Nelson, "Effect of multiple adduct fullerenes on charge generation and transport in photovoltaic blends with poly(3-hexylthiophene-2,5-diyl)," *Journal of Polymer Science Part B: Polymer Physics*, vol. 49, no. 1, pp. 45–51, 2011.

[223] E. Castro, J. Murillo, O. Fernandez-Delgado, and L. Echegoyen, "Progress in fullerene-based hybrid perovskite solar cells," *Journal of Materials Chemistry C*, vol. 6, no. 11, pp. 2635–2651, 2018.

[224] Q.-H. Zhang, W.-D. Hu, X.-F. Wang, G. Chen, J.-p. Zhang, L.-X. Xiao, and T. Miyasaka, "Fullerene Multiadducts as Electron Collection Layers for Perovskite Solar Cells," *Chemistry Letters*, vol. 46, no. 1, pp. 101–103, 2017.

[225] R. G. Dickinson, "THE CRYSTAL STRUCTURE OF TIN TETRA-IODIDE," *Journal of the American Chemical Society*, vol. 45, no. 4, pp. 958–962, 1923.

[226] Z. Lin, Y. Su, R. Dai, G. Liu, J. Yang, W. Sheng, Y. Zhong, L. Tan, and Y. Chen, "Ionic Liquid-Induced Ostwald Ripening Effect for Efficient and Stable Tin-Based Perovskite Solar Cells," *ACS Applied Materials & Interfaces*, vol. 13, no. 13, pp. 15420–15428, 2021.

[227] Q. Tai, X. Guo, G. Tang, P. You, T.-W. Ng, D. Shen, J. Cao, C.-K. Liu, N. Wang, Y. Zhu, C.-S. Lee, and F. Yan, "Antioxidant Grain Passivation for Air-Stable Tin-Based Perovskite Solar Cells," *Angewandte Chemie International Edition*, vol. 58, no. 3, pp. 806–810, 2019.

[228] Z. Zhu, C.-C. Chueh, N. Li, C. Mao, and A. K.-Y. Jen, "Realizing Efficient Lead-Free Formamidinium Tin Triiodide Perovskite Solar Cells via a Sequential Deposition Route," *Advanced Materials*, vol. 30, no. 6, 2018.

[229] N. Ito, M. A. Kamarudin, D. Hirotani, Y. Zhang, Q. Shen, Y. Ogomi, S. Iikubo, T. Minemoto, K. Yoshino, and S. Hayase, "Mixed Sn–Ge Perovskite for Enhanced Perovskite Solar Cell Performance in Air," *The Journal of Physical Chemistry Letters*, vol. 9, no. 7, pp. 1682–1688, 2018.

[230] J. Xi, Z. Wu, B. Jiao, H. Dong, C. Ran, C. Piao, T. Lei, T.-B. Song, W. Ke, T. Yokoyama, X. Hou, and M. G. Kanatzidis, "Multichannel Interdiffusion Driven FASnI3 Film Formation Using Aqueous Hybrid Salt/Polymer Solutions toward Flexible Lead-Free Perovskite Solar Cells," *Advanced Materials*, vol. 29, no. 23, 2017.

[231] Z. Yang, A. Rajagopal, and A. K.-Y. Jen, "Ideal Bandgap Organic-Inorganic Hybrid Perovskite Solar Cells," *Advanced Materials*, vol. 29, no. 47, 2017.

[232] Z. Chen, M. Liu, Z. Li, T. Shi, Y. Yang, H.-L. Yip, and Y. Cao, "Stable Sn/Pb-Based Perovskite Solar Cells with a Coherent 2D/3D Interface," *iScience*, vol. 9, pp. 337–346, 2018.

[233] T. Jiang and W. Fu, "Improved performance and stability of perovskite solar cells with bilayer electron-transporting layers," *RSC Advances*, vol. 8, no. 11, pp. 5897–5901, 2018.

[234] J. You, L. Meng, T.-B. Song, T.-F. Guo, Y. M. Yang, W.-H. Chang, Z. Hong, H. Chen, H. Zhou, Q. Chen, Y. Liu, N. de Marco, and Y. Yang, "Improved air stability of perovskite solar cells via solution-processed metal oxide transport layers," *Nature Nanotechnology*, vol. 11, no. 1, pp. 75–81, 2016.

[235] Q. Bao, X. Liu, S. Braun, and M. Fahlman, "Oxygen- and Water-Based Degradation in [6,6]-Phenyl-C 61 -Butyric Acid Methyl Ester (PCBM) Films," *Advanced Energy Materials*, vol. 4, no. 6, p. 1301272, 2014.

[236] X. Meng, J. Lin, X. Liu, X. He, Y. Wang, T. Noda, T. Wu, X. Yang, and L. Han, "Highly Stable and Efficient $FASnI_3$ -Based Perovskite Solar Cells by Introducing Hydrogen Bonding," *Advanced Materials*, vol. 31, no. 42, p. e1903721, 2019.

[237] Q. Han, Y. Wei, R. Lin, Z. Fang, K. Xiao, X. Luo, S. Gu, J. Zhu, L. Ding, and H. Tan, "Low-temperature processed inorganic hole transport layer for efficient and stable mixed Pb-Sn low-bandgap perovskite solar cells," *Science Bulletin*, vol. 64, no. 19, pp. 1399–1401, 2019.

[238] L. E. Mundt, J. Tong, A. F. Palmstrom, S. P. Dunfield, K. Zhu, J. J. Berry, L. T. Schelhas, and E. L. Ratcliff, "Surface-Activated Corrosion in Tin–Lead Halide Perovskite Solar Cells," *ACS Energy Letters*, vol. 5, no. 11, pp. 3344–3351, 2020.

[239] B. Chabot and E. Parthé, "Cs 3 Sb 2 I 9 and Cs 3 Bi 2 I 9 with the hexagonal Cs 3 Cr 2 Cl 9 structure type," *Acta Crystallographica Section B Structural Crystallography and Crystal Chemistry*, vol. 34, no. 2, pp. 645–648, 1978.

[240] M. Ameri, E. Mohajerani, M. Ghafarkani, N. Safari, and S. A. Alavi, "The investigation of the unseen interrelationship of grain size, ionic defects, device physics and performance of perovskite solar cells," *Journal of Physics D: Applied Physics*, vol. 52, no. 12, p. 125501, 2019.

[241] H. Do Kim and H. Ohkita, "Charge traps in lead-halide perovskites with different grain sizes," *Japanese Journal of Applied Physics*, vol. 57, no. 8S3, p. 08RE03, 2018.

[242] Y. Ma, P. M. Hangoma, W. I. Park, J.-H. Lim, Y. K. Jung, J. H. Jeong, S. H. Park, and K. H. Kim, "Controlled crystal facet of $MAPbI_3$ perovskite for highly efficient and stable solar cell via nucleation modulation," *Nanoscale*, vol. 11, no. 1, pp. 170–177, 2018.

[243] G. Zheng, C. Zhu, J. Ma, X. Zhang, G. Tang, R. Li, Y. Chen, L. Li, J. Hu, J. Hong, Q. Chen, X. Gao, and H. Zhou, "Manipulation of facet orientation in hybrid perovskite polycrystalline films by cation cascade," *Nature Communications*, vol. 9, no. 1, p. 2793, 2018.

[244] P. Docampo, F. C. Hanusch, N. Giesbrecht, P. Angloher, A. Ivanova, and T. Bein, "Influence of the orientation of methylammonium lead iodide perovskite crystals on solar cell performance," *APL Materials*, vol. 2, no. 8, p. 081508, 2014.

[245] Z. S. Almutawah, S. C. Watthage, Z. Song, R. H. Ahangharnejhad, K. K. Subedi, N. Shrestha, A. B. Phillips, Y. Yan, R. J. Ellingson, and M. J. Heben, "Enhanced Grain Size and Crystallinity in $CH_3NH_3PbI_3$ Perovskite Films by Metal Additives to the Single-Step Solution Fabrication Process," *MRS Advances*, vol. 3, no. 55, pp. 3237–3242, 2018.

[246] L. Gu, D. Li, L. Chao, H. Dong, W. Hui, T. Niu, C. Ran, Y. Xia, L. Song, Y. Chen, and W. Huang, "Strain Engineering of Metal–Halide Perovskites toward Efficient Photovoltaics: Advances and Perspectives," *Solar RRL*, vol. 5, no. 3, p. 2000672, 2021.

[247] C. L. Hickey and E. M. Grumstrup, "Direct Correlation of Charge Carrier Transport to Local Crystal Quality in Lead Halide Perovskites," *Nano Letters*, vol. 20, no. 7, pp. 5050–5056, 2020.

[248] T. W. Jones, A. Osherov, M. Alsari, M. Sponseller, B. C. Duck, Y.-K. Jung, C. Settens, F. Niroui, R. Brenes, C. V. Stan, Y. Li, M. Abdi-Jalebi, N. Tamura, J. E. Macdonald, M. Burghammer, R. H. Friend, V. Bulović, A. Walsh, G. J. Wilson, S. Lilliu, and S. D. Stranks, "Lattice strain causes non-radiative losses in halide perovskites," *Energy & Environmental Science*, vol. 12, no. 2, pp. 596–606, 2019.

[249] C. Li, Q. Guo, H. Zhang, Y. Bai, F. Wang, L. Liu, T. Hayat, A. Alsaedi, and Z. Tan, "Enhancing the crystallinity of $HC(NH_2)_2PbI_3$ film by incorporating methylammonium halide intermediate for efficient and stable perovskite solar cells," *Nano Energy*, vol. 40, pp. 248–257, 2017.

[250] D. Luo, W. Yang, Z. Wang, A. Sadhanala, Q. Hu, R. Su, R. Shivanna, G. F. Trindade, J. F. Watts, Z. Xu, T. Liu, K. Chen, F. Ye, P. Wu, L. Zhao, J. Wu, Y. Tu, Y. Zhang, X. Yang, W. Zhang, R. H. Friend, Q. Gong, H. J. Snaith, and R. Zhu, "Enhanced photovoltage for inverted planar heterojunction perovskite solar cells," *Science*, vol. 360, no. 6396, pp. 1442–1446, 2018.

[251] W. Nie, H. Tsai, J.-C. Blancon, F. Liu, C. C. Stoumpos, B. Traore, M. Kepenekian, O. Durand, C. Katan, S. Tretiak, J. Crochet, P. M. Ajayan, M. Kanatzidis, J. Even, and A. D. Mohite, "Critical Role of Interface and Crystallinity on the Performance and Photostability of Perovskite Solar Cell on Nickel Oxide," *Advanced Materials*, vol. 30, no. 5, p. 1703879, 2018.

[252] G. Kim, H. Min, K. S. Lee, D. Y. Lee, S. M. Yoon, and S. I. Seok, "Impact of strain relaxation on performance of α-formamidinium lead iodide perovskite solar cells," *Science*, vol. 370, no. 6512, pp. 108–112, 2020.

[253] D. Luo, R. Su, W. Zhang, Q. Gong, and R. Zhu, "Minimizing non-radiative recombination losses in perovskite solar cells," *Nature Reviews Materials*, vol. 5, no. 1, pp. 44–60, 2020.

[254] V. Kaltenhauser, T. Rath, W. Haas, A. Torvisco, S. K. Müller, B. Friedel, B. Kunert, R. Saf, F. Hofer, and G. Trimmel, "Bismuth sulphide–polymer nanocomposites from a highly soluble bismuth xanthate precursor," *Journal of Materials Chemistry C*, vol. 1, no. 47, p. 7825, 2013.

[255] W. Lou, M. Chen, X. Wang, and W. Liu, "Novel Single-Source Precursors Approach to Prepare Highly Uniform Bi_2S_3 and Sb_2S_3 Nanorods via a Solvothermal Treatment," *Chemistry of Materials*, vol. 19, no. 4, pp. 872–878, 2007.

[256] Q. Han, J. Chen, X. Yang, L. Lu, and X. Wang, "Preparation of Uniform Bi_2S_3 Nanorods Using Xanthate Complexes of Bismuth (III)," *The Journal of Physical Chemistry C*, vol. 111, no. 38, pp. 14072–14077, 2007.

[257] B. Variano, D. Hwang, C. Sandroff, P. Wiltzius, T. Jing, and N. Ong, "Quantum effects in anisotropic semiconductor clusters: Colloidal suspensions of bismuth sesquisulfide and antimony sesquisulfide," *Journal of physical chemistry*, vol. 91, no. 26, pp. 6455–6458, 1987.

[258] T. Schnabel, T. Abzieher, T. M. Friedlmeier, and E. Ahlswede, "Solution-Based Preparation of $Cu_2ZnSn(S,Se)_4$ for Solar Cells—Comparison of $SnSe_2$ and Elemental Se as Chalcogen Source," *IEEE Journal of Photovoltaics*, vol. 5, no. 2, pp. 670–675, 2015.

[259] L. Zhang, K. Wang, and B. Zou, "Bismuth Halide Perovskite-Like Materials: Current Opportunities and Challenges," *ChemSusChem*, vol. 12, no. 8, pp. 1612–1630, 2019.

[260] P. Li, H. Dong, J. Xu, J. Chen, B. Jiao, X. Hou, J. Li, and Z. Wu, "Ligand Orientation-Induced Lattice Robustness for Highly Efficient and Stable Tin-Based Perovskite Solar Cells," *ACS Energy Letters*, vol. 5, no. 7, pp. 2327–2334, 2020.

[261] K. Chen, P. Wu, W. Yang, R. Su, D. Luo, X. Yang, Y. Tu, R. Zhu, and Q. Gong, "Low-dimensional perovskite interlayer for highly efficient lead-free formamidinium tin iodide perovskite solar cells," *Nano Energy*, vol. 49, pp. 411–418, 2018.

[262] M. Chen, Q. Dong, F. T. Eickemeyer, Y. Liu, Z. Dai, A. D. Carl, B. Bahrami, A. H. Chowdhury, R. L. Grimm, Y. Shi, Q. Qiao, S. M. Zakeeruddin, M. Grätzel, and N. P. Padture, "High-Performance Lead-Free Solar Cells Based on Tin-Halide Perovskite Thin Films Functionalized by a Divalent Organic Cation," *ACS Energy Letters*, vol. 5, no. 7, pp. 2223–2230, 2020.

[263] M. Chen, M.-G. Ju, M. Hu, Z. Dai, Y. Hu, Y. Rong, H. Han, X. C. Zeng, Y. Zhou, and N. P. Padture, "Lead-Free Dion–Jacobson Tin Halide Perovskites for Photovoltaics," *ACS Energy Letters*, vol. 4, no. 1, pp. 276–277, 2019.

[264] C. Zhang, S. Wu, L. Tao, G. M. Arumugam, C. Liu, Z. Wang, S. Zhu, Y. Yang, J. Lin, X. Liu, R. E. I. Schropp, and Y. Mai, "Fabrication Strategy for Efficient 2D/3D Perovskite Solar Cells Enabled by Diffusion Passivation and Strain Compensation," *Advanced Energy Materials*, vol. 10, no. 43, p. 2002004, 2020.

[265] L. Zeng, S. Chen, K. Forberich, C. J. Brabec, Y. Mai, and F. Guo, "Controlling the crystallization dynamics of photovoltaic perovskite layers on larger-area coatings," *Energy & Environmental Science*, vol. 13, no. 12, pp. 4666–4690, 2020.

[266] F. Yang, D. Jang, L. Dong, S. Qiu, A. Distler, N. Li, C. J. Brabec, and H.-J. Egelhaaf, "Upscaling Solution–Processed Perovskite Photovoltaics," *Advanced Energy Materials*, vol. 11, no. 42, p. 2101973, 2021.

[267] D.-K. Lee and N.-G. Park, "Materials and Methods for High–Efficiency Perovskite Solar Modules," *Solar RRL*, p. 2100455, 2021.

[268] D. M. DeLongchamp, B. D. Vogt, C. M. Brooks, K. Kano, J. Obrzut, C. A. Richter, O. A. Kirillov, and E. K. Lin, "Influence of a water rinse on the structure and properties of poly(3,4-ethylene dioxythiophene):poly(styrene sulfonate) films," *Langmuir : the ACS journal of surfaces and colloids*, vol. 21, no. 24, pp. 11480–11483, 2005.

[269] A. E. Maughan, A. M. Ganose, A. M. Candia, J. T. Granger, D. O. Scanlon, and J. R. Neilson, “Anharmonicity and Octahedral Tilting in Hybrid Vacancy-Ordered Double Perovskites,” *Chemistry of Materials*, vol. 30, no. 2, pp. 472–483, 2018.

List of scientific publications

Journal Paper

J. Zillner, H. Boyen, J. Hanisch, P. Schulz, D. Desta, J. Küffner, E. Ahlswede and M. Powalla, "The Role of SnF_2 Additives on Interface and Film Formation in All Lead-Free $FASnI_3$ Perovskite Solar Cells," *under preparation for submission to Advanced Funtional Materials*, 2021.

J. Zillner, H. Boyen, G. Delport, P. Schulz, J. Hanisch, J. Küffner, E. Ahlswede and M. Powalla, "Optimization of charge transport layer interfaces in $FASnI_3$ perovskite solar cells," *under preparation*.

J. Küffner, J. Hanisch, T. Wahl, **J. Zillner**, E. Ahlswede and M. Powalla, "One-Step Blade Coating of Inverted Double-Cation Perovskite Solar Cells from a Green Precursor Solvent," *ACS Applied Energy Materials*, 2021.

J. Küffner, T. Wahl, M. Schultes, J. Hanisch, **J. Zillner**, E. Ahlswede and M. Powalla, "Nanoparticle Wetting Agent for Gas Stream-Assisted Blade-Coated Inverted Perovskite Solar Cells and Modules," *ACS Applied Materials & Interfaces*, 2020.

M.Zinßer, T. Helder, A. Bauer, T. Magorian Friedlmeier, **J. Zillner** and M. Powalla, "Optical and electrical loss analysis of thin-film solar cells combining the methods of transfer-matrix and finite elements," *submitted to Solar Energy Materials & Solar Cells*, 2021.

Conference contributions

J. Zillner, C. Wessendorf, J. Hanisch, E. Ahlswede and M. Powalla, "Lead-free Bi-based perovskite solar cells: Morphology and band gap tuning," in *nanoGe International Conference on Perovskite Solar Cells, Photonics and Optoelectronics (NIPHO 2019)*, Jerusalem, February 2019.

J. Zillner, E. Ahlswede and M. Powalla, "Interface Optimization in $FASnI_3$ Perovskite Solar Cells," in *NanoGe Fall Meeting 2020 (NFM20)*, online conference, October 2020.

J. Zillner, E. Ahlswede and M. Powalla, "Investigation of PEDOT:PSS alternative and MA-free Sn-Pb mixed perovskite solar cell," in *13th International Conference on Hybrid and Organic Photovoltaics (HOPV2021*, online conference, May 2021.